

# $^{129}\text{Xe}$ RELAXATION AND RABI OSCILLATIONS

by

Mark Earl Limes

A dissertation submitted to the faculty of  
The University of Utah  
in partial fulfillment of the requirements for the degree of

Doctor of Philosophy

in

Physics

Department of Physics and Astronomy

The University of Utah

May 2014

Copyright © Mark Earl Limes 2014

All Rights Reserved

# The University of Utah Graduate School

## STATEMENT OF DISSERTATION APPROVAL

The dissertation of \_\_\_\_\_ Mark Earl Limes \_\_\_\_\_

has been approved by the following supervisory committee members:

\_\_\_\_\_ Brian Saam \_\_\_\_\_, Chair Oct 30, 2013  
Date Approved

\_\_\_\_\_ Carleton DeTar \_\_\_\_\_, Member Oct 30, 2013  
Date Approved

\_\_\_\_\_ Christoph Boehme \_\_\_\_\_, Member Oct 30, 2013  
Date Approved

\_\_\_\_\_ Michael Vershinin \_\_\_\_\_, Member Oct 30, 2013  
Date Approved

\_\_\_\_\_ Kenneth Woycechowsky \_\_\_\_\_, Member Oct 30, 2013  
Date Approved

and by \_\_\_\_\_ Carleton DeTar \_\_\_\_\_, Chair/Dean of

the Department/College/School of \_\_\_\_\_ Physics and Astronomy \_\_\_\_\_

and by David B. Kieda, Dean of The Graduate School.

## ABSTRACT

Several studies in magnetic resonance experiment and theory are presented. The longitudinal relaxation of solid  $^{129}\text{Xe}$  is shown to have an unexpected structural dependence through experiments that provide previously unattainable reproducibility; also, groundwork is laid for theories that describe the observed data. A history of the field is given, including a theory of nuclear spin relaxation due to the coupling of the spins to the phonon bath, as well as the description of an extension of this theory. Theoretical work is also presented that involves nontraditional methods of magnetic resonance detection, such as optically and electrically detected magnetic resonance in semiconducting material. This work confirms, using computational and theoretical methods, the presence of dipolar coupling between two paramagnetic spin-half states to account for observed behavior in Rabi oscillations resulting in an increase of the Rabi frequency by a factor of  $\sqrt{2}$ ; however, it is also shown that a strong presence of exchange coupling is required. Additional Rabi oscillation studies are given that involve experimental NMR water data, which confirm predictions of Rabi oscillation beat envelopes in three different regimes of longitudinal field modulation during a magnetic resonance experiment. Ancillary material include results from: a theoretical study of Rb atomic transition strengths, transverse relaxation in dilute-spin solid  $^{129}\text{Xe}$ , and longitudinal relaxation of gaseous  $^{129}\text{Xe}$  with regards to practical hyperpolarized  $^{129}\text{Xe}$  storage.

An idea is more important than its creator.

-George Fredrick Limes, Jr., (1951-2009)

# CONTENTS

ABSTRACT .....	iii
LIST OF FIGURES .....	vii
LIST OF TABLES .....	ix
ACKNOWLEDGMENTS .....	x
CHAPTERS	
<b>1. INTRODUCTION .....</b>	<b>1</b>
1.1 Quantum Mechanics .....	1
1.2 Magnetic Resonance (MR) .....	9
1.3 Dissertation Outline .....	13
<b>2. LONGITUDINAL RELAXATION IN SOLID <math>^{129}\text{Xe}</math> .....</b>	<b>15</b>
2.1 Introduction .....	15
2.2 History of the Problem .....	16
2.2.1 Foundations of theory and experiment .....	16
2.2.2 Reincarnation via hyperpolarization .....	22
2.2.3 Review of hyperpolarized $^{129}\text{Xe}$ experimental results .....	24
2.2.4 Theoretical formulation .....	30
2.2.5 Epilogue .....	43
2.3 Methods .....	43
2.3.1 Flow-through polarizer .....	44
2.3.2 Convection cell .....	48
2.3.3 Temperature control .....	49
2.3.4 Measurement of longitudinal relaxation .....	50
2.4 Results .....	52
2.4.1 Temperature dependence of ice .....	56
2.4.2 Temperature dependence of snow .....	59
2.4.3 Additional measurements .....	64
2.5 Discussion .....	68
2.5.1 Ice theory .....	68
2.5.2 Snow theory .....	78
2.6 Summary .....	79
<b>3. DIPOLAR AND EXCHANGE COUPLING BETWEEN CARRIER PAIRS IN DISORDERED SEMICONDUCTORS UNDERGOING RESONANCE .....</b>	<b>81</b>

3.1	Introduction . . . . .	81
3.2	Intermediate-spin-pair Model with Dipolar and Exchange Coupling . .	83
3.2.1	Finer points of the Hamiltonian . . . . .	84
3.2.2	Energy basis and observable . . . . .	90
3.3	Analytical and Numerical Methods . . . . .	92
3.3.1	Rotating-frame stochastic Liouville equation . . . . .	93
3.3.2	Limiting cases of the Rabi frequencies . . . . .	94
3.3.3	Liouville-space formalism . . . . .	98
3.4	Results and Discussion . . . . .	100
3.4.1	Dipolar coupling only . . . . .	101
3.4.2	Dipolar and exchange coupling . . . . .	105
3.5	Summary and Conclusion . . . . .	110
<b>4.</b>	<b>LOW-FREQUENCY MODULATION OF LONGITUDINAL FIELD: MODIFIED RABI ENVELOPES . . . . .</b>	<b>111</b>
4.1	Introduction . . . . .	111
4.2	Theoretical . . . . .	112
4.2.1	Description of three limiting regimes . . . . .	112
4.2.2	Rabi frame . . . . .	114
4.3	Experimental . . . . .	117
4.3.1	Methods . . . . .	117
4.3.2	Results and discussion . . . . .	120
4.4	Summary . . . . .	126
 <b>APPENDICES</b>		
<b>A.</b>	<b>RB <math>P_{1/2}</math>-ORBITAL ABSORPTION-EMISSION CYCLES . . . . .</b>	<b>130</b>
<b>B.</b>	<b>DILUTE-SPIN SOLID <math>^{129}\text{Xe}</math> TRANSVERSE RELAXATION . . . . .</b>	<b>140</b>
<b>C.</b>	<b>LONGITUDINAL RELAXATION IN GASEOUS <math>^{129}\text{Xe}</math> . . . . .</b>	<b>146</b>
<b>REFERENCES . . . . .</b>		<b>156</b>

## LIST OF FIGURES

1.1 $^{87}\text{Rb}$ relative excitation probabilities are shown. . . . .	6
1.2 A demonstration of excitation in a Bloch sphere picture, using the rotating-wave approximation (RWA). . . . .	10
2.1 A comparison of experimental and theoretical values of the chemical shift in solid $^{129}\text{Xe}$ is shown. . . . .	20
2.2 A compilation of temperature-dependent solid $^{129}\text{Xe}$ $T_1$ values is shown. . . . .	25
2.3 The theoretical calculation using Raman-scattering mediating the spin-rotation interaction is shown. . . . .	34
2.4 Schematic of flow-through polarizer and freezing cell. . . . .	45
2.5 Schematic of temperature-control system and chemical shift monitoring. . . . .	47
2.6 Schematics of useful NMR probes. . . . .	52
2.7 A comparison between snow and ice $^{129}\text{Xe}$ $T_1$ data at 77 K in a magnetic field of 2 T. . . . .	55
2.8 Shown are the plots of all temperature-dependent $^{129}\text{Xe}$ ice $T_1$ data in arbitrary units. . . . .	57
2.9 Shown is temperature-dependent $^{129}\text{Xe}$ ice $T_1$ data over a temperature range of 77-155 K. . . . .	58
2.10 Multi-exponential snow $^{129}\text{Xe}$ $T_1$ data measured at $120 \pm 0.5$ K, along with $T_2^*$ temperature dependence. . . . .	60
2.11 Plots of temperature-dependent snow data labeled according to measurement date. . . . .	61
2.12 Shown are a tally of all ice and snow $^{129}\text{Xe}$ $T_1$ data, omitting the Cates data for visual acuity. . . . .	64
2.13 Shown are the results from introducing oxygen into the sample-chamber area. . . . .	65
2.14 From (a) enriched snow, (c) enriched ice, and (e) dilute-spin ice, the isotope dependence of solid $T_1$ is shown to be negligible. . . . .	67
2.15 Generic Feynman diagrams for a process involving (a) one phonon, (b) two phonons, and (c) three phonons absorbed or emitted, with unique phonons contributing to the process. . . . .	76
3.1 A simplified picture of a pi-conjugated system within molecular orbital theory in relation to the definition of the hole spin state. . . . .	85

3.2	Plots of the Fast Fourier Transform $\text{FFT}\{Q(\tau)\}$ of the observable $Q(\tau)$ as a function of the excitation frequency $\omega$ , in the regime of dipolar coupling only. . . . .	102
3.3	The strong-dipolar coupling simulation using a Pake distribution, with no exchange coupling. . . . .	104
3.4	The results of the stochastic Liouville-space simulation with varying $J/2\pi$ and $D/2\pi$ are shown. . . . .	106
3.5	The strong-dipolar coupling simulation using a Pake distribution, with exchange coupling. . . . .	109
4.1	Demonstration of the Rabi-frame Bloch sphere picture. . . . .	115
4.2	A schematic of the NMR probe and a graphical description of theoretical predictions and experimental NMR data. . . . .	119
4.3	Experimental fast-modulation data are plotted. . . . .	122
4.4	Shown is experimental confirmation of the strong-modulation regime. . . . .	124
4.5	Experimental weak-resonant data are plotted and fit to theory, along with a description of the Rabi frame at play. . . . .	127
A.1	The results of the analytical solutions to the rate equations for $^{87}\text{Rb}$ are shown. . . . .	134
A.2	The results of the analytical solution to the rate equations for $^{85}\text{Rb}$ are shown. . . . .	138
B.1	Schematics detailing the operation of the convection cell are shown. . . . .	142
B.2	Line shape data from the 5.5% $^{129}\text{Xe}$ convection cell, 161A. . . . .	143
B.3	Dilute spin line shape data from cell 161B and cell 161C. . . . .	144
C.1	Images of Rb-Xe hyperpolarization processes are shown. . . . .	147
C.2	Schematics of the coldfinger and storage cell are shown. . . . .	150
C.3	The raw data from a set of xenon-only, helium saturated, and nitrogen saturated runs are shown. . . . .	152
C.4	The raw data from a set of nitrogen dependent runs at room temperature are shown. . . . .	154

## LIST OF TABLES

2.1	Lattice parameters for solid xenon (fcc), including nearest-neighbor data.	32
2.2	Initial naturally abundant xenon, solid $^{129}\text{Xe}$ ice and snow $T_1$ values. . .	53
B.1	$^{129}\text{Xe}$ concentrations for the cells used in the dilute spin experiments. . .	141

## ACKNOWLEDGMENTS

Through the course of the work of this thesis and my graduate career, I have many people to thank. The order in which I'll thank them is work, friends, family.

To be cliché, I'd first like to thank Prof. Brian Saam for letting me in his group as it was an admittedly risky venture on his part. His guidance has been invaluable, from the initial time he spent with me on electronics, right up to the present day with writing papers and teaching me basic English again (though I'll not stop trying to reintroduce "vicinitude" into the language). A true Tigers fan (though also a Michigan Man), he leads by example, and I'll never be able to repay him for the various jams he's gotten me out of over my graduate career; situations that prove he's not only a great advisor, but a great human being—for that I thank him. Needless to say I've had those situations go completely the other way in the past, so it makes me appreciate all the more what he's done for me over these last four years. It's safe to say that a person's success in their career can be traced back to but a handful of people, and for me he is one of those people. If I had the choice to do it all over again, in his group, I would in a heartbeat—he's just that good of a boss to work for, and I'm happy to call him a friend as well.

One of the situations Brian fixed for me was that of funding, when he asked if I would be interested in working for Prof. Christoph Boehme, the second person I'd like to thank. Christoph also took a chance on me when he really didn't have to, and introduced me to the world of organic semiconductors. Seeing Christoph in action is quite remarkable, working for him and writing with him has been a pleasure and very valuable career experience. I'd also like to thank the rest of my committee, as I was lucky enough to interact with them outside of simply showing up and signing things for me. Prof. Mikail Raikh and Dr. Rachel Glenn were gracious enough to let me in on their project, and I think the end product was quality. In short, I'm lucky to have received all the opportunities that I've gotten at the University of Utah's

Department of Physics and Astronomy, working with good people makes it hard to leave, and it'll be hard to top this experience. In this vein, I'd also like to thank the Swigart Scholarship Fund for support, especially for the finishing of my dissertation and writing up the solid xenon work, as our NSF funding had been lost for that project.

Now on to the friends, of which I've made many through the years here in Utah. First and foremost concerning this work is the patience and wisdom expressed by my old lab mates in Brian's group, Dr. Eric Sorte and Dr. Zayd Ma. Eric taught me the importance and effectiveness of raw determination, and that at some point it doesn't make sense to keep talking about an experiment, just set it up in a day and go—quite a novel thought for me at the time. Zayd was also very self-motivated, and that kind of work ethic is infectious for me—he also always had just the right question that would feed my insomnia and curiosity in just the right way. (I don't send "World's Best Labmate" plaques to just anyone, you know?) I'll always remember our late nights rendezvous quite fondly, and I can honestly say I'd never be a Reverend of the Church of the Latter-day Dude if not for knowing him. Zayd always took me out of my element, in a very good and productive way, and I think our professional relationship is perfectly summed up by an analogy of him and his wonderful now-wife, Dr. Monica Allen, selecting me to preside over their wedding. I wasn't necessarily comfortable doing it, but Zayd got me through it kicking and screaming; I enjoyed every minute of it, and the end result was pretty good, if I do say so myself.

I also had the pleasure of working with a plethora of undergrads and a high school student in Brian's group that had the patience enough to listen to my convoluted ramblings; in no particular order: Elliot Nielsen, Haliagh Emerson, Laurel Hales, Oliver Jeong, Touchdown Tommy, Erik Houghtby, Matt Hunsaker, and Tom Paskvan. I'll single out Tom Paskvan (and his wife Dr. Meg) for being awesome friends and neighbors outside of work, even though we didn't have all that much time to get to know each other. Lastly in the group but certainly not least, I had the privilege of teaching the new guy, Eddie Thennel, some physics things... but he schooled me on most every other topic that was culture related. I hope a majority of these group interactions were positive for the other people too, and I've been lucky to have good

people like Eddie around me.

I keep using the word “lucky,” but I don’t use it lightly, it simply fits perfectly. I was lucky to get in the graduate class I did, at the time I did, because I’ve made some really good, what I consider life-long friends in the process of being in graduate school. When Dr. Aaron Ballard and I first worked on some homework together, and when Dr. Nick Borys and I first introduced each other in our TA training program, I had no idea we’d still be talking to this day, let alone be good friends. Apart from the vestiges of our music recording and begging the question of “Dogecoin,” Aaron and I still meet on a weekly basis to watch shows or movies, and will undoubtedly get rich with each other someday. Nick and his great wife, Stefanie, are always open to having us visit and stay with them, wherever they live, and I can only dream and patiently wait until the day we open that dive bar in the country. In the same vein of good friends, Dr. Dustin Winslow and his fiance, Dr. Michelle Hui, let me live with them when I moved back to Salt Lake City, and they were both incredibly awesome to hang out with and know in general. Michelle was, in my opinion, probably the most intelligent out of anyone in our class even though she never let on, and I still enjoy her eccentric e-mails to this day. Dustin and I came from similar backgrounds, education- and life-wise, which is probably why we hit it off quickly and remain good friends—his slowly meandering stories with no point will never be quieted, no matter how many times he asks me to stop them. Dr. Kipp van Schooten and his awesome wife, Tea, are also an extreme pleasure to know and hang out with, especially for Sunday breakfasts. Kipp has become very important in my professional life as well, and we’ve worked on many projects together, whether just bouncing off crazy ideas in private (Iroc-Z’s and Winnebago’s) or writing papers—he’s an invaluable resource for all things scientific (but Python schilling, really?). It’s the same situation for all of these people in our entry class, they were awesome to work with, but they’re even funner to hang out with in an unprofessional setting.

That notion extends to other students and post-docs I’ve worked with in the department, too. The first I’d like to mention on that list is Dr. Will Baker, because without him I’d have given up on this theoretical problem in Christoph’s group, but he convinced me to continue and it wound up to be my first first-author paper,

and Chapter 3 of this dissertation. Alex Theissen has also been generally awesome, with the highlights for me probably being a yurt excursion for Zayd's bachelor party (see above: kicking and screaming) and the Artsy Partsy's birthday bashes with Dr. Philippe Klemm. Dr. Hans Malissa knows the finer points of good beer (as well as spin techniques) and was a pleasure to get to know, ditto for Dr. Dane McCamey. There are many more people I'm leaving out for the sake of space, but I'll echo the sentiment—they were awesome to work with, but they're even funner to hang out with in an unprofessional setting.

Speaking of an unprofessional setting, I have to thank all of my Ohio friends that I grew up with and helped me along the way. I came from a relatively small, rural high school, but again I was lucky to have the class that I did, because we ended up with a few doctors, many professionals, and a few alcoholics. Speaking of alcoholics, I'll mention Adam Hock. (That joke was the thanks for everybody at Otsego High School.) The Mauk's were, and are, good friends, but we don't really know why. Pat Ryan, Brad Babcock, Sam Wright, Jay Rider, Tim Joseph, and Bob Brandeberry all had the displeasure to listen to me sing, and are all now doing well, presumably as a result of not having to see me on a regular basis. My cousin, Josh, always said I was smarter than him, but he makes more money than I'll ever make, so who's the smart one?

More influential on what I've been doing lately, are Adam Sears, Ty Brott, and Kurt Gerken. I've known Adam for what I can only describe as feeling like an eternity, and we've essentially been holding self-deprecation contests ever since. Ty, his super-cool wife, Jenn, and their families I was all lucky enough to meet through Adam, and they have been awesome to hang out with, through good times and sad pants. Kurt completes the wrecking crew we had assembled for awhile, and I only hope that someday we'll get the band back together.

I'd like to give the most, moster, and moistest thanks to my lovely wife, Heidi, who has been the most patient and understanding person I could have ever imagined through this whole process (by process, I mean me living life). I'm really glad that she came out to Utah to live with me, pretty much on a whim, and she's been ultra-supportive the entire way. In addition to amassing an insurmountable debt of

“cuddle dollars,” whatever those are, I’ll truly never be able to repay her for keeping my sanity (mostly) and having someone awesome and motivating to always hang out with. I could literally write a Tolstoy-length treatise of thanks for her, and it wouldn’t do the situation justice, so she’ll have to settle for... thanks babe. We’ll always have Man-Man in Buffalo, and I’m looking forward to you showing me the ropes of New York. In return, I’ll show you how to get a higher credit score, and teach you about compounded interest and calculus. Love you, Heidikins!

Finally, I’d like to thank my family, as probably the hardest part of being out in Utah was being away from them. My grandparents were great, with the Weaver side always playing card games and puzzles, and the Limes side giving me candy and laughs. I’m lucky to have the supportive and great extended family that I do, and it’s always a pleasure getting together with anyone and everyone. My brother Chip taught me algebra at a very young age, and my brother Matt taught me how to drink. They both have beautiful families now, and I always look forward to coming back for Christmas. My mom has been putting up with me for all of my life, and the absolute hardest part of doing this was being away from her. She is the best mom anybody could ask for, teaching me the hard, quality lessons that you can only get from good parents. Lessons such as: Nothing is free, and you get what you pay for. My dad is the one who convinced me to come back out to finish my degree, and it’s what he would have wanted out of me, so I dedicate this work to him. An electrician by trade, I truly think he’d have gotten a kick out of the experimental end of physics (and have been pretty good at it), and I think about him every day in the lab, and in my life in general. He was an awesome guy.

# CHAPTER 1

## INTRODUCTION

*I'm stuck on Hume's fork.*

The primary field this dissertation lies within is magnetic resonance theory and experiment, specifically concerning nuclear magnetic resonance (NMR) and electron paramagnetic (or spin) resonance (EPR or ESR). NMR studies presented in Chapter 2 involve solid xenon that is polarized by spin-exchange optical pumping (SEOP), thus there is some discussion of atomic physics related to this technique. Chapter 3 concerns EPR of electron-hole pairs in semiconductors, specifically electrically or optically detected magnetic resonance (EDMR and PDMR). The modulation of the longitudinal field in a magnetic resonance experiment is presented in Chapter 4, where a two-coil probe is used to detect Rabi oscillation envelopes of water undergoing magnetic resonance. Some prerequisite knowledge for this thesis is found in Halliday et al. [1], Tipler and Llewellyn [2], and Griffiths [3, 4]. The following sections contain general information about quantum mechanics and magnetic resonance that is used throughout this dissertation.

### 1.1 Quantum Mechanics

$$i\hbar \frac{\partial \Psi}{\partial t} = \hat{H} \Psi \quad (1.1)$$

Eq. 1.1 is Schrödinger's wave equation [4, 5, 6, 7], which describes the time evolution of a physical state within the framework of quantum mechanics.  $\hat{H}$  is called the Hamiltonian and represents the sum of the kinetic ( $\hat{T}$ ) and potential ( $\hat{V}$ ) energy of the system,  $\hbar$  is Planck's constant divided by the factor  $2\pi$ , and  $\Psi$  is the wave function representing the state of the system of interest. Using the density matrix  $\rho$ , essentially a method for bookkeeping of all states and coherences in the system, a

convenient rewriting of Eq. 1.1 is called the Liouville-von Neumann equation, given by

$$i\hbar \frac{\partial \rho}{\partial t} = [\rho, \hat{H}], \quad (1.2)$$

where  $[\rho, H] = \rho H - H \rho$  is a commutator [8, 9, 10, 11]. Using Dirac “bra-ket” notation, in a given basis  $|\phi_m\rangle$ , the density matrix can be defined with entries

$$\rho_{mn} = \langle \phi_m | \rho | \phi_n \rangle = \sum_i p_i \langle \phi_m | \psi_i \rangle \langle \psi_i | \phi_n \rangle, \quad (1.3)$$

with  $p_i$  the probability of finding the system in the state  $|\psi_i\rangle$ , and  $\rho$  is the density operator. Within the context of classical physical systems, the state of a particle in three dimensions can be represented by three generalized coordinates (three degrees of freedom), in addition to other identifying quantities such as charge and mass. The complete description of numerous particles’ quantum states, however, requires an additional degree of freedom for intrinsic angular momentum present in the particle, called “spin.” For a majority of this text, the interaction with the spin degrees of freedom of a system (and therefore the spin Hamiltonian) are the main focus; the motional degrees of freedom are typically restricted in some way or represented by various relaxation rates. For a particle (or nucleus) with nonzero spin there is a magnetic moment  $\boldsymbol{\mu}$  associated with the spin, the strength of which is defined by gyromagnetic ratio  $\gamma$  in NMR (or  $g$ -factors,  $g$  in ESR) along with a spin operator  $\mathbf{S}$  to indicate the direction of the magnetic moment as  $\boldsymbol{\mu}_S = \gamma \mathbf{S}$  (or  $\boldsymbol{\mu}_S = g_S \mu_B \mathbf{S} / \hbar$ ), where  $\mu_B$  is the Bohr magneton. In an absence of any magnetic field or couplings, all spin states are energy degenerate. A magnetic field splits this degeneracy along the direction of the magnetic field, an effect first observed by Zeeman, which can be represented in the spin Hamiltonian by the coupling term  $-\boldsymbol{\mu}_S \cdot \mathbf{B}$ , where  $\mathbf{B}$  is an external magnetic field.

The approximate energy levels of a hydrogen atom can be solved for by considering a Coulomb potential in a radial Schrödinger equation. The spatial part of the hydrogen wave functions is described with three quantum numbers:  $n$ ,  $l$  (or  $L$ ), and  $m$  (or  $m_L$ ). The principle quantum number is denoted  $n$ , and is related to the total energy of an atom. The angular momentum quantum number  $l = 0, 1, \dots, n - 1$  determines magnitude of the orbital angular momentum (and is also an indicator of which orbital

the electron resides in). The magnetic quantum number  $m = -l, \dots, +l$  determines the angular momentum projected onto a specified axis. Four more quantum numbers needed to describe the hydrogen atom are the spin of the nucleus  $I$  and its projection onto a specified axis  $m_I = -I, \dots, +I$ , and the spin of the electron  $S$  and its projection onto a specified axis  $m_S = -S, \dots, +S$ .

An important consequence of Eq. 1.1 is that a superposition of solutions remains a solution. The so-called superposition principle can be considered at the heart of quantum mechanics [12]. For the hydrogen atom, this means it exists in a superposition of states, which can be measured by “collapsing” or “localizing” the wave function into a specific eigenstate of the measurement operator. This strange thought persists through all of quantum mechanics, nonrelativistic and relativistic. Thus, the state of an atom can be successfully described as a superposition of a ground state and an excited state, where an admixture of the atom’s existence is a physical reality.

In the appropriate regime where any applied magnetic field is sufficiently weak, the useful quantum number for a hydrogen-like atom with no nucleus is  $m_J$ , which is an eigenvalue of the operator  $\mathbf{J} = \mathbf{L} + \mathbf{S}$ . Here,  $\mathbf{L}$  is the orbital angular momentum operator and  $\mathbf{S}$  is again the electron spin operator. Let the nuclear spin angular momentum operator in an atom be denoted by  $\mathbf{I}$ . Associated with all angular momenta of the atomic system are magnetic moments, e.g.,  $\boldsymbol{\mu}_J = g_J \mu_B \mathbf{J} / \hbar = \gamma_J \mathbf{J}$  and  $\boldsymbol{\mu}_I = g_I \mu_N \mathbf{I} / \hbar = \gamma_I \mathbf{I}$ , where  $\mu_N$  is the nuclear magneton. The addition of  $\mathbf{I}$  and  $\mathbf{J}$  is considered as the total angular momentum operator of the atom,  $\mathbf{F} = \mathbf{I} + \mathbf{J}$  (with magnetic moment  $\boldsymbol{\mu}_F = g_F \mu_B \mathbf{F} / \hbar$ ). Each of these angular momenta couple to the magnetic field  $\mathbf{B}$  with a Zeeman interaction  $-\boldsymbol{\mu} \cdot \mathbf{B}$ . The valid or “good” quantum numbers in this system are dependent on magnetic field and coupling strengths. Essentially, the composite quantum numbers  $m_F$  and  $m_J$  are a good description of the system until a decoupling mechanism such as an external magnetic field becomes sufficiently large, such that the constituent angular momenta preferentially couple to an external field rather than to each other. As an example, in the weak-field regime, the spin angular momentum of the electron  $\mathbf{S}$  and orbital angular momentum  $\mathbf{L}$  are so well-coupled that it simply is not valid to refer to one without the other; if you affect  $\mathbf{L}$  you must affect  $\mathbf{S}$ , and vice versa. An external magnetic field serves as a mechanism

to decouple  $\mathbf{I}$ ,  $\mathbf{S}$ , and  $\mathbf{L}$  from each other, and in the very high-field regime the “good” quantum numbers are  $m_I$ ,  $m_S$ , and  $m_L$ . Remarkably, solving Eq. 1.1 for a  $m_J = 1/2$  atomic state, Breit and Rabi [13] analytically discovered the energy splitting of such coupled spin states for all magnetic field values. The Breit-Rabi equation is given by

$$E = -\frac{h\nu_{\text{hfs}}}{2[I]} - \gamma_I B m_F \pm \frac{h\nu_{\text{hfs}}}{2} \sqrt{1 + \frac{4m_F(\gamma_J - \gamma_I)B}{[I]h\nu_{\text{hfs}}} + \left(\frac{(\gamma_J - \gamma_I)B}{h\nu_{\text{hfs}}}\right)^2}, \quad (1.4)$$

where  $\nu_{\text{hfs}}$  is the zero-field hyperfine splitting, and  $[I] = 2I + 1$  is the total number of available nuclear states [14].

An alkali atom, such as Rb, is well-approximated by considering only its valence electron in a hydrogen-like wavefunction. As a carry-over from the terminology from the discovery of the well-known “sodium doublet” transition lines,  $D_1$  and  $D_2$  for Rb (spin-5/2  $^{85}\text{Rb}$  or spin-3/2  $^{87}\text{Rb}$ ) correspond to the  $5^2S_{1/2} \leftrightarrow 5^2P_{1/2}$  and  $5^2S_{1/2} \leftrightarrow 5^2P_{3/2}$  transitions, respectively. Here, spectroscopic notation is given by  $n^{2S+1}L_J$ , where  $L$  is the occupied orbital and  $J$  is the total angular momentum quantum number. For both  $^{85}\text{Rb}$  and  $^{87}\text{Rb}$ , the  $D_1$  and  $D_2$  transitions are at approximately 795 nm and 780 nm. The energy of atomic transitions for  $^{85}\text{Rb}$  or  $^{87}\text{Rb}$  in a magnetic field can be calculated to a high degree using Eq. 1.4, where the zero-field hyperfine splitting can be obtained the  $D_1$  and  $D_2$  transitions.

Either the classical electromagnetic field [15, 16] or the quantum electromagnetic field [17, 18] can be written in terms of spherical harmonics, leading to a multipole expansion of electromagnetic radiation or photons. These multipoles are expressed in terms of electric (E) and magnetic (M) dipole, quadrupole, octupole, etc. moments. Many atomic physics experiments are well described within the electric dipole (E1) approximation, which, classically, is considered the leading term in an expression that represents the monochromatic field of a plane wave for sufficiently long wavelengths. It is important to note that within this approximation, at low and high magnetic fields, light cannot directly affect atomic spin states—only orbital angular momentum can be affected. However, because the orbital and spin angular momenta are strongly coupled in certain regimes, any manipulation to a state’s orbital angular momentum necessarily affects the spin. An example of this phenomenon is in a widely used technique for creation of hyperpolarized noble gas, called depopulation pumping, and

is used to optically polarize Rb atomic states [19, 20] (see Fig. 1.1). Here, the ground state has an orbital angular momentum of  $L = 0$ , so that a  $3/2 \otimes 1/2$  product space is used for angular momentum addition. The relative probabilities for excitation of each state are calculated using a change of basis from  $F, m_F$  to  $m_I, m_J$  with appropriate Clebsch-Gordan coefficients, and isolating the  $m_J \rightarrow m_J + 1$  transitions. A quick example of this calculation is given in Fig. 1.1(b), where the E1 approximation is used. In the calculation, the factors  $m, \hbar$ , and  $\omega_{fi} = (E_f - E_i)/\hbar$ , where  $E_f$  and  $E_i$  are the energies of the final and initial states, will cancel out when considering the relative probabilities of each transition as it is assumed that all  $\omega_{fi}$ 's are approximately equal. Following this analysis, every ground state is pumped out with  $\sigma_+$  light except for the  $m_F = 2$  state, as there is no allowed, available excitation transition. (An approximate calculation of the absolute probability of transition is accomplished with Fermi's golden rule,

$$d\Gamma = \frac{2\pi}{\hbar} |V_{fi}|^2 \delta(E_f - E_i), \quad (1.5)$$

which, when integrated, gives the transition probability, where  $V_{fi}$  is the matrix element between the initial and final state, and  $E_f$  ( $E_i$ ) is the final (initial) energy of the state).

Concerning the emission of light from the excited atom, the model is somewhat more complicated—to see this, first consider a simplified model where nuclear spin is neglected ( $I = 0$ ), as in Fig. 1.1(c). To obtain the correct probabilities of emission in absence of buffer gas, the total orbital angular momentum  $L = 1$  of the  $5^2P_{1/2}$  state must be considered; that is, an operator product space of  $1 \otimes 1/2$  must be used. Considering dipole (E1) radiation from the excited state, the emitted light can be of any polarization, leading to the selection rule  $\Delta m_L = +1, 0, -1$ . This allows for a finite, nonnegligible probability that an excited  $5^2P_{1/2}, m_J = +1/2$  state will de-excite to a  $5^2S_{1/2}, m_J = +1/2$  state. All of the broad strokes of depopulation pumping are contained in this simple model, and this model is, in fact, the appropriate one for the excited state when considering the extremely short lifetime (compared to the lifetime needed for the hyperfine interaction to take effect and polarize the nuclei) of the excited state due to inclusion of buffer gas. However, in order to get the exact probabilities of emission from the excited state of a bare  $^{87}\text{Rb}$  atom to the ground

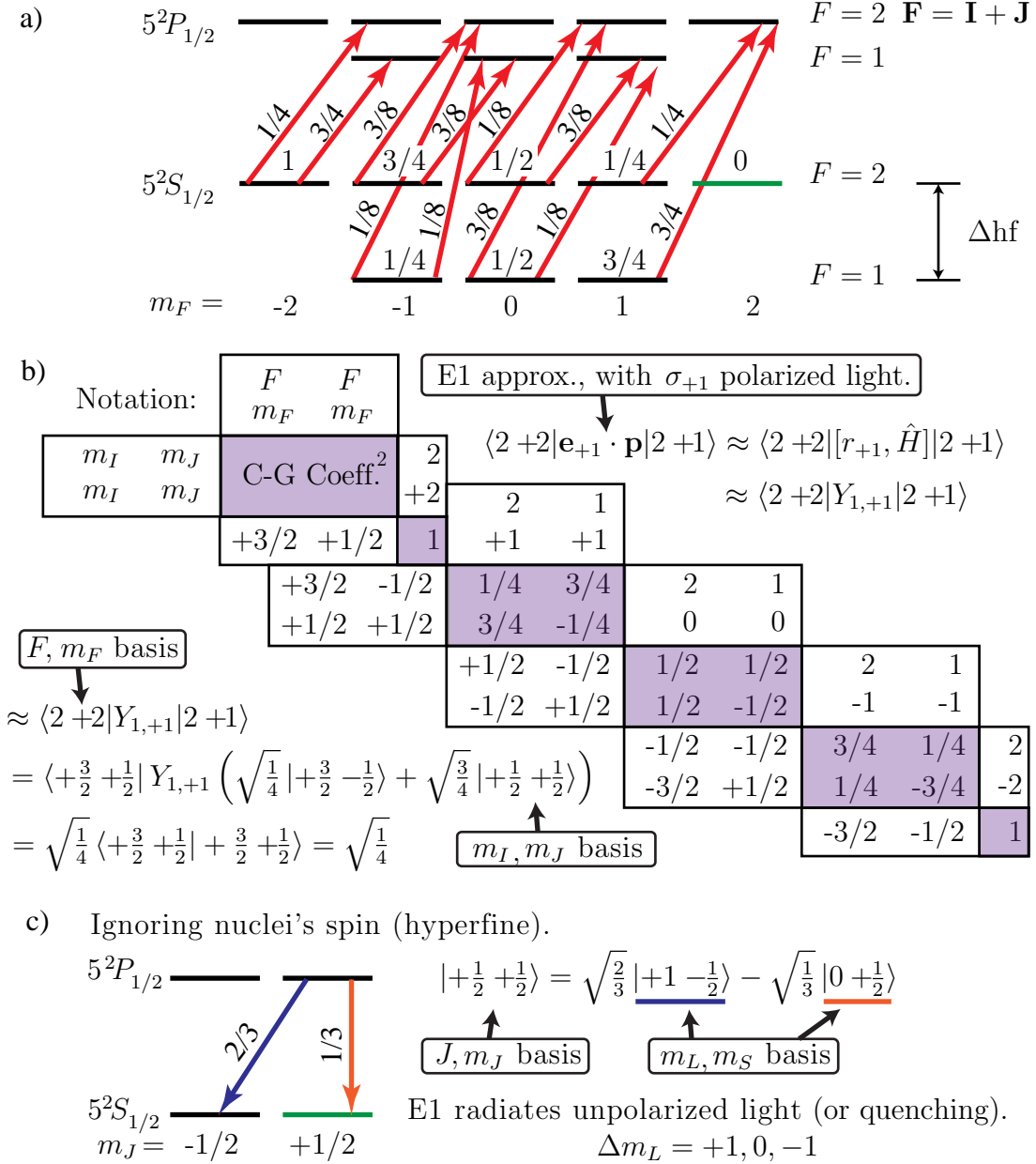


**Figure 1.1.** <sup>87</sup>Rb relative excitation probabilities are shown. (a) <sup>87</sup>Rb relative excitation probabilities are shown for 795 nm,  $\sigma_+$  light. There is no excitation from the ground  $m_F = 2$  state (in green).  $5^2S_{1/2}$  has a hyperfine interaction  $\Delta hf$ . (b) A Clebsch-Gordan Coeff. table is given for  $3/2 \otimes 1/2$  system, along with an example of the relative absorption probabilities, where  $\mathbf{e}_{+1}$  is the polarization of the light, and  $Y_{l,m}$  are spherical harmonics. (c) A simplified emission diagram is shown that neglects nuclei.

state with the hyperfine interaction considered, the state space  $3/2 \otimes 1 \otimes 1/2$  must be used. In Appendix A, a mixed model is described where the ground state  $5^2S_{1/2}$  electron has a spin-3/2 and spin-5/2 hyperfine splitting due to the  $^{87}\text{Rb}$  and  $^{85}\text{Rb}$  nuclei, with probabilities for emission-absorption of an  $I = 0$  excited  $5^2P_{1/2}$  state. In this way, in the presence of buffer gas, depopulation pumping of the Rb atom occurs using  $\sigma_+$  light tuned to the  $D_1$  transition, leading to a large polarization of the  $5^2S_{1/2}$ ,  $m_F = +2$  state. Light tuned to the  $D_2$  transition is considered negligibly polarized in comparison, as the  $m_F = +2$  state has an available transition to the  $5^2P_{3/2}$  manifold. After optically polarizing these Rb states, spin-exchange can occur between an optically pumped Rb atom and the nuclei of a noble gas (such as  $^3\text{He}$ ,  $^{129}\text{Xe}$ , or  $^{131}\text{Xe}$ ) due to wave-function overlap of the ground-state Rb electron and the noble-gas nucleus.

A fruitful quantum mechanical system called a two-level system is made from two well-defined, nondegenerate quantum states. The interesting effects of the two-level system arise from the superposition of the two basis states forming the total quantum state. Using a sufficiently broad light source, an example of a two-level system is seen from the two orbitals that comprise the  $D_1$  transition in Rb, in zero magnetic field—one state  $|0\rangle$  being the ground state (electron occupies the  $5^2S_{1/2}$  orbital), and the other  $|1\rangle$  being the excited state (electron occupies the  $5^2P_{1/2}$  orbital). The energy of each state is labelled as  $E_0$  and  $E_1$ , with an on-resonant transition frequency at  $\omega_{10} = (E_1 - E_0)/\hbar$ . In a two-level system such as this, Rabi oscillations arise from driving the system with near-resonant electromagnetic radiation [21], in which the probability to observe a particular state fluctuates sinusoidally with the Rabi frequency. Rabi oscillations in this context come from the absorption and stimulated emission that occurs from a continuous (or quantized in the Jaynes-Cummings model) electromagnetic field applied to the two-state system. The time-dependent perturbation problem is solved using either Eq. 1.1 or Eq. 1.3, and  $2V/\hbar = \Omega e^{i\omega t} |0\rangle \langle 1| + \Omega e^{-i\omega t} |1\rangle \langle 0|$  represents the rotating wave approximation (RWA)<sup>1</sup> of a sinusoidally oscillating electric field of the continuous light causing the

---

<sup>1</sup>This approximation throws away any terms arising that oscillate at twice the resonance frequency, a good approximation with a well-separated two-level system.

atomic dipole transition. If the system is initially in the ground state, the probability of observing the excited state  $|1\rangle$  with respect to time and excitation frequency is

$$P_1 = \frac{\Omega^2}{\Omega_R^2} \sin^2 \left( \frac{\Omega_R t}{2} \right), \text{ with } \Omega_R = \sqrt{\Omega^2 + (\omega - \omega_{10})^2}. \quad (1.6)$$

The parameter  $\Omega_R$  is typically defined as the Rabi frequency, although definitions sometimes vary by context.

The Rabi frequency is an important benchmark for how fast an experimentalist is able to change a quantum state within a particular system. Consider quantum computing, which relies on the superposition of bits (1's and 0's) into quantum bits (qubits), such as

$$|\Psi\rangle = c_1 |0\rangle + c_2 |1\rangle. \quad (1.7)$$

The Rabi frequency gives a measure of how fast the qubit can be flipped, making it a very important quantity for computational operations [22].

Concluding this brief overview of quantum mechanics, one of the most important results of quantum mechanics is the Heisenberg uncertainty principle [23, 24]. In terms of the standard deviation  $\sigma_{\hat{A}} = \sqrt{\langle \hat{A}^2 \rangle - \langle \hat{A} \rangle^2}$  for a Hermitian operator  $\hat{A}$ , where  $\langle \hat{A} \rangle$  is an expectation value, the uncertainty relation between two operators  $\hat{A}$  and  $\hat{B}$  is

$$\sigma_A \sigma_B \geq \frac{1}{2} | \langle [\hat{A}, \hat{B}] \rangle |, \quad (1.8)$$

with the commutator defined as  $\langle [\hat{A}, \hat{B}] \rangle = \langle \hat{A}\hat{B} - \hat{B}\hat{A} \rangle$ . An example of this uncertainty principle is the relation between position  $\hat{x}$  and momentum  $\hat{p}$ , where the relation becomes  $\sigma_x \sigma_p \geq \hbar/2$ . The uncertainty principle essentially puts an intrinsic limit on what is observable within the framework of quantum mechanics. Due to a lack of a full-fledged quantum mechanical theory of time measurements, the time-energy uncertainty principle lacks universality and depends on context [25]. Thus, there are different types of time-energy uncertainty relations that can be summarized with the relation

$$\Delta t \Delta E \gtrsim \hbar, \quad (1.9)$$

where the exact inequality and range of validity depends on the interpretation of  $\Delta t$  and  $\Delta E$ .

## 1.2 Magnetic Resonance (MR)

The beauty of magnetic resonance (MR) techniques is that the basic tenets of quantum mechanics are seen with readily accessible experiments; magnetic resonance serves as a playground for basic quantum mechanical ideas [26, 27, 28, 29, 30, 31, 32, 33, 34]. A majority of NMR experiments that occur today are of the single-coil “pulsed” flavor, with EPR catching up in this respect. The general overview of a spin-1/2 NMR experiment begins with letting some polarization of many nuclear spin states build up along a quantization axis determined by a relatively large magnetic field, which creates a net magnetization (due to thermodynamics) that arises from a net polarization of the nuclear spin states in the sample. The spin states are then manipulated with an alternating pulse of magnetic field at a frequency proportional to that of the energy splitting between the two spin states. On resonance, this pulse causes the magnetization to nutate around a static magnetic field in a frame rotating at the frequency of the alternating field, where the frame is rotating about the axis of quantization. This behavior is shown in Fig. 1.2, along with an example of the evolution of the magnetization with an off-resonance pulse. In this way, the magnetization from the spins is nutated, from parallel to the axis of quantization to a plane perpendicular—this is called a  $90^\circ$  or  $\pi/2$  pulse. The pulse is shut off, and the magnetization now in the perpendicular plane is torqued around the quantizing magnetic field, causing an electromotive force (EMF) that generates an oscillating current in the same coil that just provided the pulse; in this way, a magnetic resonance signal is seen. The exponential decay to zero of the net magnetization (and signal) in the perpendicular plane is due to the dephasing of spins relative to one another (stemming from residing in slightly different local magnetic environments), and is characterized by a transverse relaxation time  $T_2^*$ . This decay is thus entitled a free induction decay (FID). Experimentally, the transmit and receive frequencies are specifically programmed such that a fast Fourier transform (FFT) of the decay of the FID gives the local magnetic field (through frequencies) that the spins experience. The return to thermal equilibrium of the net magnetization (the spin bath equilibrated with the surrounding thermal bath) is characterized by a longitudinal relaxation time  $T_1$ .

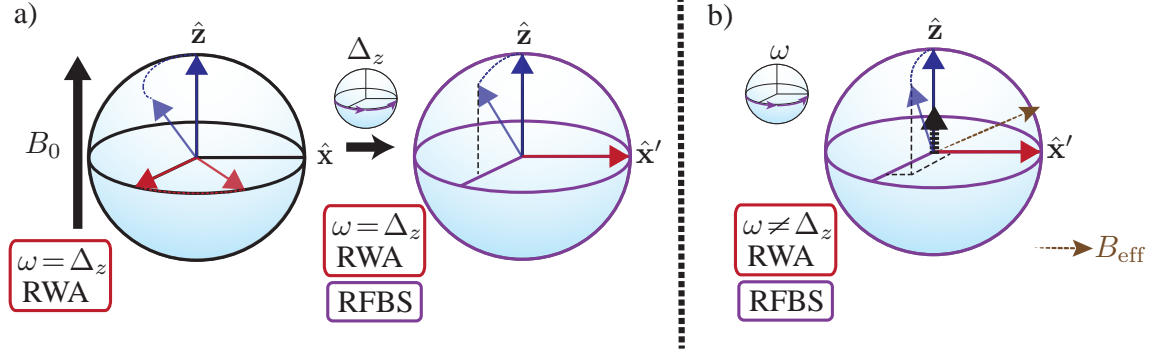


**Figure 1.2.** A demonstration of excitation in a Bloch sphere picture, using the rotating-wave approximation (RWA). (a) A demonstration of an on-resonant ( $\omega = \Delta_z$ ) excitation in a Bloch sphere picture. Note the use of the RWA. The red arrow represents one rotating component of the magnetic field, and the blue arrow represents the magnetization due to the spins.  $B_0$  is the quantizing magnetic field, and is much larger than the oscillation magnetic field in order for the RWA to be valid. The rotating frame Bloch sphere (RFBS) is indicated in purple, and in this frame, the oscillating magnetic field is static along the  $\hat{x}'$  axis, about which the magnetization rotates (causing nutation). (b) The RFBS picture of a slightly detuned excitation ( $\omega \neq \Delta_z$ ), where there is a remnant effective field from  $B_0$  along the  $\hat{z}$ -axis that results in the rotation of the magnetization  $\mathbf{M}$  around a total effective field  $B_{\text{eff}}$ .

Other novel implementations of MR involve alternative detection techniques, other than the decay of the net magnetization in the perpendicular plane. Optically and electrically detected magnetic resonance (ODMR, EDMR) are used in semiconductor studies to determine the effect of changing the electronic spin states on the emission of light from and conduction properties of materials [35, 36]. These types of detection techniques significantly enhance the sensitivity of an MR experiment, even to the extent of allowing access to a single molecule [37] or nitrogen vacancy center [38]. Magnetically resonant manipulation, as well as optical pumping, also play an important role in other extremely useful devices such as the comagnetometer [39, 40], used as a highly accurate gyroscope, and the implementation of quantum simulators [41, 42, 43].

The typical Hamiltonian describing the coupling between external magnetic fields and spin-1/2 components in a simple MR experiment including excitation is given as

$$\hat{H} = \frac{\hbar}{2}\gamma\sigma_z B_0 + \hbar\gamma\sigma_x B_1 \cos(\omega t), \quad (1.10)$$

where  $B_0$  is the field providing the quantization axis along  $\hat{z}$ ,  $B_1$  and  $\omega$  are the strength and frequency of the excitation pulse for a duration  $t$ ,  $\sigma_i$  are Pauli matrices, and  $\gamma$  is

the gyromagnetic ratio or related to the  $g$ -factor of a nuclei or electron. Notice the quasiclassical nature of this Hamiltonian, as the magnetic field is considered a classical field, and the spins are quantized. Note there is an alternative analogy of magnetic resonance that is considered the classical description, and Eq. 1.10 is considered the starting point of the quantum mechanical treatment, even though this treatment is itself a quasiclassical description. Nevertheless, the predictive power of Eq. 1.10 is seen in its ubiquitous use throughout the magnetic resonance communities. Typically the first step to analyzing spin evolution is to make the RWA (similar to the Rabi oscillation analysis for the atomic transitions above), in which the  $\cos(\omega t)$  term is recognized to be the composite of two fields, one rotating about the quantization axis at frequency  $\omega$ , and another counter-rotating about the quantization axis that is neglected (see Fig. 1.2). Terms that couple spins to other spins are added into Eq. 1.10, and many theories on how to take advantage of these couplings to give detailed information about the system have been explored—some very deeply as in 2D NMR experiments, and some still in their infancy, such as near-zero-field magnetic resonance with  $J$ -coupling [44, 45].

Both electron and nuclear spin resonance are described by Eq. 1.10, with the major difference being the frequency at which resonance occurs for the spin state, determined by  $\gamma$  or  $g$ -factor. It can be shown for a spin-1/2 particle that the  $g$ -factor must necessarily be approximately 2 [46]. This reinforces the notion that all nuclei, and even lone protons or neutrons, are not pure spin-1/2 particles as electrons are, but are composites made up of other particles [47]. Nevertheless, because the energies involved in magnetic resonance are so comparatively low in relation to strong and weak interactions that keep the nuclei or nucleons bound, these composite states can be treated as spin-1/2 quasiparticles for all intents and purposes herein.

If the entire sample is in zero field, any uncoupled spin-1/2 states quantized along a given axis will have a population of 50%  $|\uparrow\rangle$  and 50%  $|\downarrow\rangle$ . As mentioned above, the introduction of an external magnetic field to this sample causes the lifting of the spin-state degeneracy and leads to a high-energy state and a low-energy state. Thermodynamic interactions between the spin states and the surrounding environment in the sample and laboratory cause a new thermal equilibrium that

favors the spin population in the lower-energy state. This thermal equilibrium can be assigned a Boltzmann distribution and can be shown to give a polarization in the low-energy state of  $P = \tanh(\hbar\omega/2kT)$ , where  $k$  is the Boltzmann constant and  $T$  is temperature. For an example of the effect of magnetic field and temperature on polarization, consider protons in a 1 Tesla (T) field and room temperature in an uncoupled system—the polarization will be  $P = 3.45 \times 10^{-6}$  in the  $|\uparrow\rangle$  state (0.000345 %); bare electrons at 1 T and room temperature have a polarization of  $P = 1.82 \times 10^{-2}$  in the  $|\downarrow\rangle$  state (1.8 %). Remarkably, at 4 K and 12 Tesla, the electron polarization is  $P = 0.965$  (96.5 %). The magnetization  $M$  of the sample generated by this polarization in spin state can be expressed as  $M = N_v\mu P$ , where  $N_v$  is the number of particles per unit volume and  $\mu$  is the magnetic moment of a single particle. The magnetization in thermal equilibrium will necessarily point parallel to the external magnetic field for either positive or negative gyromagnetic ratios (or  $g$ -factors), an effect of nuclear or electron paramagnetism.

A complete description of the spin Hamiltonian should include all of the effects felt by all of the spins in a sample, such as dipolar broadening [48], chemical shifts [49, 50], etc., *as well as* all thermal excitations that cause spin relaxation. Representing the coupling of spins to thermal excitations (phononic fields) is quite difficult, but a rate- and thermodynamics-based solution was provided by Redfield [51, 52]. For some problems, temperature and magnetic field dependences for relaxation processes can be elucidated by considering the coupling of the phonon bath to the spin bath. In particular, it is possible for a canonical quantization of the phonons to be used to detail a specific order of phonon process [53], and a coupling mechanism of a phonon process to the spin state can be used in Fermi's golden rule (Eq. 1.5) to calculate a transition probability that directly relates to the longitudinal relaxation rates of nuclear spins.

A spin-1/2 state in a magnetic field is also a case of the two-level system. However, in a conventional NMR or ESR experiment, the direct absorption or emission of photons to excite an individual spin state is highly improbable [54, 55]. A direct analogy of the MR situation to atomic transitions being driven within the E1 approximation is, unfortunately, not accurate due to the weakness of the M1 transition. Hence, as

opposed to the atomic transition case, one photon can not be thought of as causing (or resulting from) a single transition from the low energy state to the high energy state, or vice versa. A Rabi oscillation in MR is essentially the frequency at which the net magnetization, caused by many spin states, oscillates about a coherent magnetic field. (These quasiclassical coherent states of the magnetic field can be built up quantum mechanically by Glauber’s displacement operator [56].) The evolution of the net magnetization thus is given by Eq. 1.6. It is also important to mention that, typically, the state being manipulated in an MR experiment is a pseudo-pure state [57, 58] (though pure states can be made with sufficiently high polarization or low enough number of spins), made up of many spins that lead to an ensemble measurement [59, 60]. For example, thermally polarized hydrogen in water at 2 Tesla is not a pure spin-1/2 state as it is a composite state made up of many spins, and thus an ensemble description is needed to properly describe the system. This has important ramifications for the feasibility of the use of nuclear spin states in quantum computation or quantum simulation—quite unfortunate, considering the convenient isolation from its surroundings that a spin state of a nucleus provides.

Nevertheless, MR techniques remain a standard in a variety of fields, including medical diagnostics, chemical analysis, and solid state physics. In turn, the study of the interpretations and advancement of techniques within MR remains important for all sciences.

### 1.3 Dissertation Outline

In Chapter 2, an unprecedented reproducibility in longitudinal relaxation measurements in solid xenon is demonstrated. Also, these precise measurements lead to some key disagreements with theory, which are discussed. Switching techniques from NMR to EPR, Chapter 3 presents simulations and analytical calculations of a paramagnetic spin-1/2 pair during ODMR and EDMR experiments. In particular, Rabi oscillations are discussed where the spin-1/2 pair has an exchange and dipolar coupling between them, and that a spin-1/2 pair with strong dipolar coupling leads to a  $\sqrt{2}\gamma B_1$  Rabi frequency. Chapter 4 contains the experimental NMR water results from modulating the longitudinal field, and the effects from a modulation on the

Rabi oscillation pattern. Excellent quantitative agreement with predictions is found in three regimes of interest.

The appendices include calculations of transition probabilities in Rb optical pumping, and dilute-spin solid  $^{129}\text{Xe}$  data regarding transverse relaxation. Appendix C discusses research on the relaxation mechanisms in gaseous  $^{129}\text{Xe}$ . Here, an unexpected temperature dependence on longitudinal relaxation time of  $^{129}\text{Xe}$  is investigated.

# CHAPTER 2

## LONGITUDINAL RELAXATION IN SOLID $^{129}\text{Xe}$

*“As if that blind rage had washed me clean, rid me of hope; for the first time, in that gentle indifference of the world. Finding it so much like myself—so like a brother, really—I felt that I had been happy and that I was happy again.”*

- The Stranger, *Albert Camus*

### 2.1 Introduction

Solid xenon has been studied for many years by many prolific groups. The problem of longitudinal relaxation of solid  $^{129}\text{Xe}$  in particular is an interesting one because it is notoriously difficult: computationally due to its many-body nature, and experimentally because of its history of nonreproducibility. The wave function of a xenon atom in a lattice is not completely known because of the complexity of the system. In theory, if a correct xenon wave function is used and the correct relaxation mechanism is posited, the relaxation rates are calculable from first principles. At the time of this work, the leading model gives that longitudinal relaxation in the regime of 77 K to 120 K is predominately caused by a spin-rotation interaction mediated by Raman-scattering of phonons. As presented in the literature, this model does not account for our experimental longitudinal relaxation data, and, minimally, requires adjustment to the interaction strength in order for experimental agreement to occur. An overview of the previous theoretical model and experimental data is given in Sect. 2.2.

The measurements in Sect. 2.4 have an unprecedented precision and reproducibility of solid  $^{129}\text{Xe}$  longitudinal relaxation times  $T_1$ . So-called “snow” and “ice” forms of solid xenon are measured, where an unexpected difference in  $T_1$  times is found. Temperature-dependent  $T_1$  data for ice and snow are also given and compared to

predicted relaxation times. The ice data are found to give consistently longer  $T_1$  times across the range of validity of the theory.

Practically, this work may have ramifications for the cryogenic storage of hyperpolarized xenon. In particular, flow-through xenon polarizers for lung imaging use cryogenic separation and collection of xenon, after which the xenon is transported, revolatilized, and administered to patients. If, perhaps, there are better ways to make the solid (i.e., significantly lengthen  $T_1$ ) than the methods currently being used, it is an avenue worth exploring.

## 2.2 History of the Problem

Previous to experiment, it was assumed that solid  $^{129}\text{Xe}$  would have extremely long longitudinal relaxation times limited by direct-dipolar interactions between the spin-1/2 nuclei. Unfortunately for the field of hyperpolarized noble gases, the measured longitudinal relaxation times were significantly shorter than expected (hours instead of months) at 77 K. Because of these unexpectedly short times, there was a need to understand the mechanism of relaxation in this system.

In the following sections, a brief history of theoretical and experimental results is presented as a companion for a reader delving through the literature. As such, notational changes are abundant but clearly labeled after each equation. Sect. 2.2.1 discusses the history of the theory in conjunction with the history of the experiments. Then, a discussion of more recent experimental results is given in Sect. 2.2.2, followed by a detailed explanation of the theory of the spin-rotation interaction mediated by Raman-scattering of phonons.

### 2.2.1 Foundations of theory and experiment

The spin-rotation interaction is originally proposed to account for gaseous  $^{129}\text{Xe}$  longitudinal relaxation by Adrian in his thesis work, where he deemed the mechanism too weak to cause the relaxation [61]. In 1963, Torrey reconsiders and popularizes the idea of the spin-rotation interaction to describe experimental relaxation times of gaseous and liquid  $^{129}\text{Xe}$  [62] that are observed by Streever, Hunt, and Carr [63, 64]. These papers serve to rule out the direct-dipolar interaction between nuclei (using the method of Bloembergen, Purcell, and Pound [65]) to account for the relaxation

mechanism in liquid  $^{129}\text{Xe}$ . Torrey claims that Adrian’s chosen method of approximation for a certain summation (that arises from Wick’s theory [66], determining a magnetic field at a nucleus of a diatomic molecule produced by molecular rotation) is too crude, and provides an alternative way to evaluate the chemical shift. Both Adrian and Torrey adapt a methodology presented in Ramsey’s seminal paper on chemical shifts [49].

In Ramsey’s 1950 calculation, a second-order perturbation theory is used to calculate an average-magnetic-shielding constant for each nucleus that describes frequency shifts in an NMR experiment. The assumptions made are: 1) the nuclei of the molecules are so massive compared to the electrons that the nuclei are classical and stationary, 2) the electron spin can be omitted, 3) only one nucleus in the molecule has a nonzero magnetic moment that is in the same direction as the externally applied field, and 4) there is no preferred direction for the molecules, so an average over all orientations is required. The equation for the average-magnetic-shielding constant (Eq. 10 in Ramsey [49]) is computationally impractical for a general molecule because the equation includes a summation over all excited states of the molecule. However, Ramsey shows that it is possible to relate the difficult summation to an experimentally measurable spin-rotational, magnetic-interaction constant. Using perturbation theory, Ramsey derives an equation for the average-magnetic-shielding constant for a  $^1\Sigma$  linear (diatomic) molecule,

$$\sigma = (e^2/3mc^2) \left[ \langle 0 | \sum_k 1/r_k | 0 \rangle - (1/ec\omega)(H_r - Ze\omega/cR) \right], \quad (2.1)$$

where  $e$  is the electron charge,  $m$  is the electron mass,  $c$  is the speed of light,  $r_k$  is the distance of the  $k$ th electron from the nucleus for which the shift is being calculated,  $\omega$  is the angular velocity about the center of mass,  $H_r$  is the magnetic field at that nucleus due to rotation of the diatomic system,  $Z$  is the atomic number, and  $R$  is the internuclear separation of the pair. Ramsey also elegantly shows Eq. 2.1 is obtained without using second-order perturbation theory, but with sheer physical reasoning.

Torrey bases his 1963 paper on Eq. 2.1 [62]. Torrey’s calculation yields the difference in average-magnetic-shielding constants for a xenon diatomic molecule from that of a bare xenon atom ( $\Delta\sigma_{\text{av}} = \sigma_{\text{diatomic}} - \sigma_{\text{bare}}$ ). In comparison to Hunt and Carr’s

experimental results [64], this calculation is too small by one order of magnitude. This discrepancy translates to an inaccurate magnetic field calculated at the nuclei in question. Nevertheless, Torrey states that there is little doubt the mechanism is spin-rotation. Shown in Torrey [62] is a rigid-sphere calculation which leads to a conglomeration of the longitudinal relaxation time and the difference in average magnetic shielding constants that is similar to experimental results,

$$\begin{aligned} \left[ T_1 (\langle \Delta\sigma \rangle_{\text{av(Torrey)}})^2 \right]_{\text{Torrey}} &= 3.56 \times 10^{-8} \text{ per amagat,} \\ \left[ T_1 (\langle \Delta\sigma \rangle_{\text{av(exp)}})^2 \right]_{\text{exp}} &= 3.6(\pm 0.4) \times 10^{-8} \text{ per amagat.} \end{aligned} \quad (2.2)$$

Torrey admits this calculation is probably fortuitous, and if one considers the order-of-magnitude discrepancy between  $\langle \Delta\sigma \rangle_{\text{av(Torrey)}}$  and  $\langle \Delta\sigma \rangle_{\text{av(exp)}}$ , the theory leads to a two-orders-of-magnitude discrepancy in the theoretical  $T_1$  compared to the experimental  $T_1$ . Hunt and Carr use an experimental value for  $\Delta\sigma_{\text{av}}$  in Torrey's theory (instead of Torrey's theoretical  $\Delta\sigma_{\text{av}}$ ) and calculate a longitudinal relaxation time that is slightly greater than twice the experimental value for liquid xenon.

Meanwhile, Yen and Norberg, at Washington University of St. Louis, observe a temperature-dependent chemical shift for solid  $^{129}\text{Xe}$  presented in the first published work that contains solid xenon NMR data [67]. Specifically, they report self-diffusion coefficients, resonance shifts, and transverse (spin-spin,  $T_2$ ) relaxation times for a range of pressures (saturated vapor pressures to 20 atm) and temperatures (4 K to 227 K) for naturally abundant xenon in liquid and solid phases. A limiting (lower bound) value of  $T_1$  in a solid is set,  $T_1 > 7 \times 10^3$  sec. at 125 K. The main results of the paper concern  $T_2$  values, so paramagnetic impurities such as activated charcoal in glass wool and air are introduced to shorten  $T_1$  to 900 seconds and 600 seconds, respectively, at 125 K. They mention the impurities did *not* have any effect on  $T_2$ . The solid  $^{129}\text{Xe}$   $T_2$  data over a temperature range of 90 K to 160 K matches the Van Vleck rigid-lattice dipolar theory [48] from 90 K to roughly 120 K. Between 120 K up to 160 K,  $T_2$  becomes longer than the rigid-lattice dipolar theory predicts, due to diffusion (motional narrowing). Assuming a face-centered-cubic (fcc) lattice, a temperature-dependent equation for the diffusion constant  $D$  of solid xenon is found,

$$D = 7.4(\pm 0.3)e^{-7.40(\pm 0.05) \times 10^3/RT} \text{ cm}^2/\text{sec}, \quad (2.3)$$

where  $R$  is the molar gas constant and  $T$  is temperature. A liquid diffusion coefficient corroborating Hunt and Carr's work is also given, but this result is a factor of two different than a  $^{132}\text{Xe}$  radioactive tracer experiment [68]. Yen and Norberg give the resonance shift  $\Delta H$  (chemical shift) for solid xenon as the linear equation

$$\Delta H = 10.82 - 20.4 \times 10^{-7} \rho H_0, \quad (2.4)$$

where  $\rho$  is density and  $H_0$  is the external magnetic field. The term uses a density that relates to the pressure-volume isotherm data presented by the 1963 work of Packard and Swenson [69].

In 1964, Brinkmann (at Rutgers, with Carr) also publishes solid  $^{129}\text{Xe}$  resonance-shift data [70]. From this data, it is determined that the density rate-of-change of the chemical shift for solid  $^{129}\text{Xe}$  is

$$(\partial\Delta H/\partial\rho)_{\text{solid}} = +(5.3 \pm 0.3)10^{-7} H_0. \quad (2.5)$$

The rate of change is slightly greater than that of liquid, but a *factor of four* smaller than that reported for solid  $^{129}\text{Xe}$  by Yen and Norberg ( $20.4 \times 10^{-7} H_0$ ) [67]. Following the report of this discrepancy, Lurie et al. (at Rutgers) give a theoretical treatment of the local magnetic field shift in solid xenon that, Lurie et al. state, corroborates Brinkmann's data in favor of Yen and Norberg's data [71]. None of the calculated curves fit the entire set of Brinkmann's data, as seen in Fig. 2.1 (see Lurie et al. [71]), but the calculations are much closer to Brinkmann's data than Yen and Norberg's data.

In Lurie et al. [71], the calculation is based on the extension of the diatomic  $\text{Xe}_2$  molecule to the solid phase of  $^{129}\text{Xe}$ . The assumption behind this pursuit is that the origin of the shift is the same for all phases of xenon. Building on Torrey and Ramsey's work for xenon gas, each of the twelve nearest-neighbor atoms in a fcc xenon lattice is considered a diatomic interaction, ignoring motional correlation between the atoms (the atoms are free to vibrate independently in their lattice position). Summing over the nearest neighbors, the expression for the magnetic-field shift in the solid becomes

$$\begin{aligned} \Delta H(T) &= \sum_{\text{n.n.}} \langle AH \sin^2 \theta e^{-Z(R-b)} \rangle \\ &= 12AH e^{-Z(R_0(T)-b)} (\sin^2 \theta)_0 \langle n | 1 + \frac{Z^2 u_z^2}{2} + \frac{Z(u_x^2 + u_y^2)}{2R_0} | n \rangle \end{aligned} \quad (2.6)$$

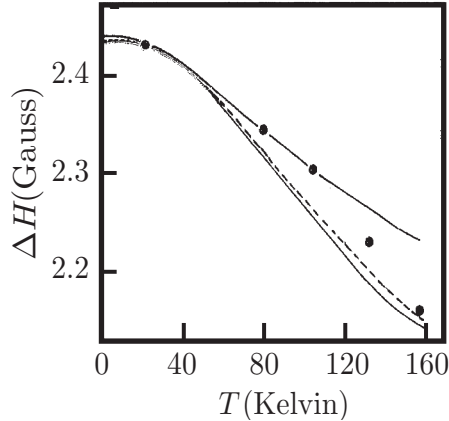


**Figure 2.1.** A comparison of experimental and theoretical values of the chemical shift in solid  $^{129}\text{Xe}$  is shown. The bold circles are Brinkmann and Carr’s data [70, 72]. The lower solid curve is computed from the Lennard-Jones 13-6 potential using  $A = 1.180 \times 10^{-4}$ . The upper solid curve is computed using a Buckingham 13-6 potential and Adrian’s calculated value of  $A$ ,  $A = 7.82 \times 10^{-5}$  [73]. The dashed curve is computed using the Lennard-Jones 13-6 potential and the value  $A = 1.07 \times 10^{-4}$ . All data and calculated values are normalized to agree at 21 K and correspond to a field of 7100 G. (See [71]).

where  $A$ ,  $Z$ , and  $b$  are parameters, with  $A$  representing a sort of interaction strength.  $H$  is the applied field,  $R$  is the separation between two atoms,  $\theta$  is the angle between  $R$  and  $H$ ,  $R_0$  is the equilibrium separation between two atoms,  $\mathbf{u}$  is the displacement from equilibrium,  $(\sin^2 \theta)_0 = 2/3$  is the equilibrium average of  $\sin^2 \theta$  over the fcc lattice, and the brackets, along with the symbol  $\langle n | |n \rangle$ , represent an average over the canonical ensemble. The value for parameter  $Z = 2.506 \text{ \AA}^{-1}$  is taken from Adrian’s 1964 work [73]. Various methods of obtaining values for  $A$  (and the dependent  $b$ ) are used, including data from Brinkmann and Carr’s complimentary 1966 work [72], dilute gas shift data of the Rutgers group, or the value presented in Adrian’s work. The value of  $A$  obtained from the Washington data is deemed implausible because it is not close enough to the liquid value of  $A$  (the Washington and Rutgers value of  $A$  in liquid xenon agree). For the canonical calculation, various potentials are used, including Lennard-Jones 13-6,

$$\phi_\epsilon(R) = \frac{6 \times 13 \times \epsilon}{7} \left[ \frac{1}{13} \left( \frac{R_0}{R} \right)^{13} - \frac{1}{6} \left( \frac{R_0}{R} \right)^6 \right], \quad (2.7)$$

and a Buckingham potential,

$$\phi_\epsilon(R) = \frac{6 \times 13 \times \epsilon}{7} \left[ \frac{1}{13} \exp\left(\frac{-13(R - R_0)}{R_0}\right) - \frac{1}{6} \left(\frac{R_0}{R}\right)^6 \right], \quad (2.8)$$

and a standard Lennard-Jones 12-6 potential. All variations of potentials and plausible  $A$  values fit with the Rutgers data better than the Washington University data.

Also in 1966, Warren and Norberg (at Washington University) study relaxation and chemical shifts in  $^{131}\text{Xe}$  due to the nuclear quadrupole moment in the spin-3/2 nuclei [74]. The quadrupolar relaxation theory used to describe the data is that of Van Kranendonk's for a solid with a Debye phonon spectrum [75]. Specifically, substituting the quadrupole moment for the dipole moment in the Waller theory of dipolar relaxation [31, 76], a theory is developed that uses the quadrupole-phonon interaction as an explanation of the data. The direct-phonon process (one phonon) is discounted as negligible and the focus is on the quadratic or "Raman" term—the term that corresponds to absorption and emission of phonons whose frequency difference is at the Larmor frequency  $\omega_0$ , or  $2\omega_0$ . A first principles calculation of the overlap, or van der Waals interactions (used to calculate the strength of the time-dependent electric-field gradients) is compared to the experimental  $T_1$  at 100 K,

$$T_{1(\text{theory})} = 1.3 \text{ s}, \quad T_{1(\text{exp})} = 0.70 \pm 0.05 \text{ s}. \quad (2.9)$$

Therefore, the theory requires half of the interaction strength to account for the data at 100 K. The other test of the theory is the temperature dependence. Notice the distinction, while the theory should presumably account for both the strength of the relaxation interaction and the temperature dependence, it is possible to claim ignorance of the exact strength of the relaxation and obtain the strength from the observed  $T_1$  *itself*, and separately test the predicted temperature dependence of  $T_1$ . By normalizing the interaction strength to experimental  $T_1$  data taken at 77 K, the temperature dependence of the theory for quadrupole relaxation via the two-phonon Raman process is shown to account for the experimental  $^{131}\text{Xe}$  data in the range of 9 K to 110 K. A temperature-dependent Debye temperature provided by Packard and Swenson [69] is used to correct the theory for temperatures above 110 K to the melting point of xenon. In all, the first principles calculation of the quadrupole relaxation via the two-phonon Raman process has the same temperature dependence, but the

calculation for the interaction strength is inaccurate. This is expected because it is difficult to determine the potential of xenon in a lattice; the gaseous xenon potential also remains not well known. Chemical-shift data for solid  $^{131}\text{Xe}$  is also given, and the value extrapolated,

$$-\frac{1}{H_0} \frac{\partial(\Delta H)}{\partial \rho} = (18.2 \pm 1.1) \times 10^{-7} \text{Å}^{-1}, \quad (2.10)$$

matches closely with Yen and Norberg's chemical shift data for  $^{129}\text{Xe}$ .

In 1967, Warren and Norberg present an extensive study of  $T_2$  for solid  $^{129}\text{Xe}$  and  $^{131}\text{Xe}$  [77]. A second moment (and in turn  $T_2$ ) for  $^{129}\text{Xe}$  is found that is approximately the same as the theoretical second moment found with Van Vleck's theory of dipolar broadening in a rigid lattice [48]. At a lower magnetic field, this experiment reaffirmed the same  $T_2$  of that reported by Yen and Norberg [67].

Finally, to end this first wave of NMR studies of solid xenon, there is another set of solid xenon NMR data, published in 1972 by Cowgill and Norberg at Washington University in St. Louis [78]. The relative chemical shift in solid  $^{131}\text{Xe}$  is found to be

$$-\frac{1}{H_0} \frac{\partial(\Delta H)}{\partial \rho} = (5.72 \pm 0.36) \times 10^{-7} \text{Å}^{-1}. \quad (2.11)$$

In this paper, they mention that they are not able to reproduce the larger shifts previously reported in solid xenon by Yen, Warren, and Norberg. This result corroborates Brinkmann and Carr's data [72] and the theoretical work provided by Lurie et al. [71], and is an order of magnitude less than the data provided by Yen and Norberg [67].

With this, there is a break in the literature for solid  $^{129}\text{Xe}$  NMR for roughly twenty years. The early results proved to be fairly volatile, with pure theory never exactly describing the data. Trends, such as similar temperature dependence, suggest that the quadrupolar-relaxation mechanism mediated by the Raman-scattering of phonons accounts for  $^{131}\text{Xe}$  experimental data. Certain experimental results, such as the chemical shift data, remain unexplained at the end of the first wave of papers. In this brief history, it is seen exactly how reproducibility and theoretical determination is a significant problem when concerning solid xenon.

### 2.2.2 Reincarnation via hyperpolarization

The early work has a lack of solid  $^{129}\text{Xe}$  longitudinal relaxation data without impurities such as oxygen. This deficiency comes from a practical problem—for con-

ventional solid NMR measurements, the relaxation times are too long for  $^{129}\text{Xe}$  for an extensive study to be worthwhile; all of the experiments in the early work monitored thermal polarization and, with  $T_1$  times for  $^{129}\text{Xe}$  reaching upwards of hours, a  $T_1$  measurement was presumably determined too long to be practical. “Conventional,” in this sense, describes experiments of the saturation-recovery type, as very high fields, low temperatures, or very large amounts of xenon would be required to observe relaxation for solid  $^{129}\text{Xe}$  in thermal equilibrium. Another problem plaguing the early work was that of impure samples. Oxygen has a detrimental effect on a reliable  $T_1$  measurement. As mentioned in Sect. 2.2.1, oxygen was purposefully introduced to cut  $T_1$  times by orders of magnitude so that  $T_2$  measurements were feasible.

Hyperpolarization of  $^{129}\text{Xe}$  provides the ability to run  $T_1$  experiments in a beneficially different way. Starting with a very large polarization in the  $^{129}\text{Xe}$ , created by hyperpolarization via spin exchange with optically pumped Rb atoms (see Appendix C), it is possible to monitor polarization loss as the  $^{129}\text{Xe}$  returns to thermal polarization. Using pulsed NMR, the large polarizations afforded by hyperpolarization techniques lead to a very large signal with very small flip angles. The small flip angles lead to minimal polarization being sacrificed for the actual process of measuring relative polarization loss. Therefore, the time required to measure  $T_1$  in a particular sample only needs to be long enough to reliably trace out the polarization decay curve (a rule of thumb is the time of measurement must be past  $T_1$ ). This method drastically reduces the run time of the experiment, when compared to methods that start from thermal polarization of the sample. With thermal polarization measurements, large flip angles and perhaps averaging are needed to see a sufficient pulsed-NMR signal of  $^{129}\text{Xe}$  at higher temperatures. A large flip angle means the method of finding  $T_1$  is limited to typical  $T_1$  NMR measurement techniques: inversion recovery, saturation recovery, etc. [31, 32, 79]. In each of these conventional NMR techniques, the first step is (typically) to wait many times  $T_1$  so that the sample has maximum thermal polarization. Therefore, *one* data point to map out the characteristic  $T_1$  curve takes multiples of  $T_1$ .  $T_1$  measurements using hyperpolarization techniques typically record 50-150 points over the course of one experiment; to get the same resolution using thermal polarization techniques, the time required is

$$\begin{aligned}
\text{Thermal Polarization Run Time} &= (\text{Time per data point}) * (\text{Data points}) \\
&= (4(\pm 1)T_1) * (100 \pm 50) = (400 \pm 200) * T_1.
\end{aligned}
\tag{2.12}$$

For  $^{129}\text{Xe}$ , a  $T_1$  of 2-3 hours at 77 K would lead to a thermal polarization experimental run time of, at minimum, weeks in order to achieve the same resolution as a hyperpolarized sample does in hours. This back-of-the-envelope calculation clearly shows that hyperpolarization gives quite an experimental advantage over thermal polarization for studying systems with extremely long  $T_1$  times.

### 2.2.3 Review of hyperpolarized $^{129}\text{Xe}$ experimental results

In 1990, Cates et al. (at Princeton) report the first-ever hyperpolarized solid  $^{129}\text{Xe}$  NMR signals [80]. Therein, the Rb in a Xe-Rb borosilicate-glass cell is optically pumped using 0.5 to 5 W of circularly polarized light at the  $D_1$  transition (795 nm). The  $^{129}\text{Xe}$  nuclei are polarized in spin-exchange collisions with the polarized Rb atoms, after which the cell is bathed in liquid nitrogen at 77 K. After crystal formation, the cell is brought to various temperatures: 77 K, 87 K, and 100-145 K. A range of magnetic field values are also used, from 0 to 1800 Gauss. Two different classes of cells are investigated; cells with high pressures (5 atm) of  $^{129}\text{Xe}$  and cells with low pressures (1 atm) of  $^{129}\text{Xe}$ . In addition, two different types of xenon are used: naturally abundant xenon and enriched xenon (72.9%  $^{129}\text{Xe}$ , 5.3%  $^{131}\text{Xe}$ ). The NMR is conducted with adiabatic fast passage to monitor polarization of the sample [31]. In this work, a difference in  $T_1$  is found that depends on the room-temperature gas pressure of the cell. Interestingly, for the low-pressure cell of enriched xenon,  $T_1 = 128.33 \pm 5$  min, and for the high-pressure cell,  $T_1 = 163.33 \pm 10$  min. (As shown in Sect. 2.4, perhaps a cell with an insufficient partial pressure of xenon is not able to pass through the liquid phase, and leads to different crystal structures.) The relaxation time for the high-pressure cell of naturally abundant xenon is reported as  $T_1 = 141.66 \pm 16.66$  min. All other obtained solid  $^{129}\text{Xe}$   $T_1$  values are plotted in two figures contained in the paper and a compilation of values is also listed in Michael Gatzke's dissertation [81]; values relevant to this thesis are plotted in Fig. 2.2. A calculation by Abragam and Goldman gives a relaxation rate due to very small concentrations ( $N_S/N_I \ll 1$ ) of impurities in a lattice [85],



$$\frac{1}{T_1} = \frac{8\pi}{5} \frac{S(S+1)}{3} \frac{N_S}{N_I} (\gamma_S \gamma_I) (\Delta H_n)^2 \frac{T_{1e}}{1 + (\gamma_I H_0 T_{1e})^2} \propto N_I. \quad (2.13)$$

Here,  $N_S$  and  $N_I$  are, respectively, the number densities of the paramagnetic impurities and spin-1/2 xenon nuclei,  $\gamma_S$  and  $\gamma_I$  are, respectively, the gyromagnetic ratios for the paramagnetic impurity and  $^{129}\text{Xe}$ ,  $\Delta H_n \approx \gamma_I \hbar N_I$  is the nuclear linewidth due to spin-spin interactions in the rigid lattice,  $T_{1e}$  is the relaxation of the electronic spin  $S$ , and  $H_0$  is the external magnetic field. Therefore, if paramagnetic impurities are causing the relaxation, enriched xenon would have a relaxation rate that is a factor of 72.9%/26% higher than that of natural xenon. However, the data show no discernible dependence on isotopic concentration of  $^{129}\text{Xe}$ . Also, the amount of Rb in the xenon lattice required with this analysis would exceed the relative concentration of Rb atoms at room temperature before freezing the xenon, furthering the evidence against this mechanism of relaxation. The Rb also serves as a “getter” for any oxygen that may be in the cell, so paramagnetic relaxation caused from  $\text{O}_2$  is also discounted. Above 120 K, natural xenon shows a slower relaxation rate than enriched xenon, indicating a dipolar-dipolar type relaxation mechanism that is caused by the onset of hopping (this also leads to motional narrowing in the NMR lineshape). The spin-rotation interaction mediated by Raman-phonon scattering is suggested as a possible relaxation mechanism below 120 K; this mechanism gives roughly the same  $T^2$  temperature dependence as the 77-120 K data.

A few things are unclear from Cates et al. [80] as a singular work; one is the calculation of the spin-phonon coupling, the other is at what magnetic field the temperature-dependent data is taken. The relaxation rate  $1/T_1$  is suggested to be dominated by Raman scattering of phonons by the nuclear spin-rotation interaction

$$V_I = \gamma_I \mathbf{I} \cdot \mathbf{N}. \quad (2.14)$$

Here,  $\gamma_I$  is now labeled as the *coupling coefficient* (not gyromagnetic ratio),  $\mathbf{N}$  is the rotational angular momentum of a  $^{129}\text{Xe}$  atom around any other xenon atom, and  $\mathbf{I}$  is the spin angular momentum of the  $^{129}\text{Xe}$  nucleus. The coupling coefficient used is

$$\gamma_I \approx nA\gamma_S/E_e, \quad (2.15)$$

where  $n$  is the effective number of outer-shell electrons involved in the interaction,  $A/h \approx 10^{10}$  Hz is the mean magnitude of the hyperfine interaction between a  $^{129}\text{Xe}$  nucleus and one of the  $n$  electrons, and  $E_e \approx 10$  eV is the energy required to excite one of the  $n$  electrons. The value of  $\gamma_S$  is here defined as the coupling constant in the spin-rotation interaction  $V_S = \gamma_S \mathbf{N} \cdot \mathbf{S}$  between the spin of a Rb atom moving with rotational angular momentum  $\mathbf{N}$  about a Xe atom. The data are best fitted with a coupling coefficient of  $\gamma_I \approx 35$  Hz, but it is unclear why this is, or how the fit is actually accomplished. Presumably the given equation

$$1/T_1 = aT^2 + be^{-E_D/kT}, \quad (2.16)$$

is used in the fitting process, but a relation between the parameter  $a$  and the coupling coefficient  $\gamma_I$  is not given. A previously measured value of  $\gamma_S/h = 1.6$  MHz [86] is used to estimate how many electrons take place ( $n \approx 7$ ) in the interaction from the approximation in Eq. 2.15. Temperature-dependent data are given, but a magnetic field value is not given for the measurement (though this is clarified in Gatzke's thesis,  $H_0 = 1800$  G [81]).

An extension to the temperature-dependent  $T_1$  of solid  $^{129}\text{Xe}$  is presented by Gatzke et al., in 1993 [82]. In the article, they attempt to reaffirm that the spin-rotation interaction is the dominating relaxation mechanism from 20 K to 120 K. A more in-depth analysis is given, using chemical-shift measurements to derive a value for the spin-rotation coupling constant

$$\frac{\gamma_I}{h} = \left( \frac{\mu_I}{I\mu_B} \right) \left( \frac{\hbar}{8\pi M r_0^2} \right) (\sigma_s - \sigma_g) = -27 \text{ Hz}. \quad (2.17)$$

Here,  $\mu_I$  is the magnetic moment of  $^{129}\text{Xe}$ ,  $\mu_B$  is the Bohr magneton,  $M$  is the average mass of a xenon atom, and  $r_0 \simeq 4.4$  Å is the equilibrium internuclear separation. Raftery et al., give a chemical shift in solid  $^{129}\text{Xe}$  at 77 K of  $(\sigma_s - \sigma_g) = 317$  parts per million (ppm) from that of gaseous  $^{129}\text{Xe}$  [87, 88]. The estimated coupling strength is used in the relaxation calculation (for the spin-rotation interaction mediated by a Raman-scattering process), giving the approximate expression (well-approximated to better than 2%<sup>1</sup>)

---

<sup>1</sup>It is unclear what 2% means from the paper in this context.

$$\frac{1}{T_1} \simeq 8.20 \times 10^4 \left(\frac{\gamma_I}{h}\right)^2 \left(\frac{h}{kT_D}\right) \left(1 + \frac{2}{3}\epsilon + 0.122\epsilon^2\right) (T^*)^9 \int_0^{1/T^*} \frac{e^x x^8}{(e^x - 1)^2} dx. \quad (2.18)$$

Here,  $T_D$  is the Debye temperature,  $T^* = T/T_D$  where  $T$  is the temperature,  $k$  is the Boltzmann constant, and the parameter  $\epsilon = (r_0/\gamma_I)d\gamma_I/dr$  accounts for the dependence of the coupling parameter on the internuclear separation  $r$ . The parameter  $\epsilon$  used is calculated by Adrian [73] to be  $\epsilon/r_0 = -2.506 \text{ \AA}^{-1}$  (see Sect. 2.2.1,  $Z = -\epsilon/r_0$ ), which the Princeton group states is confirmed by the temperature dependence of the chemical shift in  $^{129}\text{Xe}$  by Lurie et al., in 1966 [71]. The computation gives  $T_1 = 138.33$  min at 77 K, which is close to the average of the experimentally measured values at 77 K,  $T_1 = 141.66 \pm 13.33$  min. The temperature-dependent data of  $T_1$  from 4.2 to 120 K at  $H_0 \geq 1$  kG in solid  $^{129}\text{Xe}$  by Gatzke et al. [82] is given as an inset of Fig. 2.2.

At temperatures below 20 K, it is suggested that a cross relaxation with  $^{131}\text{Xe}$  limits the  $^{129}\text{Xe}$   $T_1$  to hundreds of hours at a magnetic field of 1 kG, which is considered due to the incompatibility of the spin-rotation theory in this temperature range. At 4.2 K, there is a magnetic field dependence up to 1 kG. As the magnetic field decreases drastically (less than 15 G), the  $T_1$  of  $^{129}\text{Xe}$  decreases and the polarization of the  $^{131}\text{Xe}$  increases, indicative of spin-exchange from  $^{129}\text{Xe}$  to  $^{131}\text{Xe}$  and providing evidence that cross relaxation is a mechanism in effect at these low temperatures (although also at low fields). As mentioned in the paper, this interesting effect could be employed to transfer polarization of  $^{129}\text{Xe}$  to other nuclei embedded in the lattice; a high magnetic field will preserve the  $^{129}\text{Xe}$  polarization, and lowering the magnetic field will allow polarization transfer to other nuclei. Furthering the evidence for this mechanism, an isotope-dependent measurement is also conducted at 4.2 K; enriched xenon (80.9%  $^{129}\text{Xe}$ , 3.4%  $^{131}\text{Xe}$ ) gives  $T_1 = 180$  hours, naturally abundant xenon (26.4%  $^{129}\text{Xe}$ , 21.2%  $^{131}\text{Xe}$ ) gives  $T_1 = 60$  hours. An attempt to vary the grain size by introducing helium or krypton into the cell along with xenon is also presented. The krypton-containing cell has  $T_1 = 510$  hours, much longer than the nonexponential decay of the helium-containing cell of  $T_1 = 260$  hours. From this, the Kr-Xe cell is thought to make larger grain sizes than the He-Xe cell.

Another set of solid  $^{129}\text{Xe}$  experiments at 4.2 K by Lang et al. from Ottawa, Canada was published in 2002 [89]. The Ottawa group was unable to attain the

long  $T_1$  results produced by the Princeton group. The results presented are very inconsistent within themselves, but the paper does reinforce how crystal formation has a tremendous effect on the  $^{129}\text{Xe}$  relaxation times. The sample is prepared in two ways: a flow-through set-up where hyperpolarized xenon is frozen out of a gas mixture, or a static set-up where hyperpolarized xenon is produced in a sealed cell and subsequently frozen. After formation at 77 K, and the choice is made to either “anneal” the solid at 110 K or not, after which the temperature is dropped to 4.2 K. In both the flow-through set-up and the static set-up, the annealed sample shows an increase of  $T_1$  by roughly half in each case. The Ottawa group also claims that annealing at 142 K has no effect, but it is unclear as to why it has no effect. The data in this work are sparse; each  $T_1$  curve is traced out by only four or five data points over 40-50 hours.<sup>2</sup> The work shows that formation of the xenon solid is very important in order to get quality results—if only indirectly, in that they were unable to reproduce the much longer  $T_1$  times that were obtained by the Princeton group.

The most recent solid  $^{129}\text{Xe}$  data by the Princeton group were published by Kuzma et al., in 2002 [83]. Therein, pulsed-NMR techniques are used for measurement [90] instead of the adiabatic-fast-passage measurements used in the Princeton group’s previous work. The dominant region for the theory of Raman-scattering mediating the spin-rotation interaction is narrowed from 20-120 K to 50-120 K, and below 50 K it is stated that cross relaxation to  $^{131}\text{Xe}$  becomes the dominant relaxation mechanism for  $^{129}\text{Xe}$ . The majority of the measurements map out a temperature dependence from 100 K to 161 K (the melting point of xenon) and a magnetic field dependence from 0.067 T to 1.435 T. An isotopic dependence is also explored over roughly the same temperature and field ranges; at low-magnetic fields enriched xenon (86%  $^{129}\text{Xe}$ , 0.013%  $^{131}\text{Xe}$ ) has a slightly longer  $T_1$  than naturally abundant xenon (26.4%  $^{129}\text{Xe}$ , 21.2%  $^{131}\text{Xe}$ ). The high-field (1.435 T) temperature sweep from 77 K to 120 K gives  $T_1$ ’s that are in the vicinity of Gatzke and Cates’ values. At high field, vacancy diffusion is shown to become the dominant relaxation mechanism above roughly 150 K. (At low fields, vacancy diffusion is the dominant mechanism

---

<sup>2</sup>This seems to defeat the purpose of using hyperpolarized xenon, as enough polarization should be present in the  $^{129}\text{Xe}$  for high-resolution  $T_1$  measurements.

at most temperatures.) Within the error of the data points, the Raman-scattering by spin-rotation interaction model appears to fit the  $^{129}\text{Xe}$  data taken at high field from 77 K to 150 K. The accumulation of all data relevant to this thesis is shown in Fig. 2.2. One unclear aspect of this work is an ambiguity in cell pressure during solid xenon formation and how much, if any, of the xenon became liquid during the warm-and-refreeze process. Dr. Nicholas Kuzma graciously informed us that, during his work, the NMR was used to monitor the transition at least a fraction of the time, and all three peaks corresponding to the phase of the xenon were clearly seen [91]. A very useful companion to Kuzma’s work that elucidates calculations and experimental methods is Brian Patton’s dissertation [84].

#### 2.2.4 Theoretical formulation

An in-depth theoretical study of the relaxation processes of solid xenon is given by the Princeton group that describes the spin-rotation mediated by Raman-scattering model [92]. (This model can also be applied to other systems [93].) As discussed in Sect. 2.2.1, Warren and Norberg adduce the liquid and gas  $^{131}\text{Xe}$  quadrupole relaxation mechanism as evidence that a quadrupolar relaxation mediated by Raman-scattering of phonons is the dominant relaxation mechanism in solid  $^{131}\text{Xe}$  [74]. In the same vein, because evidence indicates spin-rotation is the cause of relaxation in liquid and gas  $^{129}\text{Xe}$  (see Appendix C), the Princeton group supposes the dominant relaxation mechanism for solid  $^{129}\text{Xe}$  to be spin-rotation mediated by Raman-scattering. Paramagnetic antishielding is discussed in Fitzgerald et al. [92], but it is determined that this mechanism only plays a role in relaxation when extremely large magnetic fields are applied ( $\approx 80$  T) and is therefore neglected here. Single-crystal samples of xenon are also discussed and it is determined that this theory predicts  $T_1^S$  ( $T_1$  due to spin-rotation coupling) to be the same for single-crystal samples as for polycrystalline samples [94].

The spin-rotation interaction is given by the term

$$v = \frac{c_K}{\hbar} \mathbf{K} \cdot \mathbf{l} \cdot \boldsymbol{\omega} = c_K \mathbf{K} \cdot \mathbf{N}, \quad (2.19)$$

where  $\mathbf{K}$  is the nuclear spin operator of the  $^{129}\text{Xe}$  atom and  $\mathbf{N}$  is the angular momentum of a  $^{129}\text{Xe}$ -Xe pair rotating about a common axis. The inertial tensor  $\mathbf{l}$  and

angular velocity  $\boldsymbol{\omega}$  of a xenon atom pair is related to the the angular momentum  $\mathbf{N}$  by

$$\hbar\mathbf{N} = \mathbf{l} \cdot \boldsymbol{\omega} = \frac{M}{2}(R^2\mathbf{1} - \mathbf{R}\mathbf{R}), \quad (2.20)$$

where  $M$  is the mass of a xenon atom and  $\mathbf{1} = \mathbf{x}\mathbf{x} + \mathbf{y}\mathbf{y} + \mathbf{z}\mathbf{z}$  is a unit dyadic from Cartesian unit vectors. The theory predicts the longitudinal relaxation time to be

$$T_1^S = \frac{4\hbar^2\omega_D}{9\pi c_{K0}^2 T^{*2} \eta^S(\epsilon_0, T^*)}. \quad (2.21)$$

Here,  $T^* = T/T_D$  ( $T_D$  is the Debye temperature for xenon, see Sect. 2.2.4.2),  $\omega_D = k_B T_D / \hbar$  is the Debye frequency,  $c_{K0} = c_K(R_0)$  is the coupling coefficient at equilibrium separation  $R_0$ ,  $\epsilon_0 = \epsilon(R_0)$  where  $\epsilon(R)$  is dimensionless function that characterizes  $c_K$  with increasing internuclear separation  $R$  defined by

$$\epsilon = R \frac{d}{dR} \ln c_K, \quad (2.22)$$

and  $\eta^S(\epsilon_0, T^*)$  is a dimensionless efficiency function similar to that introduced by van Kranendonk [75] to account for the “freezing out” of phonons at low temperatures.

The coupling coefficient is calculated to be (note the notational change from Eq. 2.17 and Gatzke et al. [82])

$$\frac{c_{K0}}{\hbar} = \left( \frac{\mu_K}{K\mu_B} \right) \left( \frac{\hbar}{8\pi M R_0^2} \right) (\sigma_g - \sigma_c) = -27 \text{ Hz}. \quad (2.23)$$

Eq. 2.23 is calculated using  $M = 2.18 \times 10^{-22}$  g,  $R_0 = 4.4 \text{ \AA}$ ,  $\mu_K = -3.90 \times 10^{-24}$  erg/G,  $\mu_B = 9.27 \times 10^{-21}$  erg/G,  $K = 1/2$ , and the chemical shift found in Raftery et al. [87] is  $\sigma_g - \sigma_c = 317$  ppm. The function  $\eta$  differs greatly from zero for temperatures below the Debye temperature ( $T^* \lesssim 1$ ) and is written as

$$\eta^S(\epsilon_0, T^*) = \sum_{lm} g_m c_l(\epsilon_0) P_l(\cos(\theta_m)) D_m(T^*), \quad (2.24)$$

where  $c_l$  is a set of nonzero coefficients and  $P_l(\cos(\theta_m))$  is the Legendre polynomial of order  $l$ , both result from averaging over all possible crystal orientations;  $g_m$  and  $\theta_m$  are described in Table 2.1. Only the nearest-neighbor interactions are considered, as the coupling coefficient  $c_{K0}$  becomes much smaller and hence the interaction is negligible for the second nearest neighbor. Viewed another way, only phonon scattering processes involving the nearest-neighbor atoms are considered, and a central xenon

**Table 2.1.** Lattice parameters for solid xenon (fcc), including nearest-neighbor data. Here, the number  $m$  represents the order of the nearest neighbor ( $m = 0$  represents each constituent of the ordered pair being made up of the same nearest-neighbor atom). The number of ordered pairs in a set is given by  $g_m$ . The pair separation is  $\sigma_m R_0$ . Also tabulated are  $\cos(\theta_m)$ , where  $\theta_m$  is the angle subtended by the pair, and the asymptotic values of the weights  $D_m$  from Eq. 2.25.

$m$	$g_m$	$\sigma_m$	$\cos(\theta_m)$	$D_m(\infty)$
0	12	$\sqrt{0}$	1	1.382200
1	48	$\sqrt{1}$	1/2	0.345550
2	24	$\sqrt{2}$	0	0.320796
3	48	$\sqrt{3}$	-1/2	0.407861
4	12	$\sqrt{4}$	-1	0.448817

atom is always considered in equilibrium at the origin.

The coefficients  $D_m$  are given by the equation

$$D_m(T^*) = \frac{1}{T^{*2}} \int_0^1 du u^4 \frac{e^{u/T^*}}{(e^{u/T^*} - 1)^2} J_m^2(u), \quad (2.25)$$

where  $u$  is the phonon momentum in units of the Debye momentum  $\hbar k_D$ ,  $u = k/k_D = E/E_D$ . Here,

$$J_m(u) = 1 + j_0(u\sigma_m\phi_D) - 2j_0(u\phi_D), \quad (2.26)$$

where  $j_0$  is the spherical Bessel function  $j_0(x) = \text{sinc}(x)$ ,  $\sigma_m$  is defined as  $R_{\beta\delta}^{(0)} = \sigma_m R_0$  where  $R_{\beta\delta}^{(0)}$  is the distance between nearest-neighbor pairs, and  $\phi_D = k_D R_0 = (6\pi^2\sqrt{2})^{1/3}$  is the phase advance over the nearest-neighbor distance  $R_0$  for a phonon with the Debye wave number  $k_D$ . The coefficients  $c_l(\epsilon_0)$  are

$$\begin{aligned} c_0(\epsilon_0) &= 4 + \frac{8}{3}\epsilon_0 + \frac{4}{9}\epsilon_0^2, \\ c_2(\epsilon_0) &= \frac{2}{9}\epsilon_0^2. \end{aligned} \quad (2.27)$$

In the calculation presented in Fitzgerald et al. [92], the value for  $\epsilon_0$  is estimated to be

$$\frac{\epsilon_0}{R_0} = -2.693 \text{ \AA}^{-1} \implies \epsilon_0 = -2.693 \text{ \AA}^{-1} R_0 = -2.693 \text{ \AA}^{-1} (4.4 \text{ \AA}) = -11.8. \quad (2.28)$$

This estimate of  $\epsilon_0/R_0 = -2.693 \text{ \AA}^{-1}$  should be compared to Torrey's quoted value of Adrian's  $Z$  in Sect. 2.2.1 [62],  $-Z = \epsilon_0/R_0 = -2.506 \text{ \AA}^{-1}$ , which is within 8%

of the calculated value. Fitzgerald et al. [92] suggests that Lurie et al. [71] state the temperature-dependent chemical-shift data in  $^{129}\text{Xe}$  are not accurate enough to determine  $\epsilon_0$  (or  $Z$ ) to better than 8%. In fact, Lurie et al. demonstrate that the value of  $Z$  (or  $\epsilon_0$ ) is inconsequential to their theory to at least  $\pm 8\%$ , because they *normalize their theory* to experimental data at 27 K; their success is a theory that provides a similar temperature dependence to the data. Hence, the temperature dependence (shape/slope of the shift curve) of the Lurie et al. chemical-shift theory is not greatly affected by the value of  $Z$  (or  $\epsilon_0$ ). The magnitude of the chemical shift is, of course, affected by the value of  $Z$  (or  $\epsilon_0$ ).

Assuming the calculation that leads to the coupling coefficient (Eq. 2.23) is correct,  $T_1^S$  can be written out in terms of Debye temperature, lattice spacing, and fundamental parameters,

$$\begin{aligned} \frac{1}{T_1^S} = & \frac{9\hbar^2\mu_K^2(\sigma_g - \sigma_c)^2}{256\pi K^2\mu_B^2 M^2 R_0^2 T_D^2} \sum_m g_m \left( 4 + \frac{8}{3}\epsilon_0 + \frac{1}{3}\epsilon_0^2(2\cos^2\theta_m + 1) \right) \\ & \times \int_0^1 du u^4 \frac{e^{\frac{uT_D}{T}}}{\left(e^{\frac{uT_D}{T}} - 1\right)^2} \left[ 1 + \text{sinc}\left(u\sigma_m(6\pi^2\sqrt{2})^{\frac{1}{3}}\right) - 2\text{sinc}\left(u(6\pi^2\sqrt{2})^{\frac{1}{3}}\right) \right]^2. \end{aligned} \quad (2.29)$$

The relaxation time  $T_1^S$  is computed directly for any temperature from this expression, using temperature-dependent values lattice spacing, Debye temperature, and the parameter  $\epsilon_0$ . After showing the limit of the integrand is zero as  $u$  approaches zero, the well-behaved integral can be numerically approximated using Simpson's approximation to a desired accuracy. The results of using Eq. 2.29, along with the temperature dependencies of parameters discussed in Sect. 2.2.4.2, are shown in Fig. 2.3.

This spin-rotation mediated by Raman-scattering model (that has no free parameters as written) passes through many data points in the temperature region of interest, 77 K to 120 K, but becomes negligible in the low-temperature region, where relaxation is determined to be due to cross-polarization of  $^{129}\text{Xe}$  with  $^{131}\text{Xe}$ . The direct process, which should be dominant over the two-phonon process at low temperatures, is considered negligible. Also, at higher temperatures, this model does not account for data taken at lower magnetic field values, where relaxation due to

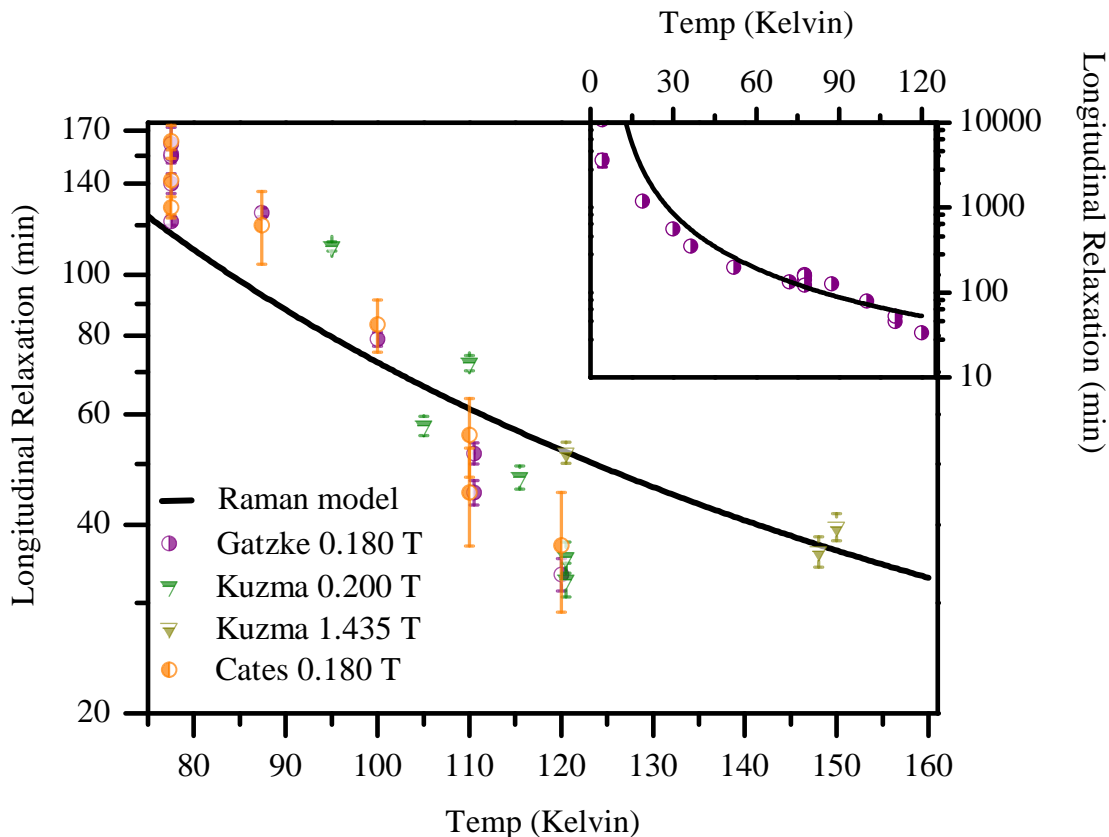


**Figure 2.3.** The theoretical calculation using Raman-scattering mediating the spin-rotation interaction is shown. Eq. 2.29, with temperature-dependent lattice spacing of Eq. 2.64 and equilibrium spin-rotation interaction of Eq. 2.65, is plotted in dark black, along with the experimental data of Fig. 2.2.

vacancy diffusion becomes dominant. The model is fit to the data and the data are somewhat scattered around the fit—anecdotally, the  $T_1$  data are notoriously difficult to reproduce. The papers by Kuzma et al. [83, 94] and Patton’s thesis [84] have the most refined versions of the theory; a theory that had its origins in the works Cates et al. [80] and Gatzke et al. [82], and was detailed in Fitzgerald et al. [92].

#### 2.2.4.1 Derivation of longitudinal relaxation time

To derive Eq. 2.29, a simple Debye model is used that assumes the speed of sound  $c_s$  of longitudinal and transverse phonons to be the same. The position  $\mathbf{R}_\nu$  of an

atom from its equilibrium position  $\mathbf{R}_\nu^{(0)}$  is given by

$$\mathbf{R}_\nu = \mathbf{R}_\nu^{(0)} + \mathbf{S}_\nu, \quad (2.30)$$

where  $\mathbf{S}_\nu$  is the displacement from equilibrium. The displacement operator and the momentum operator are written as

$$\begin{aligned} \mathbf{S}_\nu &= \sqrt{\frac{\hbar}{2NMc_s}} \sum_{\mathbf{k}j} \frac{\mathbf{x}_j}{\sqrt{k}} \left[ a_{\mathbf{k}j} e^{i\mathbf{k}\cdot\mathbf{R}_\nu^{(0)}} + a_{\mathbf{k}j}^\dagger e^{-i\mathbf{k}\cdot\mathbf{R}_\nu^{(0)}} \right], \\ \mathbf{P}_\nu &= \sqrt{\frac{\hbar Mc_s}{2N}} \sum_{\mathbf{k}j} \sqrt{k} \mathbf{x}_j \left[ i a_{\mathbf{k}j}^\dagger e^{-i\mathbf{k}\cdot\mathbf{R}_\nu^{(0)}} - i a_{\mathbf{k}j} e^{i\mathbf{k}\cdot\mathbf{R}_\nu^{(0)}} \right], \end{aligned} \quad (2.31)$$

in terms of phonon creation and annihilation operators  $a_{\mathbf{k}j}^\dagger$  and  $a_{\mathbf{k}j}$ , where  $\hbar\mathbf{k}$  is the phonon momentum and  $\mathbf{x}_j$  is a unit vector. The crystal contains  $N$  atoms with mass  $M$  in a volume  $V$ , with  $N$  phonon states of a given polarization.

Defining  $\mathbf{N}_{\beta\alpha}$  to be the angular momentum of the  $\beta$  and  $\alpha$  atoms in the crystal about their center of mass, the spin-rotation interaction of Eq. 2.19 can be written as

$$v = \sum_{\beta} c_K(R_{\beta\alpha}) \mathbf{N}_{\beta\alpha} \cdot \mathbf{K} = \frac{1}{2\hbar} \sum_{\beta} c_K(R_{\beta\alpha}) \mathbf{R}_{\beta\alpha} \times \mathbf{P}_{\beta\alpha} \cdot \mathbf{K}. \quad (2.32)$$

Here, a general operator  $\mathbf{A}_{\beta\alpha}$  is defined by  $\mathbf{A}_{\beta\alpha} = \mathbf{A}_\beta - \mathbf{A}_\alpha$ , as well as  $\mathbf{R}_{\beta\alpha} = \mathbf{R}_{\beta\alpha}^{(0)} + \mathbf{S}_{\beta\alpha}$ . The spin-rotation coefficient  $c_K(R_{\beta\alpha})$  can be expanded about  $R_{\beta\alpha}^{(0)}$  to first order in creation/annihilation operators, giving

$$\begin{aligned} c_K(R_{\beta\alpha}) &= c_K(|\mathbf{R}_{\beta\alpha}^{(0)} + \mathbf{S}_{\beta\alpha}|) = c_K(R_{\beta\alpha}^{(0)}) + \mathbf{S}_{\beta\alpha} \cdot \frac{d}{dR'} c_K(R') \nabla_{\mathbf{R}_{\beta\alpha}'} R'_{\beta\alpha} |_{R_{\beta\alpha}^{(0)}} + \dots \\ &= c_{K0} \left[ 1 + \frac{1}{c_{K0}} \frac{d}{dR'} c_K(R') |_{R_{\beta\alpha}^{(0)}} \mathbf{S}_{\beta\alpha} \cdot \frac{\mathbf{R}_{\beta\alpha}^{(0)}}{R_0} \right] = c_{K0} \left[ 1 + \frac{\epsilon_0}{R_0^2} \mathbf{S}_{\beta\alpha} \cdot \mathbf{R}_{\beta\alpha}^{(0)} \right]. \end{aligned} \quad (2.33)$$

Plugging this into Eq. 2.32 gives one- and two-phonon effects

$$v = \frac{c_{K0}}{2\hbar} \sum_{\beta} (\mathbf{R}_{\beta\alpha}^{(0)} \times \mathbf{P}_{\beta\alpha}) \cdot \mathbf{K} + \left( \mathbf{S}_{\beta\alpha} \times \mathbf{P}_{\beta\alpha} + \frac{\epsilon_0}{R_0^2} (\mathbf{S}_{\beta\alpha} \cdot \mathbf{R}_{\beta\alpha}^{(0)}) \mathbf{R}_{\beta\alpha}^{(0)} \times \mathbf{P}_{\beta\alpha} \right) \cdot \mathbf{K}, \quad (2.34)$$

where the first term ( $v^{(1)}$ ) has a single phonon creation/annihilation operator, and the second term ( $v^{(2)}$ ) under the sum involves two phonon creation/annihilation operators. The calculation that leads to Eq. 2.29 involves only the two-phonon term  $v^{(2)}$ , as all

other terms are deemed negligible.

Also negligible are two-phonon terms that involve two phonons being absorbed (or emitted) during the process. Therefore, the only transitions that are considered are between the initial state  $|i\rangle$  and final state  $|f\rangle$  where

$$\begin{aligned} |i\rangle &= |m_K = 1/2; \dots, n_{\mathbf{k}_a j_a}, n_{\mathbf{k}_e j_e}, \dots\rangle, \\ |f\rangle &= |m_K = -1/2; \dots, n_{\mathbf{k}_a j_a} - 1, n_{\mathbf{k}_e j_e} + 1, \dots\rangle. \end{aligned} \quad (2.35)$$

Here, the number of phonons (occupation number) with momentum  $\hbar\mathbf{k}_a$  and polarization  $\mathbf{x}_{j_a}$  in the mode where a phonon will be absorbed is given by  $n_{\mathbf{k}_a j_a}$ . The number of phonons in the state that a phonon will be emitted to is given by  $n_{\mathbf{k}_e j_e}$ . The final state represents the change in the number of phonons of each mode, as well as the flipped nuclear spin state. Note that this is a nonequilibrium process as the phonon occupation numbers have changed. Using Fermi's golden rule, the transition rate  $dW_{fi}$  within a solid angle  $d\Omega_e$  for the initial state to the final state is

$$dW_{fi} = \frac{2\pi}{\hbar} |\nu_{fi}|^2 \rho(E_e) d\Omega_e. \quad (2.36)$$

In k-space, each phonon takes up a volume  $8\pi^3/V$ . The relations between the Debye wave number  $k_D$ , Debye frequency  $\omega_D$ , the Debye energy  $E_D$ , and the Debye temperature  $T_D$ , Boltmann constant  $k_B$ , and atomic number density of the crystal are given by

$$k_D = \frac{\omega_D}{c_s} = \frac{E_D}{\hbar c_s} = \frac{k_B T_D}{\hbar c_s} = \left( \frac{6\pi^2 N}{V} \right)^{1/3}. \quad (2.37)$$

With the phonon energy  $E$  and phonon momentum  $k = |\mathbf{k}|$  related by  $E = \hbar c_s k$ , the number of phonon states with a particular polarization per unit energy, per unit solid angle is

$$\rho(E) = \begin{cases} 3NE^2/(4\pi E_D^3), & E < E_D; \\ 0 & E > E_D. \end{cases} \quad (2.38)$$

The relation between the conventional density of states  $D(\omega)$  and  $\rho(E)$  is then

$$\rho(E) = \frac{D(\omega)}{4\pi\hbar} \rightarrow D(\omega) = \frac{4\pi\hbar(3NE^2)}{4\pi E_D^3} = \frac{V\omega^2}{2\pi^2 c_s^3}. \quad (2.39)$$

Neglecting the difference in energy from the emitted and absorbed phonons, assume that  $E_e = E_a$ ,<sup>3</sup> and Eq. 2.36 is integrated over all directions and energies of the

---

<sup>3</sup>The energy required to flip a nuclear spin is  $|\mu_K B_0/K| \sim 10^{-20}$  erg, negligible compared to the Debye energy  $E_D \sim 10^{-14}$  erg.

emitted and absorbed phonon, along with a sum over all polarizations  $\mathbf{x}_{j_e}$  and  $\mathbf{x}_{j_a}$ , to give the rate

$$W_{fi} = \frac{2\pi}{\hbar} \sum_{j_e j_a} \int_0^{E_D} dE_a d\Omega_a d\Omega_e |v_{fi}|^2 \rho^2(E_a). \quad (2.40)$$

Taking the origin of the system to be the equilibrium position of atom  $\alpha$ ,  $\mathbf{R}_\alpha^{(0)} = 0$ , the two-phonon Raman matrix element is

$$\nu_{fi}^{(2)} = \langle f | \nu^{(2)} | i \rangle = \langle f | \frac{c_{K0}}{2\hbar} \sum_{\beta} \left( \mathbf{S}_{\beta\alpha} \times \mathbf{P}_{\beta\alpha} + \frac{\epsilon_0}{R_0^2} (\mathbf{S}_{\beta\alpha} \cdot \mathbf{R}_{\beta\alpha}^{(0)}) \mathbf{R}_{\beta\alpha}^{(0)} \times \mathbf{P}_{\beta\alpha} \right) \cdot \mathbf{K} | i \rangle. \quad (2.41)$$

Expanding  $\mathbf{S}_{\beta\alpha}$  and  $\mathbf{P}_{\beta\alpha}$  in terms of creation and annihilation operators, the first term of Eq. 2.41 becomes

$$\begin{aligned} & \frac{c_{K0}}{4N} \langle f | \sum_{\beta} \sum_{kj k' j'} \left( \frac{\mathbf{x}_j}{\sqrt{k}} \left[ a_{\mathbf{k}j} \left( e^{i\mathbf{k} \cdot \mathbf{R}_{\beta}^{(0)}} - 1 \right) + a_{\mathbf{k}j}^\dagger \left( e^{-i\mathbf{k} \cdot \mathbf{R}_{\beta}^{(0)}} - 1 \right) \right] \right. \\ & \left. \times \sqrt{k'} \mathbf{x}_{j'} \left[ i a_{\mathbf{k}' j'}^\dagger \left( e^{-i\mathbf{k}' \cdot \mathbf{R}_{\beta}^{(0)}} - 1 \right) - i a_{\mathbf{k}' j'} \left( e^{i\mathbf{k}' \cdot \mathbf{R}_{\beta}^{(0)}} - 1 \right) \right] \right) \cdot \mathbf{K} | i \rangle. \end{aligned} \quad (2.42)$$

The  $k, j, k'$ , and  $j'$  indices only select terms that cause transitions between the modes  $n_{\mathbf{k}_a j_a} \leftrightarrow n_{\mathbf{k}_a j_a} - 1$  and  $n_{\mathbf{k}_e j_e} \leftrightarrow n_{\mathbf{k}_e j_e} + 1$ . Calling  $n_{\mathbf{k}_a j_a} = n_a$  and  $n_{\mathbf{k}_e j_e} = n_e$ , the first term of Eq. 2.41 then becomes

$$\begin{aligned} & \frac{ic_{K0} \sqrt{n_a(n_e+1)}}{4N} \langle m_K = -\frac{1}{2} | \sum_{\beta} \left( \frac{\sqrt{k_e}}{\sqrt{k_a}} \mathbf{x}_{j_a} \times \mathbf{x}_{j_e} \left( e^{i\mathbf{k}_a \cdot \mathbf{R}_{\beta}^{(0)}} - 1 \right) \left( e^{-i\mathbf{k}_e \cdot \mathbf{R}_{\beta}^{(0)}} - 1 \right) \right. \\ & \left. - \frac{\sqrt{k_a}}{\sqrt{k_e}} \mathbf{x}_{j_e} \times \mathbf{x}_{j_a} \left( e^{-i\mathbf{k}_e \cdot \mathbf{R}_{\beta}^{(0)}} - 1 \right) \left( e^{i\mathbf{k}_a \cdot \mathbf{R}_{\beta}^{(0)}} - 1 \right) \right) \cdot \mathbf{K} | m_K = \frac{1}{2} \rangle. \end{aligned} \quad (2.43)$$

Using the simplification of a negligible difference in energy of the absorbed and emitted phonon  $k_e/k_a = k_a/k_e = 1$ , the first term of Eq. 2.41 can be written as

$$\frac{c_{K0} \sqrt{n_a(n_e+1)}}{2Ni} \langle -\frac{1}{2} | \sum_{\beta} \left( e^{-i\mathbf{k}_e \cdot \mathbf{R}_{\beta}^{(0)}} - 1 \right) \left( e^{i\mathbf{k}_a \cdot \mathbf{R}_{\beta}^{(0)}} - 1 \right) (\mathbf{x}_{j_e} \times \mathbf{x}_{j_a}) \cdot \mathbf{K} | \frac{1}{2} \rangle. \quad (2.44)$$

The nuclear spin operator  $\mathbf{K}$  can be rewritten in terms of unnormalized, circular basis vectors  $\mathbf{x}_{\pm} = \mathbf{x} \pm \mathbf{y}$  as

$$\mathbf{K} = K_z \mathbf{z} + (K_+ \mathbf{x}_- + K_- \mathbf{x}_+)/2. \quad (2.45)$$

Inserting this, the first term of Eq. 2.41 can be written compactly as

$$\frac{c_{K0} \sqrt{n_a(n_e+1)}}{4Ni} \sum_{\beta} \left( e^{-i\mathbf{k}_e \cdot \mathbf{R}_{\beta}^{(0)}} - 1 \right) \left( e^{i\mathbf{k}_a \cdot \mathbf{R}_{\beta}^{(0)}} - 1 \right) (\mathbf{x}_{j_e} \times \mathbf{x}_{j_a}) \cdot \mathbf{x}_+. \quad (2.46)$$

Similarly, the second term of Eq. 2.41 is found to be

$$\frac{c_{K0}\sqrt{n_a(n_e+1)}\epsilon_0}{8NiR_0^2}\sum_{\beta}(\dots)(\mathbf{x}_{j_e}\cdot\mathbf{R}_{\beta}^{(0)}\mathbf{R}_{\beta}^{(0)}\times\mathbf{x}_{j_a}-\mathbf{x}_{j_a}\cdot\mathbf{R}_{\beta}^{(0)}\mathbf{R}_{\beta}^{(0)}\times\mathbf{x}_{j_e})\cdot\mathbf{x}_+. \quad (2.47)$$

Defining  $\mathbf{n}_{\beta}=\mathbf{R}_{\beta}^{(0)}/R_0$ , and associating the direction of the magnetic field that causes a spin flip with the vector

$$\mathbf{w}_{\beta}=\mathbf{x}_{j_e}\times\mathbf{x}_{j_a}+\frac{\epsilon_0}{2}(\mathbf{x}_{j_e}\cdot\mathbf{n}_{\beta}\mathbf{n}_{\beta}\times\mathbf{x}_{j_a}-\mathbf{x}_{j_a}\cdot\mathbf{n}_{\beta}\mathbf{n}_{\beta}\times\mathbf{x}_{j_e}), \quad (2.48)$$

Eq. 2.41 can finally be written as

$$\nu_{fi}^{(2)}=\frac{c_{K0}\sqrt{n_a(n_e+1)}}{4Ni}\sum_{\beta}\left(e^{-i\mathbf{k}_e\cdot\mathbf{R}_{\beta}^{(0)}}-1\right)\left(e^{i\mathbf{k}_a\cdot\mathbf{R}_{\beta}^{(0)}}-1\right)\mathbf{w}_{\beta}\cdot\mathbf{x}_+. \quad (2.49)$$

Originally derived by Hebel and Slichter [95], the longitudinal relation time  $T_1^S$  is given by

$$\frac{1}{T_S}=W=\frac{\frac{1}{2}\sum_{\alpha\alpha'}W_{\alpha\alpha'}(E_{\alpha}-E_{\alpha'})^2}{\sum_{\alpha}E_{\alpha}^2}, \quad (2.50)$$

leading to the relation of Eq. 2.40 with  $1/T_1^S=2W_{fi}$ . Plugging in  $\nu^{(2)}$  into this equation gives

$$\begin{aligned} \frac{1}{T_1^S} &= \frac{\pi c_{K0}^2}{4N^2\hbar}\sum_{\beta\delta}\sum_{j_ej_a}\int_0^{E_D}dE_a\rho^2(E_a)n_{k_aj_a}(n_{k_ej_e}+1)\mathbf{x}_+\cdot\mathbf{w}_{\beta}\mathbf{w}_{\delta}\cdot\mathbf{x}_- \\ &\times\int d\Omega_a\left(e^{i\mathbf{k}_a\cdot\mathbf{R}_{\beta}^{(0)}}-1\right)\left(e^{-i\mathbf{k}_a\cdot\mathbf{R}_{\delta}^{(0)}}-1\right)\int d\Omega_e\left(e^{i\mathbf{k}_e\cdot\mathbf{R}_{\delta}^{(0)}}-1\right)\left(e^{-i\mathbf{k}_e\cdot\mathbf{R}_{\beta}^{(0)}}-1\right). \end{aligned} \quad (2.51)$$

The  $e^{i\mathbf{k}\cdot\mathbf{R}}$  terms can be rewritten with Legendre polynomials ( $P_l$ ) and spherical Bessel functions  $j_l$  using the expansion

$$e^{i\mathbf{k}\cdot\mathbf{R}}=4\pi\sum_{l=0}^{\infty}i^lj_l(kr)\sum_{m=-l}^{+l}P_l(\cos\theta), \quad (2.52)$$

where  $\theta$  is the angle subtended between  $\mathbf{k}$  and  $\mathbf{R}$ . After which, the solid angle integrals are analytically calculated to be

$$\int d\Omega\left(e^{i\mathbf{k}\cdot\mathbf{R}_{\delta}^{(0)}}-1\right)\left(e^{-i\mathbf{k}\cdot\mathbf{R}_{\beta}^{(0)}}-1\right)=4\pi\left(1+j_0(kR_{\delta\beta}^{(0)})-2j_0(kR_0)\right). \quad (2.53)$$

Note that  $j_0(x)=(\sin x)/x$  is simply a sinc function. The double sum over the twelve nearest neighbors  $\beta$  and  $\delta$  leads to 144 pairs of  $\beta\delta$ . The pairs can be categorized

into five sets  $\Lambda_m$  ( $m=0, 1, 2, 3, 4$ ) of  $g_m$  ordered pairs by common separation lengths  $R_{\beta\gamma}^{(0)} = \sigma_m R_0$  and angle  $\theta_m$  subtended with the atom  $\alpha$  given by  $\cos \theta_m = \mathbf{n}_\beta \cdot \mathbf{n}_\gamma$ , with values organized in Table 2.1. For pairs in a set  $\Lambda_m$ , the result of the angular integrals in Eq. 2.53 can be expressed in terms of the phonon momentum  $u = E/E_D$  as

$$J_m(u) = 1 + j_0(u\sigma_m\phi_D) - 2j_0(u\phi_D). \quad (2.54)$$

Here,  $\phi_D = k_D R_0 = (6\pi^2\sqrt{2})^{1/3}$  can be related to the phase advance over the nearest-neighbor distance  $R_0$  for a phonon with Debye wave number  $k_D$ . Specifically, this “phase advance” relation comes from the number of primitive FCC cells ( $N = 1$ ) over the volume of primitive ( $N = 1$ ) FCC cells  $V = \frac{1}{4}a^3$ , with the nearest FCC neighbor  $R_0 = a/\sqrt{2}$ , leading to a standard relation for an FCC lattice

$$k_D R_0 = \left(\frac{6\pi^2 N}{V}\right)^{\frac{1}{3}} R_0 = \left(\frac{6\pi^2 a^3 4}{2^{\frac{3}{2}} a^3}\right)^{\frac{1}{3}} = (6\pi^2\sqrt{2})^{1/3} = \phi_D, \quad (2.55)$$

where  $a^3$  defines the volume of any cubic cell [96].

In addition to the sum over nearest-neighbor atoms and phonon states, as well as the integrals over phononic energy and phonon wave-vector direction, an averaging over crystal orientation and averaging over phonon occupation numbers in thermal equilibrium are applied to Eq. 2.51 in Fitzgerald et al. [92]. The result of averaging over phonon occupation numbers in thermal equilibrium are the Bose-Einstein distributions

$$\langle n_{\mathbf{k}_a j_a} \rangle = \frac{1}{e^{E_a/k_B T} - 1} \quad \text{and} \quad \langle n_{\mathbf{k}_e j_e + 1} \rangle = \frac{e^{E_e/k_B T}}{e^{E_e/k_B T} - 1}. \quad (2.56)$$

After taking this average, and again using the simplification  $E_a = E_e$ , all terms involving energy in Eq. 2.51 are collected and rewritten in terms of the phonon momentum  $u = E/E_D$  to give the coefficients  $D_m(T^*)$  defined in Eq. 2.25. Thus, these coefficients  $D_m$  representing the change in phonon occupation numbers below the Debye temperature are not simply “fudge factors,” but arise naturally out of the theoretical derivation. Also after the averaging in Eq. 2.56, the dyadic  $\mathbf{w}_\beta \mathbf{w}_\delta$  can be summed exclusively over the phonon states  $j_e$  and  $j_a$ , resulting in the dyadic

$$\begin{aligned} \sum_{j_e j_a} \mathbf{w}_\beta \mathbf{w}_\delta &= \mathbf{2} + \epsilon_0 [\mathbf{2} - \mathbf{n}_\beta \mathbf{n}_\beta - \mathbf{n}_\delta \mathbf{n}_\delta] \\ &+ \frac{\epsilon_0^2}{2} [(\mathbf{n}_\beta \cdot \mathbf{n}_\delta)^2 \mathbf{1} - (\mathbf{n}_\beta \cdot \mathbf{n}_\delta) \mathbf{n}_\beta \mathbf{n}_\delta + (\mathbf{n}_\beta \times \mathbf{n}_\delta)(\mathbf{n}_\beta \times \mathbf{n}_\delta)], \end{aligned} \quad (2.57)$$

where the bold numerals represent the unit dyadic, e.g.,  $\mathbf{2} = 2(\mathbf{xx} + \mathbf{yy} + \mathbf{zz})$ . Eq. 2.57 can be obtained by simply expanding  $\mathbf{w}_\beta \mathbf{w}_\delta$  with Eq. 2.49 and summing terms such as

$$\sum_{j_e j_a} (\mathbf{x}_{j_e} \times \mathbf{x}_{j_a})^2 = (\hat{\mathbf{i}} \times \hat{\mathbf{j}})(\hat{\mathbf{i}} \times \hat{\mathbf{j}}) + (\hat{\mathbf{j}} \times \hat{\mathbf{i}})(\hat{\mathbf{j}} \times \hat{\mathbf{i}}) + \dots = \mathbf{2}. \quad (2.58)$$

In Kuzma et al. [94], it is shown that polycrystalline and single-crystal  $^{129}\text{Xe}$  should in fact have the same relaxation rate due to Raman-scattering that mediates spin rotation. From the treatment of the theory of symmetry presented by Landau and Lifshitz [6], a sum is done over the group of all symmetry transformations of the cube,  $O_h$ . The group  $O_h$  is composed of the octahedron group  $O$ , which has the system of axes that are the system of axes of symmetry of a cube, and the second-order rotary-reflection group  $S_2 = C_i$ , i.e.,  $O_h = O \times C_i$ . The group  $C_i$  contains two elements: the identical transformation  $E$  and the inversion  $I$ . The operation  $I$  is defined as  $I = C_2 \sigma_H$ , where  $C_N$  is the operation of rotation through an angle  $2\pi/n$  about a given axis and  $\sigma_h$  is a reflection in a plane perpendicular to a given axis. The group  $O$  contains 24 elements, and is composed of fourth-order rotations  $C_4$  having axes that pass through the centers of opposite faces (nine elements), third-order rotations  $C_3$  having axes through opposite corners (eight elements), second-order rotations  $C_2$  having axes through the midpoints of opposite edges (six elements), and the identity  $E$ . These elements are divided into five classes<sup>4</sup>:  $E$ ,  $C_3$  and  $C_3^2$  (eight elements),  $C_4$  and  $C_4^3$  (six elements),  $C_4^2$  (three elements), and  $C_2$  (six elements), all about their respective axes. The group  $O$  makes up 24 elements of  $O_h$  (and five classes), and the remainder of the elements (and classes) are simply those of  $O$  with the inversion  $I$  included with them. Thus, the group  $O_h$  contains  $g = 48$  elements divided among ten classes. The irreducible representations of  $O$  are labeled with the symbols  $\alpha = A_1, A_2, E, F_2,$  and  $F_1$ , with dimensions  $f^{(\alpha)}$  of 1, 1, 2, 3, and 3, respectively. The group  $O_h$  has  $r = 10$  irreducible representations  $G_{ij}^{(\alpha)}$ . The fundamental orthogonal relation for irreducible representations is given by

---

<sup>4</sup>A class is a set of conjugate elements of the group, where  $A$  and  $B$  are said to be conjugate if  $A = CBC^{-1}$ , where  $C$  is also an element of the group, e.g., the rotations  $C_n^k$  and  $C_n^{-k}$  belong to the same class.

$$\frac{1}{g} \sum_G G_{ri}^{(\alpha)} G_{sj}^{(\beta)} = \frac{1}{f^{(\alpha)}} \delta_{\alpha\beta} \delta_{rs} \delta_{ij}, \quad (2.59)$$

where  $\delta_{ij}$  is the Kronecker delta.

The motivation for using group theory is one of simplification—to avoid summing over 144 nearest-neighbor pairs, the symmetry of the nearest neighbors (the group  $O_h$ ) is used to reduce each sum to five terms over the sets  $\Lambda_m$ . For a function  $f(\mathbf{n}_\beta, \mathbf{n}_\delta)$ , the sum over atomic states can be written as

$$\sum_{(\beta\delta) \in \Lambda_m} f(\mathbf{n}_\beta, \mathbf{n}_\delta) = g_m \langle f \rangle_m = \frac{1}{g} \sum_G G f(\mathbf{n}_\beta, \mathbf{n}_\delta) = \frac{1}{g} \sum_G f(G^{-1} \mathbf{n}_\beta, G^{-1} \mathbf{n}_\delta), \quad (2.60)$$

where  $G^{-1}$  is the inverse group element to  $G$ . The operation of  $G$  transforms  $\mathbf{n}_\beta$  by

$$G \mathbf{n}_\beta = G \sum_i n_{\beta i} \mathbf{x}_i = \sum_{ij} n_{\beta i} \mathbf{x}_j G_{ij}^{(F_1)}, \quad (2.61)$$

where  $\mathbf{x}_i$  forms a basis for the three-dimensional irreducible representation  $F_1$ . Using this formalism on the sums of the dyadics  $\mathbf{n}_\beta \mathbf{n}_\delta$  and  $(\mathbf{n}_\beta \times \mathbf{n}_\delta)(\mathbf{n}_\beta \times \mathbf{n}_\delta)$  gives the equations

$$\begin{aligned} \sum_{(\beta\delta) \in \Lambda_m} \mathbf{n}_\beta \mathbf{n}_\delta &= g_m \langle \mathbf{n}_\beta \mathbf{n}_\delta \rangle_m = \frac{g_m}{g} \sum_{ijrs} n_{\beta i} n_{\delta j} \mathbf{x}_r \mathbf{x}_s \sum_G G_{ri}^{(F_1)} G_{sj}^{(F_1)} \\ &= g_m \frac{1}{3} \mathbf{n}_\beta \cdot \mathbf{n}_\delta = g_m \frac{1}{3} \cos \theta_m, \quad \text{and} \\ \sum_{(\beta\delta) \in \Lambda_m} (\mathbf{n}_\beta \times \mathbf{n}_\delta)(\mathbf{n}_\beta \times \mathbf{n}_\delta) &= \frac{g_m}{g} \sum_{abcd} n_{\beta a} n_{\delta b} n_{\beta c} n_{\delta d} \sum_{ijrs} \epsilon_{abi} \epsilon_{cdj} \mathbf{x}_r \mathbf{x}_s \sum_G G_{ri}^{(F_1)} G_{sj}^{(F_1)} \\ &= g_m \frac{1}{3} (\mathbf{n}_\beta \cdot \mathbf{n}_\beta \mathbf{n}_\delta \cdot \mathbf{n}_\delta - \mathbf{n}_\beta \cdot \mathbf{n}_\delta \mathbf{n}_\beta \cdot \mathbf{n}_\delta) = g_m \frac{1}{3} \sin^2 \theta_m. \end{aligned} \quad (2.62)$$

Putting this all together gives the equation

$$\mathbf{x}_+ \cdot \left[ \sum_{(\beta\delta) \in \Lambda_m} \sum_{j \in \mathcal{J}_a} \mathbf{w}_\beta \mathbf{w}_\delta \right] \cdot \mathbf{x}_- = \left( 4 + \frac{8\epsilon_0}{3} + \frac{4\epsilon_0^2}{9} \right) + \frac{2\epsilon_0^2}{9} P_2(\cos \theta_m). \quad (2.63)$$

In Fitzgerald et al. [92], instead of the use of group theory, an integral using Wigner  $D$  functions [97] is taken over all crystal orientations, which represents a polycrystalline sample with sufficiently small crystallites so that spin diffusion guarantees uniform polarization across the sample. The result obtained by this method is the same as Eq. 2.63, indicating that the average over orientation is ultimately irrelevant.

Thus, any average over crystal orientation yields the same result given in Eq. 2.63 and there arises a profound consequence of this theory—there is no dependence on the crystal structure or orientation as long as it can be assumed that a majority of the atoms reside in an fcc lattice with a sufficiently uniform polarization. Mesoscopic or macroscopic variations in grain size or crystal orientation should therefore not affect the observed  $T_1$  time, unless the phonon occupation numbers are somehow affected by this varying of grain size. However, the overlying assumption to this important result is that the phonon spectrum (considered entirely harmonic in this derivation) is unaffected by lattice structure, which is a somewhat crude approximation. In other words, the available phonon states are built up by the entire lattice, not just a single unit cell, so in actuality the phonon spectrum of a single crystal should differ phonon spectrum of a polycrystalline solid (long-wavelength modes should disappear for a polycrystalline solid).

Combining the results of the averaging over phonon occupation numbers in thermal equilibrium and summation over nearest-neighbor atoms and phonon states into Eq. 2.51, and using the appropriate abbreviations labeled above, gives Eq. 2.21, which is expanded into Eq. 2.29.

#### 2.2.4.2 Temperature dependence of parameters and model

The temperature dependence of parameters is taken into account for a more accurate calculation. This is a complicated problem because the shrinking or expansion of the lattice can have difficult-to-predict effects on the other parameters such as strength of interaction and the Debye temperature. In 1981, Granfors et al. published x-ray data of high-pressure, single-crystal solid xenon [98]. From this, a temperature-dependent lattice-spacing equation is found by fitting lattice-parameter data taken from 78 K to 161 K,

$$b(T) = 6.2764216 + 0.00180771(T - 125) + 4.57633 \times 10^{-6}(T - 125)^2 \text{ \AA}, \quad (2.64)$$

The relationship between the lattice parameter  $b$  and the nearest neighbor in an fcc lattice (such as xenon) is  $R_0 = b/\sqrt{2}$ .

The other temperature-dependent parameter accounted for in the calculation by Kuzma et al. [83], and presumably in the works Fitzgerald et al. [92] and Gatzke et

al. [82] (it is mentioned in Gatzke [81], but not written explicitly), is the strength of the spin-rotation interaction at equilibrium lattice spacing,  $c_{K0}$ . In both Kuzma et al. [83] and Patton [84], a temperature-dependent equation for the equilibrium spin-rotation interaction appears,

$$c_{K0}(T) = c_{K0}(77 \text{ K}) \left\{ 1 + 300 \text{Å}^3 [b^{-3}(T) - b^{-3}(77 \text{ K})] \right\}. \quad (2.65)$$

The spin-rotation interaction is scaled by density, according to Brinkmann and Carr [72] and Cowgill and Norberg [78], although it is unclear how these references are used to generate this scaling. From what can be garnered from the collection of literature on this work, the lattice parameter and spin-rotation interaction appear to be the only parameters that are adjusted for temperature. In Fig. 2.3, the model displayed in the literature is reproduced with only these two parameters having any temperature dependence.

### 2.2.5 Epilogue

Few questions concerning the longitudinal relaxation of solid  $^{129}\text{Xe}$  remained after this body of work was amassed. In all, Fig. 2.3 demonstrates the status of longitudinal relaxation of  $^{129}\text{Xe}$  after this revival of solid xenon work (of which a majority was conducted by Prof. Happer's group in Princeton) due to the discovery of hyperpolarization of Xe nuclei from alkali metal valence electrons. However, one problem plaguing experiments after the seminal Princeton work was the reproducibility of solid  $^{129}\text{Xe}$   $T_1$  times [89, 99, 100]. Because of the reproducibility problems, and because the spin-rotation mediated by Raman-scattering model has been accepted as correct, groups concentrated their solid xenon efforts in different areas, including: extremely low-field NMR detection using superconducting quantum interference devices (SQUIDS) [101], spatial imaging without averaging [102], spin-spin relaxation intricacies [100, 103, 104, 105, 106, 107], and the effect of the introduction of oxygen on  $^{129}\text{Xe}$   $T_1$  times [108].

## 2.3 Methods

Two different experimental set-ups are used to create solid xenon that contains hyperpolarized  $^{129}\text{Xe}$ —both involve the phenomenon of spin-exchange that occurs

between a xenon nucleus and a Rb valence electron. The first method is a flow-through polarizer, and the second is a static convection cell used for spin-exchange optical pumping. Following descriptions of these methods, there is a brief description of the temperature controller for both types of experiments. Finally, the process of measuring longitudinal relaxation is discussed.

### 2.3.1 Flow-through polarizer

In the first experimental apparatus used for these longitudinal relaxation experiments, hyperpolarized  $^{129}\text{Xe}$  is generated using a home-built, flow-through xenon polarizer [109, 110, 111, 112, 113, 114]. The general concept of the flow-through  $^{129}\text{Xe}$  polarizer is to flow a gas mixture containing small amounts of naturally abundant xenon through a optically pumped Rb vapor, and separate the hyperpolarized xenon from the gas mixture cryogenically (see Fig. 2.4). The gas mixture includes He and  $\text{N}_2$  from the University of Utah General Stores, the naturally abundant xenon is from Linde Electronics and Speciality Gases (Material Number 24086611), and the enriched xenon gas is from Spectra Gases (Serial Number 082948). Unless otherwise specified, the standard flow rate for the He,  $\text{N}_2$ , and Xe gases are 1000, 500, and 10 standard cubic centimeters per min (scm), respectively; flow rates are controlled by three Aalborg GFC Mass Flow Controllers (MFC's, models GFCS-011401, FGCS-010549, SKUW-183460). The flow-through polarizer is operated at a total system pressure of roughly 1 psig to prevent any atmospheric leaks. The gas mixture flows through a SAES PureGas purifier (Part number FT400-902) to an optical-pumping cell containing two grams of Rb (designed by Geoff Schrank [114] and fabricated by University of Utah glass blower Kevin Teaford), which sits inside of an oven that is kept at 140 °C. The temperature around the cell is kept sufficiently high so that a Rb vapor is created and the atomic ( $m_J$ ) states of the valence electron of the Rb are optically pumped (see Appendix A).

For a majority of the flow-through polarizer experiments, the Rb vapor is optically pumped by circularly polarized laser light from a 50 W thermoelectrically cooled laser diode bar from Dilas Diode Laser, Inc., Tuscon Az., (Part Number

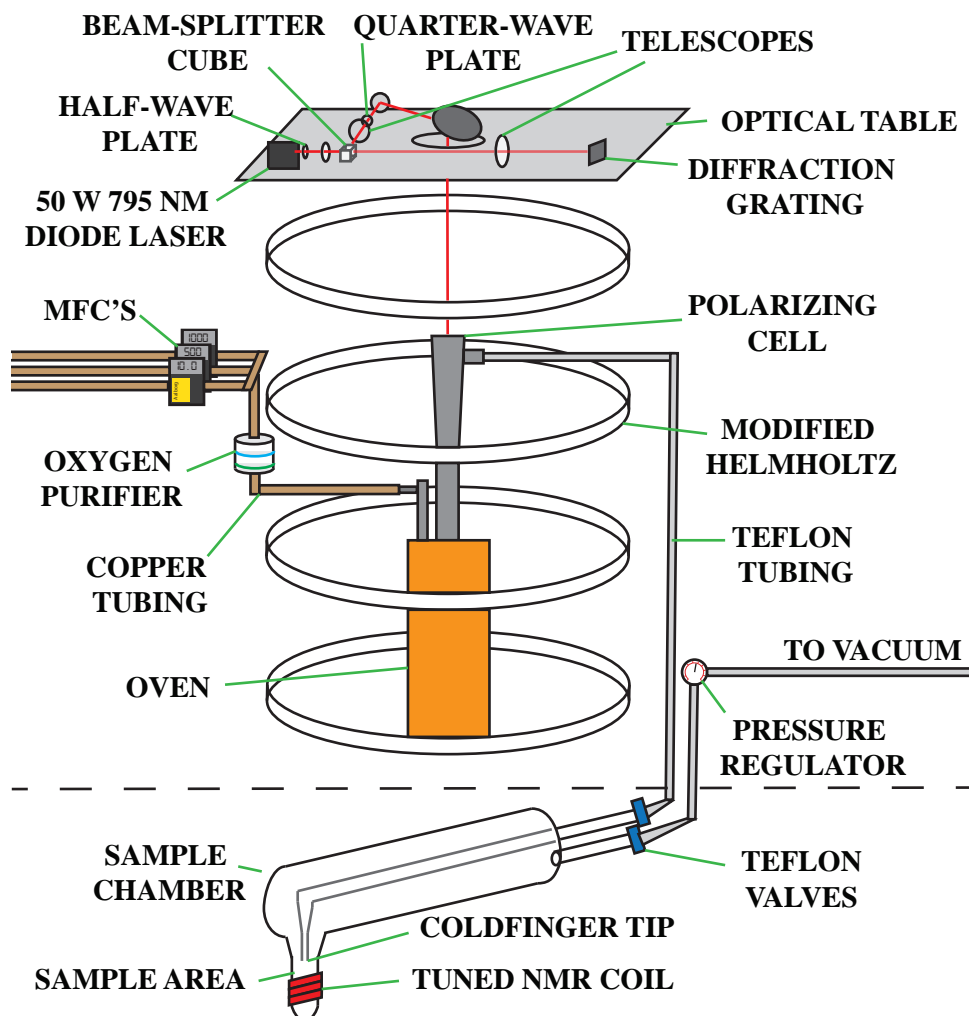


**Figure 2.4.** Schematic of flow-through polarizer and freezing cell.

MMB-795.2-50C-SS4.x).<sup>5</sup> The diode array is spectrally narrowed with feedback from a diffraction grating [115, 116, 117]. The Edmund Optics holographic diffraction grating (Part number NT43-266) feeds the first-order light back into the laser cavity. The first-order light seeds the laser cavity with a selected frequency depending on the angle and grating spacing, according to the equation

$$\lambda = 2d \sin \theta, \quad (2.66)$$

<sup>5</sup>In early experiments, a QPC 50 W laser (Part number QPC 4101-B) was used until its failure.

where  $d$  is the grating spacing and  $\theta$  is the angle from the path of the beam to the normal of the diffraction grating. In these experiments, a diffraction grating with a grating spacing of  $d = 1/2400$  mm and angle  $\theta = 72.5^\circ$  feeds back first-order light with wavelength 795 nm. A half-wave plate, in conjunction with a Thorlabs polarizing beam splitter cube (Part number PBS252), splits the optical table into a narrowing portion and optical-pumping beam portion. This is done in order to maximize the power of (and efficiently control the) light used for optical pumping [118], allowing a minimum of feedback for the frequency narrowing while sufficiently seeding the laser at a desired frequency. The optical-pumping beam is sent through a quarter-wave plate (to make the light circularly polarized for optical pumping), after which it is shaped independently of the narrowing portion and directed into the optical pumping cell.

Within the pumping cell, the xenon nuclei are hyperpolarized by the Rb vapor via spin-exchange optical pumping (SEOP) [20, 119, 120]. The gas mixture containing hyperpolarized xenon travels out of the pumping cell into room-temperature borosilicate-glass tubing, with Rb removed from the mixture by a cooling jacket around the pumping cell. The He-N<sub>2</sub>-Xe mixture is then flowed through approximately 50 ft. of tubing and connections (Swagelok polytetrafluoroethylene (PTFE)) into a borosilicate-glass sample chamber designed by Zayd Ma (see Ma [121]) and fabricated by University of Utah glassblower Kevin Teaford. The sample tip rests in the “sweet spot” of a 2-Tesla Oxford Instruments Limited horizontal-bore magnet (Serial Number C28296), to obtain maximum magnetic-field magnitude and homogeneity across the sample. During the accumulation period of xenon, the tip of the sample chamber is kept at 77 K. The gas mixture flows through the now-cold sample tip, freezing out the xenon from the mixture (the triple point for xenon is 161.405 K). The remaining He and N<sub>2</sub> is flowed back to the flow-through polarizer, to the system pressure controller and vacuum pump. A typical solid xenon accumulation time for the experiments is 20 min. After the solid xenon sample is accumulated, the sample chamber is closed off and isolated from the flow-throw polarizer, with the remaining He and N<sub>2</sub> keeping a positive pressure on the sample chamber (typical conditions hold the sample chamber at approximately 1 psig). Upon freezing the

xenon directly from the gas mixture, the solid xenon is a polycrystalline structure with presumably very small grain size. However, because the crystallites scatter white light, they are assumed large enough to be considered a bulk-type solid (however disordered the crystallites are). This type of solid xenon is denoted as “snow” due to its method of formation and appearance. The alternative preparation of solid xenon is denoted as “ice,” where the ice preparation entails an additional step in which the snow temperature is raised to the liquid xenon temperatures (160-170 K), and then refrozen at 77 K. During the temperature cycle (see Sect. 2.3.3 below), the NMR line shape of the xenon is monitored for phase changes, as displayed in Fig. 2.5(b). The entire frequency spectrum moves into a distinct, narrow liquid line when the entire xenon sample has liquefied. Evidence for the existence of a liquid line includes a chemical-shift analysis comparing solid, liquid, and gas xenon phases; there is also an absence of a liquid-phase when a purposefully low partial pressure of xenon is used and the narrow liquid line is *not* observed. After confirmation that the entire sample has become liquid, the temperature is lowered back to 77 K and the sample is solid

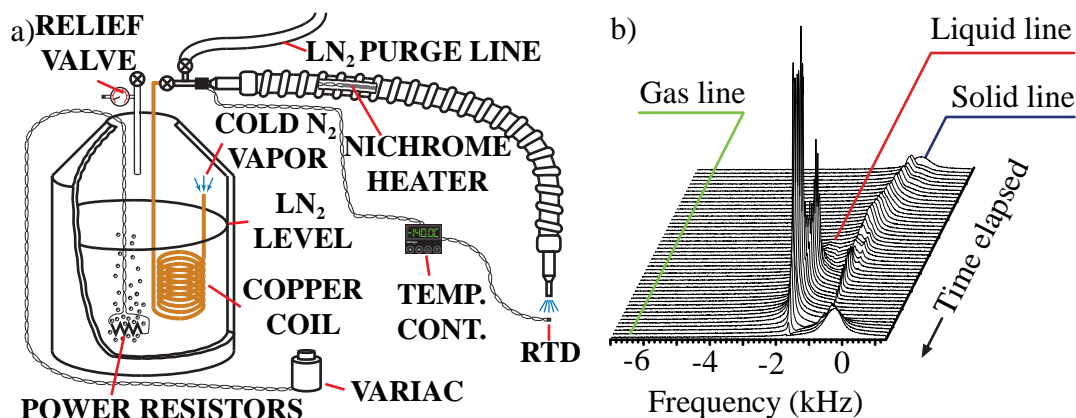


**Figure 2.5.** Schematic of temperature-control system and chemical shift monitoring. (a) A schematic of temperature-control system discussed in Sect. 2.3.3 is shown. (b) A representative data set monitoring NMR chemical shift at a magnetic field of 2.08 T during a temperature cycle that is used to create xenon ice. The sample is held at liquid xenon temperatures until the entire signal shows liquid frequencies, then the temperature is quickly lowered back to 77 K and the ice solid is obtained. The amount of time elapsed for this particular warm-and-refreeze procedure is roughly 3 min. The relative chemical shifts of gas, liquid, and solid phases of  $^{129}\text{Xe}$  are also shown.

xenon ice. The temperature is then set (see Sect. 2.3.3) and an experiment is run.

### 2.3.2 Convection cell

The other set of experiments, which explore the effect of changing isotopic concentration of  $^{129}\text{Xe}$  in the xenon ice on the  $T_1$  time, use a convection cell to create the hyperpolarized xenon solid. The convection cell is introduced in Su et al. [122] and partially described in Morgan et al. [100] and Clewett et al. [123]. A convection cell is a sealed cell that has an area where rubidium is kept for optical pumping, along with a mixture of He,  $\text{N}_2$ , and xenon gases. (The cells in use for this experiment are fabricated by University of Utah glassblower Kevin Teaford, and are filled and pull-off using a hi-vac system.) The advantage a sealed convection cell has over a flow-through polarizer is no isotopically enriched xenon gas is lost in the convection cell; the xenon gas is reused, whereas the flow-through polarizer the xenon often gets lost to the atmosphere. Any dilute-spin, solid xenon experiments are only done with the sealed convection cell. Unfortunately, only ice can be made in a convection cell, so there is no comparison between snow and ice with enriched xenon in this experimental set-up. A diagram of the convection cell and further details are given in Appendix B.

The convection cell connects an optical-pumping bulb with a sample tip area by two tubes that are over-under. During polarization of the  $^{129}\text{Xe}$  nuclei, the sample tip is kept at liquid xenon temperatures and the optical-pumping bulb is kept hot enough that a sufficient Rb vapor pressure is held for optical pumping purposes (typically greater than 100 K). The sample tip area has a tuned (tank) NMR coil around it and an RTD (resistive thermal device) affixed to the coil with thermal paste for temperature measurements. The circularly polarized light for the optical pumping is provided by a CVS 30 W diode laser that is spectrally narrowed with the first-order light from a diffraction grating. The convection cell sits inside of a 2 T horizontal-bore magnet with the optical-pumping bulb facing the laser, and the sample tip sitting in the sweet spot of the magnet. During optical pumping and xenon polarization, the  $^{129}\text{Xe}$  relative polarization is monitored by NMR, taking measurements (with a very small flip angle,  $< 0.5^\circ$ ) every minute until a large, steady-state  $^{129}\text{Xe}$  polarization is achieved. When the  $^{129}\text{Xe}$  polarization is sufficiently high or has reached a maximum,

the feedback loop for the temperature control is cut, causing the temperature to plummet, and forming hyperpolarized solid xenon. The heat provided to the oven around the optical-pumping bulb is also shut off, then the optical pumping laser. After the solid xenon is formed, the sample tip is purged with liquid nitrogen for the 77 K measurements.

### 2.3.3 Temperature control

To achieve a sample temperature of 77 K, the borosilicate-glass sample tip is kept submerged in a bath of liquid N<sub>2</sub>. An Omega Thinfilm RTD (Part number F3105) is attached directly onto the NMR coil, affixed by thermal paste (Emerson & Cumming, Product Name STYCAST 2850FT BLACK). The RTD is fed into an Omega controller (Product Number CNi166D22), where the temperature is output. The RTD is not relied on during the temperature cycle process for the ice formation—the NMR line shape is also monitored (see Fig. 2.5). To raise the temperature quickly, a warming gas of room temperature N<sub>2</sub> is flowed into the sample chamber, causing the liquid N<sub>2</sub> to quickly boil-off. This makeshift temperature-control method achieves a stability of  $\pm 3$  K for minutes at a time. After holding the temperature above the triple point of xenon (typically -108 to -100 °C) for a sufficient amount of time, the entire <sup>129</sup>Xe NMR line shape becomes the frequency of the liquid phase of xenon. The warming gas is removed and the liquid N<sub>2</sub> is allowed, once again, to flood the dewar surrounding the sample chamber.

The temperature-dependent measurements, as well as the pumping portion for the convection-cell experiments, involve the use of an active-temperature-control system, shown in Fig. 2.5(a). This system generates cold nitrogen gas (approximately 100 K) by using AC-driven power resistors controlled by a Variac to boil the liquid nitrogen inside of a pressurized dewar. The cold nitrogen gas is then pushed into a vacuum-jacket transfer line (Technifab Products, Inc., Brazil, IN). A nichrome heater is placed inside of the transfer line and is powered by a Variac AC power supply. The nichrome heater circuit is closed and opened by a Omega controller, which also reads the temperature from an RTD that is close to the sample tip. The Omega controller is programmed to provide a feedback loop between the temperature measured by an RTD at the sample tip and the nichrome cold nitrogen gas heater. A set point for

the temperature is selected on the controller for approximately  $\pm 0.3$  K stability, and the Variac supply for the nichrome heater is adjusted to set a rough range for the temperature control.

### 2.3.4 Measurement of longitudinal relaxation

Again, using the flow-through polarizer, the standard solid xenon collection period for ice or snow is about 20 min, yielding roughly 200 cubic centimeters (cc) of xenon in gas phase. The density of gaseous xenon is  $5.761 \times 10^{-3}$  g/cc, and the density of solid xenon is 3.640 g/cc, leading to roughly 0.317 cc of solid xenon in a typical experiment. The accumulation of hyperpolarized xenon is monitored by  $^{129}\text{Xe}$  NMR with extremely small pulses (less than  $0.5^\circ$ ) occurring once every minute. After a standard collection period, the hyperpolarized  $^{129}\text{Xe}$  in the solid xenon sample has a large spin polarization, leading to a large NMR signal, even when extremely small flip angles (approximately  $1^\circ$ ) are used. The initial experiments use an APOLLO NMR spectrometer (Tecmag Inc., Houston, TX) along with an Analogic 2kW radio-frequency (RF) Power Amplifier (Part Number AN8063).<sup>6</sup> After failure of the APOLLO system, a Tecmag Redstone HF2 1RX MRI NMR spectrometer (Serial number 37863) is used for pulsing and data acquisition. The Redstone spectrometer is initially used along with the Analogic amplifier. However, as the smallest pulses produced by the Analogic-Redstone combination are too unreliable at the extremely small voltages needed for this experiment, a Mini-Circuits Coaxial Amplifier (Part number ZFC-1000VH) is used as the RF power amplifier. The single-coil circuit uses a Tecmag Inc. Transcoupler II (Part number 600-0028-01) crossed-diodes passive switch, along with a Miteq Inc. 5-500 MHz preamplifier (Part number A-U-1114T-1B/4) to boost the receiving FID signal before it is inputted into the Redstone's analog-to-digital converter (ADC). To discount probe instability as a possible source of error, initial  $T_1$  experiments use two types of probes: a tuned so-called "tank" probe, and a so-called

---

<sup>6</sup>Initially, prior to the  $T_1$  experiments, an unexpected difference in the free induction decay (FID) and spin-spin relaxation time  $T_2$  is observed between the ice and snow. This discrepancy is, unfortunately, found to not be reproducible or controllable, and experimental efforts on this front are abandoned.

50-Ohm (or “flat”<sup>7</sup>) probe. Circuit diagrams of each probe type are given in Fig. 2.6, and a quality, general review of these probes and experimental NMR techniques is found in Fukushima and Roeder [79], as well as in Wheeler and Conradi [125].

Unless otherwise specified, at the beginning of each measurement, an appropriate pulse length and height is chosen such that the spectrometer’s ADC buffer is as full as possible without saturating the receiving amplifier (linearity tests are performed on all electronic equipment). Once a suitable pulse size is found, the flip angle is calibrated by taking sequential shots (much faster than  $T_1$ ) and fitting the decay of the signal caused by the RF pulse to the equation

$$\text{FID Height}(N) = A (\cos(\theta))^{(N-1)}. \quad (2.67)$$

Here,  $N$  is the pulse number,  $\theta$  is the flip angle, and  $A$  is a parameter of the fit. After the flip angle of a particular sample is calibrated, the  $T_1$  measurement begins.

For the experiments presented herein, a longitudinal relaxation, or  $T_1$  measurement, is conducted by monitoring the decay of polarization vs. time. As previously mentioned, the hyperpolarization of the  $^{129}\text{Xe}$  nuclei leads to extremely large NMR signals (some of the largest ever recorded). When dominated by uniform relaxation mechanisms, polarization typically tends to thermal equilibrium with a characteristic rate  $T_1$  in the equation (assuming thermal polarization is negligible)

$$P(t) = P(0)e^{-\frac{t}{T_1}}, \quad (2.68)$$

where  $P$  is the relative polarization and  $t$  is time. A standard rule-of-thumb for a  $T_1$  measurement is that the observation time must, at minimum, be as long as  $T_1$ , and preferably be two or three times as long as  $T_1$  for sufficient precision. Instead of using the integral of NMR frequency lineshape, a single point on the FID was monitored.<sup>8</sup> After an experiment is run, the loss of polarization due to the RF pulses with flip angle  $\theta$  is accounted for by correcting each data point with the equation

$$E_{\text{corrected}}(N) = \frac{E_{\text{raw}}(N)}{\cos(\theta)^{N-1}}, \quad (2.69)$$

---

<sup>7</sup>Called so because of the flat frequency response of the probe.

<sup>8</sup>Many comparisons between the two methods confirmed that each gives the same  $T_1$  result (within experimental error).

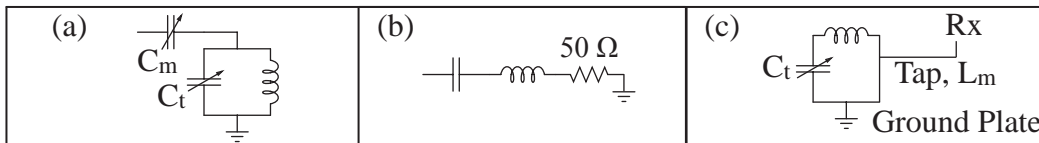


**Figure 2.6.** Schematics of useful NMR probes. (a) A tuned “tank” circuit (essentially a LC “notch” filter [124]) with a variable “tuning” capacitor,  $C_t$ , and “matching” capacitor,  $C_m$ , needed to match the transmission line impedance to the circuit element impedance at a chosen frequency. (b) A so-called  $50\ \Omega$  “flat” probe (essentially a simple RLC) resonator. The impedance of the inductor and capacitor combination are typically small enough to be negligible compared to the  $50\ \Omega$  resistor in the element. (c) A useful probe for high-frequency tuning (150-250 MHz), with a tap into a grounded resonator that affects the matching impedance through the inductance.

where  $E_{\text{corrected}}(N)$  and  $E_{\text{raw}}(N)$  are the corrected and raw experimental data points, respectively, for record number (and hence pulse number)  $N$ . The corrected data points,  $E_{\text{corrected}}(N)$ , are then fit to Eq. 2.68 to extract a characteristic longitudinal relaxation time,  $T_1$ . After a solid  $^{129}\text{Xe}$   $T_1$  measurement, the sample chamber is warmed and evacuated in preparation for the next sample and experiment; the convection cells are simply warmed.

## 2.4 Results

The experimental data are classified in two major categories: ice data and snow data. Because of the unexpected  $T_1$  results, different experimental arrangements are attempted in efforts to discount any instrumental errors that could be present; these include probe designs, cell designs, buffer gas presence, and temperature-controlling methods. In initial experiments (before the polarizer laser and spectrometer failures), the discrepancies between the  $T_1$  values of ice and snow samples at 77 K is explored. These experiments use the QPC laser on the flow-through polarizer and use the APOLLO spectrometer. The data for these initial experiments are shown in Table 2.2. With this initial data, a remarkable precision is found in the values between ice and snow. Each measurement shown is a completely different sample and, even though the probe and sample chamber is adjusted (and removed from the superconducting magnet) between many of the experiments, the difference between ice and snow  $T_1$  times is thus found to be robust and reproducible.

**Table 2.2.** Initial naturally abundant xenon, solid  $^{129}\text{Xe}$  ice and snow  $T_1$  values. The errors come from a least-squares fit. For tuned (or tank) circuit measurements (see Fig. 2.6(a)), the flip angle was not measured properly, but anecdotally smaller than  $1.5^\circ$ . The flat probe measurements (see Fig. 2.6(b)) are to discount probe effects as a possible source of experimental error. Experiments are run with and without helium and nitrogen buffer gases remaining in the sample cell. The averages of the  $T_1$  values from each type of sample are also shown.

	$T_1$ (min)	Probe	Flip Angle	Buffer Gas
Ice	$169.93 \pm 0.25$	Tank	N/A	Yes
	$168.16 \pm 0.16$	Tank	N/A	No
	$165.14 \pm 0.70$	Tank	N/A	Yes
	$168.7 \pm 1.0$	Tank	N/A	Yes
	$173.6 \pm 1.5$	Tank	N/A	Yes
	$171.44 \pm 0.32$	Flat	$2.67^\circ \pm 0.19^\circ$	Yes
	$172.02 \pm 0.31$	Flat	$3.11^\circ \pm 0.30^\circ$	No
	$166.55 \pm 0.81$	Flat	$3.02^\circ \pm 0.07^\circ$	No
	$167.30 \pm 0.33$	Flat	$3.31^\circ \pm 0.32^\circ$	Yes
Ice Average	$169.2 \pm 1.2$			
Snow	$150.79 \pm 0.43$	Tank	N/A	No
	$148.47 \pm 0.28$	Tank	N/A	Yes
	$150.80 \pm 0.25$	Tank	N/A	Yes
	$148.61 \pm 0.42$	Flat	$8.96^\circ \pm 0.05^\circ$	No
	$149.30 \pm 0.40$	Flat	$6.27^\circ \pm 0.07^\circ$	Yes
	$149.80 \pm 0.40$	Flat	$6.91^\circ \pm 0.14^\circ$	Yes
	$150.19 \pm 0.37$	Flat	$6.91^\circ \pm 0.14^\circ$	Yes
	$151.02 \pm 0.51$	Flat	$4.67^\circ \pm 0.22^\circ$	No
Snow Average	$149.87 \pm 0.54$			

One caveat is that the flip angle is not calibrated properly for the initial tank circuit measurements, although anecdotal accounts give the flip angle as smaller than  $1.5^\circ$ . This anecdotal limit comes from flip-angle calibrations that are found to give erroneous corrections—the method of mapping a flip-angle dependence with a particular sample and applying that flip-angle correction on a completely different sample (that the  $T_1$  data are taken on) leads to an inexact calibration. This comes from the tuned coil having a sensitive dependence on the sample size and shape. Because a new sample is made for each measurement, a new flip-angle calibration is needed for each sample (this is done for the temperature-dependent experiments in Sect. 2.4.1 and 2.4.2). However, the similarity of the tank and flat probe  $T_1$  values indicate that

minimal polarization loss occurred in the tank-probe measurements, such that the smallness of the flip angle gives sufficient initial results. Also shown in Table 2.2 are experiments with and without buffer gases in the sample chamber during the  $T_1$  measurement, and no measurable difference is found.

Extremely long longitudinal relaxation measurements demonstrate that the snow  $T_1$  does not tend towards the ice  $T_1$ . Using approximately the averages listed in Table. 2.2, a reciprocal difference that shows the hypothetical characteristic time,  $T_\Delta$ , of a mechanism that would cause the snow  $T_1$  to trend towards the ice  $T_1$  is given by the calculation

$$\frac{1}{T_\Delta} = \frac{1}{T_{1(\text{Snow})}} - \frac{1}{T_{1(\text{Ice})}} = \frac{1}{150} - \frac{1}{170} \implies T_\Delta \approx 22.5 \text{ h.} \quad (2.70)$$

Therefore, in this hypothetical situation, the snow  $T_1$  value would “relax” to the ice  $T_1$  value with a characteristic time of 22.5 h. Snow measurements are taken out as far as 900 min, and show no change in slope over that period, giving evidence the snow relaxation rate does not tend towards the ice relaxation rate.

After the newer Redstone system and Dilas laser calibration, a confirmation of previous ice vs. snow  $T_1$  at 77 K measurements is done; results are shown in Fig. 2.7. The new probe, sample chamber, and borosilicate-glass dewar are also fastened to a brass housing for stability. For these measurements, a proper flip-angle calibration is, again, done for the tuned coil before each experiment begins. The ice  $T_1$  data shown in Fig. 2.7 are similar to the average of Table. 2.2. The snow data are slightly lower than the average of the initial experiments, perhaps indicating oxygen or smaller crystallite sizes may have played a role in the relaxation.

The absolute solid  $^{129}\text{Xe}$  polarization from the flow-through polarizer is obtained using a comparison between the magnitude of a hyperpolarized signal and a thermally polarized signal. For this, a hyperpolarized snow signal at 77 K is taken along with many flip-angle calibrations, then the sample polarization is scrambled with RF. The magnitude of the flip-angle-corrected, hyperpolarized-snow signal is  $955400 \pm 100$ , in arbitrary units. The sample then sits at 77 K for thirteen hours, much past  $T_1$  for  $^{129}\text{Xe}$  snow, coming to a thermal polarization. The magnitude of the flip-angle-corrected, thermally polarized signal is  $26.8 \pm 5.1$ , in arbitrary units. In the high-temperature limit, the thermal polarization,  $P_0 = p_+ - p_-$ , is estimated as

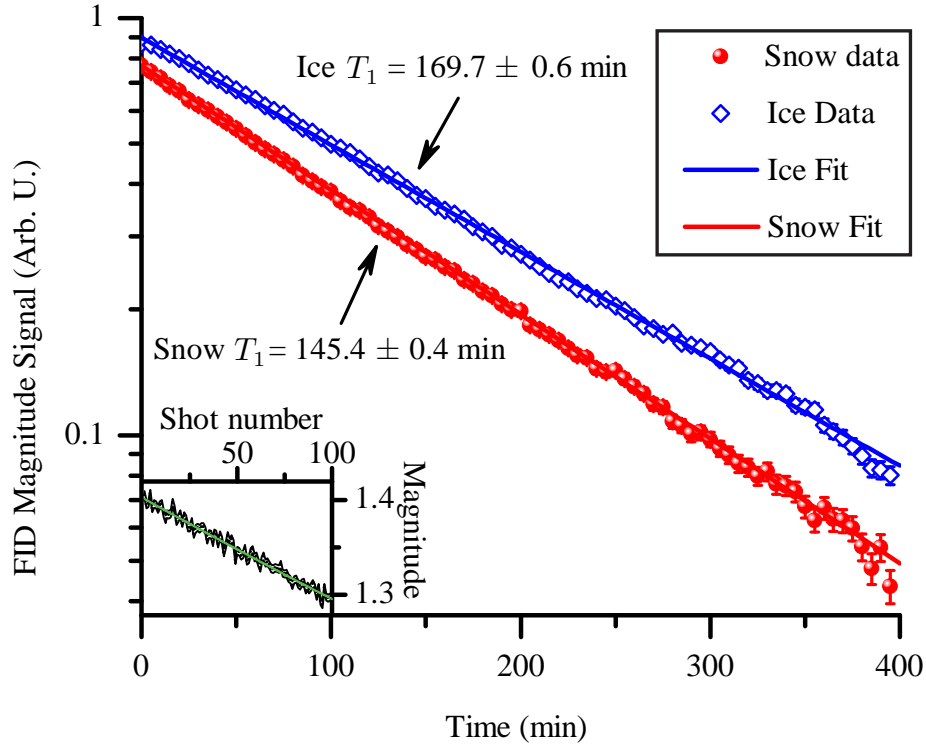


**Figure 2.7.** A comparison between snow and ice  $^{129}\text{Xe}$   $T_1$  data at 77 K in a magnetic field of 2 T. A single point on the free-induction decay (FID) is shown with arbitrary units and is monitored with a 5 min shot repetition. The ice and snow data are from separate samples generated using the flow-through polarizer described in Sect. 2.3.1. *Inset:* Flip-angle data taken prior to the ice  $T_1$  measurement. The data are fit (green line) to Eq. 2.67, obtaining a flip angle of  $0.987^\circ$  for the ice data and used in Eq. 2.69 for data correction.

$$P_0 = \frac{e^{\frac{\hbar\omega}{2kT}} - e^{-\frac{\hbar\omega}{2kT}}}{e^{\frac{\hbar\omega}{2kT}} + e^{-\frac{\hbar\omega}{2kT}}} = \tanh\left(\frac{\hbar\omega}{2kT}\right) \approx \frac{\hbar\omega}{2kT} \approx 7.6 \times 10^{-6}, \quad (2.71)$$

where  $\hbar = 1.0546 \times 10^{-34}$  m<sup>2</sup> kg/s,  $k = 1.38 \times 10^{-23}$  m<sup>2</sup> kg/(s<sup>2</sup> K),  $T = 77$  K, and  $\omega = 2\pi * 24.54 \times 10^6$  Hz. Using Eq. 2.71, an expression for the hyperpolarized snow polarization,  $P_{\text{hyp}}$ , is written in terms of the hyperpolarized signal height  $S_{\text{hyp}}$  and thermally polarized signal height  $S_0$  by

$$P_{\text{hyp}} = \frac{S_{\text{hyp}}}{S_0} P_0 \approx \frac{S_{\text{hyp}}}{S_0} \frac{\hbar\omega}{2kT} \approx \frac{955400 \pm 100}{26.8 \pm 5.1} 7.6 \times 10^{-6} \approx 27.1 \pm 5.1\%. \quad (2.72)$$

Another method to get the polarization of the solid hyperpolarized  $^{129}\text{Xe}$  is to monitor the change of the second moment as polarization decreases, and a fit to the curve yields

the absolute polarization [85].

To summarize the initial results, there is a reproducible discrepancy between ice and snow  $^{129}\text{Xe}$   $T_1$  data at 77 K. Evidence indicates this discrepancy is intrinsic to each solid, as extremely long  $T_1$  measurements show the snow  $T_1$  does not tend to the ice  $T_1$  value; i.e., the difference in  $T_1$  is not hopping to and from a surface that relaxes quickly. To further explore the validity of the theory and previous experimental studies, temperature-dependent measurements on both ice and snow are done.

### 2.4.1 Temperature dependence of ice

Temperature-dependent data are taken over the range of 77 K to 150 K for the ice-type samples. Two  $T_1$  measurements are recorded for each temperature in the set  $\{105 \pm 0.5 \text{ K}, 110 \pm 0.5 \text{ K}, 115 \pm 0.5 \text{ K}, 120 \pm 0.5 \text{ K}, 125 \pm 0.5 \text{ K}, 130 \pm 0.5 \text{ K}, 135 \pm 0.5 \text{ K}, 140 \pm 1 \text{ K}, 145 \pm 1 \text{ K}, 150 \pm 2 \text{ K}, 155 \pm 3 \text{ K}\}$ . All temperature-control methods are described in Sect. 2.3.3, and all measurement techniques are described in Sect. 2.3.4.

For the purposes of the discussion of snow in Sect. 2.4.2, the temperature-dependent  $T_1$  data are shown in Fig. 2.8. Fig. 2.8 also serves for illustrative purposes for which other groups attempting solid xenon work can directly compare their quality of results. This is currently lacking in the current literature; from a researcher's perspective  $T_1$ 's have to be assumed sufficiently obtained and only a few actual data sets are shown.<sup>9</sup> Each data set of Fig. 2.8 extends well past twice the characteristic time  $T_1$ , with a 5 min resolution between data points. The data are shown to fall along the straight-line fitting routines that use Eq. 2.68. There is a direct correlation of increasing temperature with decreasing slope and hence  $T_1$  values, aside from a few anomalous data points at 110 K and 145 K. It is important to note that the data do not tend to any other value over a measurement period, indicating that there is only one characteristic  $T_1$  for each temperature; this gives evidence of uniform relaxation mechanisms.

The ice  $T_1$  values listed in Fig. 2.8 are plotted in Fig. 2.9, along with the previous  $T_1$  values found in the literature that are also plotted in Figs. 2.2 and 2.3. The average

---

<sup>9</sup>No dubious activity is suggested, this is only an argument for showing the details of the  $T_1$  data.

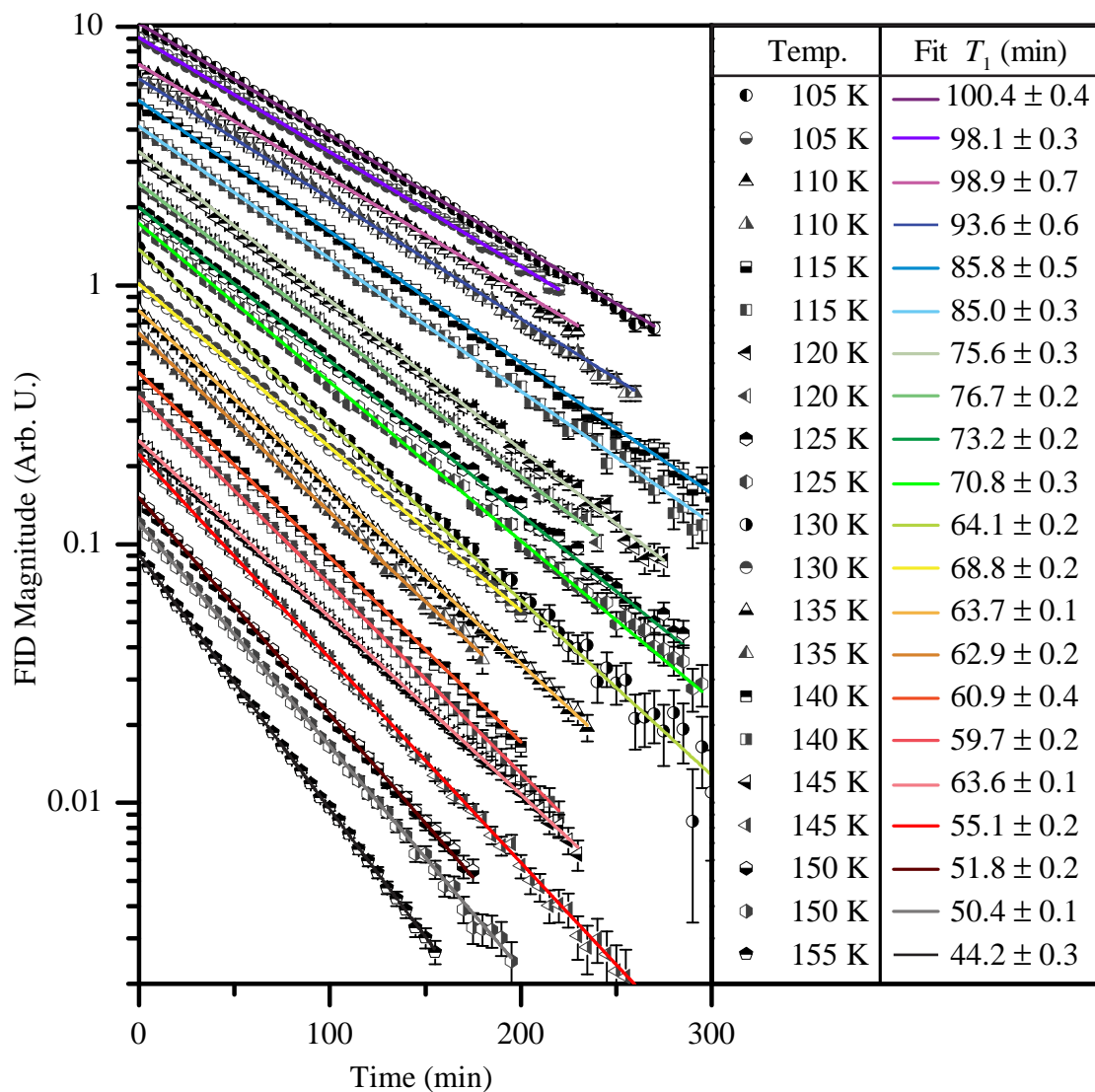


**Figure 2.8.** Shown are the plots of all temperature-dependent  $^{129}\text{Xe}$  ice  $T_1$  data in arbitrary units. The temperature generally decreases down the plot, with two measurements done at each temperature. With each temperature-specific data set there is a color-coded fit overlaid, using Eq. 2.68. A  $T_1$  is extracted and given to the right of the plot, next to the color of the fit and temperature.

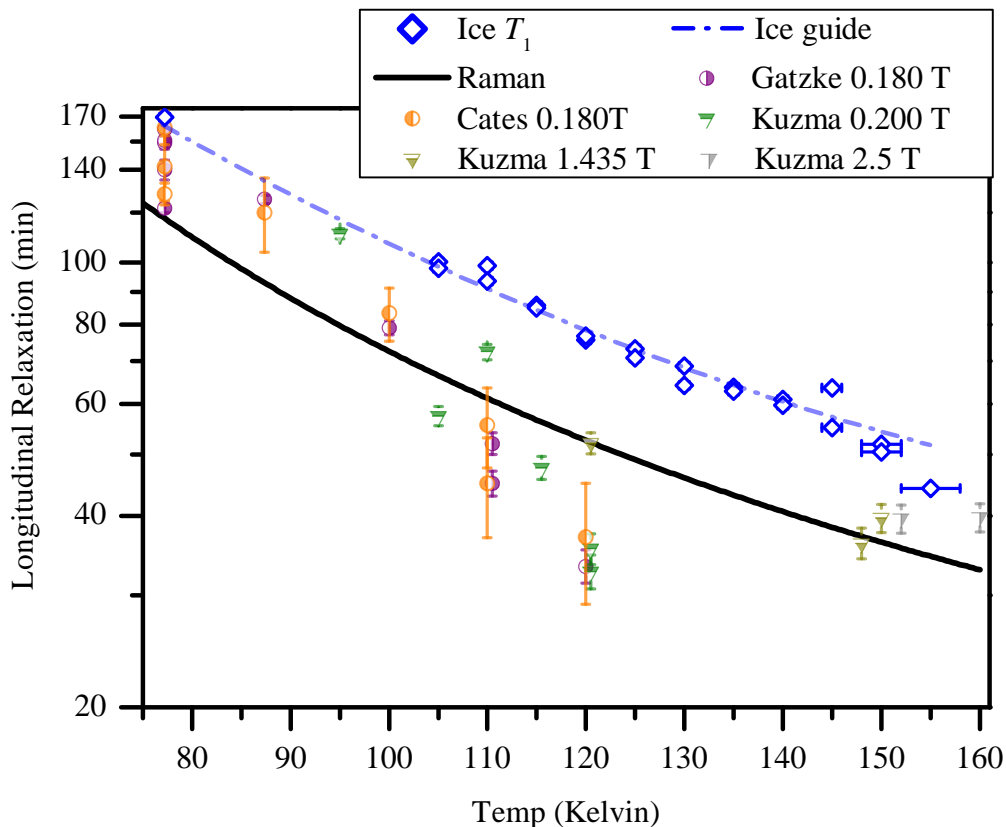


**Figure 2.9.** Shown is temperature-dependent  $^{129}\text{Xe}$  ice  $T_1$  data over a temperature range of 77-155 K. A polynomial-fit guide to the eye is also plotted, along with previous  $T_1$  data, as well as new 2.5 T data from Kuzma [91].

of all 77 K measurements is plotted and is longer than any previously recorded data, and has a  $T_1$  most similar to that of the high-pressure xenon cell reported in Cates et al. [80]. As seen in Fig. 2.9, all ice  $T_1$  values are longer than the previous  $T_1$  values. Moreover, the calculations from the spin-rotation-phonon relaxation theory discussed in Sect. 2.2.4.2, on average, predict  $T_1$  values roughly 30% lower than the ice  $T_1$  data. This unexpected theoretical discrepancy is discussed further in Sect. 2.5, where an attempt to adjust the theory is outlined. In general, shorter  $T_1$  values than expected can be explained with impurities or assuming sufficiently poor samples—this is in contrast to longer  $T_1$  values, which cannot be explained away by adding relaxation mechanisms (i.e., longer  $T_1$  typically indicates a cleaner measurement). From the

range 105 K to 150 K, the data have somewhat of a similar temperature dependence as the spin-rotation-phonon theory, although the shape of the curve does not exactly fit. Following the reasoning by Warren and Norberg, this perhaps gives evidence for the correct relaxation mechanism, with the need for better understanding the relaxation strength. The warmer measurements have larger error bars for the temperature due to the instability issues of the temperature control system. The onset of relaxation due to diffusion processes is demonstrated by the 150 K and 155 K ice measurements; even at a 2 T magnetic field, it is still reasonable to expect these high-temperature diffusion effects [83]. Also plotted are newer measurements at a higher field by Kuzma [91]. The ice data in Fig. 2.9 show an increased precision and reproducibility over the previous measurements, indicating a more robust method of sample preparation.

Experiments with the introduction of oxygen into the sample chamber are also attempted with ice at 77 K; these results are null, in that no effect on the relaxation is seen. The null oxygen result indicates that oxygen does not diffuse into the solid ice at 77 K and does not affect relaxation measurements. This is in contrast to mixing oxygen with xenon prior to xenon solid formation, where the  $T_1$  values will be severely damped [74]. From this, no oxygen is expected to be present in the xenon ice lattice at 77 K. The straightness of the data in Fig. 2.8 also give evidence that significant oxygen diffusion does not occur at any temperature for the duration for an ice  $T_1$  measurement. This straightness at the higher temperatures also shows that there is negligible oxygen content present in the sample chamber, as it would diffuse into the solid, which is taken into account in the discussion of the temperature-dependent snow data.

#### 2.4.2 Temperature dependence of snow

Temperature-dependent data are taken over the range 77 K to 140 K for the snow-type samples.  $T_1$  measurements are recorded for each temperature in the set  $\{105 \pm 0.5 \text{ K}, 110 \pm 0.5 \text{ K}, 115 \pm 0.5 \text{ K}, 120 \pm 0.5 \text{ K}, 125 \pm 0.5 \text{ K}, 130 \pm 0.5 \text{ K}, 135 \pm 0.5 \text{ K}, 140 \pm 1 \text{ K}\}$ , and are shown in Figs. 2.10 and 2.11. Multiple snow  $T_1$  measurements at 120 K are shown in Fig. 2.10(a). Similar to Fig. 2.8, the measurements are taken well past an initial characteristic  $T_1$ . For reference, a single-exponential decay is plotted along that uses  $T_1 = 55 \text{ min}$ , which is from a fit of the initial 03/29 data. All data

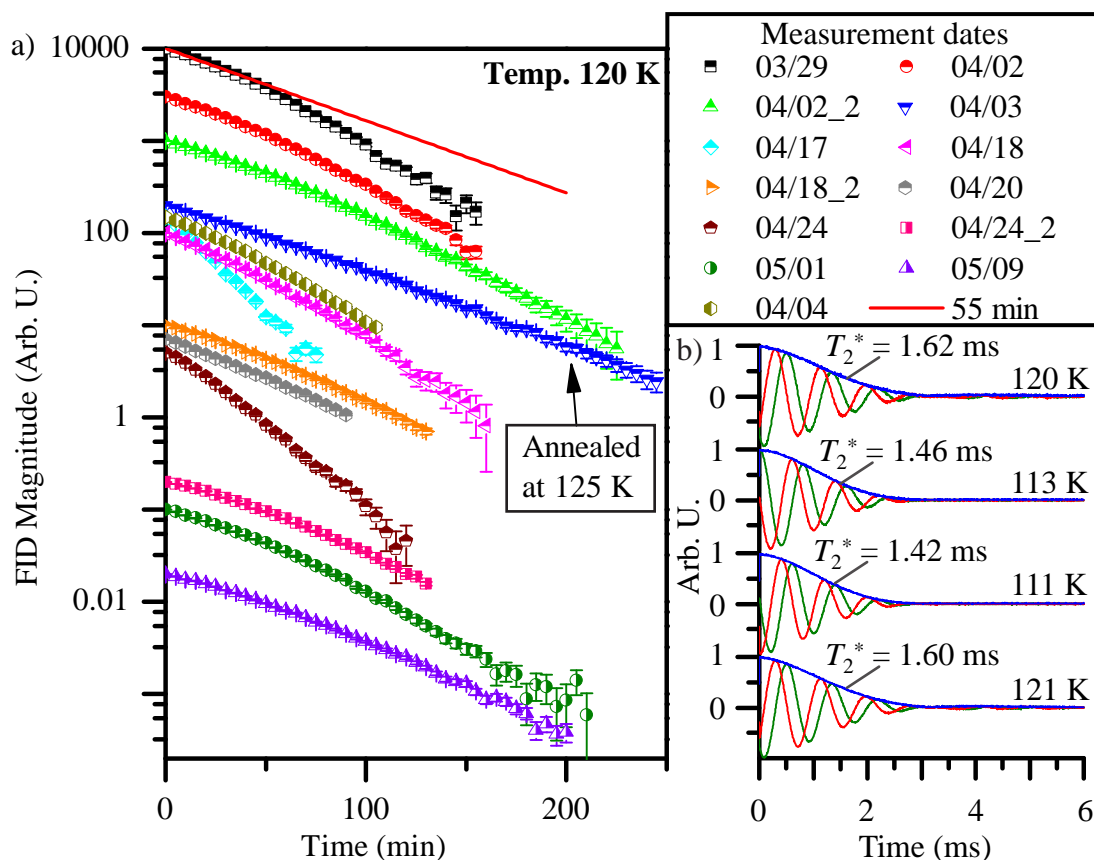


**Figure 2.10.** Multi-exponential snow  $^{129}\text{Xe}$   $T_1$  data measured at  $120 \pm 0.5$  K, along with  $T_2^*$  temperature dependence. (a) Shown are plots of multi-exponential snow  $^{129}\text{Xe}$   $T_1$  data measured at  $120 \pm 0.5$  K, arranged according to date. A single exponential with  $T_1 = 55$  min is plotted for reference. The 04/03 data are annealed at 125 K for 3 min. (b) The temperature dependence of the spin-spin relaxation time  $T_2^*$  is demonstrated. In each plot the FID magnitude (blue), real (red), and imaginary (green) lines are shown. The plots descending are taken sequentially in time with 5 min separations between each plot to allow the temperature to stabilize.

taken at 120 K are multi-exponential with a variety of characteristic times in any given measurement. In efforts to determine the cause of the multi-exponential, many different experimental configurations are attempted to ensure the relaxation is not due to an oxygen leak—a vacuum is pulled on the PTFE valves, nitrogen is supplied around the PTFE valves, the PTFE valves are replaced with new valves, an excess of purified nitrogen is introduced into the sample chamber, and the buffer gas is removed from the sample chamber. Despite this, most of the 120 K data sets show a similar change of decay rate with time. The 04/03 data are measured on a sample that is annealed at 125 K for 3 min; there is a smaller presence of a multi-exponential in the

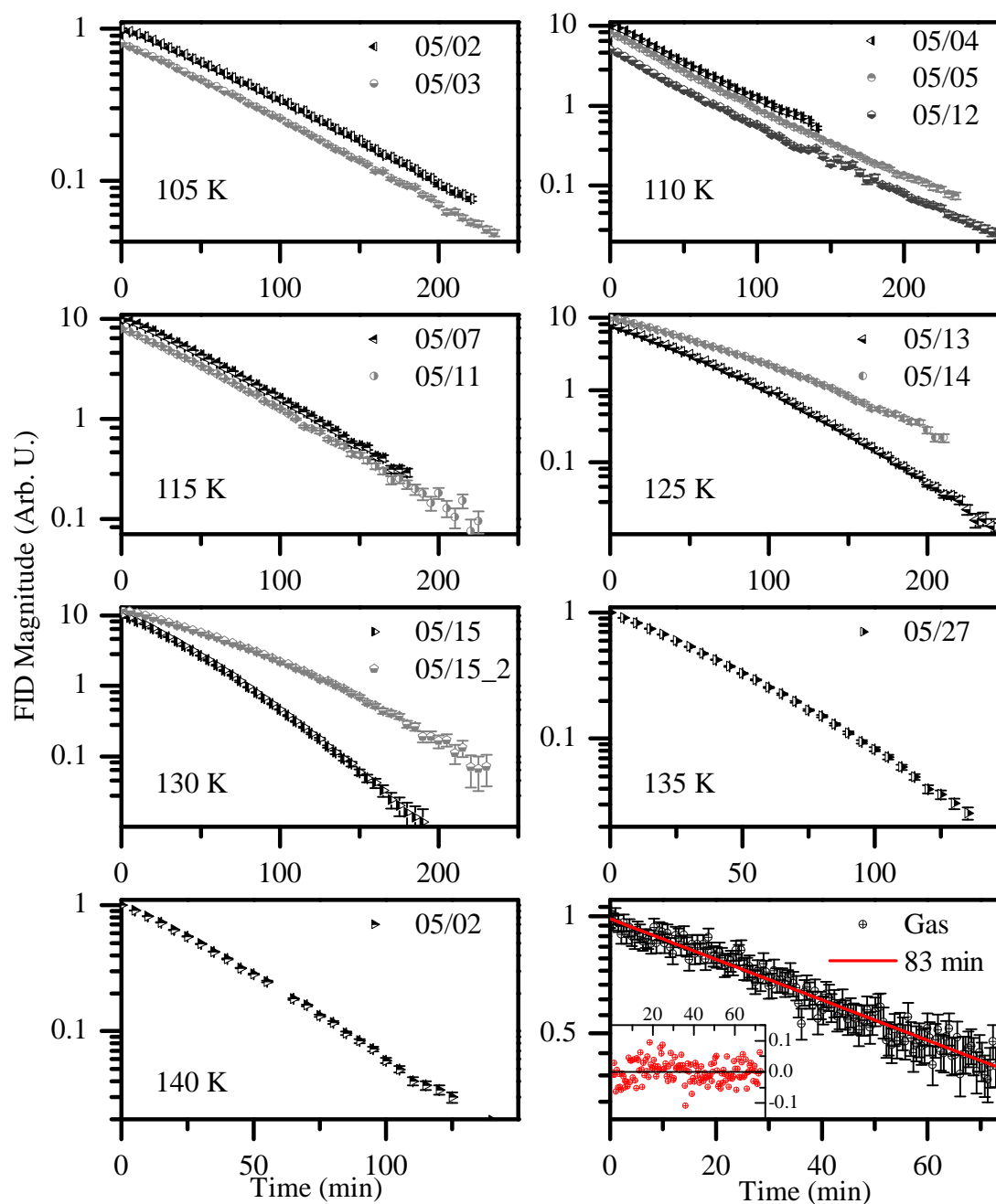


**Figure 2.11.** Plots of temperature-dependent snow data labeled according to measurement date. (a-g) Shown are plots of temperature-dependent snow data labeled according to measurement date. (h) A gas  $^{129}\text{Xe}$   $T_1$  is measured for the sample chamber, along with exponential fit. *Inset:* The residual of the exponential fit.

data, and the initial decay is similar to the initial decay of the most other 120 K data. Two exceptions to the other 120 K data are the 04/17 and 04/24 data, which have a much faster initial decay rate. Both of these measurements are taken after changes to experimental configuration (which involve removing the sample chamber from the magnet); the 04/17 data are taken after nitrogen is applied to the valves and the 04/24 data are taken after vacuum is pulled on the valves. Therefore, the possibility that remnant oxygen from the sample-chamber walls is released into the gas mixture of the sample chamber is increased. However, measurements done immediately after 04/17 and 04/24 (04/18, 04/18\_2, and 04/24\_2) are similar to the other 120 K  $T_1$  measurements. Any variation to initial decay rates of the similar 120 K snow data could be due to the variation in the  $T_1$  experiment's start point, ranging from 5 to 20 min after the beginning of the warming to 120 K (this is the range in time that it took for the temperature to stabilize at 120 K).

One possible explanation for the increasing rate of polarization decay with time is a poor thermal conductivity of the snow xenon, leading to a slow stabilization to an equilibrium temperature. If the inside of the sample remains closer to 77 K and not the 120 K temperature at the outside of the cell, the decay rate would increase as the temperature of the sample becomes warmer. This explanation is discounted with Fig. 2.10(b), where the temperature dependence of  $T_2^*$  is demonstrated. In Fig. 2.10, the raw FID magnitude, real, and imaginary data are plotted. Between each  $T_2^*$  plot, there is a waiting period of 5 min to allow for stabilization of the sample temperature. As the temperature becomes colder,  $T_2^*$  is noticeably shorter; also FID beat patterns (characteristic of solid  $^{129}\text{Xe}$ ) become less prominent, as seen by the presence and subsequent absence and reappearance of a beat at 4 ms. At 120 K the measured  $T_2^*$  is  $1.62 \pm 0.02$  ms; as the temperature drops to 113 K and 111 K, the  $T_2^*$  values, respectively, drop to  $1.46 \pm 0.02$  ms and  $1.42 \pm 0.03$  ms. After the temperature is raised up to 121 K, the  $T_2^*$  raises to  $1.60 \pm 0.02$  ms once again. Thus the FID serves as an accurate thermometer and is monitored during a  $T_1$  measurement to make sure that the temperature has not changed significantly. If the FID shape or  $T_2^*$  changes, it is a result of a change temperature. Because there is no significant observed FID change over the course of any  $T_1$  measurement of Fig. 2.10(a), it is

assumed the multi-exponential data are not a result of temperature stabilization or drift. Moreover, data indicate how quickly the temperature of the snow xenon stabilizes; it must take less than 5 min for the sample temperature to equilibrate.

In Fig. 2.11(a-g), the remaining temperature-dependent snow data are shown. Each relaxation is multi-exponential and the 105 K, 110 K, and 115 K data show similar curves within their respective temperatures. The 125 K and 130 K data have different curve shapes for each run within a temperature set. Note that the second data set in the sequence always produces a shorter initial  $T_1$ , indicating that oxygen may be responsible for some relaxation in the slower-initial- $T_1$  data. Also shown in Fig. 2.11 are the results of an experiment where the collected snow xenon is immediately volatilized after production, and the gas  $T_1$  is measured. This also helps discount oxygen as a major contribution to relaxation in the solid phases, as the gas-phase  $T_1$  becomes very short for very small amounts of oxygen. A brief discussion of possible relaxation models is discussed in Sect. 2.5.2. A complete tally of all snow and ice data are given in Fig. 2.12.

A more likely candidate for the increasing decay rate with time is an oxygen leak into the sample chamber area, but as discussed, extreme measures are taken to ensure no oxygen leaks into the cell. A purposeful introduction of oxygen in the sample chamber (flooded with air) during a 120 K measurement confirms that the presence of oxygen indeed has a considerable effect, and is fit with a single exponential with  $T_1^{\text{oxy}} = 21 \pm 1$  min; this is a similar  $T_1$  as the 04/17 data, confirming the presence of oxygen. To test the quality of the sample chamber seals, liquid and gaseous xenon  $T_1$  measurements are done. The liquid measurements are done both before and after a three-hour ice measurement, and no discernible change in  $T_1$  is found, with  $T_1 = 22 \pm 2$  min. The gaseous measurement shown in Fig. 2.11(h) yields  $T_1 = 83.5 \pm 1.5$  min, and also shows no discernible change over 70 min. From previous experiments, it is known that the presence of oxygen in either the liquid or gas phase of xenon is detrimental to  $T_1$  measurements; data with oxygen-doped solid xenon have very short  $T_1$  values on the order of minutes. The dramatic decrease of  $T_1$  shown in Fig. 2.10(a) (60 min to 30 min) would require a significant amount of oxygen in the sample chamber area—an amount that would have the characteristic  $T_1$  for  $^{129}\text{Xe}$  in liquid or gas on the order

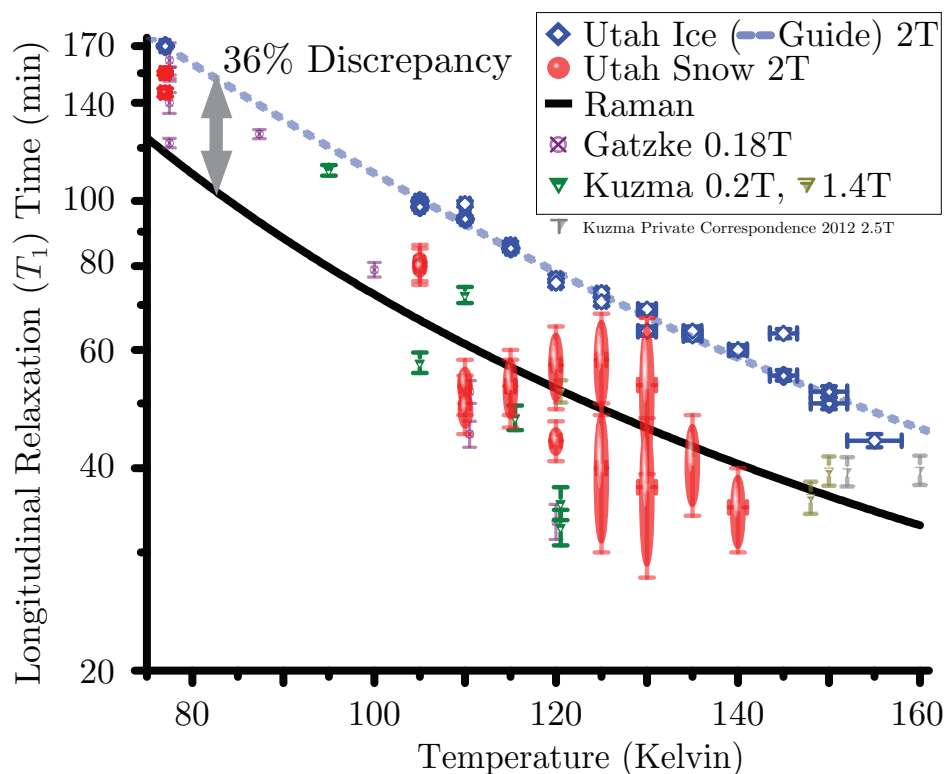


**Figure 2.12.** Shown are a tally of all ice and snow  $^{129}\text{Xe}$   $T_1$  data, omitting the Cates data for visual acuity. The large error bars on the snow the snow represent the range of the curves observed in the  $T_1$  data.

of a minute. Furthermore, the ice data in Fig. 2.8 are obtained with the exact same experimental conditions (on many occasions, the same day). As mentioned, the ice data are straight (single exponential) even for the 145 K to 155 K data, where the solid has a high vapor pressure and  $T_1$  is limited by diffusion within the solid. Therefore, any oxygen leak would be apparent from the ice data. Thus it is unlikely that oxygen plays any role, let alone is the sole cause, for all but two of the multi-exponential data sets in Fig. 2.10(a).

### 2.4.3 Additional measurements

The effect of oxygen on the relaxation of snow xenon at 77 K is studied by flooding the sample chamber with air before a  $T_1$  measurement. In Fig. 2.13, results from two such experiments are shown. The first experiment shows an increase of the initial decay rate due to the oxygen; specifically, the oxygen induces additional relaxation on the small-grain surfaces of the snow crystallites. Because atomic diffusion within

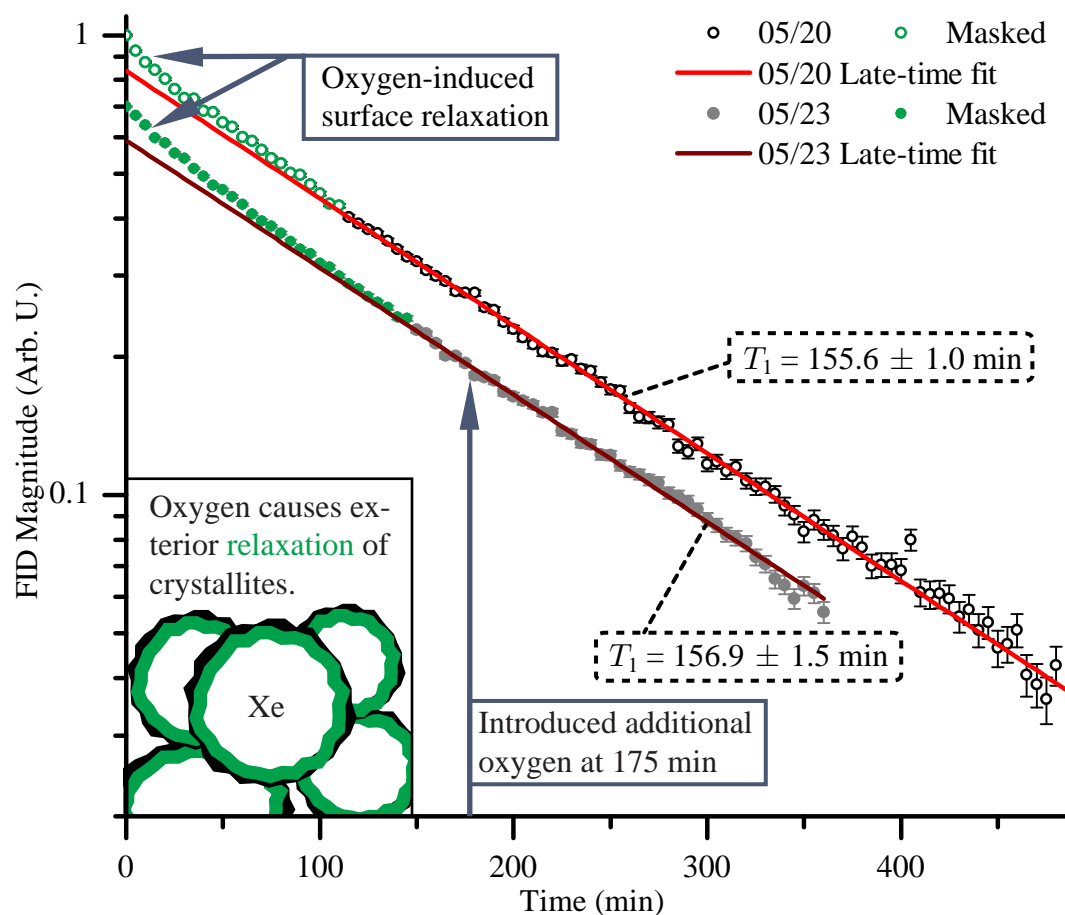


**Figure 2.13.** Shown are the results from introducing oxygen into the sample-chamber area. Two data sets are shown, labeled by date. The green data points are those masked in the exponential fit and  $T_1$  values are given for each fit. The 05/23 data have additional oxygen introduced into the cell later in the experiment, to test if the oxygen diffuses into the solid and remains “stuck.” *Inset:* An image of the supposed method of relaxation.

a crystallite is negligible at 77 K, the unpolarized crystallite surface does not have an effect on the relaxation of the bulk. The second experiment also shows an increase of the initial-decay rate due to the oxygen. In addition to the premeasurement flooding of the sample chamber with air, an additional sample-chamber flooding with air is done 175 min into the measurement; this is done to test if the initial oxygen is diffused into the lattice and relaxes its neighbors, leaving the remaining bulk unaffected. However, there is no discernible change in the  $T_1$  when additional oxygen is added to the sample chamber, indicating that the oxygen does not diffuse into the bulk; hence, only the surface of the crystallites are relaxed by the oxygen. If relaxation

of the surface is solely responsible for the lower-snow  $T_1$  values, then the bulk of the snow should tend towards the ice  $T_1$ . The  $T_1$  value that the data in Fig. 2.13 tend towards is approximately 156 min—this is 8% from the average value of the ice  $T_1$  at 77 K. Thus, there remains a difference in the structures of the bulk snow and ice that affects  $T_1$  relaxation processes; again, this is not predicted by the theory described in Sect. 2.2.4.

Isotopic variation within the xenon lattice can determine whether the relaxation mechanism is isotopically dependent. For example, if the dipolar interaction between spin-1/2 nuclei dominates relaxation, then adjustments to the concentration of the spin-1/2 species ( $^{129}\text{Xe}$ ) would have a tremendous effect on the measured  $T_1$ . Also, if the dominant relaxation mechanism is from the spin-3/2  $^{131}\text{Xe}$  (quadrupole or dipole), decreasing the spin-3/2 content will lengthen  $T_1$ . Lattices are formed with high- and low-spin-1/2 concentration (compared to naturally abundant xenon) and  $T_1$  values are measured, with results shown in Fig. 2.14. The enriched xenon is 86% spin-1/2  $^{129}\text{Xe}$  and 1.8% spin-3/2  $^{131}\text{Xe}$ . The dilute-spin xenon is 4.5% spin-1/2  $^{129}\text{Xe}$  and 4.3% spin-3/2  $^{131}\text{Xe}$ . (Natural-abundance xenon is 26.4%  $^{129}\text{Xe}$  and 21.2%  $^{131}\text{Xe}$ , with all other stable isotopes spin-less.) Enriched snow shows a multi-exponential character that initially relaxes *faster* than the naturally abundant snow, then tends towards a  $T_1$  value that is closer to that of the naturally abundant snow. From the results of the oxygen-induced surface relaxation data, an inference is made that the increased initial relaxation is from the relaxation of the additional spin-1/2 sites on the surface. The first enriched-ice experiment is taken after the enriched-snow measurement, and yields a  $T_1$  that is somewhat slower than natural-abundance ice. The second enriched-ice experiment is taken well past three times  $T_1$  in order to determine if the  $T_1$  tends to any other value—it does not. Moreover, the  $T_1$  value is much closer to the average  $T_1$  of the naturally abundant ice data, which give evidence that isotopic concentration does not play a significant role in relaxation. The second enriched-ice  $T_1$  value is smaller than the average  $T_1$  of the naturally abundant ice data, which may result from the increase of spin-1/2 sites near interstitials and grain boundaries. Finally, a dilute-spin experiment yields a  $T_1$  that is similar to all other ice  $T_1$  values. This puts an upper-limit on a potential saturation of an isotope-dependent relaxation mechanism,

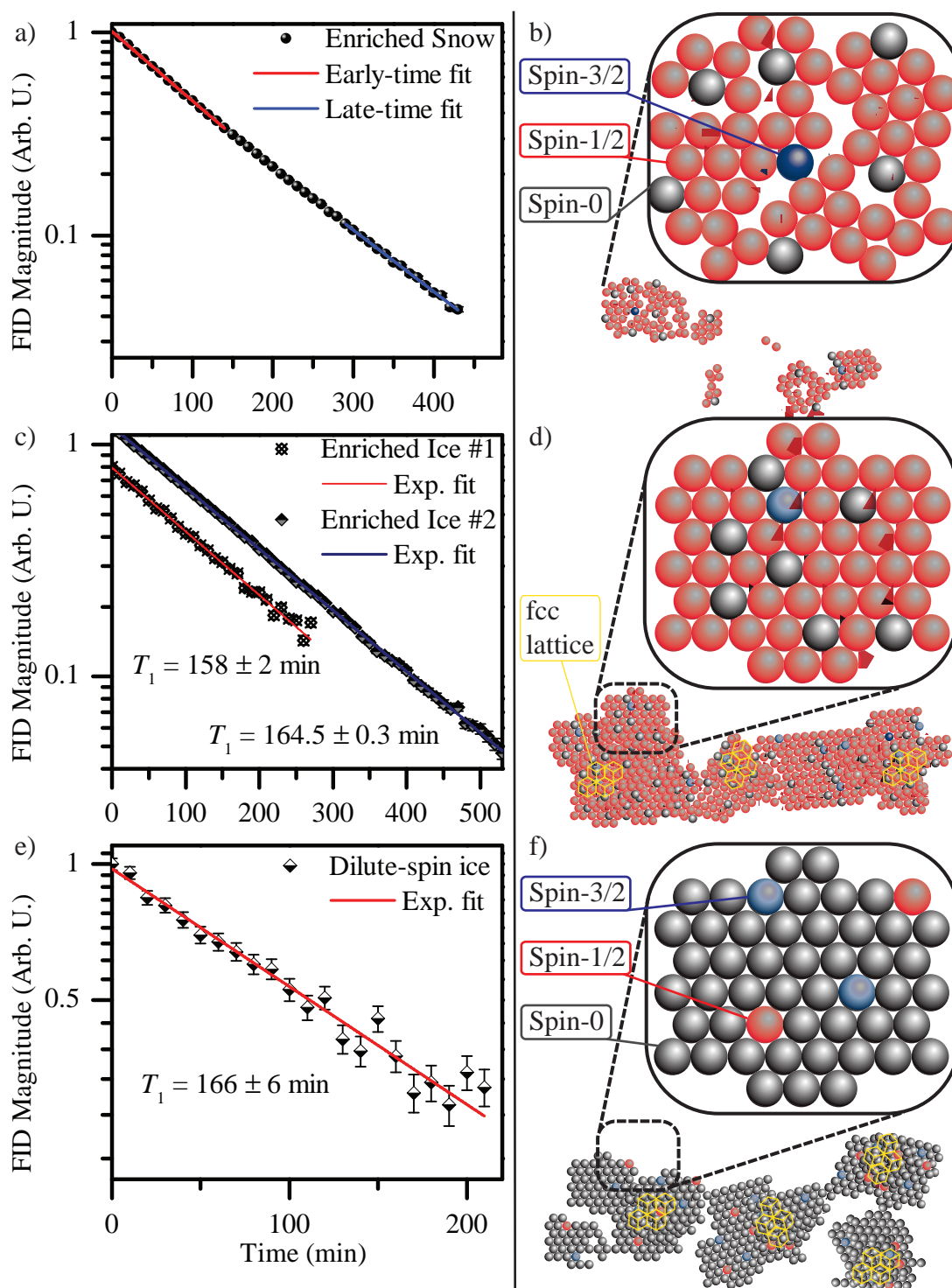


**Figure 2.14.** From (a) enriched snow, (c) enriched ice, and (e) dilute-spin ice, the isotope dependence of solid  $T_1$  is shown to be negligible. Figs. (b), (d), and (f) are images of idealized lattices corresponding to each situation.

and completely discounts a dipolar mechanism. Any mechanism due to  $^{131}\text{Xe}$  would have a significantly smaller effect in these experiments, but no large effect in  $T_1$  is seen; this indicates that  $^{131}\text{Xe}$  does not play a role in relaxation.

## 2.5 Discussion

### 2.5.1 Ice theory

To understand the mechanisms responsible for the ice data presented in Sect. 2.4.1, the formalism described in Sect. 2.2.4 is used. The ice data in Fig. 2.9 show a roughly 30% deviation from the Raman-scattering of two phonons theory across a temperature range of 77-150 K. As estimated in Fitzgerald et al. [92], the spin-rotation coupling constant used by the Happer group is  $c_{K0}/h = -27$  Hz. This calculation discounts phonon motion when calculating the paramagnetic and diamagnetic currents, which may alter the result; also calculated is a  $c_K/h = -14.1|f|^2$  Hz using a pseudopotential theory developed in Wu et al. [86], where  $f$  is a “fudge” factor that accounts for additional wave function overlap. A pairwise additive approximation (PAA) is given in Hanni et al. [126], where the effects of pairs of atoms are used for calculations—in this way it is very similar to the treatment of the Happer theory. Hanni et al. [126] consider xenon clusters of 1-12 atoms and calculate nuclear shielding tensors, nuclear quadrupole coupling tensors, and spin-rotation tensors. Considering higher-than-pair interactions for an effective PAA (PAA(eff)) for twelve xenon atoms, which is the number of nearest-neighbors in the primitive cell of an fcc lattice, the Finland group is able to successfully reproduce the chemical shift of solid xenon within 5%—they find the chemical shift  $\delta$  is  $321.56 \pm 8.87$  ppm. Though the calculation is only for twelve atoms, it matches extraordinarily well with the observed experimental chemical shift in solid xenon,  $\delta = \sigma_s - \sigma_g \approx 320$  ppm. This gives some credence to the extrapolated spin-rotation constant  $c_{K0}/h = -16.43 \pm 2.06$  Hz (found in the supplementary information of Hanni et al. [126]). Substituting this value of the spin-rotation constant into Eq. 2.21 gives a value of the solid xenon  $T_1$  to be approximately 310 min at 77 K, instead of the observed 170 min.

The xenon ice data between 77 K to 150 K in Fig. 2.9 appear to show a roughly  $T^2$  dependence of the Raman-scattering of phonons theory, and data severely departs

from the theory at temperatures less than 50 K. This departure is suggested to be the effect of quadrupolar relaxation due to spin-3/2  $^{131}\text{Xe}$  and enriched xenon data compared to naturally abundant data at 4 K show this effect, but even at very low spin-3/2 concentrations, the data do not approach the two-phonon spin-rotation theory at low temperatures. Additionally, if a fit using only the spin-rotation theory is forced through the ice point taken at 77 K (e.g., fit the curve to the spin-rotation strength, which gives  $c_{K0}/h \approx -22$  Hz), there appears to be a slight departure from the fit to the ice data. Thus, the temperature dependence of the experimental curve does exactly follow the prediction of the two-phonon theory in the 77-150 K range or the lower temperature range. The prediction of the markedly lower relaxation rate from the estimation of the spin-rotation constant obtained from the Hanni theory, combined with the two-phonon spin-rotation theory, is perhaps real, and some other relaxation mechanisms are taking place. A simplified analysis shows higher-order phonon effects have a different temperature dependence than the two-phonon, and in general, for each phonon included in the process an additional  $T$  must be multiplied to the transition rate at high temperatures,  $T > T_D$ . For example, taking an integral over  $dE_a\delta(E_a - E_c - E_d)$ , a three-phonon transition rate would appear as

$$W_{fi} = \frac{2\pi}{\hbar} \sum_{j_c j_d j_a} \int \int_0^{E_D} dE_c dE_d d\Omega_a d\Omega_c d\Omega_d |\nu_{fi}^{(3)}|^2 \rho(E_c + E_d) \rho(E_c) \rho(E_d). \quad (2.73)$$

Thus, in particular, a normal three-phonon effect has roughly a  $T^3$  temperature dependence at higher temperatures; as expected, fitting the ice data with a  $T_1 = 1/(BT^2 + CT^3)$  does not give a good fit. However, if the general function used to fit the 77-150 K ice is assumed to be  $T_1 = 1/(AT + BT^2)$ , the value of  $B$  obtained from the fit almost exactly matches the prediction of the spin-rotation coupling strength from the Hanni theory. Moreover, if the fit over the 77 K to 150 K range is plotted against the previous lower temperature data in the range of 4 K to 50 K, the fit is much closer to the observed data. Thus, a mechanism seems to be present that has a linear temperature dependence, indicating a one-phonon effect—however, the mechanism must be much stronger (i.e., much more probable) than the one-phonon, one-spin-flip model. Gathering effects from all of the data, it is seen that a linear mechanism must obey the following: 1) is not affected by external magnetic field

strength above 0.5 T, 2) is not affected by isotopic concentration, and 3) is more prominent for more disordered lattices (snow). Also, the enriched xenon ice data at 77 K presented in Sect. 2.4.3 show a somewhat counter-intuitive noneffect to (or perhaps even increase in) the relaxation rate, perhaps showing a slight increase due to dipolar-dipolar coupling.

A good candidate for the linear mechanism becomes spin-rotation mediated, in some way, by crystal defects. Owing to Brownian motion, strict diffusion of vacancies should roughly follow a  $e^{-E_A/kT}$  temperature dependence, where  $E_A$  is the activation energy of the vacancies in the lattice. The activation energy is judged from  $T_2$ , where it is shown that  $E_A/k > 2000$  K. This exponential temperature dependence is technically only good down to the Debye temperature, but in practice is good to lower values [127, 128, 129]—this clearly excludes classical or quantum diffusion of vacancies. Also, due to the speed at which the temperature stabilizes within the sample without hopping, an Umklapp-type process is present [96, 130, 131, 132]. For pure crystals, an Umklapp process dominates at high temperatures. Recall that a normal three-phonon collision,  $\mathbf{k}_1 + \mathbf{k}_2 = \mathbf{k}_3$ , does not establish thermal equilibrium in a sample, because the total momentum of the phonon gas is not changed in such a collision. Instead, a three-phonon Umklapp collision of the form  $\mathbf{k}_1 + \mathbf{k}_2 = \mathbf{k}_3 + \mathbf{G}$  is needed for thermal conduction, where a reciprocal lattice vector with length  $|\mathbf{G}| = 2\pi/a$  and  $a$  is the lattice spacing. This type of Umklapp process has previously been reported to cause a  $T^4$  dependence [31, 133, 134, 135, 136] in nuclear relaxation, and from this assessment, can be ruled out for a linear temperature mechanism. However, this  $T^4$  dependence is found by considering the interference between the direct mechanism and anharmonic Umklapp term in the Hamiltonian (this can be seen to be too weak and proportional to  $B_0$ ), and, as discussed below, there are other options for three-phonon interactions to contribute significantly to the relaxation. In this vein, one macroscopic behavior of phonons is thermal conductivity, which is grossly overestimated by considering only harmonic behavior in even a pure crystal. For example, the thermal conductivity is expressed as  $\Lambda = \frac{1}{3}C_v v_c l$ , where  $C_v$  is the specific heat per volume,  $v_c$  is the average travel velocity of a thermal excitation, and  $l$  is the mean free path of the excitation. For pure crystal insulators, the thermal

conductivity goes as  $T$  at high temperatures  $T > T_D$ . In disordered crystals or glasses, a model that describes their minimum thermal conductivity at high temperatures includes a minimum scattering time as one-half the period of vibration,  $\tau = \pi/\omega$ , leading to a velocity of  $v_c = n^{-1/3}/\tau$  [137, 138, 139, 140, 141]. At high temperatures, within this model, the thermal conductivity becomes constant with respect to temperature. Note that the thermal conductivity of a sample at very low temperatures is heavily dependent on isotopic concentration. In general, a distribution of isotopes causes scattering of phonons, and a more isotopically pure sample leads to an enhanced thermal conductivity. This could lead to a difference in relaxation that is weakly dependent on isotopic concentration. For long-wavelength phonons, the average mass of the isotope can be used for a sufficient description, thus the direct process should not be significantly altered by isotope concentration. However, the higher-energy phonons may be significantly scattered by isotopic impurity.

A key feature of the ice relaxation is that all of the data in the temperature ranges from 77 K to 150 K are clearly governed by a single exponential. Thus, if defects are causing the additional relaxation, all nuclear spins must be affected in the same way and experience the same relaxation mechanisms; this could indicate that all nuclear spins interact with some defect, or that the phonon spectrum for a given crystallite is deformed from defects. Put another way, if the effects from the defects are strictly local, there must be many defects, or a multi-exponential relaxation would be seen. Single crystal xenon is considered to have a smaller anharmonic contribution to the lattice energy than polycrystalline xenon. In phonon defect theory, the phonons can be considered highly anharmonic, with the defects serving to scatter the high-frequency phonons more readily [142, 143, 144, 145]. The low-frequency phonons are less likely to be scattered and be transmitted through defect boundaries.

The relaxation due to the self-consistency of phonons is shown to be the wrong type of mechanism to account for any sizable relaxation [146]. This theory gives that there is no magnetic field dependence due to this mechanism; however, there is also no predicted temperature dependence, causing a constant offset of the relaxation rate. If a constant offset is included into the fitting routine for the data, the shape of the fit still shows inconsistencies. The self-consistency of phonons has been shown to be

valid in very low temperature solid, quadrupolar  $^{21}\text{Ne}$  relaxation [147]. This type of mechanism is also dependent on the concentration of atoms that have spin, another feature that the observations in Sect. 2.4.3 lack, as there seems to be negligible dependence on isotopic concentration. Exotic combinations of this relaxation mechanism would be required if the self-consistency of phonons played any role whatsoever in solid  $^{129}\text{Xe}$  relaxation.

Another consideration is the  $^{131}\text{Xe}$  data of Warren and Norberg [74], which show that the relaxation has a  $T^2$  dependence in a paramagnetically impure crystal. Any linear mechanism should be present in that data as well, unless defects are unique with regards to the dipolar term in some way, or that the quadrupolar interaction with Raman scattering is much stronger than any other interaction for  $^{131}\text{Xe}$ . The  $^{129}\text{Xe}$  relaxation is quicker than the  $^{131}\text{Xe}$  at 4.2 K in their data, thought to be caused by paramagnetic centers. In their fit to data, only the  $T^2$  dependence is observed, as the strength of interaction is determined by a floating fit to the data point at 77 K. Another indication that the  $^{131}\text{Xe}$  is not affected by vacancies is that the pure samples (with no oxygen doping) follow the  $T^2$  dependence close to the melting point, indicating the effect of diffusion from vacancies is very weak in their material. The introduction of oxygen causes a much quicker relaxation in the diffusion regime. This may indicate that the pressures at which the solid is formed decreases the amount of lattice defects, and paramagnetic impurities such as oxygen relax the nuclei in a different way than crystal defects. This, and the absence of dependence on magnetic field, discounts  $F$ -centers and oxygen impurities to be responsible for the ice data [148]. Any linear temperature dependence seems absent from the  $^{131}\text{Xe}$ , perhaps simply due to the overwhelming strength of the quadrupolar interaction.

An interesting omission from the calculation provided in Fitzgerald et al. [92] and described in Sect. 2.2.4, is that of wave-vector conservation, or phonon-momentum conservation. While energy conservation is taken into account, the scattering involved with the destruction of one harmonic phonon and creation of another harmonic phonon must have a restriction on the possible momentum of the outgoing phonon. As the calculation stands, all possible  $\mathbf{k}$  vectors are summed over for both the incoming and outgoing phonons, without a Kronecker delta-type term that takes into

account the momentum conservation of incoming and outgoing phonons,  $\mathbf{k}_a = \mathbf{k}_e$ . This consideration also seems to be absent in all early versions of the problem that considers quadrupole relaxation mediated by Raman-scattering of phonons, originating with van Kranendonk [74, 75]. The conservation of momentum would arise naturally out of the problem if all lattice sites were summed over, with terms such as  $\frac{1}{N} \sum_l e^{i\mathbf{r}^l \cdot (\mathbf{k}_1 - \mathbf{k}_2)} = \Delta(\mathbf{k}_1 - \mathbf{k}_2)$ . Using the nomenclature of Reissland [142] (Eq. 3.29), define

$$\Delta(\mathbf{k}) = \begin{cases} 1 & \text{if } \mathbf{k} = \mathbf{G}, \text{ where } \mathbf{G} \text{ is a reciprocal lattice vector (including zero).} \\ 0 & \text{otherwise.} \end{cases} \quad (2.74)$$

For a two-phonon scattering process, any process that includes a nonzero  $\mathbf{G}$  is negligible. The simplification present in the problem is that a unit cell, consisting of a central atom and 12 nearest neighbors, is removed from the lattice and analyzed, and as such, the conservation of momentum is lost. Positing that a phonon momentum is not negligibly affected by a nuclear spin flip, inserting  $\Delta(\mathbf{k}_a - \mathbf{k}_e)$  into Eq. 2.51, and integrating over phonon direction yields a factor

$$4\pi(4 + 2j_0(kR_{\gamma\beta}^{(0)}) + 2j_0(2kR_0) - 8j_0(kR_0)), \text{ or,} \quad (2.75)$$

$$J_m^2(u) = 4 + 2j_0(u\sigma_m\phi_D) + 2j_0(2u\phi_D) - 8j_0(u\phi_d),$$

where the third term is the result of the summation of the two nearest neighbor distances. Only one factor of  $4\pi$  enters this calculation (as opposed to two factors in the original calculation), expectedly causing a significant decrease in the predicted relaxation rate. Specifically, at 77 K, using the Hanni theory, the predicted  $T_1$  time due to the Raman process is approximately 1500 min instead of 300 min. This modification does not change the temperature dependence of the mechanism, but the strength is affected greatly. Physically, this is seen by considering the definition of scattering within the lattice—in an inelastic process such as Raman scattering, something must change the direction of the excitation, whether it be another phonon scattering process or momentum given up to the crystal. In electron-phonon processes, in which free conduction-type electrons are considered, the momentum can be transferred from the electron's initial and final states to a phonon excitation and vice versa. However, a Raman interaction with a stationary nuclei does not inherently change the direction of the phonon excitation unless additional scattering terms are

considered. If this analysis is correct, then a plethora of interactions may actually be present to cause the observed  $T_1$  relaxation times.

A similar problem with the weakness of the harmonic Raman process (1R) to properly account quadrupole relaxation data of NaCl was discovered by van Kranendonk and Walker [149, 150, 151, 152, 153]; an anharmonic process (aR) with the roughly the same temperature and magnetic field dependence as that of the harmonic process is shown to be relevant. As shown above, the simplified analysis of the temperature dependence of the interference between the anharmonic piece of the lattice energy responsible for thermal conductivity and the direct process is shown to give a  $T^4$  dependence [133]. However, in van Kranendonk and Walker [149], it is shown that the third phonon in the process can be considered instantly absorbed (emitted) in the spin-flip process, causing the occupation number of the third phonon to drop out, resulting in an overall high-temperature  $T^2$  dependence of a three-phonon anharmonic mechanism. Also in van Kranendonk and Walker [149], a  $\Delta(\mathbf{k})$  term that requires conservation of phonon momentum arises naturally out of the calculation (there is a sum over all lattice sites). Additionally, in the case of relaxation due to an electric dipole, the 1R process implies there must be an aR process. Though the temperature dependence is similar, the fact that a process that includes virtual phonons is stronger than a process containing only “real” phonons opens up new pathways for calculation. The aR calculation also includes a term dependent on the square of the (temperature-dependent) Grüneisen parameter,  $\gamma_G$ . The Grüneisen parameter represents the pressure from a collection of vibrating states, defined as

$$\gamma_G = \frac{V}{C_V} \left( \frac{\partial S}{\partial V} \right)_T = \frac{V}{C_V} \frac{\beta}{\chi_T}, \quad (2.76)$$

where  $S(V, T)$  is entropy,  $C_V$  is the specific heat,  $\beta$  is the expansivity, and  $\chi_T$  is the compressibility. The anharmonic analysis is used successfully in describing solid  $^{83}\text{Kr}$  relaxation, an especially relevant material for solid xenon, where it is shown that the anharmonic Raman process is the proper model to account for the slight deviations of the temperature dependence of the observed relaxation [154].

The anharmonic phonon relaxation theory detailed in van Kranendonk and Walker [151] provides two very useful tools for future study of this problem: the first is the scattering-theory formalism of the anharmonic phonons, and the second is the

Green's function formalism for phonons cast in an especially elegant way for study of nuclear spin relaxation. (Prior to any continuing work, however, the question of the importance of conservation of momentum in a harmonic phonon process in the previous Raman-scattering theory needs to be resolved completely.) In the scattering-theory formalism, the anharmonic phonon states  $|n\rangle$  are considered perturbed from the harmonic phonon states  $|n\rangle_0$  using the Lippmann-Schwinger equation and the Born approximation,

$$|n\rangle = |n\rangle_0 + \frac{1}{E_n^0 - H_0 \pm i\epsilon} V_3 |n\rangle_0, \text{ with } H_0 |n\rangle_0 = E_n^0 |n\rangle_0, \quad (2.77)$$

where  $V_3$  is a third-order, anharmonic piece of the phonon potential. These anharmonic states can then simply replace the harmonic states used in previous calculations, allowing for a convenient conceptual picture of the important processes in the relaxation. The Green's function formalism is, perhaps, conceptually not as clear, but mathematically preferable in its ease of use. Forgoing any in-depth detail of this formalism, the beauty of the technique is that it directly relates the relaxation rate to a spectral density that is calculated directly from the Green's functions.

A general analysis of the multiphonon problem yields a guide for finding the temperature dependence of any given process. The various generic situations for unique phonons exiting or entering the process are shown with Feynman diagrams in Fig. 2.15, along with their resulting temperature dependence of each process. The central blob in each diagram represents any higher order effects taking place, drawing focus to the fact that only the total number of unique phonons coming in/out of a diagram contribute to a nonnegligible process's temperature dependence. Essentially, at temperatures above the Debye temperature, the temperature dependence of a phonon process is generated by the presence of a unique phonon's occupation number in the matrix element prior to the various integrations in Fermi's golden rule, in combination with the assumption that the phonons obey a Bose-Einstein distribution. If, for example, there are  $i$  unique phonons contributing to the process, the matrix element squared has  $i$  occupation numbers  $n_1, \dots, n_i$  that are averaged over using a Bose-Einstein distribution. Note that the energy spectrum of the phonons, or density of states, has no bearing on the temperature dependence at temperatures higher than

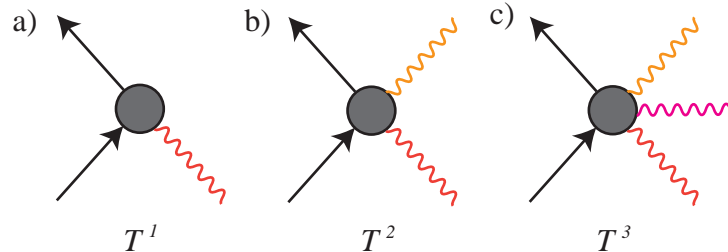


**Figure 2.15.** Generic Feynman diagrams for a process involving (a) one phonon, (b) two phonons, and (c) three phonons absorbed or emitted, with unique phonons contributing to the process. The solid lines represent an incoming and outgoing nuclear spin state, and the squiggly lines represent phonons absorbed or emitted. The center sphere represents all possible internal processes.

the Debye temperature; a particular assumption for the density of states only affects the low-temperature regime's temperature dependence. This is seen by observing that, at high temperature, the Bose-Einstein distributions for either  $\langle n \rangle$  or  $\langle n + 1 \rangle$  simplify as

$$\frac{1}{e^{u/T} - 1} \propto T, \quad \text{or} \quad \frac{e^{u/T}}{e^{u/T} - 1} \propto T. \quad (2.78)$$

Therefore, at high temperature, the product of  $i$  unique occupations numbers resulting from the matrix element squared will result in a temperature dependence of

$$\langle n_1 \rangle \cdots \langle n_i \rangle \propto T^i, \quad (2.79)$$

as shown in Fig. 2.15.

If, however, it is assumed that nonunique phonons contribute to a process, i.e., the same phonon enters and leaves the process, a different temperature dependence results. Note that this type of process for a diagram such as Fig. 2.15(b) would necessarily violate energy conservation if a spin flip is achieved, because the energy of the incoming and outgoing phonons are required to stay constant. Thus, if this type of process is to be considered seriously, an exotic mechanism such as a physical displacement of the atom's equilibrium site in the lattice due to a nuclear spin flip would be required. While a large xenon atom would not have to move its equilibrium position much within its lattice, and momentum is a conserved quantity of greater importance in scattering problems than energy, a less-exotic result leading to a linear temperature dependence would be more ideal. However, following this somewhat dirty

assumption through gives a demonstrative result of how an interesting temperature dependence occurs with considering different diagrams. Assuming that the two phonons contributing to the process in Fig. 2.15(b) are the same, the average of the product of the occupation numbers is taken, yielding terms such as  $\langle n^2 \rangle$  (this occurs instead of products of the average of the occupation numbers such as  $\langle n_1 \rangle \langle n_2 \rangle$ ). These types of terms simplify as

$$\langle n^2 \rangle = \langle n \rangle + 2 \langle n \rangle^2 \propto T + 2T^2, \quad (2.80)$$

demonstrating how like-phonons entering and leaving a process can result in a lower-order temperature dependence. As an additional example, a process that may include an analysis such as this, that does conserve energy, is that shown in Fig. 2.15(c), with two of the external phonons contributing being identical. In this situation, the identical phonons contribute the temperature dependence of Eq. 2.80, and the third phonon contributes a linear temperature dependence, resulting in a total temperature dependence of  $T^2 + 2T^3$  (this process is also extraordinarily weak for the same reasons that Fig. 2.15(a) is weak). This gives a framework to develop new, more probable relaxation mechanisms and quickly analyze their temperature dependence. Interestingly, this framework appears to be independent of a relaxation mechanism (dipolar coupling, spin-rotation coupling, etc.), so that any mechanism will give the same temperature dependence for a given phonon process—only the strength of relaxation is determined by the mechanism.

Thus, the method used throughout the nuclear relaxation literature of normalizing the data to a temperature dependent curve becomes a delicate hand-waving procedure when trying to prove a certain mechanism is present over another. Clearly, an accurate first-principles calculation is overwhelmingly difficult to achieve, and room must always be left for smaller contributions to the relaxation rate. In this way, the work of the Happer group is somewhat unique, with regards to phonon-mediated processes, in that the claim is a first-principle prediction of the relaxation rate that accounts for strength and temperature dependence. More work is being done on this front, but as history shows, proper calculations may take some time.

### 2.5.2 Snow theory

The temperature-dependent snow data are somewhat troublesome in description. For a multi-exponential decay, where the relaxation rate speeds up with time, some structural change within the sample must be taking place, if all systematic errors are minimized. The current data are unfortunately not enough to describe why the relaxation behaves in this way. Prof. Mark Conradi has suggested that an experiment where the temperature is kept fixed for half of the  $T_1$  measurement, after which the temperature of the sample is dropped to 77 K, and again raised back up to the set-point for the remainder of the experiment. One of two things would be seen by doing this type of experiment: either the relaxation process would reset and the curve would begin anew, or the relaxation process would pick up where it left off, indicating a definite structural change. Unfortunately, time restrictions did not allow for these measurements to take place, but future experiments should include this type of experiment. Before a proper snow theory is made, this issue should be resolved.

Assuming there is some structural change within the snow sample, an explanation for the data could be summarized as defect creep. Because diffusion is still minimal at the temperatures where the onset of multi-exponential behavior is observed, any creep of defects for this regime would be a slow hopping process. Imagining a more-ordered crystal in the bulk of a given crystallite, and a high-defect boundary (reasonable given the results oxygen-introduction experiment shown in Fig. 2.13), the defects in the boundary area are able to diffuse into the bulk of the crystallite, causing a continually higher relaxation rate. With this model, however, there should be a point that the defects become isotropically distributed through the crystallite, after which no additional increase in relaxation rate would be seen.

Another possibility of relaxation is a three-site model, considering a bulk solid xenon diffusing back-and-forth between a surface solid xenon, which have different  $T_1$  times due to increased crystallite deformities and defects at the surface. The third site of this model is the vapor phase of xenon throughout the cell, which phase-exchanges with the surface regime of the solid xenon. As the vapor pressure of solid xenon becomes very high at temperatures approaching the melting point of xenon, this type of model would account for the increase of the rate of change of the relaxation with

increasing temperatures. Again, this would only account for one of the possibilities of the experiment suggested above, and more experiments must take place before a snow theory is attempted.

## 2.6 Summary

The solid  $^{129}\text{Xe}$  data presented herein are the most reproducible to date. Though much work remains to understand this problem, the work contained in this thesis again opens the field of solid  $^{129}\text{Xe}$  longitudinal relaxation for further study. The findings seem to indicate that spin-rotation mediated by Raman scattering of harmonic phonons is not sufficient to describe the observed relaxation in solid ice  $^{129}\text{Xe}$ . In summary, the  $^{129}\text{Xe}$  show a structure-dependent  $T_1$  time, characterized by snow and ice. The ice data give  $T_1$  times that are roughly 30% longer than the previously accepted spin-rotation mediated by two-phonon Raman scattering theory, over a temperature range of 77-150 K. The  $T_1$  data at 77 K also show a fundamental difference between ice and bulk snow, supported by oxygen-introduction experiments on snow that indicate the surface of the snow crystallites relax faster than bulk snow. Temperature-dependent snow experiments show increasing relaxation rates with experimental run time, and this phenomenon is not well understood. Adjusting the isotopic concentration in the xenon solid demonstrates no isotope dependence on relaxation rates, confirming previous results and excluding a class of mechanisms responsible for relaxation. Delving into the theory of the nuclear spin relaxation due to interference with a phonon bath, the groundwork is laid for calculation of spin-rotation mediated by higher order and more exotic phonon mechanics, including anharmonic phonon behavior.

This leaves room for much future work, including a lower temperature range dependent  $T_1$  study (4 K to 50 K) on ice and snow in order to better determine  $T_1$  structural dependence. Snow, in particular, leaves many questions to be answered, some of which can be answered with a “start-stop” temperature-dependent experiment where the increase in relaxation rate with time is observed, the sample is dropped to 77 K, and the previous temperature is reset. The two possibilities are that, at the temperature change, the relaxation rate will continue increasing, or the

rate will start anew. Theoretically, there is still much work to do in isolating dominant mechanisms responsible for the ice data, as well as creating a satisfactory snow model after the “start-stop” experiments take place.

## CHAPTER 3

# DIPOLAR AND EXCHANGE COUPLING BETWEEN CARRIER PAIRS IN DISORDERED SEMICONDUCTORS UNDERGOING RESONANCE

*“You know, a lotta ins, lotta outs, lotta what-have-you’s.”*

*-El Duderino (if you’re not into the whole brevity thing)*

The effect of dipolar and exchange interactions within pairs of paramagnetic states on spin-dependent transport and recombination rates during magnetic resonance is studied numerically using the superoperator/Liouville-space formalism. The simulations reveal that induced Rabi oscillations control transition rates that are observed experimentally by pulsed electrically (pEDMR) and pulsed optically (pODMR) detected magnetic resonance spectroscopies. When the dipolar coupling exceeds the difference of the pair partners’ Zeeman energies, several Rabi frequency components are observed, with the most pronounced at  $\sqrt{2}\gamma B_1$  ( $\gamma$  is the gyromagnetic ratio,  $B_1$  is the excitation field). Exchange coupling does not significantly affect this nutation component; however, it does strongly influence a low-frequency component ( $< \gamma B_1$ ). Thus, pEDMR/pODMR allow the simultaneous identification of exchange and dipolar interaction strengths [155].

### 3.1 Introduction

In solids with weak spin-orbit coupling like silicon or carbon-based materials, spin-selection rules induced by spin conservation can drastically influence optical and electrical properties of materials [156, 157, 158, 159]. Because of this, a manipulation of spin states, e.g., by means of magnetic resonance, can change con-

ductivity, luminescence, or absorption. These effects are used for the investigation of the microscopic physical nature of the paramagnetic species involved in these processes, as is done with experimental techniques such as EDMR and ODMR spectroscopies. An abundance of spin-dependent processes is reported in the literature [157, 156, 158, 160, 161, 162, 163]. Most of these reports involve the Pauli-blockade effect, where a transition of two paramagnetic states with spin-1/2 into a single doubly occupied electron state with singlet configuration is controlled by the singlet content of the pair before the transition occurs. Such mechanisms are usually described by an “intermediate-pair” process, where an exclusive pair of two spins is formed. This pair then either dissociates with spin-independent probability, or undergoes a transition into the singlet state that happens with probability  $\propto |\langle S|\Psi\rangle|^2$ , where  $|\Psi\rangle$  is the spin state of the pair before the transition. This intermediate-pair model, developed by Kaplan, Solomon, and Mott (KSM) in 1978 [156], is distinct from other spin-1/2 pair models that do not require the exclusive intermediate pair (see for instance the Lepine [157] model). Many experimental EDMR [164, 165] and ODMR [166] studies show the validity of this picture for the description of several spin-dependent recombination and transport effects which involve transitions between localized electronic states. The KSM model is thus the basis for the calculation of spin-dependent transition rates presented here.

With the availability of high-power microwave sources, and the resulting development of pulsed electron paramagnetic resonance (EPR) techniques in the past twenty-five years, ODMR and EDMR are increasingly conducted as transient, pulsed (p) experiments, on time-scales where coherent spin-motion effects [167, 168, 169, 166] take place. Since coherent propagation of a quantum mechanical system is directly controlled by its Hamiltonian, this development in experimental techniques has dramatically enhanced access to the fundamental physical nature of the microscopic systems responsible for the EDMR and ODMR signals. Coherent spin effects such as spin echoes, spin-Rabi nutation, or dynamic decoupling schemes have produced a variety of experimental insights. In order to fully identify the spin effects observed with these techniques, a rigorous theoretical understanding of the signals is necessary. As pEPR spectroscopy evolved over the past decades, many studies have contributed

to the development of this understanding [170, 171], and it is now straightforward to derive information from pEPR data about Landé factors, spin-spin coupling phenomena, such as exchange coupling, dipolar coupling (which reveals distance between interacting spins), hyperfine couplings, and relaxation times, among other variables. Unfortunately, this rather comprehensive theory of pulsed EPR spectroscopy is only partially applicable to pulsed EDMR and ODMR experiments. EDMR and ODMR are performed by measurement of spin-dependent rates whose observables depend on the permutation symmetry of the involved spin pairs, i.e., the singlet and triplet content. Thus, the observable of EDMR and ODMR experiments is different than the observable of an EPR experiment. As a consequence, a spin ensemble that is simultaneously observed with EPR and EDMR/ODMR may exhibit entirely different signal behavior due to the different observables onto which the observed spin ensemble is projected.

Several recent studies aimed at developing and understanding pEDMR/pODMR signals have focused on electrically or optically detected transient nutation measurements, where a spectroscopy of observed spin-Rabi oscillation is conducted [159, 172, 173, 174, 175, 176, 177]. These studies have considered various spin-coupling regimes for the spin pair, including the absence of any spin-spin coupling [159, 172, 175], the presence of exchange interaction [173], and a disorder-induced distribution of spin-orbit interaction strengths [174, 175]. Recently, the first analytical study of coherently controlled spin-dependent transition rates within pairs of strongly exchange- and dipolar-coupled pairs was conducted [176]. However, a general numerical or analytical study for electrically or optically detected transient nutation of pairs with arbitrary spin-dipolar and spin-exchange interactions is lacking, to be filled in, in the following.

### **3.2 Intermediate-spin-pair Model with Dipolar and Exchange Coupling**

Following previous discussions of spin-dependent transitions controlled by intermediate pairs [156, 178, 159, 172, 173, 174, 175, 176], we describe the dipolar- and exchange-coupled intermediate-spin-1/2 pairs with the Hamiltonian

$$\hat{H}_{\text{spin}} = \hbar[\mathbf{B} \cdot (\gamma_a \hat{\mathbf{S}}_a + \gamma_b \hat{\mathbf{S}}_b) - J \hat{\mathbf{S}}_a \cdot \hat{\mathbf{S}}_b - D(3\hat{S}_a^z \hat{S}_b^z - \hat{\mathbf{S}}_a \cdot \hat{\mathbf{S}}_b)]. \quad (3.1)$$

Here, the first term represents the Zeeman interaction for both spin-pair partners, the second term is an isotropic exchange interaction, the third is a secular (high-field approximation) magnetic-dipole coupling, and  $\gamma_a, \gamma_b$  are the effective gyromagnetic ratios of the spin-pair partners  $a$  and  $b$ , respectively. The magnetic field

$$\mathbf{B} = \hat{\mathbf{z}}B_0 + \hat{\mathbf{x}}B_1 \cos(\omega t) - \hat{\mathbf{y}}B_1 \sin(\omega t) \quad (3.2)$$

consists of a static component  $B_0$  along the  $\hat{\mathbf{z}}$ -axis, and an oscillating component that is chosen to be in the  $\hat{\mathbf{x}}\text{-}\hat{\mathbf{y}}$  plane. When the exchange-coupling strength  $J$  and the dipolar-coupling strength  $D$  are scaled by  $\hbar$ , they can be directly compared to the Larmor separation  $\Delta\omega$  of the electron and hole. The negative signs in front of the  $D$  and  $J$  terms are chosen to represent a weakly attractive electron-hole pair [179, 180, 181]. Note that changing the sign of  $J$  and/or  $D$  do not change the results presented below (such a sign change could occur for like-charge spin pairs, e.g., bipolarons [161]).

### 3.2.1 Finer points of the Hamiltonian

Due to the antiquity of literature regarding the definition of a hole and the derivation of the exchange interaction, brief guides to each problem are included.

#### 3.2.1.1 Definition of hole spin

Although keeping track of plus-minus signs is at the crux of defining electron-hole spin interactions, electron-hole spin can be somewhat confusing to visualize, thus this section serves to eliminate any confusion arising from the concept of a hole. In Fig. 3.1, a simple molecular orbital model for excitation in a pi-conjugated system is shown. Pi-conjugation leads to the states of the p-orbitals aligned in the lowest energy configuration, and subsequently higher energy configurations come with increasing amounts of anti-aligned orbitals. Because electron pairs fill up each molecular orbital until the highest occupied molecular orbital is achieved, the spatially antisymmetric wave functions will necessarily be zero, leading to a trivial solution of the Schrödinger equation. Hence, as in the ground state of a helium atom, no symmetric spin states (i.e., the triplet states) exist in the simple pi-conjugated system, leaving only the antisymmetric spin state, the singlet. This is the reason that the triplet state

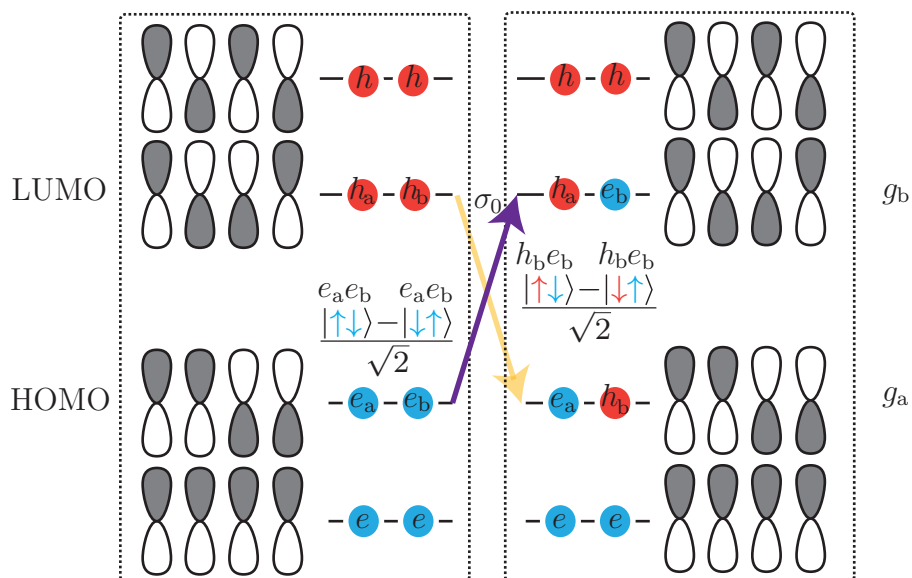


**Figure 3.1.** A simplified picture of a pi-conjugated system within molecular orbital theory in relation to the definition of the hole spin state. For demonstrative purposes, the lowest unoccupied molecular orbital (LUMO) is excited with unpolarized light from the highest occupied molecular orbital (HOMO). The remaining ground state electron in the HOMO defines the hole spin.

is considered long lived in most organic semiconductors—the ground state of the pi-conjugated or disordered system is often a singlet state. Once an electron is excited to an energetically higher molecular orbital (in Fig. 3.1, the electron is excited to the least unoccupied molecular orbital), it also excites a hole to the ground state. In order for recombination of the electron and the hole to occur, angular momentum must be conserved. Spin-orbit coupling within this model is considered negligible, so the spin state of the excited electron cannot be manipulated upon emission of a photon. This leads to a forbidden-type transition for a triplet electron-hole state to a ground state singlet. Generally, an excited state has different interaction strengths than the ground state, causing different effective  $g$ -factors for each state,  $g_a$  and  $g_b$ . Note that for simplicity, only the spins for the excited electron and hole are included in the wave function, similar to only considering the valence electron in a Rb atom.

Within this work, similar to other definitions [179], the spin state of the hole is defined in relation to the spin of the remaining ground state electrons for convenience—i.e., the hole spin-state is defined such that a singlet hole-electron pair will recombine with higher probability. The electron-hole theory is somewhat analogous to an

electron-positron system, with the caveats that two photons are not emitted upon annihilation and the effective masses are often different in the electron-hole case. Lorentz invariance leads to charge-parity-time symmetry (CPT), and assuming charge-parity symmetry, a time reversal can be written as a charge-parity reversal. In this way, the hole is academically thought of as an electron moving backwards in time, as is a positron. Thus, due to time-symmetry considerations, the hole is defined to have the opposite spin as the state that the excited electron has been excited from—a singlet electron-hole pair is excited from a ground state electron-electron singlet. Thus, consider two complementary configurations  $\mathcal{C}_e$  and  $\mathcal{C}_h$  of the model in the excited state shown in Fig. 3.1, consisting of  $x = 2$  and  $2(2l + 1) - x = 4 - x = 2$  electrons outside closed shells. Take the Slater determinants of  $\mathcal{C}_e$  to be  $\Phi_e = (m_l^a, m_s^a; m_l^b, m_s^b)$  and for  $\mathcal{C}_h$ ,  $\Phi_h = (-m_l^{a'}, -m_s^{a'}; -m_l^{b'}, -m_s^{b'})$ , where  $m_l', m_s'$  are the one-electron states unoccupied in  $\Phi_e$ , i.e., hole states. The time-reversed Slater determinant of  $\Phi_h$  is then  $\Theta\Phi_h = (m_l^{a'}, m_s^{a'}; m_l^{b'}, m_s^{b'})$ , where  $\Theta$  is the time-reversal operator. The sum over all closed shell one-electron tensor operators  $\mathcal{T}_k$  must vanish, yielding

$$\begin{aligned} \langle \Phi_e | \mathcal{T}_k | \Phi_e \rangle + \langle \Phi_h | \Theta \mathcal{T}_k \Theta | \Phi_h \rangle &= 0, \text{ or,} \\ \langle \Phi_e | \mathcal{T}_k | \Phi_e \rangle &= - \langle \Phi_h | \Theta \mathcal{T}_k \Theta | \Phi_h \rangle = - \langle \Phi_h | \pm \mathcal{T}_k | \Phi_h \rangle = \mp \langle \Phi_h | \mathcal{T}_k | \Phi_h \rangle, \end{aligned} \tag{3.3}$$

where the negative sign in the final expression corresponds to time-even operators (charge, spin-orbit coupling), and the positive sign to time-odd operators (coupling to magnetic fields).

### 3.2.1.2 The exchange interaction

A negative sign on the exchange interaction is chosen to represent the effective repulsive or weakly attractive Coloumb potential between the hole and electron in the exchange integrals. A positive sign on the electron-hole exchange interaction corresponds to a highly attractive Coloumb potential between the two states, i.e., an attraction that dwarfs the electron-electron Coloumb interactions creating the hole state. An exchange interaction arises from the need to take into account the indistinguishability between an excited-state electron and any ground-state electron, which then leads to a coupling of the hole spin and the electron spin [180, 181].

Consider the interaction of two electrons, a problem first treated by Heisenberg

and Dirac [182]. First, assuming that the electrons do not influence each other, the time-independent Schrödinger equation is

$$(\nabla_1^2 + \nabla_2^2)\Psi + \frac{8\pi^2m}{\hbar^2}[E_0 - V(\mathbf{x}_1) - V(\mathbf{x}_2)]\Psi = 0 \quad (3.4)$$

The two electrons' respective wave functions are  $\psi_1$  and  $\psi_2$ , and the general solution to the Schrödinger equation is the class of states

$$\Psi = c_1\Psi_{\text{I}} + c_2\Psi_{\text{II}} = c_1\psi_1(\mathbf{x}_1)\psi_2(\mathbf{x}_2) + c_2\psi_1(\mathbf{x}_2)\psi_2(\mathbf{x}_1), \quad (3.5)$$

with energy  $E_0$ , and  $c_1^2 + c_2^2 = 1$ . The two basis states  $\Psi_{\text{I}}$  and  $\Psi_{\text{II}}$  account for the possible swapping of positions for two indistinguishable particles (as their energy is the same).

Now consider the inclusion of a potential energy  $V_{12}$  of a spatially symmetric interaction, such as the Coloumb interaction. Solving for the energies in terms of the basis states, the secular equation becomes

$$\begin{vmatrix} E_0 + K_{12} - E & J_{12} \\ J_{12} & E_0 + K_{12} - E \end{vmatrix} = 0, \quad (3.6)$$

where  $E$  is the energy in the presence of the interaction term  $V_{12}$ ,  $K_{12} = \langle\Psi_{\text{I}}|V_{12}|\Psi_{\text{I}}\rangle = \langle\Psi_{\text{II}}|V_{12}|\Psi_{\text{II}}\rangle$ , and  $J_{12} = \langle\Psi_{\text{II}}|V_{12}|\Psi_{\text{I}}\rangle = \langle\Psi_{\text{I}}|V_{12}|\Psi_{\text{II}}\rangle$ .  $J_{12}$  is called the exchange integral and arises due to the interference between the two basis states. The secular equation yields the eigenenergies

$$E_s = E_0 + K_{12} + J_{12}, \quad E_a = E_0 + K_{12} - J_{12}. \quad (3.7)$$

Solving for the eigenstates shows that,  $E_s$  corresponds to  $\Psi_s$  and  $E_a$  corresponds to  $\Psi_a$ , where  $V_{12}$  has lifted the energy degeneracy to create the symmetric/antisymmetric states

$$\Psi_s = \frac{\Psi_{\text{I}} + \Psi_{\text{II}}}{\sqrt{2}}, \quad \Psi_a = \frac{\Psi_{\text{I}} - \Psi_{\text{II}}}{\sqrt{2}}. \quad (3.8)$$

Thus, the interaction term  $V_{12}$  adds  $K_{12} + J_{12}$  to the  $\Psi_s$  state, and  $K_{12} - J_{12}$  to the  $\Psi_a$  state. Pauli exclusion requires that only antisymmetric wave functions be used; with the inclusion of spin, the valid wave functions for the two electrons become

$$|\Psi_s\rangle |S\rangle, \quad |\Psi_a\rangle |T\rangle, \quad (3.9)$$

where  $|S\rangle$  is the singlet state and  $|T\rangle$  are the triplet states with a total spin of  $S = 0$  and  $S = 1$ , respectively. Recalling that

$$\hat{\mathbf{S}}^2 = (\hat{\mathbf{S}}_1 + \hat{\mathbf{S}}_2)^2 = \hat{\mathbf{S}}_1^2 + \hat{\mathbf{S}}_2^2 + 2\hat{\mathbf{S}}_1 \cdot \hat{\mathbf{S}}_2, \quad (3.10)$$

the product  $\hat{\mathbf{S}}_1 \cdot \hat{\mathbf{S}}_2$  takes values of  $-3/4$  for the  $|\Psi_s\rangle |S\rangle$  states, and  $1/4$  for the  $|\Psi_a\rangle |T\rangle$  state. In this way, the contribution due to the potential energy can be cast into the matrix equality

$$V_{12} = K_{12} - \frac{1}{2}J_{12} - 2J_{12}\hat{\mathbf{S}}_1 \cdot \hat{\mathbf{S}}_2, \quad (3.11)$$

to obtain  $K_{12} + J_{12}$  for the  $|\Psi_s\rangle |S\rangle$  state, and  $K_{12} - J_{12}$  for the  $|\Psi_a\rangle |T\rangle$  states.

This profound result indicates that the relative spin orientation of the two electrons causes a raising or lowering of the energy, directly obtained from considering the indistinguishability of electrons, a Coloumb potential, and considering the Pauli exclusion principle. Note that even though the exchange interaction very much looks like a powerful magnetic coupling between the two spins, the actual magnetic field forces are very, very weak. When considering only the spin contribution to the Hamiltonian, the exchange interaction between any two electrons  $i$  and  $j$  in the system is then represented by

$$V_{ij} = -2J_{ij}\hat{\mathbf{S}}_i \cdot \hat{\mathbf{S}}_j. \quad (3.12)$$

It is important to note that the exchange integral in the case of two electrons is generally positive, representing the repulsion of two electrons in an  $e^2/|\mathbf{x}_1 - \mathbf{x}_2|$  Coloumb potential. However, there do exist situations where the two electrons reside in a potential that is attractive enough to diminish or dominate the Coloumb potential, possibly causing a negative value for  $J_{ij}$ —this becomes important for the electron-hole definition.

For an electron-hole pair, the analysis of the exchange coupling gets markedly difficult due to the fact that the hole state, for our purposes, is created by the many electrons left behind in, depending on the system, the Fermi-sea or molecular orbitals. In this way, the appropriate exchange integral  $J$  should be calculated between the spatially symmetric and antisymmetric states with a Slater determinant over all electrons, excited and ground. This is also the reason there exists an exchange coupling

between a “real” particle (quasi-electron, excited electron coupled to lattice/system) and a quasiparticle (hole), even through the electron and hole clearly have a different quantum number of charge. Consider time-reversal symmetry, which gives that the Coloumb interaction is time-even, and thus the hole state is treated as having a positive charge. This causes an addition to the exchange integral over electron states of an attractive Coloumb interaction between the hole and electron proportional to  $-e^2/|\mathbf{x}_1 - \mathbf{x}_2|$ . In the case of a strongly attractive polaron pair that dominates the repulsive part due to electrons, the sign of the exchange integral  $J$  will be negative, causing a net sign flip in the spin Hamiltonian

$$V = J\hat{\mathbf{S}}_a \cdot \hat{\mathbf{S}}_b, \quad (3.13)$$

where  $J$  is defined as twice the negative exchange integral. However, in this work, a sufficiently weak attraction is assumed between the polaron electron and hole states—still giving a net positive for the electron-hole pair exchange integral, and the definition

$$V = -\hbar J\hat{\mathbf{S}}_a \cdot \hat{\mathbf{S}}_b, \quad (3.14)$$

is used in the spin Hamiltonian, where  $J$  is defined as twice the positive exchange integral, and scaled by  $\hbar$  to yield a frequency. With Eq. 3.14, as in the two-electron case, the singlet exciton state will be higher energy than the triplet exciton state—for organic polymers such as MEH-PPV, this seems to be the case.

### 3.2.1.3 The dipolar interaction

Recall that the secular approximation for the spin dipolar interaction between two particles with dipolar moments arising from spin is

$$\hat{H}_d = -\frac{1}{2} \frac{g_a g_b \mu_B^2 \hbar^2}{r^3} (3 \cos^2(\theta) - 1) (3\hat{S}_{az}\hat{S}_{bz} - \hat{\mathbf{S}}_a \cdot \hat{\mathbf{S}}_b). \quad (3.15)$$

The dipolar strength term  $D$  is referenced to  $\theta = 0$ , where the two particles are aligned with the external, quantizing magnetic field. It is seen with  $\theta = 0$ , that the minimum energy will come from spins aligned and the maximum energy will come from spins anti-aligned. As shown above, time-reversal symmetry dictates that the hole be treated with a negative charge when applying time-odd operators, such as the

magnetic moment operator. Thus, taking  $g_a$  and  $g_b$  to be the same sign, this would require no change in the magnetic field effect experienced by a hole or electron, and a negative sign should be associated with the dipolar strength term. Thus, the dipolar term  $D$  throughout is defined as  $D_{\theta=0} = g_a g_b \mu_B^2 \hbar / r^3$ , where  $D$  is scaled by  $\hbar$  to yield a frequency. The effect of changing  $\theta$ , though, enters when considering randomly distributed spin, and in particular for this work, is taken into account using a Pake distribution. Note again that in the cases of  $g_a$  or  $g_b$  having opposite signs, or where exchange interaction is dominated by an attractive Coloumbic potential, the main arguments and conclusions presented in the following will not change, but one should be aware of these intricacies before applying this model to other systems.

### 3.2.2 Energy basis and observable

The spin-pair Hamiltonian in absence of radiative excitation ( $B_1 = 0$ ) is rotated into an energy eigenbasis by a Jacobi rotation,  $\hat{H}_{\text{en}} = U^\dagger \hat{H}_{\text{spin}} U$ , with the resulting eigenbasis given by

$$U^\dagger \begin{pmatrix} |\uparrow\uparrow\rangle \\ |\uparrow\downarrow\rangle \\ |\downarrow\uparrow\rangle \\ |\downarrow\downarrow\rangle \end{pmatrix} = \begin{pmatrix} |\uparrow\uparrow\rangle \\ \cos(\phi) |\uparrow\downarrow\rangle - \sin(\phi) |\downarrow\uparrow\rangle \\ \cos(\phi) |\uparrow\downarrow\rangle + \sin(\phi) |\downarrow\uparrow\rangle \\ |\downarrow\downarrow\rangle \end{pmatrix}, \quad (3.16)$$

where  $\cot(2\phi) = \frac{\Delta\omega}{J-D}$ . In the case of either strong dipolar or strong exchange interaction, the energy eigenbasis becomes a set of singlet and triplet states. With strong dipolar coupling,  $\phi \rightarrow -\frac{\pi}{4}$  ( $D \rightarrow \infty$ ,  $J \rightarrow 0$ ), the energy eigenbasis becomes  $\{|T_+\rangle, |T_0\rangle, |S\rangle, |T_-\rangle\}$ ; strong exchange coupling,  $\phi \rightarrow +\frac{\pi}{4}$  ( $J \rightarrow \infty$ ,  $D \rightarrow 0$ ), produces an energy eigenbasis  $\{|T_+\rangle, |S\rangle, |T_0\rangle, |T_-\rangle\}$ . In either one of these strong coupling cases, the only ESR-allowed transitions are those within the triplet manifold, leading to a strong triplet ESR signal. However, because the triplet-singlet transition probability is zero, there is no observable pODMR/pEDMR signal. Any intermediate case (e.g.,  $J \approx D \approx \Delta\omega$ ) will have an energy eigenbasis of  $\{|T_+\rangle, |2\rangle, |3\rangle, |T_-\rangle\}$ , where  $|2\rangle$  and  $|3\rangle$  will each have a mixture of singlet and triplet content defined by the relative magnitudes of the dipolar and exchange strengths. Therefore, the transitions between states are uniquely governed by the collection of system parameters  $D$ ,  $J$ , and  $\Delta\omega$ .

For pODMR/pEDMR experiments on intermediate-spin-pair processes, the observable depends on the permutation symmetry of the individual pairs, contrary to most conventional spectroscopy experiments which probe polarization states. An extended discussion of such intermediate-pair related pEDMR/pODMR observables is given by Gliesche et al. [173], who established the connection of the spin density operator  $\hat{\rho}$  of an ensemble of spin- $\frac{1}{2}$  pairs to a spin-dependent rate transient

$$Q(\tau) = \int_0^{\tau} R(t) dt = \sum_{i=i}^4 (\hat{\rho}_{ii}(\tau) - \hat{\rho}_{ii}^S) (1 - e^{-r_i \tau}), \quad (3.17)$$

which follows coherent spin excitation. In Eq. 3.17, the density matrix is in the  $4 \times 4$  energy eigenbasis representation and the time-dependent function  $R(t)$  is the spin-dependent rate after the pulse excitation, which is assumed to end at  $t = 0$ . Because  $R(t)$  is a current for pEDMR experiments, the integral  $Q(\tau)$  becomes a number of charge carriers which undergo spin-dependent transitions due to the resonant spin excitation. The dependence of  $Q$  on the pulse length  $\tau$  will reveal information about how the density operator  $\hat{\rho}$  evolves from the steady state to a coherent state due to the resonant excitation. Thus,  $Q(\tau)$  is an easily accessible observable for the coherently manipulated spin ensemble, representing either the number of charge carriers (for pEDMR) or photons (for pODMR).

The transient evolution of  $Q(\tau)$  during the pulse is Fourier transformed (denoted  $\text{FFT}\{Q(\tau)\}$ ) in order to make the frequency components of the coherent spin motion explicit. A comparison of experimentally obtained Rabi frequency spectra with calculations presented gives insight into the nature of the spin-pair Hamiltonian. As the spin-pair Hamiltonian crucially depends on the microscopic nature of the spin pairs, pEDMR/pODMR experiments are superb probes to gain unambiguous experimental access to spin-dependent transport and recombination processes.

Again, following previous descriptions [178, 159, 172, 173, 174, 175, 176], the evolution of the density operator  $\hat{\rho}$  is described by a stochastic Liouville equation

$$\partial_t \hat{\rho} = \frac{i}{\hbar} [\hat{\rho}, \hat{H}_{\text{en}}] + S[\hat{\rho}], \quad (3.18)$$

where the stochastic term  $S[\hat{\rho}] = S_{\text{cr}}[\hat{\rho}] + S_{\text{an}}[\hat{\rho}]$  is the sum of creation and annihilation terms of the spin pairs.

As shown elsewhere [159], the recombination probabilities for the different energy eigenbasis states are given by  $r_i = r_S |\langle i|S\rangle|^2 + r_T |\langle i|T\rangle|^2$ , where  $r_S$  and  $r_T$  are the singlet and triplet recombination probabilities, respectively. Using Eq. 3.16, the various recombination rates can be expressed in terms of the coupling parameters by

$$r_{1,4} = r_T \quad (3.19)$$

$$r_{2,3} = \frac{1}{2}r_S \left( 1 \mp \frac{J-D}{\sqrt{(J-D)^2 + (\Delta\omega)^2}} \right) + \frac{1}{2}r_T \left( 1 \pm \frac{J-D}{\sqrt{(J-D)^2 + (\Delta\omega)^2}} \right). \quad (3.20)$$

The eigenstates  $|1\rangle$  and  $|4\rangle$  always remain pure triplet states ( $|T+\rangle$  and  $|T-\rangle$ , respectively); their recombination rates are thus not affected by any coupling within the spin pair. When strong coupling such as  $D \gg \Delta\omega$  is present, then  $r_2 = r_S$  and  $r_3 = r_T$  (for  $J \gg \Delta\omega$ ,  $r_2 = r_T$  and  $r_3 = r_S$ ). The dissociation rate coefficient  $d$  is assumed to be spin independent. In the energy eigenbasis, the stochastic annihilation term  $S_{\text{an}}[\hat{\rho}]$  has matrix elements in a convenient form,  $\{S_{\text{an}}[\hat{\rho}]\}_{ij} = (r_i + r_j + 2d)\frac{\rho_{ij}}{2}$ . The pair generation is also assumed to only create pairs in an energy eigenstate,  $\{S_{\text{cr}}[\hat{\rho}]\}_{ij} = \delta_{ij}\frac{k}{4}$ , where  $k$  is the net generation rate of all four states. This creation term is the only inhomogeneous contribution to Eq. 3.18. In this paper we neglect the Redfield relaxation matrix, an assumption that is valid in the short-time regime ( $\tau < \frac{1}{r_S} \sim T_2 < \frac{1}{r_T} \ll T_1$ ). For the purpose of obtaining sufficient resolution, some pulse lengths violate this assumption.

### 3.3 Analytical and Numerical Methods

The following section outlines the study of the observable  $Q(\tau)$  that results from the coherent excitation of the spin pair. Eq. 3.18 is a set of sixteen coupled inhomogeneous ordinary differential equations (ODEs) that were previously solved using a Runge-Kutta or comparable ODE solver [172, 173, 174]. These computationally intensive methods make the convolution of distributions of many parameters ( $J$ ,  $D$ , bandwidth of pulse, etc.) impractical without a supercomputer. Two techniques are used that lead to a significant decrease in computation time. In Sect. 3.3.1 the first step of the computation is detailed, which is a transformation into the rotating frame.

Once in the rotating frame, several limiting cases of the Rabi nutation frequencies are demonstrated in Sect. 3.3.2. The limiting cases of overall weak coupling, strong exchange coupling, strong dipolar coupling, and a large difference in dipolar and exchange coupling are described. Sect. 3.3.1 also includes an analytical description of the  $\sqrt{2}\gamma B_1$  Rabi frequency component that occurs in the presence of strong dipolar coupling. These limiting cases provide significant insight into qualitative features observed in the numerically calculated general cases, such as resonance location, Rabi frequency, and signal amplitude.

In addition to the use of the rotating frame, the calculation of the time-dependent change of the density matrix was aided by the use of Liouville-space formalism, and is discussed in Sect. 3.3.3. A direct consequence of this formalism is that the inhomogeneous stochastic Liouville equation is cast into a readily tractable and solvable form. Compared to previous work [172, 173], the speed of the simulation allows us to perform a larger and more detailed study of  $Q(\tau)$ 's dependence on dipolar  $D$  and exchange  $J$  interactions with respect to the Larmor frequency separation  $\Delta\omega$  and the excitation-field strength  $B_1$ .

In Sect. 3.4, representative results of these simulations are given and discussed. Using the methods from Sect. 3.3, we simulate  $Q(\tau)$  for a range of values  $D$  and  $\Delta\omega$  with a fixed excitation field  $B_1$ . Then,  $Q(\tau)$  is simulated as a function of  $D$  and  $J$  with a fixed  $\Delta\omega$  and  $B_1$ . Finally,  $Q(\tau)$  is simulated with small and large exchange coupling strengths, along with a complete Pake distribution of dipolar interaction strengths.

### 3.3.1 Rotating-frame stochastic Liouville equation

The rotating frame corresponds to a transformation of the Hamiltonian from the energy eigenbasis:  $\hat{H}_R = R^\dagger \hat{H}_{\text{en}} R$ . The rotating-frame density matrix is then given by  $\hat{\rho}_R = R^\dagger \hat{\rho} R$ . Here,  $R = R_z^{\frac{1}{2}} \otimes R_z^{\frac{1}{2}}$  is the  $4 \times 4$  spin-1/2 pair rotation operator, and  $R_z^{\frac{1}{2}}$  is the rotation operator for a spin-1/2 state around the  $\hat{z}$ -axis by an angle  $\omega t$ . The resulting rotating-frame Hamiltonian is

$$\hat{H}_R = \frac{\hbar}{2} \begin{pmatrix} 2\omega_0 - \frac{J}{2} - D & \gamma B_1 \text{cs}_- & \gamma B_1 \text{cs}_+ & 0 \\ \gamma B_1 \text{cs}_- & \frac{J}{2} + D + \sqrt{\Delta\omega^2 + (J-D)^2} & 0 & \gamma B_1 \text{cs}_- \\ \gamma B_1 \text{cs}_+ & 0 & \frac{J}{2} + D - \sqrt{\Delta\omega^2 + (J-D)^2} & \gamma B_1 \text{cs}_+ \\ 0 & \gamma B_1 \text{cs}_- & \gamma B_1 \text{cs}_+ & -2\omega_0 - \frac{J}{2} - D \end{pmatrix}, \quad (3.21)$$

and has no explicit time dependence, with  $\text{cs}_+ = \cos(\phi) + \sin(\phi)$  and  $\text{cs}_- = \cos(\phi) - \sin(\phi)$ . Note that the energy levels for the energy eigenbasis ( $E_1$ ,  $E_2$ ,  $E_3$ , and  $E_4$ ) reside on the diagonal. The average of the spin-pair Larmor frequencies is labeled as  $\omega_0 = (\omega_a + \omega_b)/2$  and Larmor frequency separation  $\Delta\omega = \omega_a - \omega_b$ . The Rabi frequency of each spin is assumed to be the same ( $\gamma_a B_1 \approx \gamma_b B_1$ ), allowing for explication of the results in terms of a single on-resonance Rabi frequency  $\gamma B_1$ . Neglecting the very small difference in the individual-spin Rabi frequencies symmetrizes the simulations about  $\omega - \omega_0 = 0$ , rather than demonstrating an inconsequential asymmetry. After an additional time-independent term  $\hat{F} = R^\dagger \partial_t R$  is absorbed into an effective Hamiltonian  $\hat{H} = \hat{H}_R - \hat{F}$ , the rotating-frame stochastic Liouville equation becomes

$$\partial_t \hat{\rho}_R = \frac{i}{\hbar} [\hat{\rho}_R, \hat{H}] + S[\hat{\rho}_R]. \quad (3.22)$$

As expected from this transformation, the only term left with time dependence in Eq. 3.22 is the rotating-frame density matrix  $\hat{\rho}_R$ .

### 3.3.2 Limiting cases of the Rabi frequencies

Useful equations that elucidate limiting cases are derived from finding the single-transition Rabi frequencies of the rotating-frame Hamiltonian given in Eq. 3.21. By considering an induced transition between only two of the available four states and solving a  $2 \times 2$  eigenvalue problem, it is shown that the single-transition Rabi frequencies are

$$\Omega_{ij} = \sqrt{(1 \mp \sin 2\phi) (\gamma B_1)^2 + (\omega - \omega_{ij})^2}. \quad (3.23)$$

The negative sign in the first term under the radical on the right hand side gives the Rabi frequencies for the  $|T_\pm\rangle \leftrightarrow |2\rangle$  transitions between the pure triplet states and  $|2\rangle$  state ( $(i, j) = \{(T_+, 2); (T_-, 2)\}$ ). The plus sign in Eq. 3.23 gives the Rabi frequencies for the  $|T_\pm\rangle \leftrightarrow |3\rangle$  transitions between the pure triplet states and  $|3\rangle$  energy eigenstate ( $(i, j) = \{(T_+, 3); (T_-, 3)\}$ ). In general, there are four resonant frequencies,

$\omega_{ij} = (E_i - E_j)/\hbar$ . If an on-resonant excitation frequency  $\omega$  is applied such that  $\omega = \omega_{ij}$ , the second term under the radical in Eq. 3.23 vanishes.

### 3.3.2.1 Weak and effectively weak coupling

For the first limiting case, let the coupling terms  $J$  and  $D$  approach zero. In this weak-coupling regime,  $|J| + |D| \ll \Delta\omega$ , the first term in Eq. 3.23 tends towards the limit  $(1 \mp \sin 2\phi) \rightarrow 1$  and there is only an on-resonance Rabi oscillation frequency of a single uncoupled spin,  $\gamma B_1$ . There are two resonant transitions with a two-fold degeneracy corresponding to the Larmor frequency of each spin in the pair. If there is a sufficient excitation-field strength  $B_1$ , both uncoupled spins will nutate coherently, creating a spin-beating effect with a  $2\gamma B_1$  Rabi frequency component [163, 183]. If the Larmor separation  $\Delta\omega$  is zero (indicating that the gyromagnetic ratios of the electron and the hole are the same), there is only one transition that has a degeneracy of four and a Rabi frequency  $\gamma B_1$ .

For the second limiting case consider an effectively weak coupling, where the difference in coupling strengths becomes much less than the Larmor separation,  $|J - D| \ll \Delta\omega$ . In this limit there are four nondegenerate resonant transitions. As in the weak regime, a pair in the effectively weak regime has a Rabi frequency  $\gamma B_1$  equal to that of a single uncoupled spin.

Both weak and effectively weak coupling leave the energy eigenbasis completely unaffected by the rotation performed in Eq. 3.16. In the latter case, this happens even though the couplings  $J$  and  $D$  could individually be quite large compared to  $\Delta\omega$ . However, the resonance frequencies for each transition will be shifted due to the increased coupling strengths. This nondegenerate energy spectrum distinguishes the effectively weak coupling from weak coupling.

### 3.3.2.2 Strong dipolar coupling

Now consider the limiting case of strong dipolar coupling,  $|D| \gg |\Delta\omega|$ , with no exchange coupling,  $J = 0$ . As  $D$  gets large,  $\sin 2\phi \rightarrow -1$ , and the four resonant single-transition frequencies, offset from  $\omega_0$ , are approximately

$$\omega_{\pm,2} \approx \pm\left(\frac{3D}{2} + \frac{\Delta\omega^2}{4D}\right), \quad \omega_{\pm,3} \approx \pm\left(\frac{D}{2} - \frac{\Delta\omega^2}{4D}\right). \quad (3.24)$$

The first term under the radical on the right hand side of Eq. 3.23 is  $(1 - \sin 2\phi) \rightarrow 2$  for the  $|T_{\pm}\rangle \leftrightarrow |2\rangle$  transitions, and  $(1 + \sin 2\phi) \rightarrow 0$  for the  $|T_{\pm}\rangle \leftrightarrow |3\rangle$  transitions. Therefore, strong dipolar coupling within the pair yields an on-resonance Rabi frequency of  $\sqrt{2}\gamma B_1$  for each transition between the pure triplet states and the  $|2\rangle$  state. The  $T_{\pm} \leftrightarrow |2\rangle$  transition probabilities are large, but have an overall reduction of the pEDMR/pODMR signal, owing to the strong triplet character of the  $|2\rangle$  state.

A  $\sqrt{2}\gamma B_1$  Rabi frequency is therefore predicted for any spin-1/2 pair with sufficient Larmor separation and strong enough dipolar coupling. When strongly coupled, an applied excitation necessarily affects both spins in a pair, even if only a monochromatic excitation is applied. The strong dipolar coupling (like a strong exchange coupling [173]) allows access to only one quantum state, and prohibits isolating an individual spin within the spin pair. This behavior has been well known from traditional magnetic resonance spectroscopy [170, 184] and, without explicit theoretical proof, it has already been applied to experimental pODMR [185, 186] and pEDMR [186, 187] data.

### 3.3.2.3 Strong exchange coupling

Now consider the strong exchange coupling regime, where  $|J| \gg |\Delta\omega|$ , with no dipolar coupling,  $D = 0$ . As  $J$  gets large,  $\sin 2\phi \rightarrow 1$ , and the resonant single-transition frequencies, offset from  $\omega_0$ , are approximately

$$\omega_{\pm,2} \approx \pm \left( J + \frac{\Delta\omega^2}{4J} \right), \quad \omega_{\pm,3} \approx \mp \frac{\Delta\omega^2}{4J}. \quad (3.25)$$

The first term under the radical on the right hand side of Eq. 3.23 is  $(1 + \sin 2\phi) \rightarrow 2$  for the  $|T_{\pm}\rangle \leftrightarrow |3\rangle$  transitions, and  $(1 - \sin 2\phi) \rightarrow 0$  for the  $|T_{\pm}\rangle \leftrightarrow |2\rangle$  transitions. The single-transition analysis predicts a  $\sqrt{2}\gamma B_1$  Rabi frequency for the  $|T_{\pm}\rangle \leftrightarrow |3\rangle$  transitions. However, this naive analysis does not take into account that the splitting in the  $|T_{\pm}\rangle \leftrightarrow |3\rangle$  transition frequencies is so small that the transitions will be driven simultaneously by  $B_1$ . Therefore, Eq. 3.23 is no longer valid, and a multiple-transition analysis must be used. The  $|T_{\pm}\rangle \leftrightarrow |2\rangle$  transitions are far away from  $\omega_0$  and have Rabi frequencies approaching zero. Because of this, the strong exchange-coupling regime can be analyzed using only the  $|T_{\pm}\rangle \leftrightarrow |3\rangle$  transitions. In fact, if one of the  $|T_{\pm}\rangle \leftrightarrow |3\rangle$  transitions is forbidden in the simulation, say  $|T_+\rangle \leftrightarrow |3\rangle$ , a single sharp resonance

with a Rabi frequency of  $\sqrt{2}\gamma B_1$  is seen. If an excitation frequency of  $\omega = \omega_0$  is applied, two of the three rotating-frame energy eigenvalues in the multiple-transition analysis are degenerate. This simplifies the eigenvalue problem significantly, and the (three-state) Rabi frequency is found to be

$$\Omega = \sqrt{\frac{\Delta\omega^2}{4J} + 2(1 + \sin 2\phi)(\gamma B_1)^2} \approx 2\gamma B_1, \quad (3.26)$$

for the  $|T_+\rangle \leftrightarrow |3\rangle \leftrightarrow |T_-\rangle$  transition. Note that the single-transition Rabi frequencies for  $|T_\pm\rangle \leftrightarrow |3\rangle$  do not merely add to a total  $2\sqrt{2}\gamma B_1$  Rabi frequency. An in-depth, more general analytical treatment of these multiple-transition Rabi frequencies is given in Glenn et al. [176]. Perhaps more interesting is applying a driving frequency  $\omega$  that is slightly off from  $\omega_0$ ; all three rotating-frame energy eigenvalues for the  $|T_+\rangle \leftrightarrow |2\rangle \leftrightarrow |T_-\rangle$  transitions are non-degenerate and there appears to be a Rabi frequency slightly larger than  $\gamma B_1$  on resonance. If the power of the excitation field is lowered, only a  $\gamma B_1$  Rabi frequency is seen in the case of uncoupled pairs, whereas a strongly exchange-coupled pair always has a  $2\gamma B_1$  component, provided the signal is strong enough. This fact has served to distinguish uncoupled and strongly exchange-coupled states in experimental studies [163, 183].

### 3.3.2.4 Large difference in exchange and dipolar strengths

The final limiting case we considered is taking the difference in coupling strengths to be large with respect to the separation of the Larmor frequencies, and the exchange strength to be greater than the dipolar strength,  $J - D \gg \Delta\omega$ . This limit yields  $(1 - \sin 2\phi) \rightarrow 0$  for the  $|T_\pm\rangle \leftrightarrow |2\rangle$  transitions, and  $(1 + \sin 2\phi) \rightarrow 2$  for the  $|T_\pm\rangle \leftrightarrow |3\rangle$  transitions. The resonant single-transition frequencies, offset from  $\omega_0$ , are now

$$\begin{aligned} \omega_{\pm,2} &\approx \pm \left( J + \frac{D}{2} + \frac{\Delta\omega^2}{4(J-D)} \right), \\ \omega_{\pm,3} &\approx \pm \left( \frac{3D}{2} - \frac{\Delta\omega^2}{4(J-D)} \right). \end{aligned} \quad (3.27)$$

The presence of dipolar coupling splits the transition frequencies enough that the single-transition analysis for Eq. 3.21 becomes valid again. Therefore, in the limit of a large difference in dipolar and exchange coupling strengths, a Rabi frequency of  $\sqrt{2}\gamma B_1$  will occur when on resonance with the  $|T_\pm\rangle \leftrightarrow |3\rangle$  transitions, and the  $|T_\pm\rangle \leftrightarrow |2\rangle$  transitions have a vanishingly small transition probability.

The other limit in the strong-coupling regime that we do not describe in detail is the difference in coupling strengths, large with respect to the separation in Larmor frequencies, with dipolar strength greater than the exchange strength,  $D-J \gg \Delta\omega$ . An analysis similar to that given above shows that the  $\sqrt{2}\gamma B_1$  Rabi frequency components exist, but have resonances far away from the central average  $\omega_0$  of the spin-pair Larmor frequencies. These limiting cases are referred to during the discussion of the features appearing in the results of the following simulations. In general, only a resonance between up to four nondegenerate states can be solved for exactly, a consequence of the nonexistence of a unique solution for a quintic or higher polynomial.

### 3.3.3 Liouville-space formalism

The rotating-frame description is now reformulated using Liouville operator space, also known as superoperator formalism [33, 20], to increase the computational power of the simulation. This technique was also used recently in a model for magnetic-field effects in disordered semiconductors [188]. The essence of this reformulation is the representation of the state population as a  $16 \times 1$  column vector  $\rho$  instead of the typical  $4 \times 4$  density matrix  $\hat{\rho}$ . Operations involving  $\hat{A}$  are associated with corresponding superoperators  $A$ . Note that this formalism produces no new physics, but simply recasts the problem such that a convenient, tractable solution to Eq. 3.22 is obtained.

Using superoperator formalism, the rotating-frame inhomogeneous stochastic Liouville equation (Eq. 3.22) can be rewritten in the compact form

$$\partial_t \rho_R = \frac{i}{\hbar} H \rho_R + S_{\text{an}} \rho_R + K = G \rho_R + K. \quad (3.28)$$

Here,  $H \rho_R$  is the abbreviated superoperator form of the commutator  $[\hat{\rho}_R, \hat{H}]$ .  $H$  is a  $16 \times 16$  superoperator that can be written as

$$H = \begin{pmatrix} \hat{H} - IH_{11} & IH_{12} & IH_{13} & IH_{14} \\ IH_{21} & \hat{H} - IH_{22} & IH_{23} & IH_{24} \\ IH_{31} & IH_{32} & \hat{H} - IH_{33} & IH_{34} \\ IH_{41} & IH_{42} & IH_{43} & \hat{H} - IH_{44} \end{pmatrix}, \quad (3.29)$$

where  $I$  is the  $4 \times 4$  identity matrix and  $H_{ij}$  are the matrix elements of the  $4 \times 4$  Hamiltonian  $\hat{H}$ . In Eq. 3.28,  $S_{\text{an}}$  is a time-independent diagonal  $16 \times 16$  matrix of the appropriate stochastic annihilation terms corresponding to  $S_{\text{an}}[\hat{\rho}]$ . The creation

term  $K$  is a time-independent  $16 \times 16$  matrix consisting of the appropriate stochastic creation/generation terms corresponding to  $S_{\text{cr}}[\hat{\rho}]$  and is the sole inhomogeneous part of Eq. 3.28. The superoperator  $G$  is merely the addition of  $\frac{i}{\hbar}H$  and  $S_{\text{an}}$ ; it is a symmetric and relatively sparse matrix with 160 zeroes.

A steady-state density matrix  $\rho^S$  is used to define  $\rho(0)$ , the density matrix at time  $t=0$ , and is obtained by neglecting the coherent excitation ( $B_1=0$ ) and finding a steady-state superoperator  $G_S$  from Eq. 3.28. Using the variation-of-parameters method, the ODE in Eq. 3.28 is solved analytically by

$$\begin{aligned}\rho_R(t) &= e^{Gt}(\rho(0)+G^{-1}K)-G^{-1}K, \\ \rho(0) &= G_S^{-1}K,\end{aligned}\tag{3.30}$$

where  $\rho(0)$  is the initial density matrix and  $e^{Gt}$  is the time-evolution superoperator for the density matrix.

Calculating the exponential  $e^{Gt}$  for a large number of time steps is computationally intensive, but is simplified by selecting a time-step resolution  $t_{\text{step}}$  and using an iterative process,

$$\rho_R(n * t_{\text{step}}) = (e^{G * t_{\text{step}}})^n (\rho(0) + G^{-1}K) - G^{-1}K .\tag{3.31}$$

One exponential is calculated for each selection of parameters in  $G$  (including excitation frequency  $\omega$ ), and the problem is reduced to many matrix multiplications. In addition to calculating the matrix exponential, an inverse matrix must also be calculated to solve Eq. 3.30. (These two calculations prevent a general analytic solution and consume the most computational time.) The matrix exponential is computed using the Padé approximation, and the matrix inverses are computed using Gaussian elimination with partial pivoting. The inverse of the steady-state superoperator  $G_S$  needs to be computed once for each selection of parameters, excluding the excitation frequency  $\omega$ .

The use of these techniques decreases the computation time of  $\hat{\rho}(t)$  by three orders of magnitude compared to the conventional ODE solvers that are used in previous studies [172, 173, 174]. This makes the simulation of complex distributions

possible.<sup>1</sup> For example, the distributions computed below are superpositions of 2880 separate simulations generated at a resolution that would be impractical using conventional ODE solvers on a standard personal computer. The Liouville-space technique is verified by successfully generating the uncoupled and exchange-coupled simulations previously generated using ODE solvers [172, 173]. Then the simulations obtained for dipolar-coupled pairs are corroborated by ODE-based simulations (e.g., MATLAB solver ODE113). From the simulations it is possible to describe the nature of the coupling within the pair that leads to experimentally observed spin-dependent transport and recombination processes.

### 3.4 Results and Discussion

The simulations are used to generate a representative database of different coupling strengths and Larmor separations. Specifically, dipolar coupling is discussed within the intermediate-spin-pair model to account for  $\sqrt{2}\gamma B_1$  Rabi frequencies of experimental pODMR or pEDMR data in disordered semiconductors [185, 186, 187]. However, it is found that dipolar coupling alone does not account for certain data—exchange coupling must also be included.

For each of the simulations a set of global parameters is used. Evolving  $\hat{\rho}(\tau)$  during the application of a 2  $\mu\text{s}$  excitation pulse, the observable  $Q(\tau)$  is calculated with a 4001-step resolution for a range of pulse frequencies  $\omega$ , where the range of  $\omega$  is covered with an 801-step resolution. The center frequency is chosen as  $\omega_0/2\pi = 10$  GHz (within the microwave X-band) with the Larmor separation  $\Delta\omega$  centered on this value. For all simulations we also choose a  $B_1$  strength such that  $\gamma B_1/2\pi = 10$  MHz. The rate coefficients for singlet recombination, triplet recombination, and dissociation are assigned values of  $r_S^{-1} = 1 \mu\text{s}$ ,  $r_T^{-1} = 100 \mu\text{s}$ , and  $d^{-1} = 1 \text{ms}$ , respectively. Note that for all simulations presented in this study, the singlet and triplet recombination parameters  $r_S$  and  $r_T$ , respectively, are kept at these constant values. This is done despite the expectation that, for any given pair system, these rate coefficients (which represent the transitions matrix elements for the electronic pair decay rates) also possess strong implicit dependences on the intrapair exchange

---

<sup>1</sup>The MATLAB code can be requested from the author at [limes.mark@gmail.com](mailto:limes.mark@gmail.com).

coupling  $J$ . However, this effect is not the focus of this study as it will always depend on the electronic wave function of the two pair partners and, thus, on the physical nature of any given spin-pair implementation. By keeping  $r_S$  and  $r_T$  independent of  $J$  in this simulation, the decay is assessed of the EDMR signal magnitude that is due to the exchange- and dipolar-coupling-induced shift of the spin-pair eigenstates toward the singlet/triplet basis. All scales of the EDMR signals presented in the following compare to the maximum relative intensities of entirely uncoupled spin pairs. To ensure all singlet information is recorded after the excitation, the observable (Eq. 3.17) is integrated up to a time  $t_0 = 4r_3^{-1}$ , with  $r_3$  defined in Eq. 3.19. This is done to offset the effects of the inherent signal reduction that arises as the exchange-coupling or dipolar-coupling strength is increased. The generation rate  $k$  is chosen such that the initial (steady-state) pure-triplet populations of the density matrix are approximately 0.05 ( $\rho_{11}^S(0) = \rho_{44}^S(0) \approx 0.05$  in the  $4 \times 4$  representation). All values are taken to be representative of measurement conditions that can be realized in the laboratory, following Gliesche et al. [173]. Important physical information garnered from the simulations are the relative positions and amplitudes of the Rabi frequency components  $\Omega$  and their dependence on the different coupling strengths.

### 3.4.1 Dipolar coupling only

Here the dipolar-coupling strength  $D$  is varied with respect to the Larmor separation  $\Delta\omega$ , with a negligibly small exchange interaction  $J$ . Displayed in Fig. 3.2 are simulations with Larmor separations of  $\Delta\omega/2\pi = 1$  MHz, 20 MHz, and 40 MHz; mapped against dipolar coupling strengths  $D/2\pi = 1$  MHz, 10 MHz, and 50 MHz. These are chosen as representative values of  $\Delta\omega/2\pi$  and  $D/2\pi$  (smaller, approximately equal, and larger) relative to the excitation-field strength  $\gamma B_1/2\pi = 10$  MHz. General features of these data include the resonance curves at  $\gamma B_1$ ,  $\sqrt{2}\gamma B_1$ , and  $2\gamma B_1$ , which appear variously as a function of  $\Delta\omega/2\pi$  and  $D/2\pi$ . The prominent vertical lines in Fig. 3.2(d) and (g) result from extremely long integration times compounded with the continuous rotation into “leaky” singlet states.

Weak dipolar coupling ( $D/2\pi = 1$  MHz) is shown in the top row of Fig. 3.2[(a)-(c)]; reproducing qualitative features of the weakly coupled pair discussed in Rajevac et al. [172]. (The small differences from an uncoupled pair are the result of a slight

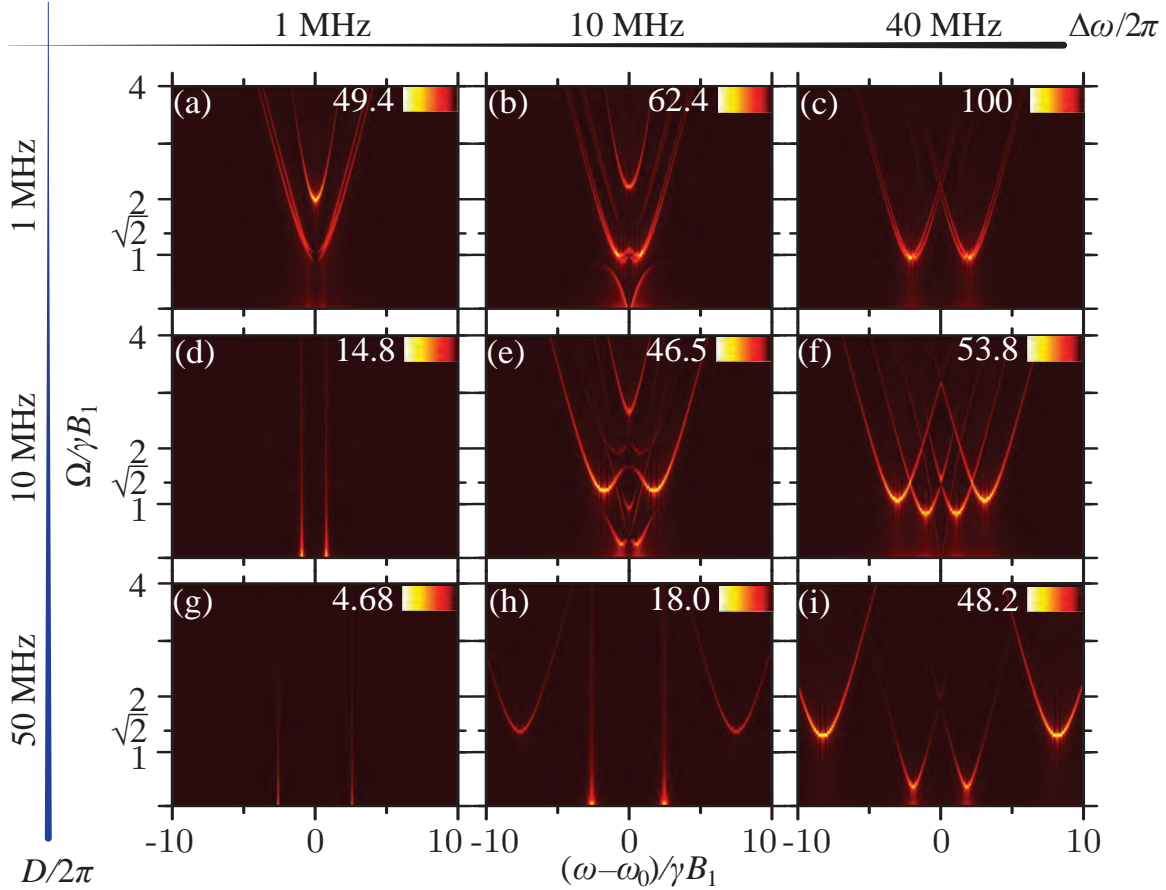


**Figure 3.2.** Plots of the Fast Fourier Transform  $\text{FFT}\{Q(\tau)\}$  of the observable  $Q(\tau)$  as a function of the excitation frequency  $\omega$ , in the regime of dipolar coupling only. The signal intensity for each plot is normalized to plot (c) and given by the number next to the color scale, which indicates the highest magnitude signal intensity in the scale for that plot. Simulations are done with Larmor separations of  $\Delta\omega/2\pi = 1$  MHz [plots (a), (d), and (g); left column],  $\Delta\omega/2\pi = 20$  MHz [plots (b), (c), and (h); center column], and  $\Delta\omega/2\pi = 40$  MHz [plots (c), (f), and (i); right column]; mapped against dipolar-coupling strengths of  $D/2\pi = 1$  MHz [plots (a)-(c), first row],  $D/2\pi = 10$  MHz [plots (d)-(f), second row], and  $D/h = 50$  MHz [plots (g)-(i), third row]. The excitation strength is  $\gamma B_1/2\pi = 10$  MHz.

splitting of the resonances caused by weak dipolar coupling.) All plots in the top row of Fig. 3.2 have on-resonance single-transition Rabi frequencies of  $\gamma B_1$ . The multiple-transition Rabi frequencies arise from simple addition and subtraction of the single-transition Rabi frequencies (see Rajevac et al. [172]). Thus a weak-dipolar regime leads to no measurable  $\sqrt{2}\gamma B_1$  Rabi frequency components. Fig. 3.2(a) has an on-resonance Rabi frequency of  $2\gamma B_1$  due to a spin-beating effect from the coherent nutation of both spins [172, 183]. Also, the intensity in Fig. 3.2(a) is approximately half that of Fig. 3.2(c); this results directly from the relative triplet/singlet content of the eigenbasis in Eq. 3.16. The (d)-(f) row of Fig. 3.2 has an intermediate-dipolar strength ( $D/2\pi = 10$  MHz =  $\gamma B_1$ ) and no strong  $\sqrt{2}\gamma B_1$  Rabi frequency components. Indeed, this  $\sqrt{2}\gamma B_1$  component is barely visible in Fig. 3.2(d), much weaker than the bright vertical lines.

Strong dipolar coupling ( $D/2\pi = 50$  MHz) is shown in the last row of Fig. 3.2. When the Larmor separation is less than the dipolar strength,  $\Delta\omega < \gamma B_1 < D$  [Fig. 3.2(g)], there is a weak nonvisible (due to bin size) transition with a  $\sqrt{2}\gamma B_1$  Rabi frequency. Both Fig. 3.2(h) and Fig. 3.2(i) show a strong  $\sqrt{2}\gamma B_1$  Rabi frequency component. Fig. 3.2(h) has a dipolar-coupling strength greater than the Larmor separation, and both are greater than or comparable to the excitation strength,  $D > (\Delta\omega \approx \gamma B_1)$ . Fig. 3.2(i) has a Larmor frequency separation and dipolar-coupling strength approximately equal, but both are greater than the excitation strength,  $(\Delta\omega \approx D) > \gamma B_1$ . Thus a Rabi frequency of  $\sqrt{2}\gamma B_1$  only occurs in the regime where dipolar-coupling strength is greater than both the Larmor separation and the excitation strength,  $D \geq \Delta\omega, D > \gamma B_1$ . The limits of this regime are discussed in Sect. 3.3.2.2.

Each column of Fig. 3.2 reflects the observable intensity getting weaker with increasing dipolar-coupling strength; this is because the spin pair is approaching a triplet-singlet energy eigenbasis. Another trend occurring down each column is the separation of the on-resonance positions increasing with dipolar-coupling strength, also demonstrated with Eq. 3.24.

Operating in a regime of strong  $\sqrt{2}\gamma B_1$  Rabi components, a more-realistic spin-pair distribution in a disordered material is generated. Indeed, many materials

with pronounced spin-selection rules are disordered semiconductors, including those for which the significance of the dipolar interaction has been discussed [185, 186, 187]. In a disordered environment, the orientation of a spin pair with respect to an applied magnetic field can be entirely random. The strengths of the dipolar fields are highly orientation dependent because of the inherently anisotropic spin-dipolar interaction, even if a fixed spin-pair distance is considered (rather than a distribution of distances). The well-known Pake distribution accounts for this random orientation [189, 190]. Fig. 3.3 is a simulation using a Pake distribution with a dipolar coupling strength of  $D/2\pi = 80$  MHz, a Larmor separation of  $\Delta\omega/2\pi = 40$  MHz, and  $J = 0$ . Fig. 3.3(a) is

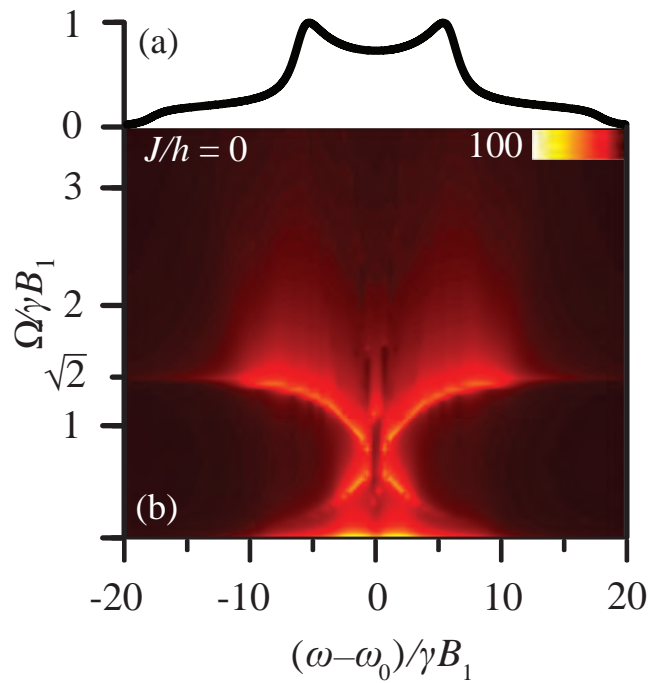


**Figure 3.3.** The strong-dipolar coupling simulation using a Pake distribution, with no exchange coupling. (a) The distribution of dipolar-coupling strengths for the simulation shown in (b). The distribution is a Pake doublet with Larmor separation  $\Delta\omega/2\pi = 40$  MHz and dipolar-coupling strength of  $D/2\pi = 80$  MHz convoluted with a Lorentzian with a half-width of 10 MHz. (b) Plot of the Fast Fourier Transform  $\text{FFT}\{Q(\tau)\}$  of the observable  $Q(\tau)$  as a function of the excitation frequency  $\omega$ . The signal intensity is normalized and given by the number next to the color scale, which indicates the highest magnitude signal intensity. The simulation uses the distribution in Fig. 3.3(a), with no exchange coupling  $J = 0$ . The excitation strength is  $\gamma B_1/2\pi = 10$  MHz.

created using a 2880-point Pake distribution convolved with a 10 MHz FWHM (full width at half max) Lorentzian function to account for power broadening due to the excitation pulse. Simulations are generated for the 2880 dipolar-coupling strengths and, using relative weights from Fig. 3.3(a), averaged to produce Fig. 3.3(b).

A comparison of Fig. 3.3(b) with experimental pEDMR and pODMR data [185, 186, 187] strongly supports the notion that the strong transitions with a Rabi frequency of  $\sqrt{2}\gamma B_1$  arise from a strong dipolar interaction. However, other characteristics of Fig. 3.3(b) do not match experimental data. The strong low-Rabi-frequency components ( $\approx 0.4\gamma B_1$ ) of Fig. 3.3(b) are not seen in pODMR of hydrogenated amorphous silicon (a-Si:H), as seen in Fig. 8 of Lips et al. [185] or Fig. 1a of Herring et al. [186]. Low Rabi-frequency components ( $\approx 0.1\text{-}0.2 \gamma B_1$ ) are seen in pEDMR of hydrogenated amorphous silicon nitride (a-SiN<sub>x</sub>:H), given in Fig. 2(e) of Lee et al. [187]. However, the same data also show a  $\sqrt{2}\gamma B_1$  Rabi frequency relatively flat with respect to excitation frequency compared to the curved shape in Fig. 3.3(b). From these discrepancies it is concluded that dipolar coupling alone cannot account for the pODMR/pEDMR data reported in the literature.

### 3.4.2 Dipolar and exchange coupling

Within the simulation, exchange coupling is now introduced between the spin pairs in addition to the dipolar coupling. The parameter space for the simulation is quickly growing; we give a small representation in Fig. 3.4.

Fig. 3.4 has plots of the Fast Fourier Transform  $\text{FFT}\{Q(\tau)\}$  of the observable  $Q(\tau)$  as a function of the excitation frequency  $\omega$ . The signal intensity for each plot is normalized to plot (a) and given by the number next to the color scale, which indicates the highest magnitude signal intensity in the scale for that plot. Simulations are done with a Larmor separation of  $\Delta\omega/2\pi = 40$  MHz. Dipolar-coupling strengths are  $D/2\pi = 0$  [plots Fig. 3.4(a),(e),(i),(m),(q), first column],  $D/2\pi = 10$  MHz [plots Fig. 3.4(b),(f),(j),(n),(r), second column],  $D/2\pi = 40$  MHz [plots Fig. 3.4(c),(g),(k),(o),(s), third column],  $D/2\pi = 80$  MHz [plots Fig. 3.4(d),(h),(l),(p),(t), fourth column]; mapped against exchange-coupling strengths of  $J/2\pi = 0$  [plots Fig. 3.4(a)-(d), first row],  $J/2\pi = 10$  MHz [plots Fig. 3.4(e)-(h), second row],  $J/2\pi = 50$  MHz

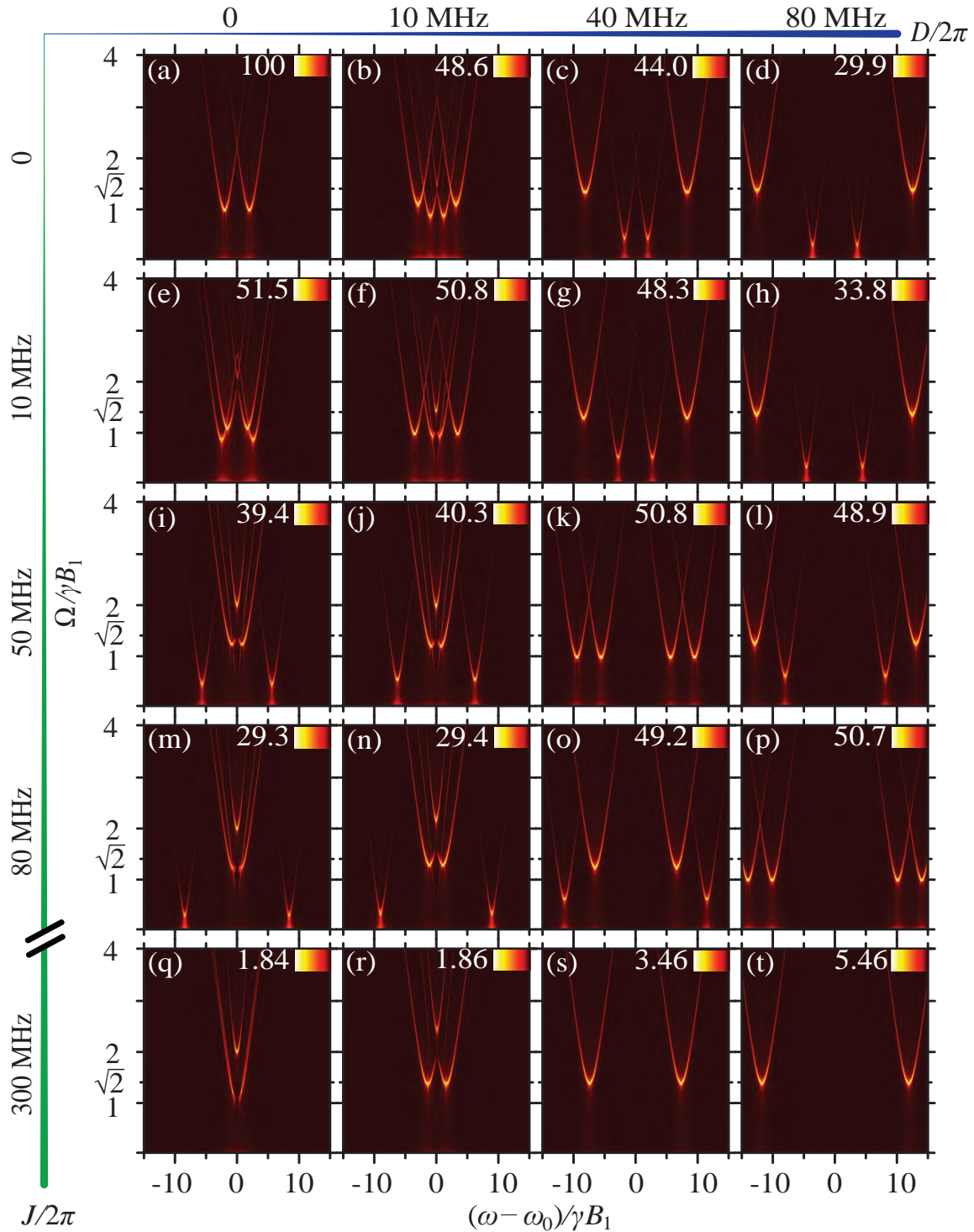


**Figure 3.4.** The results of the stochastic Liouville-space simulation with varying  $J/2\pi$  and  $D/2\pi$  are shown. (a)-(t) are the results of  $J/2\pi$  and  $D/2\pi$  varied (0-300 MHz and 0-80 MHz, respectively) with fixed  $\Delta\omega/2\pi = 40$  MHz and  $\gamma B_1/2\pi = 10$  MHz. The relative strengths are plotted on the color scale.

[plots Fig. 3.4(i)-(l), third row],  $J/2\pi = 80$  MHz [plots Fig. 3.4(m)-(p), fourth row],  $J/2\pi = 300$  MHz [plots Fig. 3.4(q)-(t), fifth row]. With the exception of Fig. 3.4(a), dipolar- and exchange-coupling strengths are chosen greater than or equal to the excitation strength  $\gamma B_1/2\pi = 10$  MHz. Fig. 3.4(a) is an uncoupled spin pair that satisfies the weak-coupling limit described in Sect. 3.3.2.1; two resonances are located at the Larmor frequencies of the electron and hole and have Rabi frequencies of  $\gamma B_1$ . The uncoupled spin pair yields the maximum relative intensity (100) in Fig. 3.4. Fig. 3.4(f) and Fig. 3.4(p) are in the effectively-weak-coupling limit also described in Sect. 3.3.2.1, where the dipolar- and exchange-coupling strengths are equal ( $J = D$ ). Fig. 3.4(k) has approximately equal dipolar- and exchange-coupling strengths with on-resonance Rabi frequencies slightly offset from  $\gamma B_1$ .

The (a)-(d) row of Fig. 3.4 is similar to the (c),(g),(k),(o),(s) column of Fig. 3.2; there is no exchange interaction present and the relative intensity of  $\text{FFT}\{Q(\tau)\}$  decreases with increasing dipolar coupling strength. The distribution in Fig. 3.3(b) can be thought of as generated from intermediate values between and including Fig. 3.4[(a)-(d)]. The sequence across the (a)-(d) row of Fig. 3.4 best illustrates the discussion in Sect. 3.3.2.2; the two  $|T_{\pm}\rangle \leftrightarrow |2\rangle$  transitions are split from the center frequency  $\omega_0$  and trend upwards to the strong dipolar-coupling limit with a  $\sqrt{2}\gamma B_1$  Rabi frequency. The two  $|T_{\pm}\rangle \leftrightarrow |3\rangle$  transitions are also split from the center frequency but are approaching their strong-coupling limit (zero Rabi frequency).

As discussed in the strong-exchange-coupling limit of Sect. 3.3.2.3, the single-transition analysis fails to account for the observed Rabi frequencies; this is explicitly seen down the (a),(e),(i),(m),(q) column of Fig. 3.4, for the two  $|T_{\pm}\rangle \leftrightarrow |3\rangle$  transitions. Indeed the observed frequencies are not  $\sqrt{2}\gamma B_1$  and 0 as would be obtained from Eq. 3.23; multiple transitions must be considered to obtain the correct values. The intricate details of the resonance positions and strengths near  $\omega - \omega_0 = 0$  with strong exchange coupling and finite dipolar-coupling strength (best seen in Figs. 3.4(j),(n), and (r)) are described analytically in Glenn et al. [176]. As shown by comparing Fig. 5 and Fig. 6 in Glenn et al. [176], these details can be predicted exactly for this regime. The (a),(e),(i),(m),(q) column in Fig. 3.4 is an extension of the simulations shown in the third column of Fig. 2 in Gliesche et al. [173], where the exchange interaction

is considered without the dipolar interaction. With increasing exchange-coupling strength the  $|T_{\pm}\rangle \leftrightarrow |2\rangle$  transitions are split further about  $\omega_0$ , while the  $|T_{\pm}\rangle \leftrightarrow |3\rangle$  on-resonance frequency positions remain unaffected. This is seen down each column of Fig. 3.4 and from Sects. 3.3.2.3 and 3.3.2.4. The role dipolar coupling plays is shown by a common trend throughout all rows of Fig. 3.4. An increase of dipolar-coupling strength creates a greater energy splitting, causing a particular transition to tend further from  $\omega_0$  and making the single-transition analysis of Eq. 3.23 valid. Therefore, a  $\sqrt{2}\gamma B_1$  Rabi frequency is present if the dipolar coupling is strong enough. From these general trends, it is determined that *only* the combination of strong dipolar and even stronger exchange (see Fig. 3.4[(r)-(t)]) yields strong  $\sqrt{2}\gamma B_1$  Rabi frequency components without any strong low-frequency ( $0-\gamma B_1$ ) components.

Using this analysis Fig. 3.5(b) is generated, which shows a distribution simulation similar to that of Fig. 3.3(b) but with a strong exchange coupling. This distribution samples from the regime where there is a large difference between exchange- and dipolar-coupling strengths with  $J > D > \Delta\omega > \gamma B_1$ ,  $J - D \gg \Delta\omega$ . Fig. 3.5(b) has a flat Rabi frequency of  $\sqrt{2}\gamma B_1$  and exhibits no strong low-Rabi-frequency components. It also exhibits some  $2\gamma B_1$  components. These same characteristics are found in the experimental data of Lips et al. [185], Herring et al. [186], and Lee et al. [187].

The pODMR data of a-Si:H in Fig. 8 of Lips et al. [185] is almost identical to Fig. 3.5(b), showing strong  $\sqrt{2}\gamma B_1$  Rabi-frequency components, weak components around  $2\gamma B_1$ , and no low-frequency components. Thus, the spin-pair model predicts that both dipolar and exchange coupling are responsible for the pODMR data of Lips et al. [185]. Moreover, the simulations show that the relative coupling strengths present in this data are in a regime with a large difference in exchange- and dipolar-coupling strengths, with  $J > D$ . This analysis supports the discussion presented in Lips et al. [185] that suggested dipolar coupling is the cause for the observed data; it further predicts that strong exchange coupling is also present.

The pODMR of a-Si:H geminate pairs in Fig. 3a of Herring et al. [186] is also very similar to the simulation in Fig. 3.5(b), with the caveat that there appears to be the presence of weakly coupled spins that produce strong  $\gamma B_1$  Rabi frequencies. In that data set, the strong transitions with a Rabi frequency of  $\sqrt{2}\gamma B_1$  are flat with

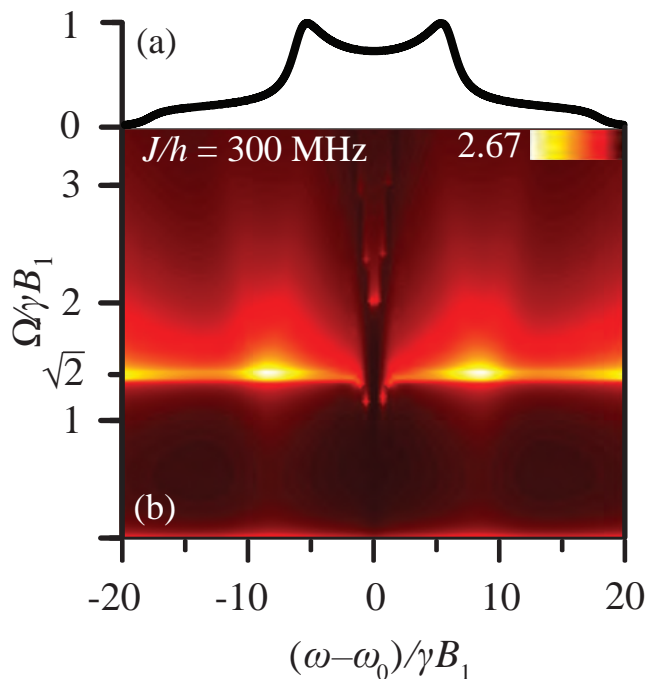


**Figure 3.5.** The strong-dipolar coupling simulation using a Pake distribution, with exchange coupling. (a) The distribution of dipolar-coupling strengths for the simulation shown in (b). The distribution is a Pake doublet with Larmor separation  $\Delta\omega/2\pi = 40$  MHz and dipolar-coupling strength of  $D/2\pi = 80$  MHz convoluted with a Lorentzian with a half-width of 10 MHz. (b) Plot of the Fast Fourier Transform  $\text{FFT}\{Q(\tau)\}$  of the observable  $Q(\tau)$  as a function of the excitation frequency  $\omega$ . The signal intensity is normalized to Fig. 3.3(b) and given by the number next to the color scale, which indicates the highest magnitude signal intensity. The simulation uses the distribution in Fig. 3.5(a), with an exchange-coupling strength of  $J/2\pi = 300$  MHz. The excitation strength is  $\gamma B_1/2\pi = 10$  MHz.

respect to excitation frequency but become abruptly weaker; this is characteristic of the Pake distribution in Fig. 3.5(b), which also has a strong  $\sqrt{2}\gamma B_1$  component becoming abruptly weaker at an excitation frequency of  $(\omega - \omega_0)/\gamma B_1 = 10$ . These experimental data also have no lower-Rabi-frequency components ( $0-\gamma B_1$ ), which is shown to be a defining characteristic of the regime in which there is a large difference in exchange- and dipolar-coupling strengths with  $J > D$ . Therefore, it is determined that the geminate pairs show the characteristics of weakly coupled pairs mixed with strongly dipolar-coupled pairs as discussed in Herring et al. [186], with the additional prediction of the presence of a strong exchange coupling.

Finally, the pEDMR data in Fig. 3e of Lee et al. [187] show broad  $\sqrt{2}\gamma B_1$  Rabi frequency components and weak  $\gamma B_1$  Rabi frequency components. Again, this could be characteristic of a resonance involving mostly uncoupled pairs and some strong exchange- and dipolar-coupled pairs. However, the presence of both strong dipolar and exchange coupling cannot explain the strong low-frequency (approximately  $0.2\gamma B_1$ ) components present in the Lee et al. [187] data. Perhaps the curvature leading to the  $\sqrt{2}\gamma B_1$  limit seen in Fig. 3.3 cannot be seen in the Lee et al. [187] data because of a low number of dipolar-coupled pairs. However, if the strong low-frequency components are due to strong dipolar coupling alone, it is expected (from Fig. 3.3) that the  $\sqrt{2}\gamma B_1$  component would be as strong as the low-frequency component, and the data does not have this feature. Therefore the conclusion is that dipolar-coupled pairs can explain the  $\sqrt{2}\gamma B_1$  Rabi frequencies in the a-SiN<sub>x</sub>:H data presented in Lee et al. [187], but whether exchange is present cannot be confirmed or rejected due to the weak signal strength of the strongly coupled pairs relative to the uncoupled pairs in that data.

### 3.5 Summary and Conclusion

Numerical and analytical methods are used to investigate the role of the dipolar interaction for electrically and optically detected Rabi oscillation frequencies of intermediate-spin-pair systems. A general description of the physics of pEDMR and pODMR transient-nutation experiments was given that includes dipolar and exchange interactions, the Larmor separations within the intermediate pairs, and the excitation-field strength. An intermediate-spin-pair model is presented that corroborates previous numerical studies that included weakly coupled pairs only [183, 172] and exchange-coupled pairs only [173]. The model also supports experimental studies that attributed the observation of  $\sqrt{2}\gamma B_1$  Rabi-frequency components with pODMR/pEDMR of disordered semiconductors [185, 186, 187] to the presence of strong dipolar coupling within the spin-pair model. It is shown that pODMR data of a-Si:H presented in Lee et al. [185] and Herring et al. [186] can be explained within an intermediate-pair model in the regime of strong dipolar coupling and stronger exchange coupling,  $(J - D)^2 \gg \Delta\omega^2$ ,  $J > D > \Delta\omega > \gamma B_1$ .

# CHAPTER 4

## LOW-FREQUENCY MODULATION OF LONGITUDINAL FIELD: MODIFIED RABI ENVELOPES

*A Rabi cacophony.*

### 4.1 Introduction

The sensitivity of Rabi oscillations to low-frequency modulation (5-100 kHz) of the static longitudinal magnetic field  $B_0$  is studied [191]. Three regimes are considered: strong modulation (compared to the driving field strength  $B_1$ , 1-10 G), fast modulation (compared to the non-modulated Rabi frequency  $\Omega_R$ ), and weak-resonant modulation. The mapping of a weakly driven two-level system with modulation onto a strongly driven system without modulation suggests that different regimes of spin dynamics, previously known for a strongly driven system (i.e., multiphoton resonances [192, 193, 194]), are realized under easily accessible conditions with proper choice of modulation frequency and amplitude. The experiments are straightforward to achieve in the laboratory, but can be mapped to more unconventional NMR conditions where  $B_1$  strength is much greater than  $B_0$ .

In the extreme limit of strong-modulation regime, the longitudinal field is essentially swept into and out of resonance, but the analytical derivation remains valid for achievable experimental conditions. Fast-strong modulation emulates the regime of a driving frequency  $\omega$  much larger than the resonant frequency  $\gamma B_0$  and  $B_1$  strength much greater than  $B_0$ . Similar to experimental results in atomic physics, an effectively shorter magnetic moment is created (from averaging due to the fast-modulating field) that causes a slowing of the Rabi frequency. Additional corrections are required when using a strong modulation strength, and are also seen experimentally. Weak-resonant modulation gives rise to an envelope of the Rabi oscillations. The shape of this

envelope is highly sensitive to the detuning of  $\omega$  and strength of modulation field, where a departure from the nonmodulated Rabi oscillation is seen and fitted using a function derived from Floquet analysis [195]. The weak modulation strength allows for a second rotating-wave approximation (RWA) to a doubly rotating frame called the Rabi frame.

The following contains a brief description of theoretical results found in Glenn et al. [191] and description of the Rabi frame, along with a thorough description of the experimental techniques and results that confirm theoretical predictions.

## 4.2 Theoretical

### 4.2.1 Description of three limiting regimes

There are three regimes discussed in Glenn et al. [191] that are briefly summarized in this section—the fast-modulation regime, the strong-slow regime, and the weak-resonant regime. The system studied is a two-level spin system undergoing a double excitation; one is a low-frequency excitation parallel to a quantizing magnetic field  $B_0$ , and the other is a conventional resonance of the Zeeman split  $\Delta_z$  using a field oscillating perpendicular to  $B_0$ . After taking a rotating-wave approximation (RWA), the time evolution of the amplitudes  $D_{+\frac{1}{2}}$  and  $D_{-\frac{1}{2}}$  of the two spin orientations is given by the equations

$$i\dot{D}_{\pm\frac{1}{2}} = \pm\frac{\delta + \varepsilon(t)}{2}D_{\pm\frac{1}{2}} + \frac{\Omega_R}{2}D_{\mp\frac{1}{2}}. \quad (4.1)$$

Here,  $\delta = \Delta_z - \omega$ , where  $\omega$  is the frequency of the excitation along the  $\hat{\mathbf{x}}$ -axis,  $\Omega_R$  is the on-resonance Rabi frequency  $\Omega_R = g\mu_0 B_1$ , and  $\varepsilon(t)$  is the modulation along the  $\hat{\mathbf{z}}$ -axis. With  $\varepsilon(t) = 0$  and assuming the upper Zeeman level is completely unoccupied at  $t = 0$  ( $P_{+\frac{1}{2}}(0) = 0$ ), the well-known Rabi result [196, 197] is recovered,

$$P_{+\frac{1}{2}}(t) = \frac{\Omega_R^2}{\omega_0^2} \sin^2 \frac{\omega_0 t}{2}, \quad (4.2)$$

where  $\omega_0 = \sqrt{\delta^2 + \Omega_R^2}$ . From the two equations in 4.1, a simple elimination of variables is completed, an excitation of  $\varepsilon(t) = \varepsilon_m \cos(\omega_m t)$  is assumed, and the limits corresponding to the three different regimes are taken.

The first regime considered is the fast-modulation regime, where  $\omega_m \gg \Omega_R$ , by making the substitutions

$$\bar{D}_{\pm\frac{1}{2}} = D_{\pm\frac{1}{2}}(t)e^{\mp\frac{i\varepsilon_m}{2\omega_m}\sin\omega_m t}. \quad (4.3)$$

For a sufficiently weak modulation field  $\varepsilon_m$ , a result commonly found in atomic physics literature [198, 199] is obtained,

$$P_{+\frac{1}{2}}(t) = \sin^2\left(\frac{\Omega_R}{2}J_0\left(\frac{\varepsilon_m}{\omega_m}\right)t\right), \quad (\text{Eq. 24}) \quad (4.4)$$

where  $J_0(x)$  is a zero-order Bessel function. Matching with Glenn et al. [191], Eq. 4.4 is referred to as Eq. 24. For a sufficiently strong modulation field, corrections to Eq. 24 manifest (the following equations are also referenced to Glenn et al. [191]). Written in terms of  $\bar{D}_{+\frac{1}{2}}$ , the correction is the second term in

$$\begin{aligned} \bar{D}_{+\frac{1}{2}} = & -i \sin\left(\frac{\Omega_R}{2}J_0\left(\frac{\varepsilon_m}{\omega_m}\right)t\right) \\ & - \frac{i\Omega_R}{2\omega_m} \int_0^{\omega_m t} d\phi \left[ e^{-\frac{i\varepsilon_m}{\omega_m}\sin\phi} - J_0\left(\frac{\varepsilon_m}{\omega_m}\right) \right] \cos\eta\phi, \quad (\text{Eq. 25}) \end{aligned} \quad (4.5)$$

where  $\eta = \frac{\Omega_R}{2\omega_m}J_0\left(\frac{\varepsilon_m}{\omega_m}\right)$ . Thus, with stronger modulation strength  $\varepsilon_m$ , the more the corrections will affect the shape of the Rabi envelope.

The second regime is the strong-slow regime,  $\varepsilon_m \gg \Omega_R \gg \omega_m$ . The predictions in this regime are good for time intervals near

$$t = t_k = \left(\frac{\pi}{2} + \pi k\right)\omega_m^{-1}, \quad (4.6)$$

when  $\varepsilon(t)$  passes through zero. This regime yields the second-order differential equation

$$\ddot{D}_{+\frac{1}{2}} + \left[ i\frac{\varepsilon_m\omega_m}{2} + \frac{\varepsilon_m^2\omega_m^2 t_1^2 + \Omega_R^2}{4} \right] D_{+\frac{1}{2}} = 0. \quad (4.7)$$

Defining a characteristic time  $\tau = (\varepsilon_m\omega_m)^{-1/2}$  and a parameter  $\nu = -i\Omega_R^2/(4\varepsilon_m\omega_m)$ ,  $P_{+\frac{1}{2}}(t_1)$  can be cast in terms of parabolic cylinder functions,  $\mathcal{D}_\nu$  [200], as

$$P_{+\frac{1}{2}}(t_1) = \frac{1}{4 \sinh\left(\frac{\pi|\nu|}{2}\right)} \left| \mathcal{D}_\nu\left(e^{\frac{\pi i}{4}}\frac{t_1}{\tau}\right) - \mathcal{D}_\nu\left(-e^{\frac{\pi i}{4}}\frac{t_1}{\tau}\right) \right|^2. \quad (\text{Eq. 36}) \quad (4.8)$$

Interestingly, the saturation value of  $P_{+\frac{1}{2}}(t_1)$  for  $t_1 \gg \tau$  is found to be

$$P_{+\frac{1}{2}}(\infty) = \frac{1 - e^{-\pi|\nu|}}{2}. \quad (\text{Eq. 37}) \quad (4.9)$$

Thus, as either the driving frequency  $\omega_m$  or excitation strength  $\varepsilon_m$  becomes larger, the saturation level lowers.

The final regime considered is the weak-resonant regime,  $\omega_m \approx \Omega_R$ ;  $\varepsilon_m \ll \Omega_R$ . Here, Floquet analysis [195] is used to derive an on-resonance ( $\omega = \Delta_z$ ) prediction of the probability to be in the  $+1/2$  state,

$$\begin{aligned}
 P_{+1/2} = & \frac{1}{\kappa^2 + 1} \left[ \sin^2 \left( \frac{\Omega_R}{2} + \frac{\varepsilon_m}{4} \kappa \right) t \right. \\
 & + \frac{\kappa}{2(\sqrt{\kappa^2 + 1} - \kappa)} \sin^2 \left( \frac{\Omega_R}{2} + \frac{\varepsilon_m}{4} (\kappa - \sqrt{\kappa^2 + 1}) \right) t \\
 & \left. - \frac{\kappa}{2(\sqrt{\kappa^2 + 1} + \kappa)} \sin^2 \left( \frac{\Omega_R}{2} + \frac{\varepsilon_m}{4} (\kappa + \sqrt{\kappa^2 + 1}) \right) t \right]. \quad (\text{Eq. 44})
 \end{aligned}
 \tag{4.10}$$

Here,  $\kappa = 2(\omega_m - \Omega_R)/\varepsilon_m$  is a dimensionless factor introduced for convenience. The maximum modulation will occur when  $\kappa = 1$ . A so-called “nontrivial feature” occurs with exactly  $\omega_m = \Omega_R$ ; when  $\kappa = 0$ , the Rabi oscillations are unaffected by the modulation. This nontrivial feature, as well as the description of the maximum modulation are understood by a two-level, doubly rotating-frame Bloch-sphere picture shown in Fig. 4.1.

### 4.2.2 Rabi frame

To better understand the doubly rotating-frame Bloch-sphere picture, or Rabi frame, a typical Rabi oscillation viewed in the Rabi frame is useful to picture. In Fig. 4.1(a), a standard nonrotating frame picture of the on-resonant  $B_1$  excitation ( $\omega = \Delta_z$ ) and its effect on the magnetization  $\mathbf{M}$  is shown. Note that the rotating-wave approximation (RWA) has already been made in the first diagram. Recall the quantizing  $B_0$  field is much larger than all field involved in this approximation. As the  $B_1$  excitation field rotates around the  $\hat{\mathbf{z}}$ -axis, the magnetization  $\mathbf{M}$  is nutated. After making a transformation into the frame rotating about the  $\hat{\mathbf{z}}$ -axis by a frequency  $\omega = \Delta_z$ , the effect of the on-resonant  $B_1$  excitation is seen clearly in the rotating-frame Bloch sphere (RFBS, with a purple Bloch sphere in Fig. 4.1). The  $B_1$  excitation is considered static along the rotating  $\hat{\mathbf{x}}'$ -axis, and, because the effect of the  $B_0$  field has been transformed away in this rotating frame, the torque on the magnetization  $\mathbf{M}$  is solely due to  $B_1$ . In this way, the effect of the  $B_1$  excitation is clearly seen, and the Rabi oscillation is easily viewed as the magnetization nutating around the

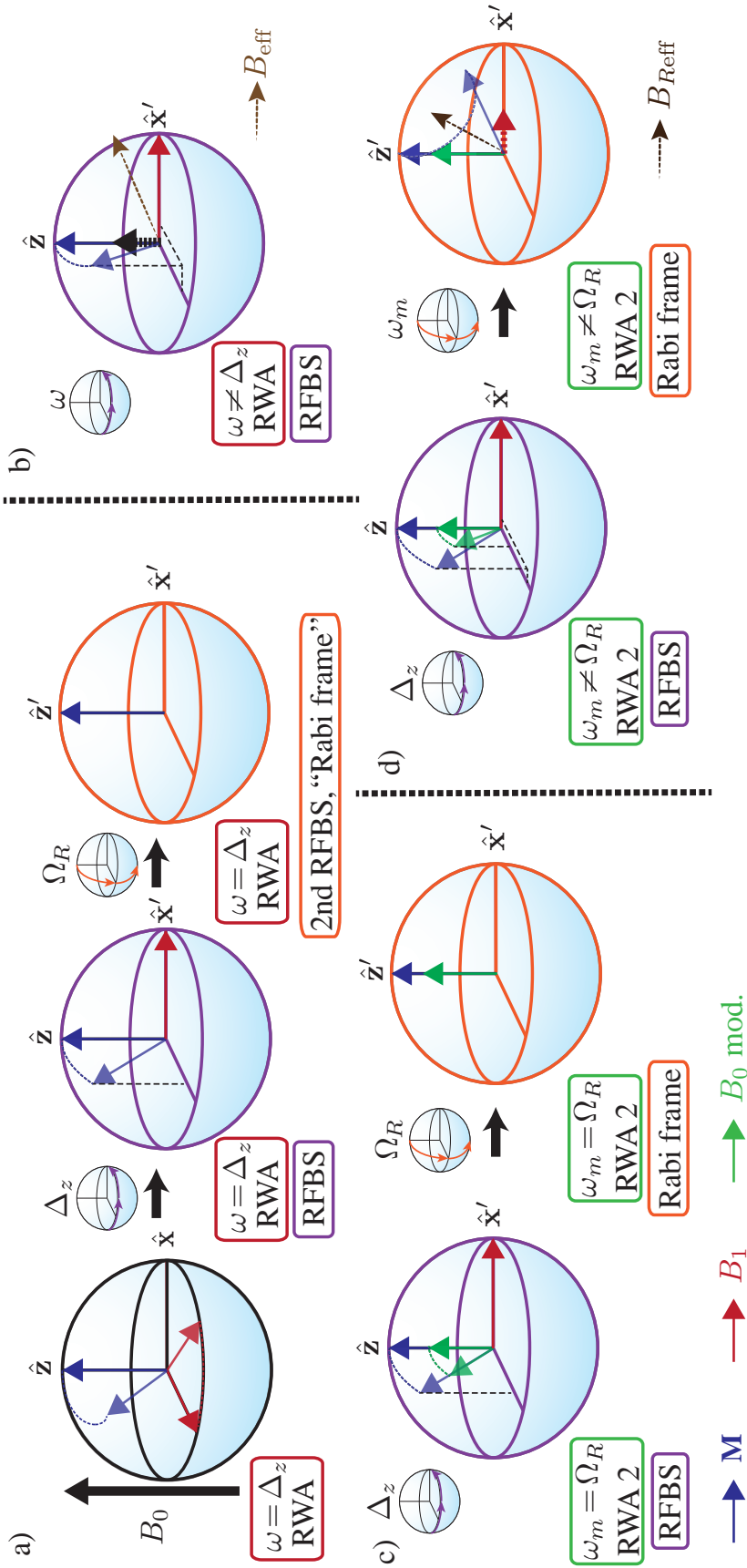


**Figure 4.1.** Demonstration of the Rabi-frame Bloch sphere picture. (a) A demonstration of an on-resonant ( $\omega = \Delta_z$ ) excitation in a doubly rotating-frame Bloch sphere (RFBS) called the Rabi frame. Note the use of the rotating-wave approximation (RWA). (b) Recall the RFBS picture of a slightly detuned excitation ( $\omega \neq \Delta_z$ ), where there is a remnant effective field along the  $\hat{z}$ -axis that results in the rotation of the magnetization  $\mathbf{M}$  around a total effective field  $B_{\text{eff}}$ . (c) A second RWA is made for the modulation field and its result in the Rabi frame is shown for  $\omega_m = \Omega_R$ , and the nontrivial feature of an unaffected Rabi oscillation is seen. (d) The more general case of  $\omega_m \neq \Delta_z$  is seen, where a direct analogy to (b) can be made and a Rabi frame effective field  $B_{\text{Reff}}$  makes the effect of the modulation explicit.

$\hat{\mathbf{x}}'$ -axis. For purely demonstrative purposes, now make a superfluous rotation about the rotating  $\hat{\mathbf{x}}'$ -axis at the Rabi frequency  $\Omega_R$ . In this second RFBS (denoted with an orange Bloch sphere in Fig. 4.1), called the Rabi frame, the  $B_1$  field has now also been transformed away, and there is no field to torque the magnetization  $\mathbf{M}$  in this frame. Thus, in the Rabi frame,  $\mathbf{M}$  will simply remain static along the new  $\hat{\mathbf{z}}'$ -axis for an on-resonant  $B_1$  excitation ( $\omega = \Delta_z$ ).

Fig. 4.1(b) shows the result of a detuned  $B_1$  excitation ( $\omega \neq \Delta_z$ ) in the RFBS. This is a standard textbook result that allows one to easily visualize the effect of an off-resonance pulse. The detuned pulse  $\omega$  leads to a frame rotating at the excitation frequency  $\omega$ , which causes the quantizing  $B_0$  field to not be completely transformed away (unlike the completely transformed away  $B_0$  field in Fig. 4.1(a)). This remnant effective  $B_0$  field in the rotating frame adds to the static  $B_1$  field along the  $\hat{\mathbf{x}}'$ -axis, leading to a total effective field  $B_{\text{eff}}$  that the magnetization  $\mathbf{M}$  is nutated about. In this way, the effect of an off-resonance pulse on the Rabi oscillation is seen, and it is clear that a complete nutation from a  $|+1/2\rangle$  state along the  $\hat{\mathbf{z}}$  direction to a  $|-1/2\rangle$  state along the  $-\hat{\mathbf{z}}$  direction is *not* obtained.

The addition of the longitudinal modulation  $\varepsilon_m \cos \omega_m t$ , when  $\omega_m = \Omega_R$ , is seen in Fig. 4.1(c). Here, a second RWA is made for the modulation field, which is valid in the regime where  $\varepsilon_m \ll \Omega_R$ , just as the first RWA is valid when  $B_1 \ll B_0$ . Thus, the green vector in Fig. 4.1(c) that represents the  $B_0$  modulation strength is exactly half of the field produced by the coil, leading to a modulation strength of  $\varepsilon_m/2$ . In the on-resonant ( $\omega = \Delta_z$ ) RFBS, it is clear that the longitudinal modulation field caused by  $\varepsilon_m$  remains parallel to the magnetization  $\mathbf{M}$ . In the same picture transformed to the Rabi frame rotating at the Rabi frequency  $\Omega_R$ , both the magnetization  $\mathbf{M}$  and modulation field remain static along the  $\hat{\mathbf{z}}'$ -axis. Hence, the nontrivial behavior of a nonaffected Rabi oscillation when  $\omega_m = \Omega_R$ , or  $\kappa = 0$ , is easily seen in the Rabi frame description of the problem. Because  $\mathbf{M}$  and the modulation field under a second RWA are always parallel, the modulation field causes no torque on  $\mathbf{M}$  and has no effect on the Rabi oscillation. Although, this constantly parallel action is, in essence, a case of spin locking, a widely used technique throughout NMR.

Finally, Fig. 4.1(d) shows the RFBS and Rabi frame description of a longitudinal

modulation frequency that is not equal to the Rabi frequency ( $\omega_m \neq \Omega_R$ ), as well as an on-resonant  $B_1$  excitation ( $\omega = \Delta_z$ ). The effect is somewhat confusing in the RFBS description, as the magnetization  $\mathbf{M}$  rotates around the summation of the static  $B_1$  field along  $\hat{\mathbf{x}}'$  and the rotating green vector that represents the modulation field; this is a very nonintuitive description that is reminiscent of the laboratory-frame diagram in Fig. 4.1(a). If the transformation to the Rabi frame rotating with a frequency of  $\omega_m$  is made, then the situation is analogous to the RFBS description of the off-resonant, nonmodulated excitation shown in Fig. 4.1(b). In Fig. 4.1(d), the  $B_1$  field is not completely transformed away, leaving an effective field due to the  $B_1$  pulse along the  $\hat{\mathbf{x}}'$ -axis. The remnant effective  $B_1$  field adds to the static longitudinal modulation field along the  $\hat{\mathbf{z}}'$ -axis, combining for a total effective field  $B_{\text{Reff}}$  that the magnetization  $\mathbf{M}$  is torqued about. Therefore, the envelope to the Rabi oscillation caused by the longitudinal modulation can be viewed from the path  $\mathbf{M}$  takes in the Rabi frame. Moreover, this model retains quantitative accuracy much like the RFBSs in Fig. 4.1(a) and (b). As an example let us consider the case of maximum modulation, where the beats in the Rabi frequency are most pronounced—this corresponds to a  $B_{\text{Reff}}$  that is  $45^\circ$  between  $\hat{\mathbf{x}}'$  and  $\hat{\mathbf{z}}'$  and in the  $\hat{\mathbf{x}}'$ - $\hat{\mathbf{z}}'$  plane. In this situation, the magnetization is rotated completely along the  $\hat{\mathbf{x}}'$  direction and returned to the  $\hat{\mathbf{z}}'$ -axis. Quantitatively, this corresponds to the green and red vectors in Fig. 4.1(d) being exactly equal—this means  $\varepsilon_m/(2\gamma) = (\omega_m - \Omega_R)/\gamma$ , or  $2(\omega_m - \Omega_R)/\varepsilon_m = 1$ . Recall that the theoretical predictions required maximum modulation for exactly this situation,  $\kappa = 1$ . Thus, the use of this conceptual picture is clear; with the Rabi-frame description, the intricacies of the evolution of the spin system are easily visualized.

## 4.3 Experimental

### 4.3.1 Methods

The introduction of the longitudinal modulation field  $\varepsilon(t)$  to investigate the general behavior of Rabi oscillations is highly compatible with conventional experimental NMR methods of inductive detection in thermally generated spin ensembles. For the large  $B_0$  field generally required to achieve sufficient signal-to-noise ratio (SNR), the condition  $B_1 \ll B_0$  is hard to avoid, but an additional small-amplitude modulation

parallel to  $B_0$  is easily realized below. The three regimes elucidated in Sect. 4.2.1 are explored using straightforward NMR of protons in water (gyromagnetic ratio ( $g_H\mu_N = \gamma = 4.25775$  kHz/G, where  $\mu_N$  is the nuclear magneton). The only additional precaution is to ensure a stable and highly homogeneous RF driving field  $B_1$  across the sample, so that Rabi oscillations can be observed over many periods. All experiments are performed in a horizontal-bore, 2-Tesla superconducting magnet (Oxford Instruments). A conventional solenoidal single-coil transmit/receive probe (5 turns, 1 cm diam and 2.5 cm long) is series tuned with a capacitor to the proton Zeeman resonance at 88.8 MHz. A 50- $\Omega$  resistor in series with the elements provides a matching impedance to the transmit and receive amplifiers. This “low-Q” probe sacrifices SNR for a robust a flat frequency response that is required due to the accompanying modulation field [79, 125]. The modulation field is provided by a 5-cm-radius Helmholtz pair (coaxial with the main  $B_0$  field) that is wound on a form that has the probe coil at its center (see Fig. 4.2(a)) (designed and built by Rachel Glenn and Zayd Ma). The water sample is centered in the two coils, and occupies roughly 25% of the  $B_1$  coil volume; it is contained in a small PTFE tube, which provides a closer magnetic-susceptibility matching to water than that of borosilicate glass. The low filling factor and PTFE tube both serve to increase  $B_1$ -field homogeneity across the sample area. An NMR spectrometer (Tecmag Redstone, model HF2-1RX) with two independent transmission channels is used to transmit pulses to both the 88.8 MHz proton probe and the 0-100 kHz modulation coils, and subsequently to acquire and digitize the free-induction-decay (FID) signal generated in the probe coil. (An interesting twist on the use of this experimental apparatus would be to detect Rabi oscillations directly with a 0-100 kHz probe.) The  $B_1$  RF pulse is amplified with a 2kW amplifier (Tomco model BTO2000-AlphaSA) conventionally designed for solid-state NMR, but whose high output power allowed the coherent nutation of the proton spins through many Rabi-oscillation periods in a fairly short pulse time. The  $B_0$ -modulation pulse is provided by a DC-50 kHz amplifier normally used for gradient coils in imaging applications (Techron AN7780); the inductance of the Helmholtz pair is matched to the specifications of the gradient amplifier in order to minimize ring-down and associated cross-talk to the NMR coil. Although the DC-50

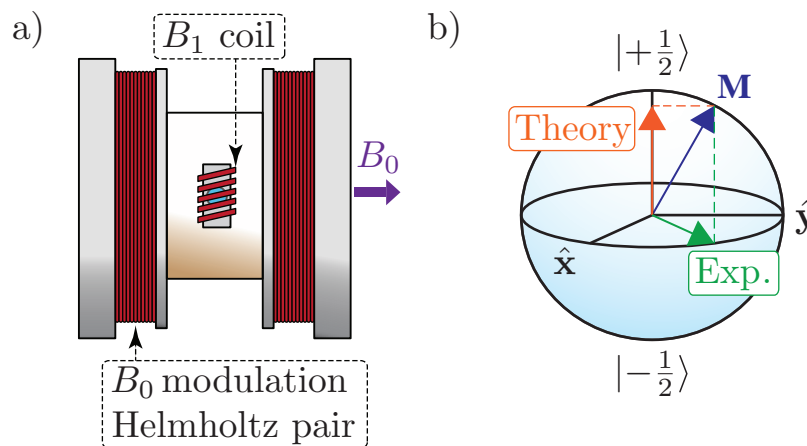


**Figure 4.2.** A schematic of the NMR probe and a graphical description of theoretical predictions and experimental NMR data. (a) A schematic of the NMR probe used in the experiments. A traditional NMR coil ( $B_1$ ) is accompanied by a  $B_0$  modulation Helmholtz pair that is coaxial with the  $B_0$  field. (b) Graphical description of the relation between theoretical predictions and experimental NMR data. The theoretical predictions have the magnetization  $\mathbf{M}$  projected onto the  $\hat{z}$ -axis of the Bloch sphere. The experimental data are the projection of the magnetization onto the  $\hat{x}$ - $\hat{y}$  plane of the Bloch sphere. Eq. 4.11 relates the theory to experiment.

kHz amplifier is also used for the 50-100 kHz frequency range, the roll-off in applied power is well documented and moreover, consistent from pulse-to-pulse. Transverse relaxation ( $T_2^*$ ) caused by remaining inhomogeneity in the magnetic fields are seen in the following data by the overall decay of the nonmodulated signal after many Rabi oscillations.

The FID signals are acquired on resonance ( $\delta = 0$ ) and single-shot (no signal averaging); in Sect. 4.3.2, with the data presented as FID signal strength vs.  $B_1$  pulse length. Each data point displayed is the result of examining the corresponding FID to determine the magnitude of the transverse magnetization at a fixed time delay ( $\approx 0.2$  ms) from the end of the  $B_1$  RF pulse (it is shown that the integral under the curve of Fourier-transformed FID produces the same results, within error). The  $B_1$  and modulation pulses are essentially applied simultaneously, with the modulation pulse nominally starting at  $\varepsilon(t) = 0$  just as the  $B_1$  pulse starts. It is assumed that the  $B_1$ -pulse amplitude is fixed and the pulse length is linearly related to the nutation angle of the proton spins. Because of slight transient changes in power delivered by the RF amplifier at the very beginning of the  $B_1$  pulse (minimized by using a

low-Q probe), this linear relationship is most accurately observed for longer pulse times. Indeed,  $\Omega_R$  is determined experimentally using nonmodulated data, where the average of frequency of the late-time oscillations is taken. With this caveat, the plots shown below represent Rabi oscillations in the three modulation regimes of interest. To decrease the overall data acquisition time, the water sample contained dissolved copper sulfate ( $\text{CuSO}_4$ ) to reduce the longitudinal relaxation time  $T_1$  to  $\approx 100$  ms. This decreases the standard wait-time between pulses, which is at least several time  $T_1$  to allow the magnetization to recover to its thermal-equilibrium value. Intrinsic transverse relaxation (characterized by  $T_2$ ) is typically on the order of  $T_1$  in weakly interacting liquids. Transverse decoherence caused by residual inhomogeneity (characterized by  $T_2^* < T_2$ ) in the  $B_1$  field, which manifests most clearly in the data as the overall decay of the nonmodulated Rabi oscillations after many characteristic periods.

Note that the predictions made in Sect. 4.2.1 are formulated in terms of the projection of the magnetization onto the  $\hat{\mathbf{z}}$ -axis of the Bloch sphere (see Fig. 4.2(b)). Rabi oscillations occur between the high- and low-energy states defined by  $B_0$ , where the low-energy state has magnetization parallel to  $B_0$ . However, the observable in a conventional NMR experiment is the projection of the magnetization onto the  $\hat{\mathbf{x}}\text{-}\hat{\mathbf{y}}$  plane of the Bloch sphere. Noting also that the initial conditions at time  $t = 0$  for our predictions have  $P_{+\frac{1}{2}} = 0$ , whereas the experiments have  $P_{+\frac{1}{2}} = 1$ , a simple transformation of the  $\hat{\mathbf{z}}$ -axis prediction to the  $\hat{\mathbf{x}}\text{-}\hat{\mathbf{y}}$  plane can be accomplished by

$$P_{\perp} = \sin \left[ \arccos(2P_{+\frac{1}{2}} - 1) \right] = 2\sqrt{P_{+\frac{1}{2}} - P_{+\frac{1}{2}}^2}. \quad (4.11)$$

The experimentally measured transverse magnetization data are represented by  $P_{\perp}$  and then are compared to theory by transforming the predictions according to Eq. 4.11. The initial peak of the nonmodulated Rabi-oscillation data, which appear in black in each figure, is used to define  $P_{\perp} = 1$  and to normalize the corresponding data.

### 4.3.2 Results and discussion

The first regime experimentally confirmed is the fast-modulation regime,  $\omega_m \gg \Omega_R$ , which gives two predictions that are tested: the first, detailed with Eq. 24, is that the Rabi frequency  $\Omega_R$  is altered for a fast modulation regardless of modulation

strength; the second, detailed with Eq. 25, is sufficiently strong modulation  $\epsilon_m$  will cause higher-order corrections to Eq. 24 to manifest. The picture in the “rotating frame” that results from the application of the RWA, is that of an average nutation of the magnetization in the  $\hat{y}$ - $\hat{z}$  plane, superimposed with much faster wiggles, which for small modulation amplitudes are transverse the  $\hat{y}$ - $\hat{z}$  plane. For larger modulation amplitudes, the wiggles move the magnetization appreciably along the surface of the Bloch sphere, giving rise to a time-average decrease in the component of the magnetization that is in the  $\hat{y}$ - $\hat{z}$  plane and subject to a torque generated by  $B_1$ . This leads directly to the slowing down of the Rabi nutation expressed by Eq. 24. A similar effect is seen with experiments in atomic physics where a spin-1/2 atomic state is coupled to a high-frequency RF field [198, 199]; a way to visualize this is the magnetic moment of the spin is averaged to create an effectively smaller magnetic moment. The wiggles also lead to the fast modulation component at  $\omega_m$ , expressed in Eq. 25, that is superimposed on the slowed-down Rabi oscillations. Fig. 4.3(a) demonstrates that the corresponding experiments are sensitive to even the small decrease in the effective Rabi frequency  $\Omega_R J_0(\epsilon_m/\omega_m)$  that appears for weak modulation. These data are fit with Eq. 24, multiplied by a decaying exponential that accounts for the  $T_2^*$  decay, which is primarily due to the magnetic field inhomogeneities from the  $B_1$  coil. The Rabi frequency  $\Omega_R$  and modulation amplitude  $\epsilon_m$  are experimentally determined, respectively, by examining the nonmodulated data and by measuring the current through the modulation coils. The early-time, fast-modulation data appears to follow the nonmodulated data; however, as the pulse length and number of Rabi cycles increase, the slight decrease of the effective Rabi frequency  $\Omega_R J_0\left(\frac{\epsilon_m}{\omega_m}\right)$  caused by fast-modulation becomes apparent. Thus, the prediction from Eq. 24 accurately describes the frequency components of the spin system undergoing fast-modulation.

Fig. 4.3(b) shows data in the regime of strong-fast modulation  $\epsilon_m, \omega_m \gg \Omega_R$ , where corrections found in Eq. 25 become apparent. As predicted, the slowing-down effect on the Rabi oscillations now becomes more pronounced, and the small modulation at frequency  $\omega_m$  described by Eq. 25 rides on top of the envelope given by Eq. 24. A peculiar effect seen in the data and predicted in the theory is the leveling-off of the magnetization near a  $90^\circ$  flip angle, where the magnetization remains pinned on the

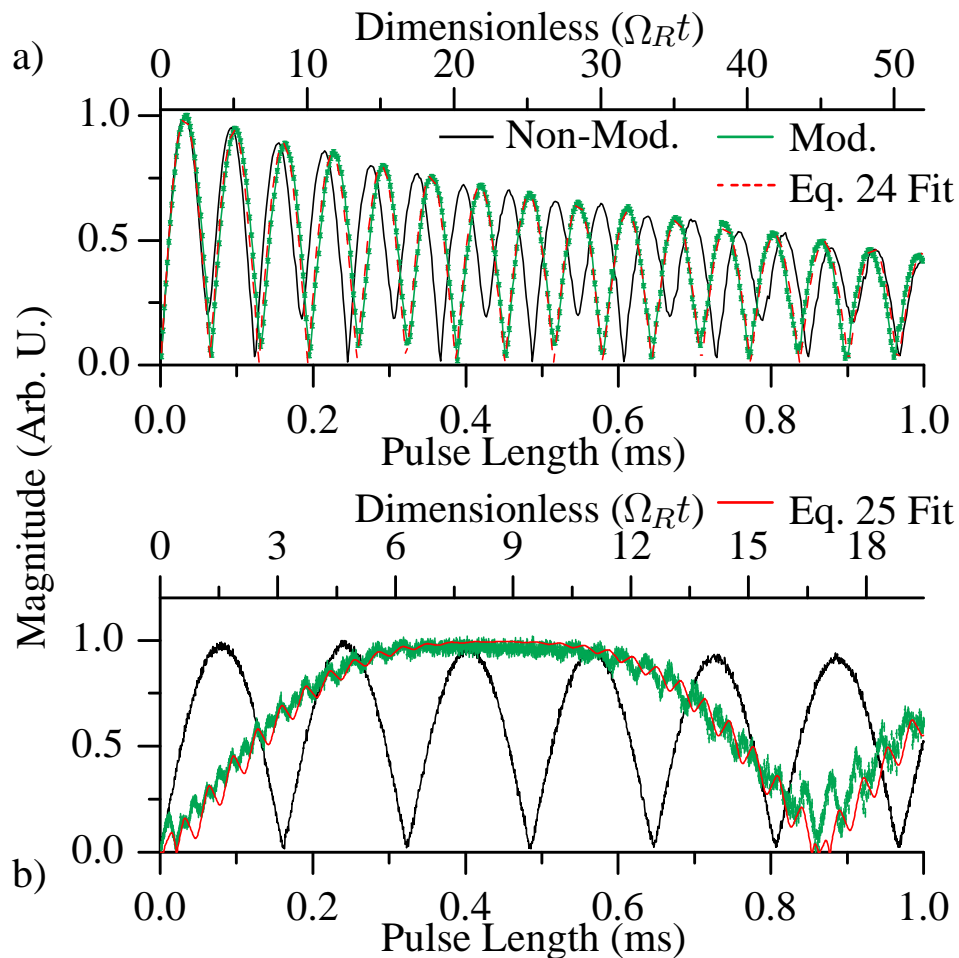


**Figure 4.3.** Experimental fast-modulation data are plotted. The magnitude of the FID is mapped against pulse length and dimensionless units  $\Omega_R t$ . (a) Shown is data that confirm the predictions of Eq. 24. Data without modulation are shown in black, with the Rabi frequency found to be  $\Omega_R/2\pi = 8.26 \pm 0.05$  kHz. Fast-modulation data are shown in green, where a modulation frequency of  $\omega_m/2\pi = 43.1 \pm 0.01$  kHz is applied. The results of a fit using Eq. 24 along with parameters for characteristic decay time and overall magnitude ( $Ce^{-t/T_2} * \text{Eq. 24}$ ) are shown in dashed red, overlaying the fast-modulation data. The fit parameters found are  $\Omega_R/2\pi = 8.23 \pm 0.01$  kHz,  $\varepsilon_m/2\pi\gamma = 4.88 \pm 0.04$  G,  $C = 1.02 \pm 0.02$ ,  $T_2 = 1.2 \pm 0.6$  ms. (b) Shown are data that confirm the predictions of Eq. 25. Data without modulation are shown in black, with the Rabi frequency found to be  $\Omega_R/2\pi = 3.10 \pm 0.02$  kHz. Fast-modulation data are shown in green, where a modulation frequency of  $\omega_m/2\pi = 31.5 \pm 0.01$  kHz is applied. The results of a fit using Eq. 25 are shown in red, overlaying the fast-modulation data. The fit used the experimental modulation frequency  $\omega_m$ , and found parameters are  $\Omega_R/2\pi = 2.5 \pm 0.5$  kHz and  $\varepsilon_m/2\pi\gamma = 11.8 \pm 0.1$  G.

$\hat{\mathbf{x}}\text{-}\hat{\mathbf{y}}$  plane. In the fit to the data to Eq. 25 only  $\varepsilon_m$  is used as a free parameter; for various technical reasons, larger modulation amplitudes are more difficult to measure experimentally. The Rabi frequency  $\Omega_R$  as determined from the nonmodulated data is a fixed parameter in the fit. Note that the  $\approx 25\%$  reduction (due to smaller  $B_1$ ) in the value of  $\Omega_R$  determined from the nonmodulated data appears to have eliminated the effects of  $T_2^*$  decay that is present in the nonmodulated data of Fig. 4.3(b), as compared to similar data in Fig. 4.3(a).

In the strong-modulation regime  $\varepsilon_m \gg \Omega_R \gg \omega_m$ , the picture in the rotating frame is that the slowly sweeping modulation field brings the spins into resonance for only a short fraction of the modulation period; in the remaining time the modulation field is so large that the effective field in the the rotating frame lies along the  $\hat{\mathbf{z}}$ -axis—the spins are essentially out of resonance, and do not nutate. The experiment has  $\varepsilon_m$  at most only a few times  $\Omega_R$  and thus did not achieve the limit  $\varepsilon_m \gg \Omega_R$  to a degree sufficient to turn off the nutation completely, even when  $|\varepsilon(t)|$  was near a maximum. However, the seemingly complicated data seen in the lower half of Fig. 4.4 are still understood to a significant degree. Nontrivial behavior of the Rabi oscillations occurs when  $\varepsilon(t)$  is near zero with periodicity  $\pi/\omega_m \approx 0.166$  ms, as per Eq. 4.6. These critical regions of time are marked by dramatic changes in the oscillation behavior lasting about one Rabi period  $2\pi/\Omega_R$ , whereas there is a relatively steady-state oscillation for the remainder of the modulation period. In general, the prediction in Eq. 36 can only be applied when the initial spin state is know, which is only true for the data in the lower half of Fig. 4.4 for the critical region just after  $t = 0$ .

Hence, the upper half of Fig. 4.4 shows an expanded view of the first 0.05 ms of this data set, which is fit to Eq. 36, multiplied by an overall constant  $C$ . The constant  $C$  is introduced to account for the possibility that the magnetization has not actually attained a maximum projection on the  $\hat{\mathbf{x}}\text{-}\hat{\mathbf{y}}$  plane. The shape of Eq. 36 is heavily dependent on this fact, so a best-fit to the shape of the data in Fig. 4.4 is used. The fit shown determines the parameters  $\Omega_R/2\pi = 27.2 \pm 0.6$  kHz,  $\varepsilon_m/2\pi\gamma = 18.1 \pm 0.7$  G,  $\omega_m/2\pi = 3 \pm 0.1$  kHz, and  $C = 0.77 \pm 0.2$ . A possible reason for the fit's high Rabi frequency compared to the nonmodulated Rabi frequency is that the modulation pulse is not completely in phase with the  $B_1$  pulse. This would cause a shift in

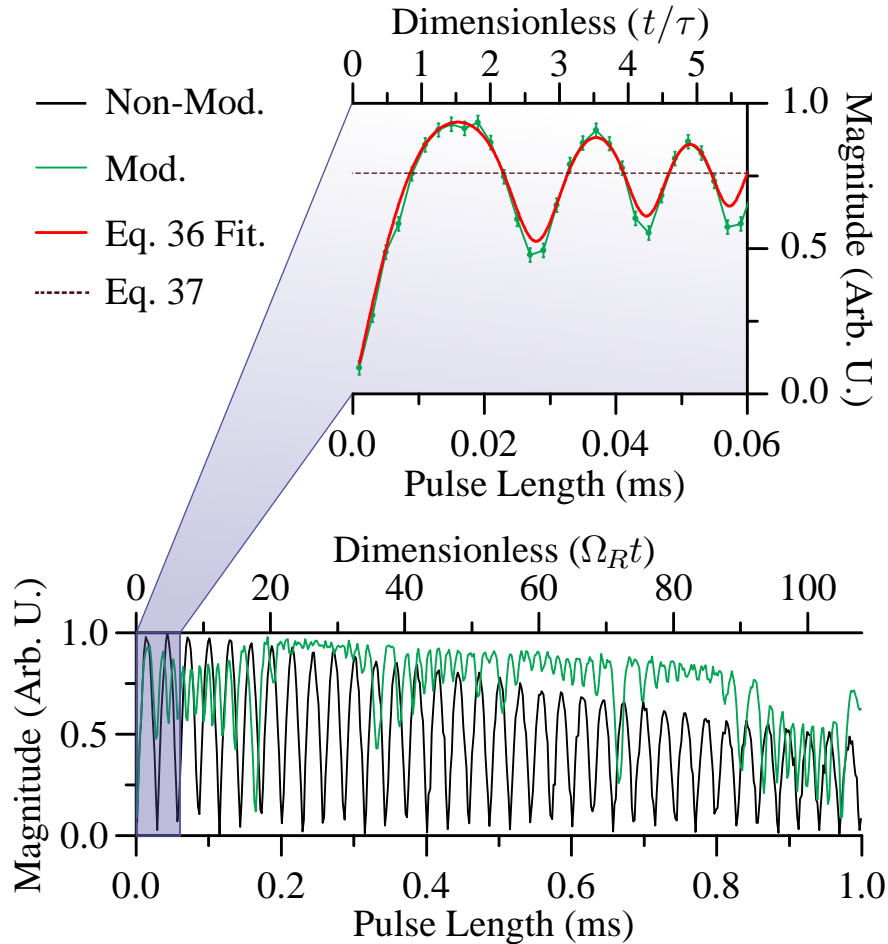


**Figure 4.4.** Shown is experimental confirmation of the strong-modulation regime. The magnitude of the FID is mapped against pulse length and dimensionless units  $\Omega_R t$ . Data without modulation are shown in black, with the Rabi frequency found to be  $\Omega_R/2\pi = 17.2 \pm 0.1$  kHz. Strong-modulation data are shown in green, where a modulation frequency of  $\omega_m/2\pi = 3 \pm 0.1$  kHz is applied. The results of an early-time fit using Eq. 36 with a parameter for overall magnitude ( $C \cdot \text{Eq. 36}$ ) are shown in red overlaying a close-up of the early-time strong-modulation data. The fit parameters used to generate the fit from Eq. 36 are  $\Omega_R/2\pi = 27.2 \pm 0.6$  kHz,  $\varepsilon_m/2\pi\gamma = 18.1 \pm 0.7$  G,  $\omega_m/2\pi = 3 \pm 0.1$  kHz, and  $C = 0.77 \pm 0.02$ , yielding  $|\nu| = 0.80 \pm 0.06$ . An asymptote is calculated from Eq. 37 and plotted with a dashed maroon line.

the effective Rabi frequency determined by  $\sqrt{\omega_0^2 + \Omega_R^2}$ , so that the modulation field strength  $\varepsilon_m/2\pi\gamma$  exactly when the  $B_1$  pulse begins is found to be

$$\varepsilon_m/2\pi\gamma = \frac{\sqrt{\Omega_{\text{Reff}}^2 - \Omega_R^2}}{\gamma} = \frac{\sqrt{(27.2 \text{ kHz})^2 - (17.2 \text{ kHz})^2}}{4.25775 \text{ kHz/G}} \approx 5 \text{ G}, \quad (4.12)$$

which is well within the range of the maximum found modulation field. Using the extracted values of  $\Omega_R$ ,  $\omega_m$ , and  $\varepsilon_m$ , the parameter  $|\nu| = 0.80 \pm 0.06$  is calculated. Using  $|\nu|$ , an estimate for the early-time asymptote  $P_{\perp}(\infty)$  (note the early-time data do not reach a complete  $180^\circ$  flip of state) and are plotted with a dashed line in Fig. 4.4. Note again, with respect to the fit that  $\varepsilon_m$  and the other parameters derived from it are extremely sensitive to whether the magnetization reaches the  $\hat{\mathbf{x}}\text{-}\hat{\mathbf{y}}$  plane ( $P_{\perp} = 1$ ). The precision quoted for all parameters may thus be somewhat underestimated. Nonetheless, the data and fit clearly show the decreasing oscillation period characteristic of the parabolic cylinder function on which the theory in this regime is based.

The qualitative features of the data in Fig. 4.4 away from the early-time region can also be understood. In each consecutive period determined by  $\pi/\omega_m \approx 0.166$  ms, a new period of behavior is seen that is predicted by Eq. 36 if the initial spin state is well known, as well as a new asymptotic behavior. As the critical time period near a zero-crossing of  $\varepsilon_m$  ends, the magnetization vector finds itself at some particular angle to the  $\hat{\mathbf{z}}$ -axis that would then essentially not change in the limit  $\varepsilon_m \gg \Omega_R$  until the next zero-crossing. Even when this limit is not well satisfied, if the magnetization is close to being in the  $\hat{\mathbf{x}}\text{-}\hat{\mathbf{y}}$  plane, nutation about an effective field that is mostly along the  $\hat{\mathbf{z}}$  direction will produce only small, second-order changes in the FID amplitude as the spins nutate: a clear example occurs from 0.2 ms to 0.3 ms; here the FID amplitude is very close to maximum and there is a barely perceptible nutation. Larger oscillations occur for lower values of the FID amplitude when the magnetization is well away from the  $\hat{\mathbf{x}}\text{-}\hat{\mathbf{y}}$  plane, with the largest occurring between about 0.85 ms and 0.95 ms. Note that the dephasing that occurs due to  $B_1$  inhomogeneity appears to be decreased by the strong-slow modulation. The modulation field has the effect of continuously refocusing the spins in the rotating frame  $\hat{\mathbf{y}}\text{-}\hat{\mathbf{z}}$  plane, analogous to the way a Hahn echo refocuses dephased transverse magnetization precessing about an

inhomogeneous  $B_0$  [201].

The study of the weak-resonant modulation regime  $\Omega_R \approx \omega_m \gg \varepsilon_m$  focuses on the limit where the  $B_1$  pulse is on resonance with the Zeeman splitting, with the theoretical prediction for the spin dynamics is given by Eq. 44. In this regime, beats manifest in the Rabi oscillations; the depth of the modulation is determined by the parameter  $\kappa$ . Fig. 4.5 shows a typical example; a fit of the modulated data to Eq. 44 is qualitatively reasonable and clearly exhibits the beat envelope. Quantitatively, a high-quality fit over the entire time interval is made difficult by the extreme sensitivity of  $\kappa$ , which contains a small difference  $(\omega_m - \Omega_R) \ll \Omega_R$ . This small difference contains experimental errors in  $\omega_m$  and  $\Omega_R$ , which lead to relatively large fluctuations in  $\kappa$ , so an ideal  $\kappa = 1$  measurement is hard to obtain. Because of the above complications, the experimental parameters are considered as floating parameters, and separate fits are done for two time intervals: “early” and “late,” as shown in Fig. 4.5(a). The values of  $\kappa$  extracted from both fits are reasonably close to each other:  $0.54 \pm 0.14$  for early-time and  $0.40 \pm 0.12$  for late-time fits. This discrepancy in  $\kappa$  is attributed to the slow drift with time of the Rabi frequency and the modulation-pulse parameters. The evidence that this drift affects the fit can already be inferred from Fig. 4.3 for the fast-modulation regime; dephasing due to  $B_1$  homogeneity is suppressed by the modulation field, again analogous to a Hahn echo refocusing process. Also shown in Fig. 4.5(a) and (b) are the Rabi frame descriptions of the evolution of the magnetization. The envelopes in the Rabi oscillations are visualized from the Rabi frame; the shape of the slow beat pattern is traced out in the Rabi frame, with the higher frequency Rabi oscillations given by the speed of the nutation of the Rabi frame. The rephasing of the spins that comprise the magnetization can also be seen easily from the Rabi frame description shown in Fig. 4.5—the modulation field causes a constant twisting of the spins around the modulation field, leading to the continuous refocusing of the spins.

## 4.4 Summary

Experimentally, the nontrivial modifications to Rabi nutations predicted with equations in Sect. 4.2.1 have been verified across a broad range of modulation-field

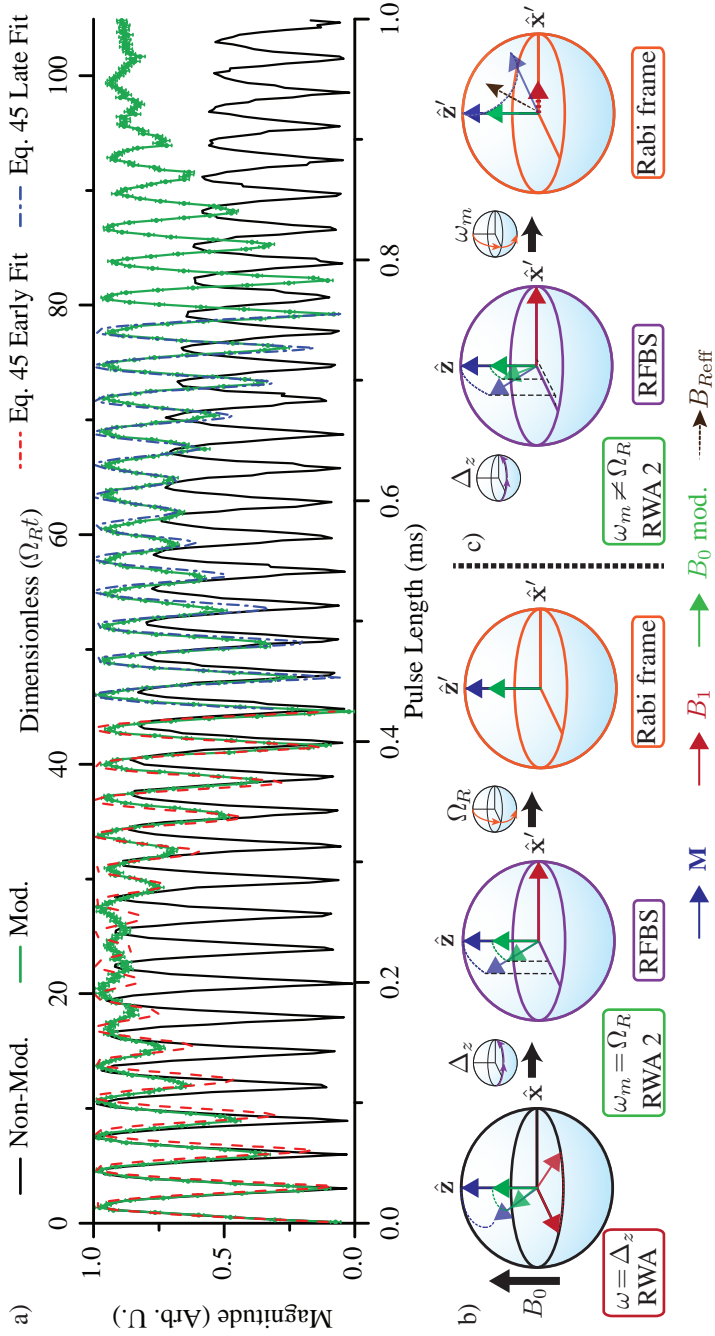


**Figure 4.5.** Experimental weak-resonant data are plotted and fit to theory, along with a description of the Rabi frame at play. (a) Shown is experimental confirmation of the weak-resonant regime. The magnitude of the FID is mapped against pulse length and dimensionless units  $\Omega_R t$ . Data without modulation are shown in black, with the Rabi frequency found to be  $\Omega_R/2\pi = 16.7 \pm 0.7$  kHz. Weak-resonant modulation data are shown in green, where a modulation frequency of  $\omega_m/2\pi = 17.2 \pm 0.01$  kHz is applied. The results of an early-time fit using Eq. 45 are shown in dashed red, overlaying the fast-modulation data. The fit parameters found for the early-time fit are  $\Omega_R/2\pi = 16.5 \pm 0.2$  kHz,  $\varepsilon_m/2\pi\gamma = 0.91 \pm 0.04$  G, and  $\omega_m/2\pi = 17.56 \pm 0.05$ , yielding  $\kappa = 0.54 \pm 0.14$ . The results of a late-time fit using Eq. 45 are shown in dashed blue, overlaying the fast-modulation data. The fit parameters found for the late-time fit are  $\Omega_R/2\pi = 17.0 \pm 0.2$  kHz,  $\varepsilon_m/2\pi\gamma = 1.2 \pm 0.1$  G, and  $\omega_m/2\pi = 18.03 \pm 0.09$  yielding  $\kappa = 0.40 \pm 0.12$ . (b) A sequence describing the conventional RWA and RFBS, with the addition of a second rotating-frame (Rabi frame) and second RWA to the  $B_0$  modulation field; the appearance of the  $B_0$ ,  $B_1$ ,  $B_0$  mod., and  $M$  vectors in each respective frame is shown. (c) A RFBS and Rabi-frame Bloch sphere are shown with a detuning of modulation pulse ( $\omega_m \neq \Omega_R$ ), causing  $B_{\text{Reff}}$  due to an effective  $B_1$  in the Rabi frame.

frequencies and amplitude with fairly simple NMR experiments on protons in water. These experiments are relatively easy to obtain in the laboratory and give the experimentalist a tool to access previously difficult-to-obtain ensemble evolutions in NMR, such as regimes outside of the conventional high-field limit where  $B_1$  excitation strengths are comparable to  $B_0$ .

The results shown here are potentially applicable to important areas of magnetic resonance itself. Consideration of  $B_0$ -modulation in NMR harkens back to the pioneering work of Redfield [202], and has applications in rotary saturation and rotational echoes [203, 204], adiabatic pulsing and cross polarization [205, 206], as well as line-narrowing techniques [207, 208, 209]. Note that the apparent self-refocusing of the dephasing due to  $B_1$ -inhomogeneities observed in Fig. 4.5 is of particular interest, since complicated rf-pulse rotations about the effective field are currently often used to accomplish this refocusing. In applications involving hyperpolarized noble gases, the attainable signal-to-noise ratio is only weakly dependent on the applied magnetic field; this has led to efforts [210] to do magnetic resonance imaging (MRI) at (more convenient and cost-effective) low  $B_0$ , for which the regime  $B_1 \sim B_0$  can become relevant.

In the monumental Redfield paper (his first on magnetic resonance), different saturation effects are studied in solids. Saturation is an effect where the spin bath stops accepting energy from the RF bath. Redfield's novel contribution was to realize the typical (BPP) saturation description eventually failed and moreover, did not obey the laws of thermodynamics. The BPP saturation description is given by

$$\frac{dE}{dt} \approx \frac{W}{1 + 2WT_1}, \quad (4.13)$$

where  $W$  is the transition probability. With the thermodynamic argument, he proves that for high  $B_1$ , the Bloch equations predict an irreversible process where entropy decreases. In fact, even a weak perturbation has drastic effects if applied long enough. His solution: if  $B_1$  remains on resonance for sufficient amount of time, the internal equilibrium will be described by a Boltzmann distribution defined by a spin temperature with regards to an effective Hamiltonian. Redfield reviews results in solids that show the absorption and dispersion do not decrease at the same rate with increasing saturation ( $B_1$  field), and that both lines are in fact narrowed rather than

broadened; these experimental findings both contradict previous saturation theory. The solution to this problem is to calculate the absorption and dispersion lines from the rotating-frame Bloch equations. For pulsed NMR, conventional saturation theory gives that if the spins are saturated,  $M_z$  is zero and  $M_x$  is *also* zero. Redfield's saturation gives that  $M_z$  is zero only if the pulse is on resonance (there can be remnant  $M_z$  along the effective field), and  $M_x$  is nonzero.

In Redfield [202], a rotary saturation experiment is described in which a continuous-wave NMR experiment is conducted with the sweep frequency at (or close to) the Rabi frequency  $\Omega_R$ . During such an experiment, the dispersion derivative signal goes to a minimum, and zero in some cases. This makes sense when one recalls that the dispersion is essentially a measure of the magnetization along the  $\hat{\mathbf{x}}'$ -axis in the rotating frame. When the modulation takes the  $B_1$  driving field through the on-resonant frequency, the dispersion also passes through zero. If the field modulation ( $\omega_m$ ) is at the same frequency as the Rabi frequency  $\Omega_R$ , the effect can again be easily explained from the Rabi frame 4.1. Once the second RWA for the modulation field is made, then the magnetization will always be aligned with the rotating modulation field. This reduces the torque due to the modulation field to zero, so that the magnetization never rotates around the  $\hat{\mathbf{z}}$ -axis, and thus there is zero projection of the magnetization on the rotating-frame  $\hat{\mathbf{x}}'$ -axis—no dispersion, and no dispersion derivative signal. If the modulation frequency is not equal to the Rabi frequency, the effect is also seen in the Rabi frame; the magnetization will now rotate around the  $\hat{\mathbf{z}}'$ -axis, causing a projection on the  $\hat{\mathbf{x}}'$ -axis in the rotating frame. Perhaps the combination of these ideas can yield new spectroscopic techniques.

Glenn et al. [191] also has a main result of multiphoton-type processes [198, 211, 212] that are also accessible with longitudinal field modulation. These multiphoton-type processes are accessed with  $\omega_m^{(p)} = \Omega_R/(2p + 1)$ , similar to the conventional  $\omega^{(p)} = \Delta_z/(2p + 1)$  typically associated with multiphoton resonances. Due to time restrictions, these multiphoton-type resonances are not explored.

## APPENDIX A

### RB $P_{1/2}$ -ORBITAL ABSORPTION-EMISSION CYCLES

*“Those are my principles, and if you don’t like them... well, I have others.”*

*- Groucho Marx*

The efficiency of light and maximum possible polarization are important considerations for the optically pumping of alkali metal in the presence of buffer gas [213, 214]. In the following it is found that, when the nuclei of the ground state is considered, the efficiency of light is substantially decreased in the presence of buffer gas.

Using the simplified model that neglects hyperfine coupling and nuclei spin, it is seen in Fig. 1.1 that the relative probability of an atom absorbing a  $\sigma_+$  is 1 for the  $|m_j = -1/2\rangle$  state, and 0 for the  $|m_j = +1/2\rangle$  state. Recall that once in the excited  $5P_{1/2}^2$  state the  $L = 1, m_L = 0$  nature of the state must be considered in order to obtain the correct transition probabilities. In this way, it is found that the probability for emission from the excited  $|+1/2\rangle$  state is  $1/3$  to the  $5^2S_{1/2} | +1/2\rangle$  ground state, and  $2/3$  to the  $5^2S_{1/2} | -1/2\rangle$  ground state. From these relative probabilities of absorption and emission, a brief calculation gives that  $3/2$  photons must be absorbed in order to fully polarize the Rb atom. In Happer and Winjngaarden [215], a rate-based explanation of the needed  $3/2$  photons is shown, but the idea can be explained conceptually; it requires, on average, three photons to polarize a  $| -1/2\rangle$  ground state to  $| +1/2\rangle$ , but recall that the initial atom is *unpolarized* with a state description of  $1/2 | -1/2\rangle + 1/2 | +1/2\rangle$ . Thus, only half of the three photons is needed in order to fully polarize the atom within this model. The average number of photons required to polarize the atom gives a clear idea of the ideal efficiency of the optical pumping light. The situation improves when buffer gas is considered, as the buffer gas can be considered to both scramble the excited state population and randomize the transition

probabilities—both give the relative probabilities of emission from the excited state to be 1/2 to the  $|+1/2\rangle$  ground state and 1/2 to the  $|−1/2\rangle$  state. Thus, the average number of photons required to polarize the atom in the presence of buffer gas within this model is  $2/2 = 1$  photon.

Now consider the more complicated situation, with the inclusion of nuclei interaction. For  $^{87}\text{Rb}$  atoms, the nuclei have spin-3/2. From Sect. 1.1, recall the probabilities of absorption are calculated in the  $3/2 \otimes 1/2$  operator product space for  $I = 3/2$  and  $J = 1/2$ . This is reasonable for the  $5^2S_{1/2}$  state as it is a true  $L = 0$  state. The collation of absorption or excitation probabilities into a matrix  $A$  yields

$$A = \begin{array}{c} \langle 2\ 2| \quad \langle 2\ 1| \quad \langle 1\ 1| \quad \langle 2\ 0| \quad \langle 1\ 0| \quad \langle 1\ -1| \quad \langle 2\ -1| \quad \langle 2\ -2| \\ \begin{array}{l} |2\ 2\rangle \\ |2\ 1\rangle \\ |1\ 1\rangle \\ |2\ 0\rangle \\ |1\ 0\rangle \\ |1\ -1\rangle \\ |2\ -1\rangle \\ |2\ -2\rangle \end{array} \end{array} \begin{pmatrix} 0 & \frac{1}{16} & \frac{3}{16} & 0 & 0 & 0 & 0 & 0 \\ 0 & 0 & 0 & \frac{1}{32} & \frac{3}{32} & 0 & 0 & 0 \\ 0 & 0 & 0 & \frac{3}{32} & \frac{1}{32} & 0 & 0 & 0 \\ 0 & 0 & 0 & 0 & 0 & \frac{1}{32} & \frac{3}{32} & 0 \\ 0 & 0 & 0 & 0 & 0 & \frac{1}{32} & \frac{3}{32} & 0 \\ 0 & 0 & 0 & 0 & 0 & 0 & 0 & \frac{3}{16} \\ 0 & 0 & 0 & 0 & 0 & 0 & 0 & \frac{1}{16} \\ 0 & 0 & 0 & 0 & 0 & 0 & 0 & 0 \end{pmatrix}.$$

The emission probabilities are found in a similar method as the nonnuclei case, where the  $1 \otimes 1/2$  product space must be considered when calculating the probability of dipole radiation. Including the spin-3/2 nuclei, the  $3/2 \otimes 1 \otimes 1/2$  product space should be considered. As an example, the probability of emission from the  $5^2P_{1/2} |1\ 1\rangle$  state is shown. The state is first rewritten by changing bases using Clebsch-Gordan coefficients,

$$\begin{aligned} |1\ 1\rangle &= \sqrt{\frac{3}{2}} | \frac{3}{2} \ -\frac{1}{2} \rangle - \sqrt{\frac{1}{4}} | \frac{1}{2} \ +\frac{1}{2} \rangle, \quad \text{switching from } F, m_F \text{ to } m_I, m_J, \\ &= \sqrt{\frac{3}{4}} \sqrt{\frac{1}{3}} | \frac{3}{2} \ 0 \ -\frac{1}{2} \rangle - \sqrt{\frac{3}{4}} \sqrt{\frac{2}{3}} | \frac{3}{2} \ -1 \ \frac{1}{2} \rangle \\ &\quad - \sqrt{\frac{1}{4}} \sqrt{\frac{2}{3}} | \frac{1}{2} \ +1 \ -\frac{1}{2} \rangle + \sqrt{\frac{1}{4}} \sqrt{\frac{1}{3}} | \frac{1}{2} \ 0 \ +\frac{1}{2} \rangle, \quad \text{from } m_I, m_J \text{ to } m_I, m_L, m_S. \end{aligned}$$

The selection rules for unpolarized dipolar emission are  $\Delta m_L = +1, 0, -1$ , and the state must become a ground  $S$  state with  $L = 0$ . The excited states thus fall to the

$F, m_F$  basis ground state as

$$\begin{aligned}
\sqrt{\frac{1}{12}} \left| \frac{3}{2} \ 0 \ -\frac{1}{2} \right\rangle &\rightarrow \sqrt{\frac{1}{12}} \sqrt{\frac{1}{4}} |2 \ 1\rangle + \sqrt{\frac{3}{12}} \sqrt{\frac{3}{4}} |2 \ 1\rangle, \\
-\sqrt{\frac{1}{2}} \left| \frac{3}{2} \ -1 \ \frac{1}{2} \right\rangle &\rightarrow -\sqrt{\frac{1}{2}} |2 \ 2\rangle, \\
-\sqrt{\frac{2}{12}} \left| \frac{1}{2} \ +1 \ -\frac{1}{2} \right\rangle &\rightarrow -\sqrt{\frac{2}{12}} \sqrt{\frac{1}{2}} |2 \ 0\rangle - \sqrt{\frac{2}{12}} \sqrt{\frac{1}{2}} |1 \ 0\rangle, \\
\sqrt{\frac{1}{12}} \left| \frac{1}{2} \ 0 \ +\frac{1}{2} \right\rangle &\rightarrow \sqrt{\frac{1}{12}} \sqrt{\frac{3}{4}} |2 \ 1\rangle - \sqrt{\frac{1}{12}} \sqrt{\frac{1}{4}} |1 \ 1\rangle.
\end{aligned}$$

This gives the relative probabilities to fall into each state from  $|2 \ 1\rangle$  as,

$$\begin{aligned}
\langle 2 \ 2 | E | 2 \ 1 \rangle &\sim \frac{1}{6}, \\
\langle 1 \ 1 | E | 2 \ 1 \rangle &\sim \frac{1}{8}, \\
\langle 2 \ 1 | E | 2 \ 1 \rangle &\sim \frac{5}{24}, \\
\langle 2 \ 0 | E | 2 \ 1 \rangle &\sim \frac{1}{4}, \\
\langle 1 \ 0 | E | 2 \ 1 \rangle &\sim \frac{1}{4}.
\end{aligned}$$

Here, assuming the differences in lifetime for each state is negligible,  $E$  is a symmetric matrix that corresponds to the probability of emission from each excited state,

$$E = \begin{array}{l} \begin{array}{cccccccc} \langle 2 \ 2 | & \langle 2 \ 1 | & \langle 1 \ 1 | & \langle 2 \ 0 | & \langle 1 \ 0 | & \langle 1 \ -1 | & \langle 2 \ -1 | & \langle 2 \ -2 | \end{array} \\ \begin{array}{l} |2 \ 2\rangle \\ |2 \ 1\rangle \\ |1 \ 1\rangle \\ |2 \ 0\rangle \\ |1 \ 0\rangle \\ |1 \ -1\rangle \\ |2 \ -1\rangle \\ |2 \ -2\rangle \end{array} \end{array} \begin{pmatrix} \frac{1}{3} & \frac{1}{6} & \frac{1}{2} & 0 & 0 & 0 & 0 & 0 \\ \frac{1}{6} & \frac{5}{24} & \frac{1}{8} & \frac{1}{4} & \frac{1}{4} & 0 & 0 & 0 \\ \frac{1}{2} & \frac{1}{8} & \frac{5}{24} & \frac{1}{12} & \frac{1}{12} & 0 & 0 & 0 \\ 0 & \frac{1}{4} & \frac{1}{12} & \frac{1}{6} & \frac{1}{6} & \frac{1}{12} & \frac{1}{4} & 0 \\ 0 & \frac{1}{4} & \frac{1}{12} & \frac{1}{6} & \frac{1}{6} & \frac{1}{12} & \frac{1}{4} & 0 \\ 0 & 0 & 0 & \frac{1}{12} & \frac{1}{12} & \frac{5}{24} & \frac{1}{8} & \frac{1}{2} \\ 0 & 0 & 0 & \frac{1}{4} & \frac{1}{4} & \frac{1}{8} & \frac{5}{24} & \frac{1}{6} \\ 0 & 0 & 0 & 0 & 0 & \frac{1}{2} & \frac{1}{6} & \frac{1}{3} \end{pmatrix}.$$

From the literature [19, 20], it is determined that only the ground spin state, or more accurately  $m_J$ , is accounted for in hyperpolarization of gases. Thus, it is sufficient

to only tally the  $m_J$  states when calculating the polarization, which, again using the Clebsch-Gordon coefficients for the  $S$  ground state, are written as the projector

$$P = \begin{pmatrix} \langle 2\ 2| & \langle 2\ 1| & \langle 1\ 1| & \langle 2\ 0| & \langle 1\ 0| & \langle 1\ -1| & \langle 2\ -1| & \langle 2\ -2| \\ 1 & 1/2 & -1/2 & 0 & 0 & 1/2 & -1/2 & -1 \end{pmatrix}.$$

Another useful projection is that representing the depletion in the ground state due to the absorption, which is simply the sum of the absorption matrix  $A$  down the columns, and put on the diagonal of a matrix  $D$ . A simple probabilistic argument does not suffice when calculating the number of photons required to polarize the atom; the actual solution leads to a multi-exponential rise, where the late-time photons (photons absorbed when the atom is close to complete polarization) are less efficient than the early-time photons (see. Fig. A.1). Thus, eight coupled ODEs are necessary to analyze the problem. Considering an unpolarized atom, the initial ground state number densities in zero field are written as

$$\rho^t(0) = \begin{pmatrix} \rho(2\ 2) & \rho(2\ 1) & \rho(1\ 1) & \rho(2\ 0) & \rho(1\ 0) & \rho(1\ -1) & \rho(2\ -1) & \rho(2\ -2) \\ 1/8 & 1/8 & 1/8 & 1/8 & 1/8 & 1/8 & 1/8 & 1/8 \end{pmatrix},$$

where the superscript  $t$  represents the transpose of the matrix. Solving the rate equations, the probabilities of occupation in the ground state  $\rho(t)$  during excitation-emission cycle for a pumping rate  $2R = 1$  are

$$\begin{aligned} \partial_t \rho(t) &= (EA - D)\rho(t), \\ \rho(t) &= e^{(EA-D)t} \rho(0) \end{aligned} \tag{A.1}$$

The amount of polarization gained from the first absorbed photon in this system is 0.0482. This is a sizable difference from the polarization gained from one absorbed photon in the neglected nuclei case,  $1/3$ . By inspection of Fig. A.1, it is seen that in order to reach  $1 - e^{-1}$  of the maximum polarization for a single atom, the time it takes is roughly  $28/2R$ , compared to the neglected nuclei case of  $3/2R$ —this is roughly an order of magnitude difference. The relative average number of photons scattered off of each respective state is given by

$$n_i = \int_0^\infty \frac{dn_i}{dt} dt = \int_0^\infty A\rho(t) dt = -A(EA - D)^{-1} \rho(0). \tag{A.2}$$

The relative number of photons gives the total amount of photons scattered off of each state, but the average number of photons needed to excite each state must be

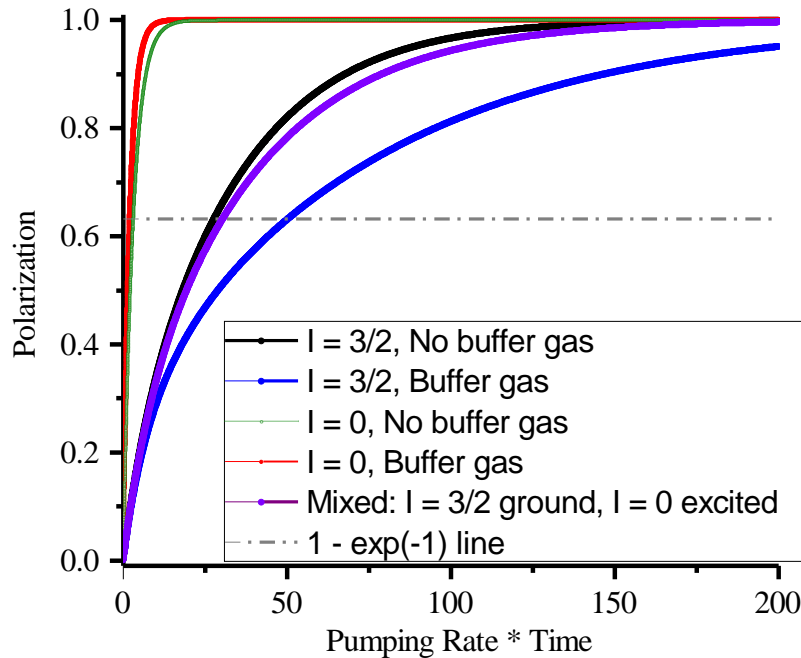


**Figure A.1.** The results of the analytical solutions to the rate equations for  $^{87}\text{Rb}$  are shown. The five different cases are neglected nuclei with and without buffer gas, spin-3/2 nuclei with and without buffer gas, and a mixed case where the ground state has spin-3/2 nuclei and neglected nuclei in the excited state due to the short lifetimes from inclusion of buffer gas. The buffer gas serves to randomize the probability of falling from a particular state.

taken into account; e.g., it takes on average 16 photons to excite the  $|2\ 1\rangle$  state. Thus, using Eq. A.2, the average number of photons needed to polarize the atom in the absence of buffer gas becomes 30.619. Here it becomes apparent that the multi-exponential behavior of the spin-3/2 nuclei case drastically affects the efficiency of the later time photons because of the discrepancy between the time  $28/2R$  it takes for the polarization to reach  $1 - e^{-1}$  and the average number photons to obtain complete polarization, which is approximately 30 (note that a  $3/2R$  time in the zero-spin nuclei corresponds  $3/2$  photons on average).

Interestingly, when buffer gas and the complete randomization of the emission is introduced (causing the emission matrix  $E$  to be filled with  $1/8$  in every entry), the amount of polarization gained by the first photon absorbed *decreases* slightly to 0.0469—again, this is a sizable difference from the polarization gained from the

neglected nuclei, buffer gas case,  $1/2$ . In turn, inspection of the Fig. A.1 gives that the time it takes to reach  $1 - e^{-1}$  of maximum polarization is roughly  $50/2R$ , compared to the neglected-nuclei, buffer-gas case of  $2/2R$ . Here, the multi-exponential behavior is exaggerated, and the number of photons calculated using Eq. A.2 becomes 62.666. This makes sense qualitatively, as an atom has a  $1/8$  probability to leak back into the  $|2 -2\rangle$  state once excited.

The apparent upshot to introducing sufficient buffer gas is that the nuclei do not “have time to react” to the electron transitions because the correlation time of the excited state is far too short due to quenching of that state by the buffer gas [216, 217]. In Bhaskar et al. [217], it is estimated the typical hyperfine precession rate for the nuclear spin of cesium atoms in the  $7P$  state (the second excited P state) to be  $\omega_{\text{hfs}} \leq 6 \times 10^8 \text{ s}^{-1}$ , with recollision orientation time  $\tau_c \leq 10^{-10} \text{ s}$  and quenched lifetime with 100-200 torr of nitrogen as  $\tau_q \leq 10^{-1} \text{ s}$ . This estimates the probability of conservation of nuclear spin polarization in an emission-absorption cycle to be  $1 - \omega_{\text{hfs}}^2 \tau_c \tau_q \geq 0.95$ . Thus, in the presence of buffer gas, the simplified picture of the 0-spin nuclei for Rb, with a weaker hyperfine strength and in the first excited state, can be considered as a good approximation for the excited state. However, for the small fraction of nuclei that have time to be affected by the hyperfine interaction in the excited state, the photons will be surprisingly inefficient due to buffer gas randomization.

The zero-spin nuclei approximation is only good for the excited state because, in the ground state, there is typically sufficient time for the nuclei and electron to influence one another. This is seen from exciting the ground hyperfine states with magnetic resonance—six different transitions are seen instead of only one. The correct model for  $^{87}\text{Rb}$  then, in the case of sufficient buffer gas, is a mixed model that considers pumping out of the  $m_J$  states in  $3/2 \otimes 1/2 \ 5^2S_{1/2}$  manifold, and quenching randomly from a  $J = 1/2$ ,  $5^2P_{1/2}$  state. This essentially corresponds to treating the absorption-emission process with the neglected nuclei buffer gas model (50% chance to flip the state), while keeping track of the ground nuclear state. Note, at zero-field, the states comprising the  $F = 2$  manifold are energy degenerate with each other, as in the  $F = 1$  manifold; this would cause fast mixing of the ground states in their respective

manifold if there is a mechanism for angular momentum transfer (i.e., buffer gas); this effect is ignored. Following this line of reasoning, the absorption-emission matrix becomes

$$EA_M = \begin{matrix} & \langle 2\ 2| & \langle 2\ 1| & \langle 1\ 1| & \langle 2\ 0| & \langle 1\ 0| & \langle 1\ -1| & \langle 2\ -1| & \langle 2\ -2| \\ \begin{matrix} |2\ 2\rangle \\ |2\ 1\rangle \\ |1\ 1\rangle \\ |2\ 0\rangle \\ |1\ 0\rangle \\ |1\ -1\rangle \\ |2\ -1\rangle \\ |2\ -2\rangle \end{matrix} & \left( \begin{array}{cccccccc} 0 & \frac{1}{32} & \frac{3}{32} & 0 & 0 & 0 & 0 & 0 \\ 0 & \frac{1}{32} & 0 & \frac{3}{64} & \frac{3}{64} & 0 & 0 & 0 \\ 0 & 0 & \frac{3}{32} & \frac{1}{64} & \frac{1}{64} & 0 & 0 & 0 \\ 0 & 0 & 0 & \frac{1}{16} & 0 & \frac{1}{64} & \frac{3}{64} & 0 \\ 0 & 0 & 0 & 0 & \frac{1}{16} & \frac{1}{64} & \frac{3}{64} & 0 \\ 0 & 0 & 0 & 0 & 0 & \frac{1}{32} & 0 & \frac{3}{32} \\ 0 & 0 & 0 & 0 & 0 & 0 & 0 & \frac{3}{32} \\ 0 & 0 & 0 & 0 & 0 & 0 & 0 & \frac{1}{8} \end{array} \right) \end{matrix}.$$

Here, the time it takes to reach  $1 - e^{-1}$  of the polarization is roughly  $30/2R$ , and the average number of photons to completely polarize the atom in the pure  $|2\ 2\rangle$  state is 41.666, see Fig. A.1. This surprising result is explained by realizing that there exists beneficial situations in the non-buffer gas,  $I = 3/2$  consideration, where there is a substantial and beneficial leak from the  $|2\ 1\rangle$  state to the  $|1\ 1\rangle$  state; the  $|1\ 1\rangle$  state is more efficient for the light to enter the  $|2\ 2\rangle$  state. An average of 11.7 photons is needed to completely deplete the  $|2\ 1\rangle$  state in the absence of buffer gas, and with buffer gas, 19 photons are needed. The most efficient state in both situations,  $|2\ -2\rangle$ , is also a clear indicator of how the buffer gas can serve as a detriment to photon efficiency. Without the buffer gas, an average of 0.857 photons is needed to pump out of the  $|2\ -2\rangle$  state, and with the buffer gas, an average of 1 photon is needed. The total probability of excitation and absorption to and from the  $|2\ -2\rangle$  state is only 0.104 for the atom with no buffer gas, but 0.125 for the buffer gas state. In addition, the hyperfine interaction in the excited state allows for mixing of the  $|2\ -1\rangle$  and  $|1\ -1\rangle$  states, leading to a possible path of

$$|2\ -2\rangle_g \rightarrow |2\ -1\rangle_e \rightarrow (|2\ 0\rangle_g, |1\ 0\rangle_g),$$

where the subscripts  $g$  and  $e$  state for excited and ground state; as clear from the matrix  $EA_M$ , these types of paths are simply not available for the nonnuclei case. In

fact, the only state that requires less average photons scattered off of it, in order to polarize the atom, for buffer gas case compared to nonbuffer gas case, is the  $|1 -1\rangle$  state, with average photon numbers 3 and 6.91, respectively. In this way, it becomes clear that other states in the nonbuffer gas case use the  $|1 1\rangle$  state as an efficient path to the  $|2 2\rangle$  state, which is the only ground state with complete  $m_J = +1/2$  polarization.

For the  $^{85}\text{Rb}$  isotope, a spin-5/2 nuclei is considered. The ground state of the  $^{85}\text{Rb}$  atom requires a  $5/2 \otimes 1/2$  product space, leading to twelve states. Following a similar calculation as for the  $^{87}\text{Rb}$  atom, rate equations and their solution are found using Eq. A.1—the results are shown in Fig. A.2. The details of this calculation are not shown; in general the emission-absorption probabilities are calculated using Clebsch-Gordon coefficients, such as  $\langle I, J; m_I, m_J | I, J; F, m_F \rangle = \langle m_I, m_J | F, m_F \rangle$ , and selection rules for the E1 approximation. These relative probabilities are written with the equations

$$|F', m'_F\rangle_f \langle F', m'_F | m'_I, m'_J \rangle^2 | \langle m'_I, m'_J | L_+ | m_I, m_J \rangle |^2 \langle m_I, m_J | F, m_F \rangle^2 \langle F, m_F |_i, \quad (\text{A.3})$$

for absorption of a  $\sigma_+$  photon, and

$$|F, m_F\rangle_f \langle F, m_F | m_I, m_J \rangle^2 | \langle \frac{1}{2}, m_J | m_L, m_S \rangle |^2 | \langle m_I, 0, m_S | L_j | m'_I, m'_L, m'_S \rangle |^2 \\ \times | \langle m'_L, m'_S | \frac{1}{2}, m'_J \rangle |^2 | \langle m'_I, m'_J | F', m'_F \rangle |^2 \langle F', m'_F | \quad (\text{A.4})$$

for the emission, where  $j = +, -, \text{ or } 0$ , the prime designates the excited state, and  $i, f$  are the initial and final ground state, respectively, and a sum is taken over all internal states. For the buffer gas randomization of the excited state, all probabilities of the emission are randomized. The zero-spin nuclei case is somewhat simpler, as the excited  $F', m'_F$  states are neglected. The average number of photons needed to completely polarize the atom into the  $|3 3\rangle$  state is found to be 71.904, 170.400, and 115.4 for the nonbuffer gas, buffer gas, and mixed (spin-5/2 nuclei ground state, spin-0 nuclei excited state) cases, respectively. Also, by inspection of Fig. A.2, the time taken to obtain  $1 - e^{-1}$  of the polarization is roughly 60/2R, 112/2R, and 69/2R for the nonbuffer gas, buffer gas, and mixed cases, respectively. Note that

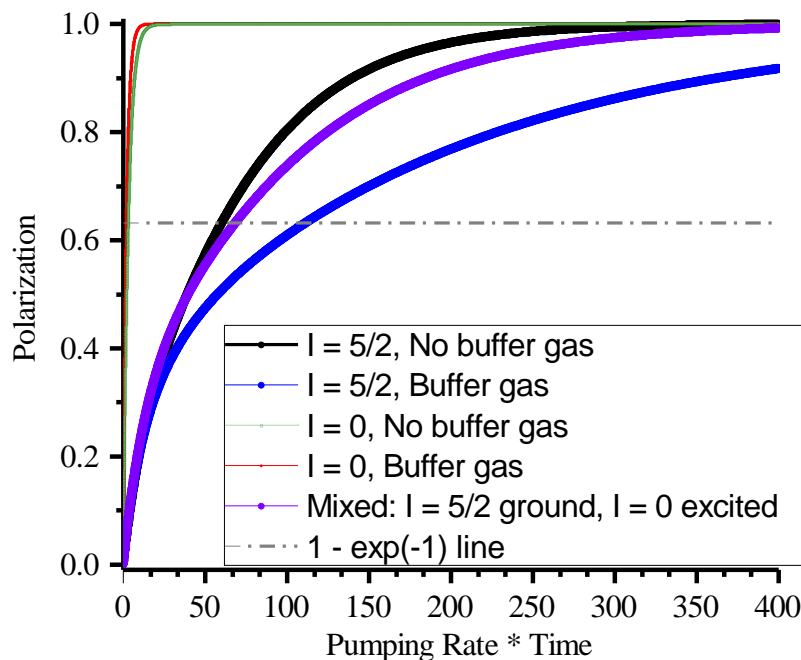


**Figure A.2.** The results of the analytical solution to the rate equations for  $^{85}\text{Rb}$  are shown. The five different cases are neglected nuclei with and without buffer gas, spin-5/2 nuclei with and without buffer gas, and a mixed case where the ground state has spin-5/2 nuclei and neglected nuclei in the excited state due to the short lifetimes from inclusion of buffer gas. The buffer gas serves to randomize the probability of falling from a particular state.

the mixed case has a higher initial photon efficiency than the nonbuffer gas case, but the multi-exponential behavior dominates and causes the efficiency of the late-time photons to drop significantly. The additional angular momentum in the spin-5/2 nuclei exaggerates the multi-exponential behavior and causes the efficiency of a photon to drop by at least 1/2 in each respective case when compared to the spin-3/2 nuclei cases.

In both  $^{85}\text{Rb}$  and  $^{87}\text{Rb}$ , the photon efficiency in optical pumping plummets when the nuclear spins are considered in the problem, and it is seen from the above analysis that the departure from the simplified nonnuclei case is quite drastic. As  $^{85}\text{Rb}$  is found in nature at 72.17% and  $^{87}\text{Rb}$  at 27.83%, the average number of photons needed to completely polarize a single atom in a naturally abundant idealistic Rb vapor with buffer gas is 94.88—at nearly two orders of magnitude difference, this is quite a

departure from the model that yields one-photon per atom. A proper simulation would also include the lifetime/relaxation of the ground state, magnetic field effects (Hanle depolarization and initial Boltzmann distribution), and any stimulated emission caused by an immense amount of laser light, representing typical conditions used in current spin-exchange optical pumping experiments. In order to decrease the effectiveness of the nuclei to prevent polarization, it seems that a higher intensity of light should decrease the lifetime of the ground state. Unfortunately, increasing the intensity of light leads to a higher probability of stimulated emission. The stimulated emission will serve as a detriment to the build-up of polarization in an individual atom, but in a Rb vapor the identical photons created will likely polarize two more atoms—saturation from stimulated emission should occur over the entire sample, though, for an extremely high intensity of laser light.

# APPENDIX B

## DILUTE-SPIN SOLID $^{129}\text{Xe}$ TRANSVERSE RELAXATION

*“A child of five would understand this. Send someone to fetch a child of five.”*

*- Groucho Marx*

The following appendix contains data taken on dilute, hyperpolarized  $^{129}\text{Xe}$  solid lattices, created within a convection cell. The motivation for obtaining these data is, initially, to explore the effect of narrowing in magnetic resonance lines in diluted crystals in solid xenon [218, 204]. Narrowing by spin dilution in the lattice is a consequence of the average nearest spin distance increasing with increasing dilution; essentially, the effect of dipolar broadening [48] is diminished by decreasing the amount of spins in the lattice. The narrowing effect in the dilute  $^{129}\text{Xe}$  solid is seen to some extent, but there is an interesting dependence on the freezing time of solid xenon that affects the shape of the resonance line shapes. This change in line shape becomes more pronounced and unusual as the concentration of  $^{129}\text{Xe}$  decreases. The theory for the narrowing of the line, observed previously, determines that the onset of narrowing will occur around roughly 10% spin-1/2 lattice occupation, and be fully narrowed by 1%. It is found that the cause of this effect must be related to crystal structure, but the specifics of the physical description remain unclear. Shape effects are discounted as the samples in each case are frozen from the same amount of liquid that occupies the same space.

A variety of isotopic concentrations are made in different convection cells from two enriched xenon bottles. The cells used in these experiments are listed in Table B.1. The enriched  $^{129}\text{Xe}$  bottle has isotopic concentrations of 7.8%  $^{128}\text{Xe}$ , 90%  $^{129}\text{Xe}$ , and 1.1%  $^{130}\text{Xe}$ . The other bottle used is an enriched  $^{132}\text{Xe}$  bottle, with isotopic concentrations of 3.8%  $^{131}\text{Xe}$ , and 95.4%  $^{132}\text{Xe}$ . (Both bottles are provided by the

**Table B.1.**  $^{129}\text{Xe}$  concentrations for the cells used in the dilute spin experiments.  $^{131}\text{Xe}$  concentrations can be had by using the isotopic concentrations of the two different enriched bottles used for cell manufacture.

Cell	Percent $^{129}\text{Xe}$
160B	9%
161A	5.5%
161B	1.1%
161C	0.5%

Linde, Inc.) Hence, the less  $^{129}\text{Xe}$  in the lattice, the higher the relative amount of  $^{131}\text{Xe}$  compared to  $^{129}\text{Xe}$ ; future experiments should use enriched  $^{128}\text{Xe}$  or enriched  $^{134}\text{Xe}$ , in order to minimize the  $^{131}\text{Xe}$  content in the lattice. These cells have a certain lifetime associated with them, in that the overall polarization of  $^{129}\text{Xe}$  starts to decrease after extended use, and a new cell is needed. All cells are manufactured by University of Utah glassblower Kevin Teaford, and all cells are prepared and filled in the Saam group’s high-vacuum system. More details on the operation and methods of convection cells are given in Sect. 2.3.2.

A schematic of the convection cell and experimental procedure is shown in Fig. B.1. With a cell such as this, the thermal demands are quite high, so the quality of the glassblowing needs to be quite high. The general idea of the cell is to have a closed environment where optically pumped Rb can undergo spin exchange with a vapor of xenon, and the xenon vapor phase exchanges with an isolated liquid xenon bath, far away from any Rb. In this way, a pure xenon crystal is made, without any Rb frozen in the lattice. The crux of generating the hyperpolarized solid xenon lies in the phase exchange of the hyperpolarized gas and the accumulated liquid in the sample tip. The difference in line shape seen below is dependent on the time passed between liquid xenon temperatures and 77 K, defined as fast and slow, where fast is on the order of seconds, and slow is on the order of minutes—the exact time passed is hard to determine with the current temperature control methods.

The first indication of strangeness comes from the decay data for the 9% cell 160B, which show a slight asymmetry with a slow freezing time, that can not be

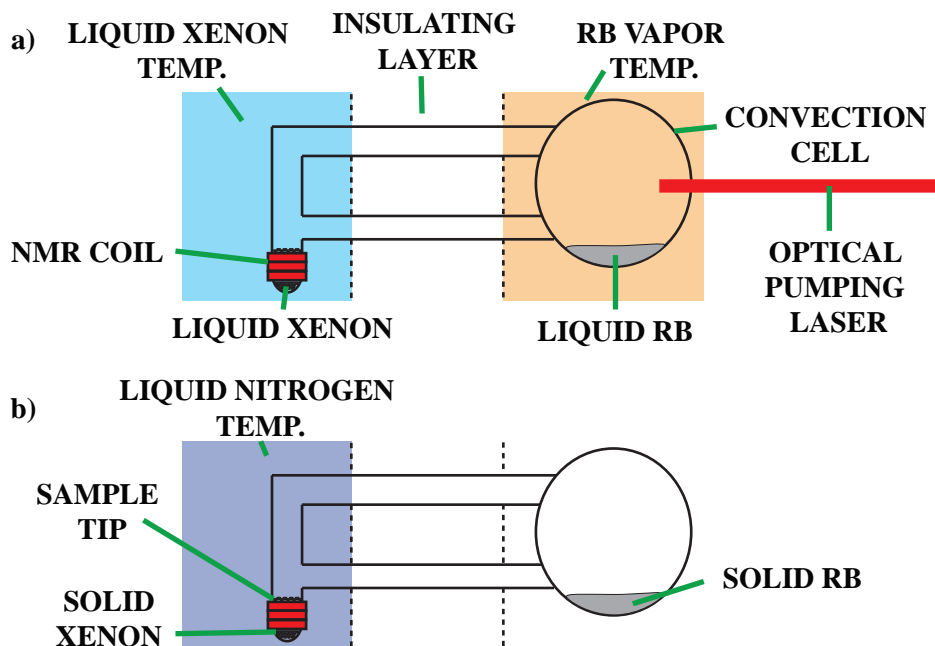


**Figure B.1.** Schematics detailing the operation of the convection cell are shown. (a) A schematic of the borosilicate convection cell an operational procedure is shown. Rb vapor is optically pumped, and the Rb undergoes spin exchange with the xenon vapor. The xenon vapor exchanges phase with the liquid xenon in the sample tip, accumulating hyperpolarized liquid xenon. (b) After sufficient polarization is obtained in the liquid xenon, solid xenon is formed, by dropping the temperature of the sample tip to 77 K.

reasonably fit with a single Gaussian.<sup>1</sup> This asymmetry disappears and becomes a single Gaussian with a fast freezing time. With this cell, it is shown that temperature gradients throughout the sample are not the cause, as when freezing slow, the line shape remains the same after keeping the back of the cell engulfed in liquid nitrogen for 15 min; quick thermal stabilization throughout a solid xenon sample is also heavily indicated with the  $T_1$  results from Sect. 2.4.

All other cells exhibit different asymmetries depending on freezing time. The results from the 5.5%  $^{129}\text{Xe}$  cell 161A are shown in Fig. B.2, with the real or absorptive channel of a dual-channel spectrometer (Techmag Apollo) phased and normalized plotted against frequency from the carrier frequency 24.57 MHz (2 T field provided

<sup>1</sup>Figures of data are omitted to conserve space in this already-bloated work, as the lower  $^{129}\text{Xe}$  percentages show more dramatic, but similar, effects.

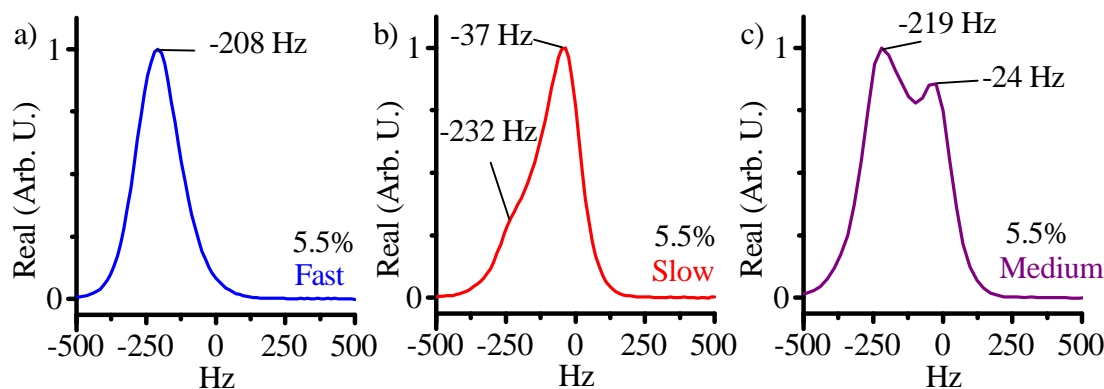


**Figure B.2.** Line shape data from the 5.5%  $^{129}\text{Xe}$  convection cell, 161A. (a) Freezing fast gives a single Gaussian shape. (b) Freezing slow gives double peaks with a frequency separation of roughly 200 Hz. (c) Intermediate freezing time (30 s to 90 s) gives a more pronounced left peak. The resolution binning in frequency space is roughly 13 Hz, therefore the left and right peaks can be mapped to the peaks from the other graphs.

by an Oxford superconducting magnet). The resolution in frequency space in each graph is roughly 13 Hz, so the peaks are safely related to one another across each graph. Similar to the 9% cell, the asymmetry disappears with a fast freezing time, and the line shape becomes a close to a single Gaussian, but requires an additional peak to properly fit. Freezing slow yields a decrease in the left peak, but a sharp increase in the peak that is roughly 200 Hz to the right of the left peak. By freezing intermediately, with a time of 30 s to 90 s (again, the actual timing of the temperature drop of the sample is hard to gauge with the temperature control scheme), both the left and right peaks become pronounced. By adjusting the freeze time, the relative height of the left and right peaks can be adjusted; the slower the freeze, the more pronounced the right peak becomes, and vice versa. The spread peak to peak is 8.33 ppm (parts per million), representing a 0.2 Gauss difference in local field. The experiments are again rerun after keeping the cell at 77 K for roughly 20 min, and no change in line shape is present; in addition, the fast and slow line shapes are easily reproducible after removal and reinsertion of the cell, and changing coils. There are also some early indications that the flip angle of each peak is slightly different, suggesting a different coupling strength to the local spin environment, but the early tests are inconclusive.

The results from the 1.1%  $^{129}\text{Xe}$  cell 161B and the 0.5%  $^{129}\text{Xe}$  cell 161C are shown in Fig. B.3. In the 1.1% cell, the fast freezing again produces basically one peak, with perhaps some hints of smaller peaks at other frequencies. The slow freezing in the 1.1% yields more pronounced edge peaks on top of the single peak. For the 0.5% cell, the line shape with fast freezing is the narrowest single peak of all cells experimented with. In turn, the slow freezing of the 0.5% cell has, perhaps, the most drastic effect on the lineshape, where two additional peaks not apparent in the fast freezing become very pronounced.

Overall, this data indicates that the NMR line shape of solid  $^{129}\text{Xe}$  greatly depends

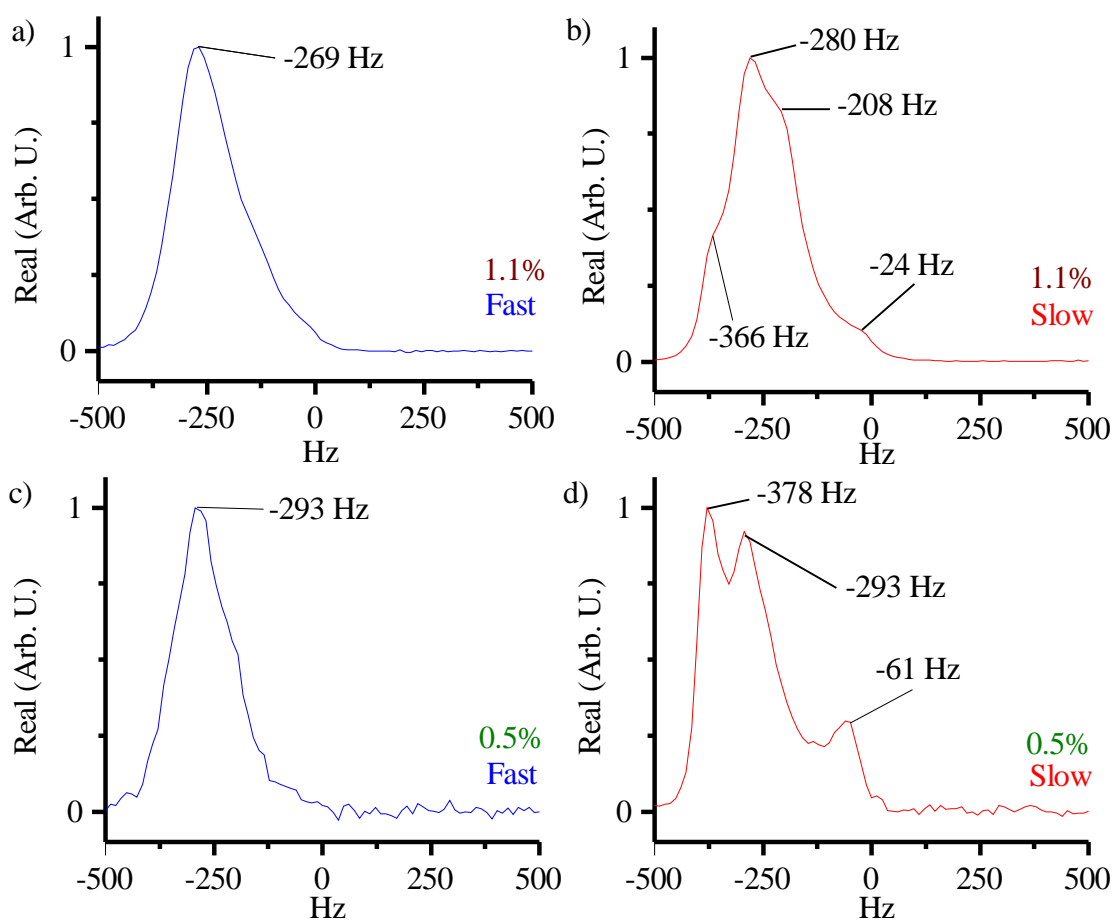


**Figure B.3.** Dilute spin line shape data from cell 161B and cell 161C. (a-b) Line shape data from cell 161B, the 1.1%  $^{129}\text{Xe}$  cell, fast freezing in (a) blue, and slow freezing in (b) red. (c-d) Line shape data from cell 161C, the 0.5%  $^{129}\text{Xe}$  cell, fast freezing in (c) blue, and slow freezing in (d) red.

on structure of the crystal. This effect is perhaps masked, but still present, with high concentrations of  $^{129}\text{Xe}$  in the lattice. If this is the case, then a spin-flip narrowing or spin-locking experiment should give different line shapes depending on crystal formation (see Chapter 2 for the difference in  $T_1$  between ice and snow), even in naturally abundant xenon; unfortunately, physically spinning the sample would probably not be fruitful as the solid is inherently weakly bound, the spinning would most likely alter the solid in some fundamental way. The slightly different frequencies could also be due to the remnant spin-3/2 nuclei in the lattice (recall the enriched spin-less isotope used was  $^{132}\text{Xe}$ , which will naturally have some  $^{131}\text{Xe}$  remaining due to the purification process). It is unclear how there would be a significant difference due to  $^{131}\text{Xe}$  in a  $^{129}\text{Xe}$  line shape by freezing quickly or slowly. A future experiment could allow for  $^{131}\text{Xe}$  detection, or manipulation, as the  $T_1$  of  $^{131}\text{Xe}$  should increase with decreasing concentration due to the quadrupolar interaction, mediated by Raman scattering, being the dominant relaxation mechanism in solid  $^{131}\text{Xe}$ . While there is not sufficient data herein to come to a definite conclusion, the results are intriguing in that the line shapes did not simply narrow up into a Lorentzian, as predicted for dilute spins in a lattice. Different isotopic concentrations of  $^{129}\text{Xe}$  and  $^{131}\text{Xe}$ , the only two stable, spin carrying xenon nuclei, should be explored in the future.<sup>2</sup> The underlying structure of the solid must depend on freezing rate in a critical way, as the slow freezing essentially should allow for some annealing of the solid on its path to 77 K. Between this, and the study of Chapter 2, there seems to be a wealth of basic solid-state NMR research to be done on solid xenon that benefits from the hyperpolarization of xenon isotopes.

---

<sup>2</sup>There are currently four new convection cells with different isotopic concentration awaiting in the Saam lab.

# APPENDIX C

## LONGITUDINAL RELAXATION IN GASEOUS $^{129}\text{Xe}$

*“Time flies like an arrow; fruit flies like a banana.”*

*- Groucho Marx*

### C.1 Introduction

The hyperpolarization of the noble-gas nuclei is achieved by the process of spin-exchange optical pumping (SEOP), by which the polarization of Rb atoms (see Appendix A) is transferred to the noble-gas [19, 119, 120]. Hyperpolarized xenon is used in a variety of interesting applications, including medical imaging [219, 220, 221, 222, 223, 224], materials and protein characterization [225, 226, 123, 227], and magnetometers [228]. This appendix includes a brief description of the history and process of Xe-Rb hyperpolarization, followed by a brief description of the history and theory of longitudinal relaxation ( $T_1$ ) of  $^{129}\text{Xe}$ .

The first assignment given to the author by Prof. Saam was the repair of a low-frequency NMR spectrometer [229], which makes the detection of gaseous hyperpolarized  $^3\text{He}$  and  $^{129}\text{Xe}$  at 30-125 kHz possible. After rebuilding the pulse-receive section of the low-frequency NMR spectrometer and minimizing noise, the spectrometer is ready to be utilized for experiments. The impetus for this experimental set-up was to create a protocol for characterizing the effectiveness of gaseous  $^{129}\text{Xe}$  storage cell coatings, and reaching the self-imposed goal of a 10-hour  $T_1$  time at high pressures of xenon, in low magnetic field, and non-cryogenic temperatures. However, the primary goal of the experiment changed after the initial accumulation of data, to explore an unexpected  $T_1$  temperature dependence previously reported in Berry-Pusey et al. [230] and Anger et al. [231, 232]. Also explored is the surprising adverse effect of including high pressures of  $N_2$  buffer gas at high temperatures. Below, this process of xenon

isolation and measurement is briefly discussed.

## C.2 Rb-Xe Hyperpolarization

The effect of noble-gas nuclei coupling to and relaxing polarized alkali-metal valence-electron states has its origins in Herman et al. [233] and Bouchiat et al. [234, 235]. This effect is suggested to be a hyperfine coupling, where the alkali valence electron polarization is coupled to the nuclear spin state during the short lifetime of a Rb-Xe van der Waals molecule. In the spin Hamiltonian, the relevant terms are

$$H = A\mathbf{I} \cdot \mathbf{S} + \gamma\mathbf{S} \cdot \mathbf{N} + \alpha\mathbf{K} \cdot \mathbf{S}. \quad (\text{C.1})$$

Here,  $A$  is the hyperfine coupling within the alkali atom,  $\mathbf{I}$  is the nuclear spin operator of the alkali atom,  $\gamma$  is the spin-rotation coupling strength,  $\mathbf{S}$  is the alkali-electron spin operator, and  $\mathbf{N}$  is the rotational angular momentum of the alkali-noble gas pair around its center of mass,  $\alpha$  is the strength of the overlap of the wavefunctions of alkali electron and noble-gas nuclei, and  $\mathbf{K}$  is the spin operator of the noble-gas nuclei (see Fig. C.1(a) for details) [236, 237, 238, 239]. The last term is the overlap term that represents the hyperfine interaction between the alkali electron and the noble-gas nuclei, hence the name “hyperpolarization.” This process is not a very efficient one, as

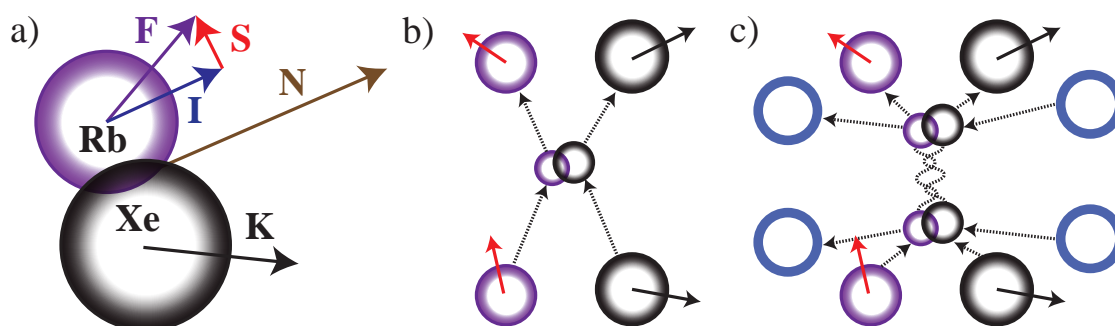


**Figure C.1.** Images of Rb-Xe hyperpolarization processes are shown. (a) A graphical description of Eq. C.1, where all angular momenta are represented by arrows. (b) Example of binary collision between Rb and Xe, where a Rb and Xe collide then separate, and some angular momentum polarization is deposited in the Xe nuclei. (c) Example of a three-body collision between Rb, Xe, and a third body that provides the rotational energy change for molecule formation and break-up. This process becomes dominant at lower gas pressures.

most of a Rb electron's spin is lost to the spin-rotation coupling in the dimer—a sizable fraction of the electron spin is dumped into the rotation angular momentum of a Rb-Xe pair [240]. The spin of the nuclei  $\mathbf{K}$ , however, does not couple well to the rotational angular momentum, so any small fraction of Rb electron spin polarization lost to the nuclei will be accumulate and build up a strong nuclei polarization [241, 242]. There are two primary ways that Rb-Xe dimers form: in binary collisions and longer lived dimers caused by a three-body collision [243, 244], where binary collisions dominate in the high pressure regime (approximately 300 Torr). This is seen as the lifetime of the longer lived molecules is decreased significantly enough that only effective binary collisions occur (see Fig. C.1).

### C.3 Theory

Relaxation in gaseous  $^{129}\text{Xe}$  is previously thought to be due to the spin-rotation interaction mediated by binary collisions [245, 246]; essentially, transient  $^{129}\text{Xe-Xe}$  dimers are formed for a time on the order of picoseconds, and cause relaxation of the nuclei. However, Chann et al. show that persistent dimers, on the order of hundreds of picoseconds, are formed (in a way similar to three-body collisions causing formation of longer lived Rb-Xe molecules) and are a major source of relaxation in many regimes [247]. The difference between transient and persistent dimers is profound in that, before the discovery of persistent dimers, additional relaxation had been thought to be due to interaction with the wall. This caused wall relaxation times to be overestimated, and led to inaccurate interpretations of experimental coating data. Armed with this additional information, cell coatings are better characterized.

From the results of Anger et al. [231], and Berry-Pusey et al. [230], a semi-phenomenological equation for the total gaseous  $^{129}\text{Xe}$  relaxation rate  $\Gamma$  is developed,

$$\Gamma = \frac{[\text{Xe}]}{56.1 \text{ h}} \left( \frac{T_0}{T} \right)^{\frac{1}{2}} + \frac{1}{4.59 \text{ h}} \left( 1 + r \frac{[\text{B}]}{[\text{Xe}]} \right)^{-1} \left( \frac{T_0}{T} \right)^2 + \Gamma_w. \quad (\text{C.2})$$

Here,  $[\text{Xe}]$  is the number density of xenon in amagats,  $[\text{B}]$  is the number density of buffer gas,  $r$  is the break-up coefficient of the buffer gas,  $T_0 = 293 \text{ K}$ ,  $T$  is the temperature that the experiment is conducted at, and  $\Gamma_w$  is the relaxation rate of the wall. Note that any relaxation due to magnetic field gradients is ignored in this expression. The first term in Eq. C.2 is the term due to transient  $^{129}\text{Xe-Xe}$

dimers; this was the first term discovered, as all early experiments had very high pressures of xenon in order to obtain any signal (see Hunt and Carr [64]). The second term represents the relaxation due to persistent  $^{129}\text{Xe}$ -Xe dimers, with an additional phenomenological  $T^2$  temperature dependence added. This temperature dependence is unexpected from a simple statistical mechanical analysis, as shown in Anger et al. [231].

## C.4 Methods

In this work, a flow-through polarizer is used to isolate gaseous, hyperpolarized xenon into a borosilicate glass cell. The method of the accumulation of hyperpolarized xenon is similar to that described in Sect. 2.3.1, with the main differences being the accumulation cell and accumulation time. Prior to accumulation, a gaseous  $^{129}\text{Xe}$  storage cell is attached to the flow-through polarizer via the coldfinger, and evacuated. The accumulation cell (designed by Geoff Schrank and manufactured by University of Utah glassblower Kevin Teaford) in this experiment is a large coldfinger that is held at 77 K (see Fig. C.2(a)), where naturally abundant xenon is accumulated from a 1000:500:10 sccm ratio of He:N<sub>2</sub>:Xe for roughly 50 min. After accumulation of solid xenon, the coldfinger is evacuated of all remaining gas, and isolated from the rest of the system using the coldfinger valves (the flow-through polarizer is shut down during this step). The storage cell is then evacuated, and while the coldfinger is isolated, the frozen xenon is revolatilized by removing the liquid nitrogen dewar surrounding the coldfinger and applying a bath of boiling water to the exterior of the coldfinger. The total revolatilization time takes less than 30 s if done properly, and speed is needed during this process or the  $^{129}\text{Xe}$  will quickly lose its built-up polarization in the phase transition. Once all of the xenon is gas, the storage cell is isolated from the remainder of the system, and a connection is opened between the coldfinger and storage cell, filling the approximately 150 cc storage cell to roughly 14.5 psig.

The storage cell is closed and transported to the center of an oven in a measurement field held at roughly 30 Gauss provided by a large Helmholtz coil, and a Litz coil tuned to 45.45 kHz is placed on the tip of the storage cell. At this point, a pure xenon  $T_1$  measurement takes place, or buffer gas (helium or nitrogen)

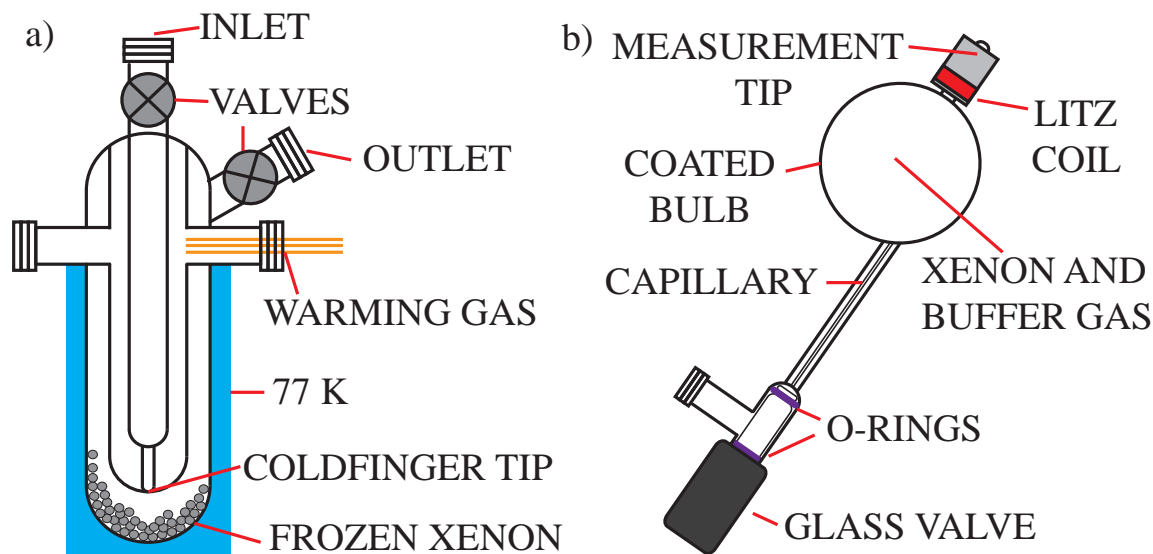


**Figure C.2.** Schematics of the coldfinger and storage cell are shown. (a) Schematic of coldfinger used in gaseous  $^{129}\text{Xe}$   $T_1$  relaxation experiments. The exterior of the coldfinger is held in liquid nitrogen, and warming gas is supplied to the coldfinger tip to prevent freezing. Frozen xenon is accumulated in the bottom of the coldfinger. (b) A schematic of a coated gaseous  $^{129}\text{Xe}$  storage cell is shown. The capillary discourages polarization loss to the valve, but allows quick access for buffer gas filling. The majority of the xenon experiences intrinsic relaxation due to persistent and transient dimers, as well as wall relaxation. A 150-200 turn Litz-wire wound coil is tuned to a frequency of 45.45 kHz, and causes a negligible loss in polarization due to the pulse.

is introduced for a pressure dependent  $T_1$  measurement. The buffer gas is introduced using a stainless steel flexible transfer line attached to a purified nitrogen or helium bottle, with a roughing pump in line. The transfer line is first blown out with the buffer gas when attaching the transfer line to the storage cell, then evacuated and “rinsed” multiple times using the roughing pump and buffer gas. The gauge on the buffer gas controls the rough pressure desired in the storage cell, with an exact measurement of the storage cell pressure measured after the  $T_1$  measurement takes place. Xenon pressure in the cell is obtained by calibrating the pressure measured on the flow-through polarizer, after recording the values of the pure xenon pressures after their  $T_1$  measurements. After getting the desired ratio of buffer gas to xenon, the PTFE air-flow oven can be set up until the melting point of PTFE, but the two types of Litz wire used have coating temperature limits of 180°C and 210°, becoming

the temperature-limiting factor in this experiment.

After the temperature and buffer gas ratio is set, a  $T_1$  experiment is ran. The home-built, low-field spectrometer is modified to have its trigger taken over by a National Instruments LabVIEW program and NIDAQ card, developed to automatically trigger and record the FID generated by the pulse-receive of the spectrometer. The SNR for a single shot at the beginning of the experiment is roughly 10-1. After sufficient data are taken (usually two-three times longer than  $T_1$ ), the data are processed using a MATLAB<sup>®</sup> script. The MATLAB<sup>®</sup> code zero-fills, apodizes, FFT's, and autophases the single channel NMR data, after which the line shape is integrated over a set range.<sup>1</sup> The processed data are then plotted against time and fit using a single exponential using Origin, extracting  $T_1$  for a given measurement.

A simple protocol to characterize the <sup>129</sup>Xe storage cell coatings goes as follows:

1. Choose a set of coatings to be experimented upon.
2. Run a set of temperature dependent, xenon-only experiments with the coated cell.
3. Run a set of temperature dependent, buffer-gas saturated experiments.
4. Back out a wall rate using Eq. C.2.
5. Purposefully degrade the coating by introducing oxygen into the cell, and flush out cell.
6. Repeat steps 2-3 to determine durability of coating.

## C.5 Results and Discussion

The first set of experiments undertaken compared three different coatings: an 18-member hydrocarbon, an 8-member hydrocarbon, and an 8-member fluorocarbon. (A study was to be attempted using PFTE bags, but another group published the results of that study [248].) Of the three, the 18-member hydrocarbon, in cell 151B, performed the best (longest  $T_1$ ) and remained the most durable and reproducible

---

<sup>1</sup>The code can be requested from the author at [limes.mark@gmail.com](mailto:limes.mark@gmail.com).

(the  $T_1$  at room temperature, xenon-only remained consistent) over the course of three years, although the full protocol is not undertaken on the cell, as it is used for the remainder of the experiments presented here.

The first set of experiments using cell 151B resulted from the attempt to complete the cell-coating characterization protocol, and are shown in Fig. C.3. In these experiments, the temperature range is explored up to 200 °C, which is below the limit of the coating on the Litz wire for the NMR coil. When the nitrogen saturation runs are attempted with a 9:1 to 10:1  $N_2$  to xenon ratio, an interesting result appears in that, while the saturation of nitrogen helps at room temperature, there seems to be a somewhat harmful effect taking place with increased temperature. The presence of an oxygen leak, or oxygen contamination in the purified nitrogen bottle, is eliminated entirely by attempt to run the nitrogen through various-quality level filters, and

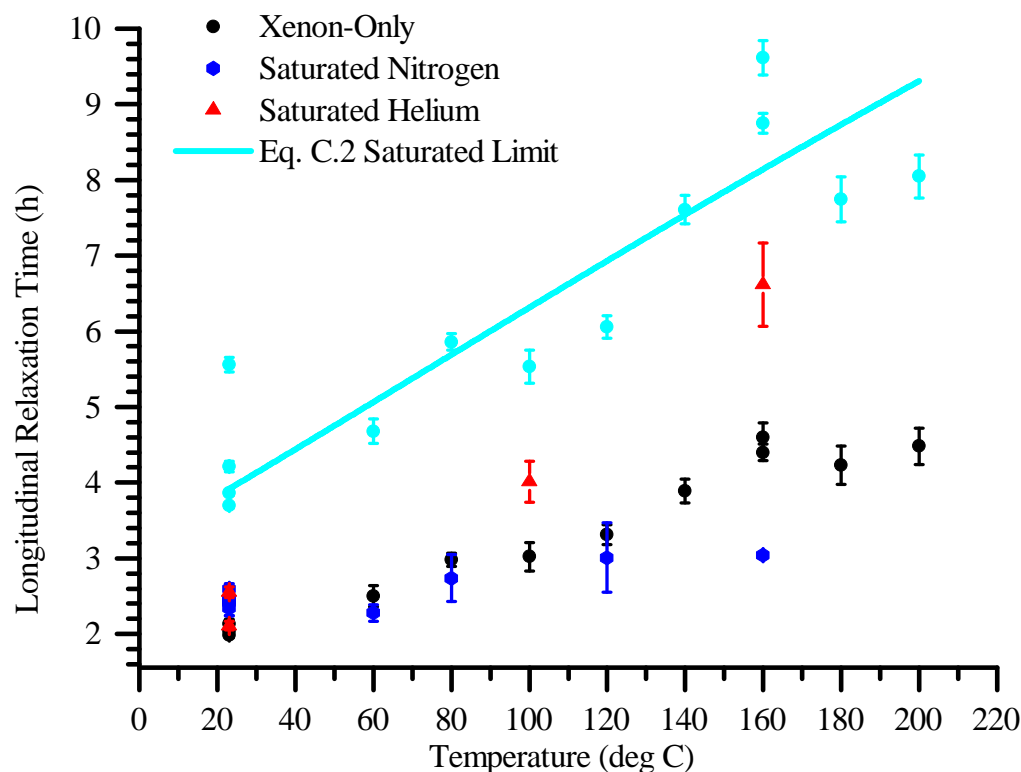


**Figure C.3.** The raw data from a set of xenon-only, helium saturated, and nitrogen saturated runs are shown. In light blue is the expected limit extracted from Eq. C.2, along with a fit to an Arrhenius equation.

helium-leak checking the filling connection during every filling with nitrogen. This is also suggested by the data at room temperature showing an increase in  $T_1$ , indicating there is not much oxygen present in the  $N_2$  bottle.

Also shown in Fig. C.3 is the result of the same ratio of He buffer gas to xenon, in a range of 9:1 to 10:1, using the exact same filling station, with nonpurified helium. Because the He:Xe ratio is not considered to be in saturation, it is very surprising that He buffer gas is much more effective than  $N_2$  at higher temperatures. Moreover, He was previously found to be considerably less effective in breaking up persistent xenon dimers than  $N_2$ ; in Eq. C.2,  $r = 0.25$  for He compared to  $r = 1.0$  for  $N_2$  as measured by Chann et al. [247], and  $r = 0.5$  for  $N_2$  as measured by Anger et al. [231]. Running the He experiment in the same set-up as  $N_2$  gives another indication that oxygen is not playing a role of increased relaxation. In light blue in Fig. C.3, there is also a plot of the increase in  $T_1$  due to saturation of buffer gas (shutting off of the persistent term) predicted by Eq. C.2. Thus, if Eq. C.2 is correct, the He has not yet approached saturation, which is expected from the previous work. The fit to the predicted saturation data also loosely follows an Arrhenius fit, which would indicate that a  $T^2$  temperature dependence is present in the xenon-only data, but more data are required to justify this claim in this way.

From the data in Fig. C.3, there arises a need to further understand the dependence of  $^{129}\text{Xe}$   $T_1$  relaxation on  $N_2$  pressure. The preliminary results of the  $N_2$  pressure-dependent measurements at room temperature are shown in Fig. C.4. Interestingly, the data seem to saturate much earlier than the 7:1 ratio as previously expected. Also of interest are the two fits to the data, both using Eq. C.2, with a floating break-up coefficient  $r$  and wall relaxation rate  $\Gamma_w$ . The difference in the two fits stems from using a floating term in front of the persistent dimer piece of Eq. C.2, or fixing the term at 4.59 h. If the term is fixed at 4.59 h (green fit), then the break-up coefficient for  $N_2$  is extraordinarily small at  $r = 0.13 \pm 0.02$ , and somewhat *weaker* than the previously measured He break-up coefficient. The green fit also produces  $1/\Gamma_w = 4.20 \pm 0.12$  h, a wall relaxation time that is in line with the predicted plots shown in Fig. C.3. If the persistent timer term is allowed to float (blue fit), then it is found to have a value of  $8.03 \pm 0.94$  h, roughly double of the fixed fit. In addition,

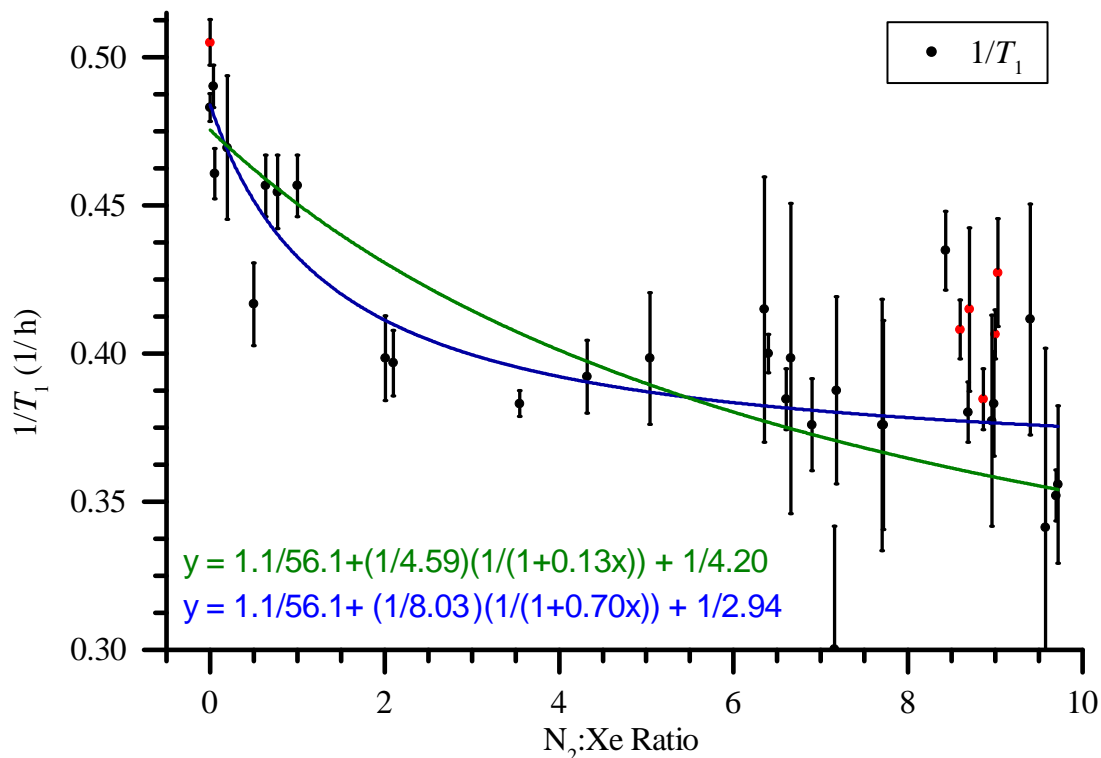


**Figure C.4.** The raw data from a set of nitrogen dependent runs at room temperature are shown. Also shown are two fits to the data using Eq. C.2, with the red points excluded due to experimental error. The green fit has the number in front of the persistent term in Eq. C.2 fixed at 4.59. The blue fit has a floating number in front of the persistent term. Both fits have a floating break-up coefficient  $r$  and wall relaxation rate  $\Gamma_w$ .

the floating blue fit gives  $r = 0.70 \pm 0.34$ , in line with previous measurements, and a wall relaxation time of  $1/\Gamma_w = 2.94 \pm 0.12$  h, which is much closer to the actual room temperature data shown in Fig. C.3. However, all of this is quite speculative until higher quality data are found at low and high  $N_2$ :Xe ratios, as it is difficult to determine which fit is more accurate from the ratios of 6-10.

In quasiconclusion, there is much future work to be done on this front. With the findings presented in Cleveland et al. [249] regarding  $N_2$ - $^{83}\text{Kr}$  relaxation, it is not unexpected to see a turnaround in  $^{129}\text{Xe}$   $T_1$  from increasing  $N_2$  pressure. High-field experiments are currently underway to achieve this turnaround if one exists, as very low xenon pressures are needed to obtain signal at very high field with hyperpolarized

$^{129}\text{Xe}$ . Thus, very high ratios of  $\text{N}_2$  to xenon can be obtained, at least 50:1 with initial projections. The results of this experiment will be telling in one way or the other, as in, if no turnaround point for  $T_1$  with increasing  $\text{N}_2$  pressure is seen, there is an unexpected temperature-dependence with saturated  $\text{N}_2$ ; if there is simply a lower turnaround point than expected, it would give key information in the alteration to Eq. C.2. Also underway are experiments that fully map the temperature and ratio dependence of He in  $^{129}\text{Xe}$  storage cells, as He may be more effective than initially predicted.<sup>2</sup> The results of this work will have a lofty impact on the characterization of coatings for  $^{129}\text{Xe}$  storage cells, and perhaps in  $^{129}\text{Xe}$   $T_1$  mechanisms in writ large.

---

<sup>2</sup>Chann et al., in [247], use a quartz cell, which helium is known to leak through to some extent.

## REFERENCES

- [1] D. Halliday, R. Resnick, and J. Walker, *Fundamentals of Physics* (John Wiley & Sons, New York, 2002).
- [2] P. A. Tipler and R. Llewellyn, *Modern Physics* (W. H. Freeman, New York, 2002).
- [3] D. J. Griffiths, *Introduction to Electrodynamics* (Prentice Hall, Upper Saddle River, 1999).
- [4] D. J. Griffiths, *Introduction to Quantum Mechanics* (Prentice Hall, Upper Saddle River, 1995).
- [5] E. Schrödinger. Phys. Rev. **28**, 1049 (1926).
- [6] L. D. Landau and E. M. Lifshitz, *Quantum Mechanics: Non-Relativistic Theory* (Butterworth-Heinemann, Oxford, 1977).
- [7] J. J. Sakurai and S. F. Tuan, *Modern Quantum Mechanics* (Addison-Wesley Publishing Company, Boston, 1994).
- [8] J. von Neumann, Göttinger Nachrichten **1**, 245 (1927).
- [9] U. Fano, Rev. Mod. Phys. **29**, 74 (1957).
- [10] R. P. Feynman, *Statistical Mechanics: A Set Of Lectures* (Westview Press, Boulder, 1998).
- [11] F. Schwabl, *Statistical Mechanics* (Springer-Verlag GmbH, Dubai, 2002).
- [12] R. P. Feynman, R. B. Leighton, M. L. Sands, and M. A. Gottlieb, *The Feynman Lectures on Physics* (Pearson/Addison-Wesley, Boston, 1963).
- [13] G. Breit and I. I. Rabi, Phys. Rev. **38**, 2082 (1931).
- [14] J. Singh (unpublished, 2009).
- [15] L. D. Landau and E. M. Lifshitz, *The Classical Theory of Fields* (Butterworth-Heinemann, Oxford, 1975).
- [16] J. D. Jackson, *Classical Electrodynamics* (Wiley, New York, 1975).
- [17] W. Heitler, *The Quantum Theory of Radiation* (Dover, New York, 1954).
- [18] V. B. Berestetskii, E. M. Lifshitz, and L. P. Pitaevskii, *Quantum Electrodynamics* (Butterworth-Heinemann, Oxford, 1982).

- [19] W. Happer, *Rev. Mod. Phys.* **44**, 169 (1972).
- [20] W. Happer, Y.-Y. Jau, and T. Walker, *Optically Pumped Atoms* (Wiley, Weinheim, 2010).
- [21] I. I. Rabi, J. R. Zacharias, S. Millman, and P. Kusch, *Phys. Rev.* **53**, 318 (1938).
- [22] M. A. Nielsen and I. L. Chuang, *Quantum Computation and Quantum Information* (Cambridge University Press, Cambridge, 2000).
- [23] W. Heisenberg, *Z. Phys.* **43**, 172 (1927).
- [24] H. P. Robertson, *Phys. Rev.* **34**, 163 (1929).
- [25] P. Busch, In *Time in Quantum Mechanics*, edited by J. G. Muga, R. S. Mayato, and I. L. Egusquiza (Springer, Berlin, 2007).
- [26] E. M. Purcell, H. C. Torrey, and R. V. Pound, *Phys. Rev.* **69**, 37 (1946).
- [27] F. Bloch, *Phys. Rev.* **70**, 460 (1946).
- [28] R. K. Wangsness and F. Bloch, *Phys. Rev.* **89**, 728 (1953).
- [29] F. Bloch, *Phys. Rev.* **102**, 104 (1956).
- [30] J. A. Pople, *High-resolution Nuclear Magnetic Resonance* (McGraw-Hill, New York, 1959).
- [31] A. Abragam, *Principles of Nuclear Magnetism* (Oxford University Press, London, 1983).
- [32] C. P. Slichter, *Principles of Magnetic Resonance* (Springer, New York, 1996).
- [33] R. Ernst, G. Bodenhausen, and A. Wokaun, *Principles of Nuclear Magnetic Resonance in One and Two Dimensions* (Oxford University Press, London, 1987).
- [34] B. Cowan, *Nuclear Magnetic Resonance and Relaxation* (Cambridge University Press, Cambridge, 2005).
- [35] C. Boehme, *Dynamics of Spin-dependent Charge Carrier Recombination* (Cuvillier Verlag, Göttingen, 2003).
- [36] K. J. van Schooten, Ph.D. thesis, University of Utah, 2013.
- [37] J. Wrachtrup, C. von Borczyskowski, J. Bernard, M. Orritt, and R. Brown, *Nature* **363**, 244 (1993).
- [38] G.-Q. Liu, X.-Y. Pan, Z.-F. Jiang, N. Zhao, and R.-B. Liu, *Sci. Rep.* **2**, 432 (2012).
- [39] T. W. Kornack, R. K. Ghosh, and M. V. Romalis, *Phys. Rev. Lett.* **95**, 230801 (2005).

- [40] M. P. Ledbetter, I. M. Savukov, V. M. Acosta, D. Budker, and M. V. Romalis, *Phys. Rev. A* **77**, 033408 (2008).
- [41] A. D. Ballard, Ph.D. thesis, Univeristy of Utah, 2010.
- [42] C. Ospelkaus, U. Warring, Y. Colombe, K. R. Brown, J. M. Amini, D. Leibfried, and D. J. Wineland, *Nature* **476**, 181 (2011).
- [43] J. W. Britton, B. C. Sawyer, A. C. Keith, C.-C. J. Wang, J. K. Freericks, H. Uys, M. J. Biercuk, and J. J. Bollinger, *Nature* **484**, 489 (2012).
- [44] M. P. Ledbetter, T. Theis, J. W. Blanchard, H. Ring, P. Ganssle, S. Appelt, B. Blümich, A. Pines, and D. Budker, *Phys. Rev. Lett.* **107**, 107601 (2011).
- [45] T. Theis, J. W. Blanchard, M. C. Butler, M. P. Ledbetter, D. Budker, and A. Pines, *Chem. Phys. Lett.* **580**, 160 (2013).
- [46] P. A. M. Dirac, *The Principles of Quantum Mechanics* (Oxford University Press, Oxford, 1981).
- [47] N. A. Jelly, *Fundamentals of Nuclear Physics* (Cambridge University Press, Cambridge, 1990).
- [48] J. H. Van Vleck, *Phys. Rev.* **74**, 1168 (1948).
- [49] N. F. Ramsey, *Phys. Rev.* **78**, 699 (1950).
- [50] N. F. Ramsey, *Phys. Rev.* **86**, 243 (1952).
- [51] A. G. Redfield, *IBM J. Res. Dev.* **1**, 19 (1957).
- [52] A. G. Redfield, *Science* **164**, 1015 (1969).
- [53] A. A. Abrikosov, L. P. Gorkov, I. E. Dzyaloshinski, and I. E. Dzialoshinskii, *Methods of Quantum Field Theory in Statistical Physics* (Dover Publications, New York, 1975).
- [54] D. I. Hoult and B. Bhakar, *Concepts Magn. Reson.* **9**, 277 (1997).
- [55] J. Jeener and F. Henin, *J. Chem. Phys.* **116**, 8036 (2002).
- [56] R. J. Glauber, *Phys. Rev.* **131**, 2766 (1963).
- [57] N. C. Menicucci and C. M. Caves, *Phys. Rev. Lett.* **88**, 167901 (2002).
- [58] B. P. Lanyon, M. Barbieri, M. P. Almeida, and A. G. White, *Phys. Rev. Lett.* **101**, 200501 (2008).
- [59] P. O. Boykin, T. Mor, V. Roychowdhury, and F. Vatan, *Natural Computing* **9**, 329 (2010).
- [60] J. A. Jones, *Prog. Nucl. Magn. Reson. Spect.* **59**, 91 (2011).
- [61] F. J. Adrian, Ph.D. thesis, Cornell University, 1955.

- [62] H. C. Torrey, Phys. Rev. **130**, 2306 (1963).
- [63] R. L. Streever and H. Y. Carr, Phys. Rev. **121**, 20 (1961).
- [64] E. R. Hunt and H. Y. Carr, Phys. Rev. **130**, 2302 (1963).
- [65] N. Bloembergen, E. M. Purcell, and R. V. Pound, Phys. Rev. **73**, 679 (1948).
- [66] G. C. Wick, Phys. Rev. **73**, 51 (1948).
- [67] W. M. Yen and R. E. Norberg, Phys. Rev. **131**, 269 (1963).
- [68] J. Naghizadeh and S. A. Rice, J. Chem. Phys. **36**, 2710 (1962).
- [69] J. R. Packard and C. A. Swenson, J. Phys. Chem. Solids **24**, 1405 (1963).
- [70] D. Brinkmann, Phys. Rev. Lett. **13**, 187 (1964).
- [71] J. Lurie, J. L. Feldman, and G. K. Horton, Phys. Rev. **150**, 180 (1966).
- [72] D. Brinkmann and H. Y. Carr, Phys. Rev. **150**, 174 (1966).
- [73] F. J. Adrian, Phys. Rev. **136**, A980 (1964).
- [74] W. W. Warren and R. E. Norberg, Phys. Rev. **148**, 402 (1966).
- [75] J. Van Kranendonk, Physica **20**, 781 (1954).
- [76] I. Waller, Z. Phys. **79**, 370 (1932).
- [77] W. W. Warren and R. E. Norberg, Phys. Rev. **154**, 277 (1967).
- [78] D. F. Cowgill and R. E. Norberg, Phys. Rev. B **6**, 1636 (1972).
- [79] E. Fukushima and S.B. Roeder, *Experimental Pulse NMR: A Nuts and Bolts Approach* (Westview Press, Boulder, 1993).
- [80] G. D. Cates, D. R. Benton, M. Gatzke, W. Happer, K. C. Hasson, and N. R. Newbury, Phys. Rev. Lett. **65**, 2591 (1990).
- [81] M. Gatzke, Ph.D. thesis, Princeton University, 1992.
- [82] M. Gatzke, G. D. Cates, B. Driehuys, D. Fox, W. Happer, and B. Saam, Phys. Rev. Lett. **70**, 690 (1993).
- [83] N. N. Kuzma, B. Patton, K. Raman, and W. Happer, Phys. Rev. Lett. **88**, 147602 (2002).
- [84] B. Patton, Ph.D. thesis, Princeton University, 2007.
- [85] A. Abragam and M. Goldman, *Nuclear Magnetism: Order and Disorder* (Clarendon, Oxford, 1982).
- [86] Z. Wu, T. G. Walker, and W. Happer, Phys. Rev. Lett. **54**, 1921 (1985).

- [87] D. Raftery, H. Long, T. Meersmann, P. J. Grandinetti, L. Reven, and A. Pines, *Phys. Rev. Lett.* **66**, 584 (1991).
- [88] D. Raftery, H. Long, L. Reven, P. Tang, and A. Pines, *Chem. Phys. Lett.* **191**, 385 (1992).
- [89] S. Lang, I. L. Moudrakovski, C. I. Ratcliffe, J. A. Ripmeester, and G. Santyr, *Appl. Phys. Lett.* **80**, 886 (2002).
- [90] B. Saam, Ph.D. thesis, Princeton University, 1995.
- [91] N. N. Kuzma (private communication, 2012).
- [92] R. J. Fitzgerald, M. Gatzke, David C. Fox, G. D. Cates, and W. Happer, *Phys. Rev. B* **59**, 8795 (1999).
- [93] A. J. Vega, P. A. Beckmann, S. Bai, and C. Dybowski, *Phys. Rev. B* **74**, 214420 (2006).
- [94] N. N. Kuzma, D. Babich, and W. Happer, *Phys. Rev. B* **65**, 134301 (2002).
- [95] L. C. Hebel and C. P. Slichter, *Phys. Rev.* **113**, 1504 (1959).
- [96] C. Kittel, *Introduction to Solid State Physics* (Wiley, New York, 1971).
- [97] D. A. Varshalovich, A. N. Moskalev, and V. K. Khersonskii, *Quantum Theory of Angular Momentum: Irreducible Tensors, Spherical Harmonics, Vector Coupling Coefficients, 3 Nj Symbols* (World Scientific, London, 1988).
- [98] P. R. Granfors, A. T. Macrander, and R. O. Simmons, *Phys. Rev. B* **24**, 4753 (1981).
- [99] G. L. Samuelson, Ph.D. thesis, University of Utah, 2005.
- [100] S. W. Morgan, Ph.D. thesis, University of Utah, 2007.
- [101] D. M. TonThat, M. Ziegeweid, Y.-Q. Song, E. J. Munson, S. Appelt, A. Pines, and J. Clarke, *Chem. Phys. Lett.* **272**, 245 (1997).
- [102] Y.-Q. Song, R. E. Taylor, and A. Pines, *Solid State Nucl. Magn. Reson.* **10**, 247 (1998).
- [103] S. W. Morgan, B. V. Fine, and B. Saam, *Phys. Rev. Lett.* **101**, 067601 (2008).
- [104] E. G. Sorte, B. V. Fine, and B. Saam, *Phys. Rev. B* **83**, 064302 (2011).
- [105] E. G. Sorte, B. V. Fine, and B. Saam, *Phys. Rev. B* **85**, 174425 (2012).
- [106] B. V. Fine, T. A. Elsayed, E. G. Sorte, and B. Saam, *Phys. Rev. B* **86**, 054439 (2012).
- [107] E. G. Sorte, Ph.D. thesis, University of Utah, 2011.

- [108] J. W. McNabb, D. N. Balakishiyeva, and A. Honig, *J. Magn. Reson.* **188**, 206 (2007).
- [109] B. Driehuys, G. D. Cates, E. Miron, K. Sauer, D. K. Walter, and W. Happer, *Appl. Phys. Lett.* **69**, 1668 (1996).
- [110] R. Seydoux, A. Pines, M. Haake, and J. A. Reimer, *J. Phys. Chem. B* **103**, 4629 (1999).
- [111] A. L. Zook, B. B. Adhyaru, and C. R. Bowers, *J. Magn. Reson.* **159**, 175 (2002).
- [112] I. C. Ruset, S. Ketel, and F. W. Hersman, *Phys. Rev. Lett.* **96**, 053002 (2006).
- [113] G. Schrank, Z. Ma, A. Schoeck, and B. Saam, *Phys. Rev. A* **80**, 063424 (2009).
- [114] G. M. Schrank, Ph.D. thesis, University of Utah, 2009.
- [115] B. Chann, I. Nelson, and T. G. Walker, *Opt. Lett.* **25**, 1352 (2000).
- [116] T. G. Walker, B. Chann, and I. A. Nelson, US 6,584,113 B1, 06 (2003).
- [117] E Babcock, B. Chann, I. A. Nelson, and T. G. Walker, *Appl. Opt.* **44**, 3098 (2005).
- [118] Z. Buchta, O. Číp, and J. Lazar, *Meas. Sci. Tech.* **18**, N77 (2007).
- [119] T. G. Walker and W. Happer, *Rev. Mod. Phys.* **69**, 629–642 (1997).
- [120] S. Appelt, A. B. Baranga, C. J. Erickson, M. V. Romalis, A. R. Young, and W. Happer, *Phys. Rev. A* **58**, 1412 (1998).
- [121] Z. Ma, Ph.D. thesis, University of Utah, 2012.
- [122] T. Su, G. L. Samuelson, S. W. Morgan, G. Laicher, and B. Saam, *Appl. Phys. Lett.* **85**, 2429 (2004).
- [123] C. F. M. Clewett, S. W. Morgan, B. Saam, and T. Pietra, *Phys. Rev. B* **78**, 235402 (2008).
- [124] P. Horowitz and W. Hill, *The Art of Electronics* (Cambridge University Press, Cambridge, 1989).
- [125] D. D. Wheeler and M. S. Conradi, *Concepts Magn. Reson.* **40A**, 1 (2012).
- [126] M. Hanni, P. Lantto, and J. Vaara, *Phys. Chem. Chem. Phys.* **11**, 2485 (2009).
- [127] W. Franklin, *Phys. Rev.* **180**, 682 (1969).
- [128] B. G. Dick, *Phys. Rev. B* **16**, 3359 (1977).
- [129] V. Hizhnyakov and G. Benedek, *Euro. Phys. J. B* **43**, 431 (2005).
- [130] R. E. Peierls, *Quantum Theory of Solids* (Clarendon Press, Oxford, 1996).

- [131] G. Leibfried, *Handbuch der Physik* (Springer-Verlag, Berlin, 1955).
- [132] P. Carruthers, *Rev. Mod. Phys.* **33**, 92 (1961).
- [133] G. R. Kutsishvili. *Publ. Georg. Inst. Sci.* **IV**, 1 (1956).
- [134] R. L. Mieher, *Phys. Rev. Lett.* **4**, 57 (1960).
- [135] R. L. Mieher, *Phys. Rev.* **125**, 1537 (1962).
- [136] C. P. Poole and H. A. Farach, *The Theory of Magnetic Resonance* (John Wiley & Sons, Hoboken, 1972).
- [137] R. O. Pohl, *Amer. J. Phys.* **55**, 240 (1987).
- [138] D. G. Cahill and R. O. Pohl, *Ann. Rev. Phys. Chem.* **39**, 93 (1988).
- [139] D. G. Cahill, S. K. Watson, and R. O. Pohl, *Phys. Rev. B* **46**, 6131 (1992).
- [140] R. O. Pohl, X. Liu, and E. J. Thompson, *Rev. Mod. Phys.* **74**, 991 (2002).
- [141] P. E. Hopkins and E. S. Piekos, *Applied Physics Letters* **94**, 181901 (2009).
- [142] J. A. Reissland, *The Physics of Phonons* (Wiley, New York, 1973).
- [143] W. Eisenmenger and A. A. Kaplianskii, *Nonequilibrium Phonons in Nonmetallic Crystals* (North-Holland Publ., Amsterdam, 1986).
- [144] G. P. Srivastava, *The Physics of Phonons* (A. Hilger, Briston, 1990).
- [145] J. M. Ziman. *Electrons and Phonons: The Theory of Transport Phenomena in Solids* (OUP Oxford, Oxford, 2001).
- [146] P. A. Fedders, *Phys. Rev. B* **15**, 3297 (1977).
- [147] B. E. Sirovich and R. E. Norberg, *Phys. Rev. B* **15**, 5107 (1977).
- [148] B. V. Rollin and J. Hatton, *Phys. Rev.* **74**, 346 (1948).
- [149] J. Van Kranendonk and M. Walker, *Phys. Rev. Lett.* **18**, 701 (1967).
- [150] M. B. Walker, *Phys. Rev.* **162**, 199 (1967).
- [151] J. Van Kranendonk and M. B. Walker, *Can. J. Phys.* **46**, 2441 (1968).
- [152] A. Pietila, *J. Phys. C* **7**, 211 (1974).
- [153] R. C. Zamar and C. E. González, *Phys. Rev. B* **51**, 932 (1995).
- [154] D. F. Cowgill and R. E. Norberg, *Phys. Rev. B* **8**, 4966 (1973).
- [155] M. E. Limes, J. Wang, W. J. Baker, S.-Y. Lee, B. Saam, and C. Boehme, *Phys. Rev. B* **87**, 165204 (2013).
- [156] D. Kaplan, I. Solomon, and N.F. Mott, *J. Phys. Lett.* **39**, 51 (1978).

- [157] D. J. Lepine, Phys. Rev. B **6**, 436 (1972).
- [158] E. L. Frankevich, A. A. Lymarev, I. Sokolik, F. E. Karasz, S. Blumstengel, R. H. Baughman, and H. H. Hörhold, Phys. Rev. B **46**, 9320 (1992).
- [159] C. Boehme and K. Lips, Phys. Rev. B **68**, 245105 (2003).
- [160] D. R. McCamey, G. W. Morley, H. A. Seipel, L. C. Brunel, J. van Tol, and C. Boehme, Phys. Rev. B **78**, 045303 (2008).
- [161] J. Behrends, A. Schnegg, K. Lips, E. A. Thomsen, A. K. Pandey, I. D. W. Samuel, and D. J. Keeble, Phys. Rev. Lett. **105**, 176601 (2010).
- [162] R. Müller, P. Kanschä, S. Von Aichberger, K. Lips, and W. Fuhs, J. of Non-Cryst. Solids **266**, B:1124–1128 (2000).
- [163] W. J. Baker, D. R. McCamey, K. J. van Schooten, J. M. Lupton, and C. Boehme, Phys. Rev. B **84**, 165205 (2011).
- [164] W. J. Baker, K. Ambal, D. P. Waters, R. Baarda, H. Morishita, K. van Schooten, D. R. McCamey, J. M. Lupton, and C. Boehme, Nat. Commun. **3**, 898 (2012).
- [165] H. Morishita, L. S. Vlasenko, H. Tanaka, K. Semba, K. Sawano, Y. Shiraki, M. Eto, and K. M. Itoh, Phys. Rev. B **80**, 205206 (2009).
- [166] S.-Y. Lee, S.-Y. Paik, D. R. McCamey, J. Yu, P. L. Burn, J. M. Lupton, and C. Boehme, J. Amer. Chem. Soc. **133**, 2019 (2011).
- [167] C. Boehme and K. Lips, Phys. Rev. Lett. **91**, 246603 (2003).
- [168] D. R. McCamey, H. A. Seipel, S.-Y. Paik, M. J. Walter, N. J. Borys, J. M. Lupton, and C. Boehme, Nat. Mater. **7**, 723 (2008).
- [169] A. R. Stegner, C. Boehme, H. Huebl, M. Stutzmann, K. Lips, and M. S. Brandt, Nat. Phys. **2**, 835 (2006).
- [170] A. Schweiger and G. Jeschke, *Principles of Pulse Electron Paramagnetic Resonance* (Oxford University Press, Oxford, 2001).
- [171] N. M. Atherton, *Principles of Electron Spin Resonance* (Ellis Horwood, Chichester, 1993).
- [172] V. Rajevac, C. Boehme, C. Michel, A. Gliesche, K. Lips, S. D. Baranovskii, and P. Thomas, Phys. Rev. B **74**, 245206 (2006).
- [173] A. Gliesche, C. Michel, V. Rajevac, K. Lips, S. D. Baranovskii, F. Gebhard, and C. Boehme, Phys. Rev. B **77**, 245206 (2008).
- [174] C. Michel, A. Gliesche, S. D. Baranovskii, K. Lips, F. Gebhard, and C. Boehme, Phys. Rev. B **79**, 052201 (2009).
- [175] R. Glenn, W. J. Baker, C. Boehme, and M. E. Raikh, Phys. Rev. B **87**, 155208 (2013).

- [176] R. Glenn, M. E. Limes, B. Saam, C. Boehme, and M. E. Raikh, *Phys. Rev. B* **87**, 165205 (2013).
- [177] S.-Y. Lee, S. Paik, D. R. McCamey, and C. Boehme, *Phys. Rev. B* **86**, 115204 (2012).
- [178] R. Haberkorn and W. Dietz, *Solid State Commun.* **35**, 505 (1980).
- [179] A. Abragam and B. Bleaney. *Electron Paramagnetic Resonance of Transition Ions*. (Oxford University Press, London, 1970).
- [180] P. W. Anderson, in *Theory of Magnetic Exchange Interactions: Exchange in Insulators and Semiconductors*, edited F. Seitz and D. Turnbull (Academic Press, New York, 1963).
- [181] R. J. Elliot, in *Polarons and Excitons*, edited by C. G. Kuper and G. D. Whitfield (Plenum Press, New York, 1963).
- [182] J. H. Van Vleck. *The Theory of Electric and Magnetic Susceptibilities* (Oxford University Press, Oxford, 1952).
- [183] D. R. McCamey, K. J. van Schooten, W. J. Baker, S.-Y. Lee, S.-Y. Paik, J. M. Lupton, and C. Boehme, *Phys. Rev. Lett.* **104**, 017601 (2010).
- [184] A. Weber, O. Schiemann, B. Bode, and T. F. Prisner, *J. Magn. Reson.* **157**, 277 (2002).
- [185] K. Lips, C. Boehme, and T. Ehara, *J. of Optoelect. Adv Mater.* **7**, 13 (2005).
- [186] T. W. Herring, S.-Y. Lee, D. R. McCamey, P. C. Taylor, K. Lips, J. Hu, F. Zhu, A. Madan, and C. Boehme, *Phys. Rev. B* **79**, 195205 (2009).
- [187] S.-Y. Lee, S.-Y. Paik, D. R. McCamey, J. Hu, F. Zhu, A. Madan, and C. Boehme, *Appl. Phys. Lett.* **97**, 192104 (2010).
- [188] A. I. Shushin, *Phys. Rev. B* **84**, 115212 (2011).
- [189] G. E. Pake, *J. Chem. Phys.* **16**, 327 (1948).
- [190] B. Blümich. *Essential NMR: For Scientists and Engineers* (Springer, Berlin, 2005).
- [191] R. Glenn, M. E. Limes, B. Pankovich, B. Saam, and M. E. Raikh, *Phys. Rev. B* **87**, 155128 (2013).
- [192] Y. Prior, J. A. Kash, and E. L. Hahn, *Phys. Rev. A* **18**, 2603 (1978).
- [193] Y. Zur, M. H. Levitt, and S. Vega, *J. Chem. Phys.*, **78**, 5293 (1983).
- [194] A. S. M. Windsor, C. Wei, S. A. Holmstrom, J. F. D. Martin, and N. B. Manson, *Phys. Rev. Lett.* **80**, 3045 (1998).
- [195] J. H. Shirley, *Phys. Rev.* **138**, B979 (1965).

- [196] I. I. Rabi, Phys. Rev. **51**, 652 (1937).
- [197] I. I. Rabi, N. F. Ramsey, and J. Schwinger, Rev. Mod. Phys. **26**, 167 (1954).
- [198] S. Haroche, C. Cohen-Tannoudji, C. Audoin, and J. P. Schermann, Phys. Rev. Lett. **24**, 861 (1970).
- [199] C. Cohen-Tannoudji and D. Guéry-Odelin, *Advances In Atomic Physics: An Overview* (World Scientific, London, 2011).
- [200] H. Bateman and A. Erdélyi, *Higher Transcendental Functions* (McGraw-Hill, New York, 1953).
- [201] E. L. Hahn and D. E. Maxwell, Phys. Rev. **88**, 1070 (1952).
- [202] A. G. Redfield, Phys. Rev. **98**, 1787 (1955).
- [203] T. Gullion, Chem. Phys. Lett. **246**, 325 (1995).
- [204] A. Pines, M. G. Gibby, and J. S. Waugh, J. Chem. Phys. **59**, 569 (1973).
- [205] S. Hediger, B. H. Meier, and R. R. Ernst, J. Chem. Phys. **102**, 4000 (1995).
- [206] M. Garwood and L. DelaBarre, J. Magn. Reson. **153**, 155 (2001).
- [207] H. Kessemeier and W.-K. Rhim, Phys. Rev. B **5**, 761 (1972).
- [208] H. Hatanaka and N. Tabuchi, J. Magn. Reson. **155**, 119 (2002).
- [209] H. Hatanaka, M. Sugiyama, and N. Tabuchi, J. Magn. Reson. **165**, 293 (2003).
- [210] R. W. Mair, M. I. Hrovat, S. Patz, M. S. Rosen, I. C. Ruset, G. P. Topulos, L. L. Tsai, J. P. Butler, F. W. Hersman, and R. L. Walsworth, Magn. Reson. Med. **53**, 745 (2005).
- [211] F. Bloch and A. Siegert, Phys. Rev. **57**, 522 (1940).
- [212] V. N. Ostrovsky and E. Horsdal-Pedersen, Phys. Rev. A **70**, 033413 (2004).
- [213] B. Lancor and T. G. Walker, Phys. Rev. A **82**, 043417 (2010).
- [214] M. V. Romalis, Phys. Rev. Lett. **105**, 243001 (2010).
- [215] W. Happer and W.A. Wijngaarden, Hyperfine Inter. **38**, 435 (1987).
- [216] R. W. Schmieder, A. Lurio, W. Happer, and A. Khadjavi, Phys. Rev. A **2**, 1216 (1970).
- [217] N. D. Bhaskar, J. Camparo, W. Happer, and A. Sharma, Phys. Rev. A **23**, 3048 (1981).
- [218] C. Kittel and E. Abrahams, Phys. Rev. **90**, 238 (1953).

- [219] B. M. Goodson, Y.-Q. Song, R. E. Taylor, V. D. Schepkin, K. M. Brennan, G. C. Chingas, T. F. Budinger, G. Navon, and A. Pines, *Proc. Nat. Acad. Sci.* **94**, 14725 (1997).
- [220] W. Kilian, F. Seifert, and H. Rinneberg, *Magn. Reson. Med.* **51**, 843 (2004).
- [221] K. Ruppert, J. F. Mata, J. R. Brookeman, K. D. Hagspiel, and J. P. Mugler, *Magn. Reson. Med.* **51**, 676 (2004).
- [222] Z. I. Cleveland, G. P. Cofer, G. Metz, D. Beaver, J. Nouls, S. Sivaram Kaushik, M. Kraft, J. Wolber, K. T. Kelly, H. Page McAdams, and B. Driehuys, *PLoS ONE* **5**, e12192 (2010).
- [223] I. Dregely, J. P. Mugler, I. C. Ruset, T. A. Altes, J. F. Mata, G. W. Miller, J. Ketel, S. Ketel, J. Distelbrink, F. W. Hersman, and K. Ruppert, *J. Magn. Reson. Imag.* **33**, 1052 (2011).
- [224] S. S. Kaushik, Z. I. Cleveland, G. P. Cofer, G. Metz, D. Beaver, J. Nouls, M. Kraft, W. Auffermann, J. Wolber, H. Page McAdams, and B. Driehuys, *Magn. Reson. Med.* **65**, 1154 (2011).
- [225] T. Rõõm, S. Appelt, R. Seydoux, E. L. Hahn, and A. Pines, *Phys. Rev. B* **55**, 11604 (1997).
- [226] L. Schröder, T. J. Lowery, C. Hilty, D. E. Wemmer, and A. Pines, *Science* **314**, 446 (2006).
- [227] X. Zhou, D. Graziani, and A. Pines, *Proc. Nat. Acad. Sci.* **106**, 16903 (2009).
- [228] M. P. Ledbetter, S. Pustelny, D. Budker, M. V. Romalis, J. W. Blanchard, and A. Pines, *Phys. Rev. Lett.* **108**, 243001 (2012).
- [229] B. T. Saam and M. S. Conradi, *J. Magn. Reson.* **134**, 67 (1998).
- [230] B. N. Berry-Pusey, B. C. Anger, G. Laicher, and B. Saam, *Phys. Rev. A* **74**, 063408 (2006).
- [231] B. C. Anger, G. Schrank, A. Schoeck, K. A. Butler, M. S. Solum, R. J. Pugmire, and B. Saam, *Phys. Rev. A* **78**, 043406 (2008).
- [232] B. Anger, Ph.D. thesis, University of Utah, 2008.
- [233] R. M. Herman, *Phys. Rev.* **136**, A1576 (1964).
- [234] C. C. Bouchiat, M. A. Bouchiat, and L. C. L. Pottier, *Phys. Rev.* **181**, 144 (1969).
- [235] M. A. Bouchiat, J. Brossel, and L. C. Pottier, *J. Chem. Phys.* **56**, 3703 (1972).
- [236] N. D. Bhaskar, W. Happer, and T. McClelland, *Phys. Rev. Lett.* **49**, 25 (1982).
- [237] W. Happer, E. Miron, S. Schaefer, D. Schreiber, W. A. van Wijngaarden, and X. Zeng, *Phys. Rev. A* **29**, 3092 (1984).

- [238] X. Zeng, Z. Wu, T. Call, E. Miron, D. Schreiber, and W. Happer, *Phys. Rev. A* **31**, 260 (1985).
- [239] G. D. Cates, R. J. Fitzgerald, A. S. Barton, P. Bogorad, M. Gatzke, N. R. Newbury, and B. Saam, *Phys. Rev. A* **45**, 4631 (1992).
- [240] C. H. Volk, T. M. Kwon, and J. G. Mark, *Phys. Rev. A* **21**, 1549 (1980).
- [241] N. D. Bhaskar, W. Happer, M. Larsson, and X. Zeng, *Phys. Rev. Lett.* **50**, 105 (1983).
- [242] S. R. Schaefer, G. D. Cates, T.-R. Chien, D. Gonatas, W. Happer, and T. G. Walker, *Phys. Rev. A* **39**, 5613 (1989).
- [243] N. Ramsey, E. Miron, X. Zeng, and W. Happer, *Chem. Phys. Lett.* **102**, 340 (1983).
- [244] Y.-Y. Jau, N. N. Kuzma, and W. Happer, *Phys. Rev. A* **66**, 052710 (2002).
- [245] B. Driehuys, G. D. Cates, and W. Happer, *Phys. Rev. Lett.* **74**, 4943 (1995).
- [246] I. L. Moudrakovski, S. R. Breeze, B. Simard, C. I. Ratcliffe, J. A. Ripmeester, T. Seideman, J. S. Tse, and G. Santyr, *J. Chem. Phys.* **114**, 2173 (2001).
- [247] B. Chann, I. A. Nelson, L. W. Anderson, B. Driehuys, and T. G. Walker, *Phys. Rev. Lett.* **88**, 113201 (2002).
- [248] H. E. Möller, Z. I. Cleveland, and B. Driehuys, *J. Magn. Reson.* **212**, 109 (2011).
- [249] Z. I. Cleveland and T. Meersmann, *Chem. Phys. Chem.* **9**, 1375 (2008).